Die approbierte gedruckte Originalversion dieser Dissertation ist an der TU Wien Bibliothek verfügbar.
The approved original version of this doctoral thesis is available in print at TU Wien Bibliothek.

TECHNISCHE UNIVERSITÄT WIEN

HEPHY ÖAW

DISSERTATION

Measurement of the $t\bar{t}\gamma$ cross section and effective field theory interpretation with the CMS experiment

zur Erlangung des akademischen Grades

Doktor der Technischen Wissenschaften

im Rahmen des Studiums

Technische Physik

eingereicht von

Dipl.-Ing. Lukas Lechner BSc
Matrikelnummer 01125704

ausgeführt am Institut für Hochenergiephysik
der Österreichischen Akademie der Wissenschaften

unter der Betreuung von
Priv.-Doz. Dipl.-Ing. Dr. Robert Schöfbeck

Wien, 26. September 2021

Unterschrift Betreuer

Unterschrift Verfasser

Die approbierte gedruckte Originalversion dieser Dissertation ist an der TU Wien Bibliothek verfügbar.
The approved original version of this doctoral thesis is available in print at TU Wien Bibliothek.

Abstract

The standard model (SM) of particle physics, a theory of the currently known elementary particles and their fundamental interactions, provides predictions in agreement with experimental results up to the highest achievable precision. It is one of the most stringently tested theories, still known to be incomplete. If we suppose that new particles are too heavy for discovery at the Large Hadron Collider (LHC) at CERN, indirect effects can still be discernible in deviations in kinematic spectra at much lower energies. Because the top quark plays a crucial rôle in many beyond the SM theories, its interactions are sensitive probes of new physics phenomena. In particular, the measurement of the inclusive and differential cross sections of a top quark pair in association with a photon ($t\bar{t}\gamma$) will access the electromagnetic top quark coupling.

A data set of $137\,\mathrm{fb}^{-1}$ integrated luminosity of proton-proton collisions at a center-of-mass energy of $\sqrt{s} = 13\,\mathrm{TeV}$, recorded by the CMS experiment during the LHC Run 2 (2016–2018) data taking, is used for the measurement of the inclusive and differential $t\bar{t}\gamma$ cross sections. Events are selected by requiring one charged lepton (electron or muon), one isolated photon, and at least three jets from the hadronization of quarks, where at least one has to originate from a bottom quark. The photon may be emitted from an initial-state quark, the top quark, or any decay product of the top quark. The inclusive cross section of the $t\bar{t}\gamma$ process is measured for a photon transverse momentum greater than $20\,\mathrm{GeV}$ and absolute value of the pseudorapidity $|\eta| < 1.4442$. The measured $t\bar{t}\gamma$ cross section in the fiducial phase space of $798 \pm 7\,(\mathrm{stat}) \pm 48\,(\mathrm{syst})$ fb is in good agreement with the SM prediction of 773 ± 135 fb from simulations at next-to-leading order in quantum chromodynamics. Differential cross section measurements are performed in several kinematic observables and unfolded to the particle level, allowing for comparisons to theoretical predictions. The measurements are interpreted in terms of the SM effective field theory and are used to set constraints on anomalous electromagnetic dipole interactions of the top quark that are the most stringent to date.

Die approbierte gedruckte Originalversion dieser Dissertation ist an der TU Wien Bibliothek verfügbar.
The approved original version of this doctoral thesis is available in print at TU Wien Bibliothek.
TU Bibliothek Your knowledge hub WIEN

Die approbierte gedruckte Originalversion dieser Dissertation ist an der TU Wien Bibliothek verfügbar.
The approved original version of this doctoral thesis is available in print at TU Wien Bibliothek.

Kurzfassung

Das Standardmodell (SM) der Teilchenphysik, eine Theorie der derzeitig bekannten Elementarteilchen und deren Wechselwirkungen, liefert präzise Vorhersagen in Übereinstimmung mit experimentellen Ergebnissen. Es zählt, trotz bekannter Unvollständigkeit, zu einer der am strengsten getesteten Theorien. Ist die Masse neuer Teilchen für derzeitige Teilchenbeschleuniger wie dem Large Hadron Collider (LHC) am CERN jedoch nicht erreichbar, so wird der Nachweis ihrer Existenz in Abweichung kinematischer Spektren der SM Teilchen bei geringeren Energien sichtbar. Das Top-Quark spielt in vielen Theorien jenseits des SM eine wichtige Rolle. Seine Wechselwirkungen, im Speziellen die elektromagnetische Top-Quark-Photon Kopplung, sind sensitiv auf Einflüsse neuer Physik. Die Messung der inklusiven und differentiellen Produktionswechselwirkungsquerschnitte eines Top-Quark Paares in Verbindung mit einem Photon ($t\bar{t}\gamma$) ermöglicht den Zugang zu dieser Kopplung.

Für die Messung der inklusiven und differentiellen $t\bar{t}\gamma$ Produktionswechselwirkungsquerschnitte wird ein vom CMS Experiment in der LHC Run 2 (2016–2018) Datenaufnahme aufgezeichneter Datensatz von $137\,\text{fb}^{-1}$ integrierter Luminosität an Proton-Proton Kollisionen bei einer Schwerpunktsenergie von $\sqrt{s} = 13\,\text{TeV}$ verwendet. Zur Analyse herangezogene Ereignisse müssen ein geladenes Lepton (Elektron oder Myon), ein isoliertes Photon, mindestens drei Jets aus der Hadronisierung von Quarks, von denen mindestens einer von einem Bottom-Quark stammt, aufweisen. Das Photon kann von einem Quark im Anfangszustand, dem Top-Quark oder den Zerfallsprodukten des Top-Quarks emittiert werden. Der inklusive Produktionswechselwirkungsquerschnitt des $t\bar{t}\gamma$ Prozesses wird für einen transversalen Photon-Impuls größer als 20 GeV und einem Absolutwert der Pseudorapidität $|\eta| < 1.4442$ gemessen. Der gemessene $t\bar{t}\gamma$ Produktionswechselwirkungsquerschnitt von $798 \pm 7\,(\text{stat}) \pm 48\,(\text{syst})$ fb ist in guter Übereinstimmung mit der SM Vorhersage von 773 ± 135 fb in Simulationen nächst-führender Ordnung in Quantenchromodynamik. Differentielle Produktionswechselwirkungsquerschnittsmessungen werden in diversen kinematischen Observablen durchgeführt und auf die Teilchenebene entfaltet, was einen Vergleich mit theoretischen Vorhersagen ermöglicht. Die Messungen werden im Kontext der effektiven Feldtheorie des SM interpretiert und für die derzeit stärkste Einschränkung anormaler elektromagnetischer Dipolmomente des Top-Quarks verwendet.

Die approbierte gedruckte Originalversion dieser Dissertation ist an der TU Wien Bibliothek verfügbar.
The approved original version of this doctoral thesis is available in print at TU Wien Bibliothek.
TU Bibliothek Your knowledge hub WIEN

Die approbierte gedruckte Originalversion dieser Dissertation ist an der TU Wien Bibliothek verfügbar.
The approved original version of this doctoral thesis is available in print at TU Wien Bibliothek.

Contents

Die approbierte gedruckte Originalversion dieser Dissertation ist an der TU Wien Bibliothek verfügbar.
The approved original version of this doctoral thesis is available in print at TU Wien Bibliothek.
TU Bibliothek Your knowledge hub WIEN

Die approbierte gedruckte Originalversion dieser Dissertation ist an der TU Wien Bibliothek verfügbar.
The approved original version of this doctoral thesis is available in print at TU Wien Bibliothek.
TU Bibliothek Your knowledge hub WIEN

Chapter 1

Introduction

The standard model (SM) of particle physics [1–3] successfully describes the interaction of all known elementary particles at an extreme precision, from the low-energy regime up to the TeV scale. It was completed in 2012 when the CMS [4] and ATLAS [5] collaborations of the Large Hadron Collider (LHC) at CERN announced the discovery of the Higgs boson, the last missing piece of the SM. Already predicted in 1964 [6, 7], the discovery is yet another success for the SM. However, despite the extraordinary success and predictive power, its era will end. It does not include gravity, cannot describe dark energy [8, 9], or provide a suitable dark matter candidate [9–13]. The SM is known to be an incomplete theory that needs to be replaced at energy scales much higher than accessible at current particle colliders, such as the LHC.

The top quark, discovered in 1995 [14, 15], is the heaviest elementary particle of the SM. It is the only quark with a lifetime much shorter than the timescale of hadronization and decays almost exclusively to a W boson and a bottom quark. In contrast to other SM fermions, its Yukawa coupling to the Higgs boson is close to unity. Due to its unique properties, the top quark plays a crucial rôle in many beyond the SM (BSM) theories [16–22] and is expected to couple to hypothetical new particles in those models. However, if those new particles are too heavy and thus, cannot be produced resonantly, BSM effects can still be visible in deviations of top quark couplings to other SM particles from its predictions. In this case, the SM effective field theory (SM-EFT) [23–29] provides a model-independent method to parametrize possible unknown physics effects, which becomes the theoretical tool for exploring the imprints of BSM particles.

This thesis describes the measurement of inclusive and differential cross sections of a top quark pair in association with a photon ($t\bar{t}\gamma$). Measurements of this process allow for accessing the top quark-photon coupling, where any deviation from the SM prediction is indicative of new-physics effects. A large amount of collision data is needed to be analyzed to reach the precision regime for measurements of the small $t\bar{t}\gamma$ production cross section. The CMS experiment has collected a data set of $137\,\mathrm{fb}^{-1}$ of proton-proton (pp) collisions at a center-of-mass energy of $\sqrt{s} = 13\,\mathrm{TeV}$. The collision data was recorded during the Run 2 (2016–2018) data taking of the LHC and is analyzed in the presented results of this thesis. The measurements are the first $t\bar{t}\gamma$ cross section measurements using a data set collected by the CMS experiment at a center-of-mass energy of 13 TeV.

TU Bibliothek Your knowledge hub WIEN
Die approbierte gedruckte Originalversion dieser Dissertation ist an der TU Wien Bibliothek verfügbar.
The approved original version of this doctoral thesis is available in print at TU Wien Bibliothek.

The inclusive $t\bar{t}\gamma$ cross section is measured in a fiducial phase space with one highly energetic photon and one isolated electron or muon. At least three jets from the hadronization of quarks are required, where at least one has to originate from a bottom quark. The photon is measured for a transverse momentum $p_T(\gamma) > 20\,\text{GeV}$ and absolute value of the pseudorapidity $|\eta(\gamma)| < 1.4442$. It may be emitted from an initial-state quark, the top quark, or any decay product of the top quark. The differential cross section measurements are performed in the kinematic observables of $p_T(\gamma)$, $|\eta(\gamma)|$, and the angular separation of the photon and the lepton $\Delta R(\ell, \gamma)$. The observed distributions are unfolded to the particle level, allowing for comparisons to theoretical predictions. In addition, statistical and systematic covariance matrices of the differential measurements at the particle level are provided for future reinterpretations of the results.

The results are interpreted in terms of SM-EFT in the Warsaw basis [30], formed by 59 dimension-six Wilson coefficients. The measurements are used to set constraints on the dimension-six operators inducing electroweak dipole moments of the top quark, leading to the tightest direct limits on anomalous top quark couplings to the photon to date.

A more detailed introduction to the SM, the top quark, and SM-EFT is given in Chapter 2. An overview of the CERN LHC and the CMS detector is provided in Chapter 3, followed by a detailed discussion on the analysis strategy, the background estimation methods, systematic uncertainties, and the results of the inclusive and differential cross section measurements of the $t\bar{t}\gamma$ process in Chapter 4. Technical methods, sensitivity studies, and resulting confidence intervals of the SM-EFT interpretation are shown in Chapter 5. The conclusion is given in Chapter 6 and additional material is provided in Appendix A.

The results of this thesis are published in Ref. [31], and tabulated results are provided in HEPData [32]. Results were presented by the author on behalf of the CMS collaboration at the 55TH RENCONTRES DE MORIOND [33], the LHCTOP 2021 [34], and the JOINT ANNUAL MEETING OF ÖPG AND SPS 2021 [35] conferences. Several additional contributions to publications were provided during the work on this thesis:

Peer-reviewed

[31] CMS Collaboration. "Measurement of the inclusive and differential $t\bar{t}\gamma$ cross sections in the single-lepton channel and EFT interpretation at $\sqrt{s} = 13\,\text{TeV}$". *Submitted to JHEP* (2021). arXiv: 2107.01508

[36] CMS Collaboration. "Measurement of the inclusive and differential $t\bar{t}\gamma$ cross section and EFT interpretation in the dilepton channel at $\sqrt{s} = 13\,\text{TeV}$". *Prepared for submission to JHEP* (2021). URL: https://bit.ly/39lEmAn

[37] S. Chatterjee, N. Frohner, L. Lechner, R. Schöfbeck, and D. Schwarz. "Tree boosting for learning EFT parameters". *Submitted to Comput. Phys. Commun.* (2021). arXiv: 2107.10859

[38] S. Fernbach, L. Lechner, A. Maas, S. Plätzer, and R. Schöfbeck. "Constraining the Higgs valence contribution in the proton". *Phys. Rev. D* 101 (2020), p. 114018. DOI: 10.1103/PhysRevD.101.114018. arXiv: 2002.01688

Die approbierte gedruckte Originalversion dieser Dissertation ist an der TU Wien Bibliothek verfügbar.
The approved original version of this doctoral thesis is available in print at TU Wien Bibliothek.
TU Bibliothek Your knowledge hub WIEN

Non-peer-reviewed

[33] L. Lechner. "$t\bar{t}+\gamma$ inclusive and differential measurement by CMS". *Submitted to ARISF* (2021). Proceedings of the 55th Rencontres de Moriond 2021 Electroweak Interactions and Unified Theories. URL: https://bit.ly/2XARsaV

[39] N. Andari et al. "Report on the ECFA early-career researchers debate on the 2020 European Strategy Update for Particle Physics" (2020). arXiv: 2002.02837

[40] P. Azzi et al. "Report from working group 1: Standard model physics at the HL-LHC and HE-LHC". *CERN Yellow Rep. Monogr.* 7 (2019), p. 1. DOI: 10.23731/CYRM-2019-007.1. arXiv: 1902.04070

Die approbierte gedruckte Originalversion dieser Dissertation ist an der TU Wien Bibliothek verfügbar.
The approved original version of this doctoral thesis is available in print at TU Wien Bibliothek.
TU Bibliothek Your knowledge hub WIEN

Die approbierte gedruckte Originalversion dieser Dissertation ist an der TU Wien Bibliothek verfügbar.
The approved original version of this doctoral thesis is available in print at TU Wien Bibliothek.

Die approbierte gedruckte Originalversion dieser Dissertation ist an der TU Wien Bibliothek verfügbar.
The approved original version of this doctoral thesis is available in print at TU Wien Bibliothek.

Chapter 2

The top quark in the standard model and beyond

The SM of particle physics [1–3] is the unbeaten theory of elementary particles and their interactions. It is known to be incomplete, triggering a great effort in looking for possible BSM physics and the search for unknown particles. Although the mass of new particles may exceed the energy reachable by the LHC, small deviations in kinematic spectra from SM predictions can still give a hint on their origin.

This chapter gives a theoretical introduction to the SM, its shortcomings, and the special rôle of the top quark. The SM-EFT [23–29] is introduced as the theoretical tool for describing possible unknown physics effects in a model-independent way.

2.1 The standard model of particle physics

The SM incorporates elementary matter particles that form the visible universe and messenger particles that mediate the fundamental forces. It is a quantum field theory (QFT) based on local gauge symmetries, describing the interaction of elementary particles up to the highest energies achievable by current particle colliders. In the following, the SM particle content and their fundamental interactions are introduced. Additionally, a brief mathematical description of the SM symmetry groups and the mechanism of electroweak symmetry breaking (EWSB), giving mass to elementary particles, is provided. An overview of modern event-generation techniques in this section introduces the simulation of SM interactions, essential for comparing experimental results to predictions. This section does not intend to give a complete description of the SM, but rather introduces vital ingredients of its formalism. A detailed discussion can be found in the literature, where this section is based on the description given in Ref. [41].

2.1.1 Elementary particles and interactions

Two types of elementary particles are incorporated in the SM. According to their spin, they are grouped into fermions, half-integer spin matter particles, and bosons, integer spin force carriers, mediating SM interactions. The SM allows for a mathematical description

of the strong, weak, and electromagnetic interaction, three of the four known fundamental forces. Gravity is no part of the SM. While the gravitational force, described by the theory of general relativity [42], has far-reaching effects in the macroscopic universe, it is insignificantly weak on the level of elementary particles and thus, can be neglected in high-energy particle physics.

Bosons and fundamental interactions

Spin-1 vector bosons mediate the fundamental forces. While massless gluons (g) and photons (γ) mediate the strong and electromagnetic force, respectively, the weak force is mediated by massive charged $W^{\pm}$ or neutral Z bosons. However, a naive vector boson mass term in the SM formalism is not gauge invariant. After the discovery of weak neutral currents at the Gargamelle experiment [43] at CERN, the nonzero mass of the weak gauge bosons was puzzling. A solution was proposed by Higgs, Englert, and Brout in 1964 [6, 7] by introducing EWSB, generating masses for massive SM fermions and these heavy gauge bosons. This mechanism additionally gives rise to the only known spin-0 scalar boson, the Higgs boson (H).

SM particles interact via the fundamental forces and thus couple to vector bosons according to their charge. For the electromagnetic interaction, the electric charge is quantized in units of the elementary electric charge e. Thus, electrically charged particles, such as $W^{\pm}$ bosons, interact with the photon. For the weak and strong interaction, the charges are the isospin and the color charge, respectively.

The electromagnetic force is known to have an infinite range. For the strong interaction, the range is limited due to the gluon self-coupling, having far-reaching consequences in high-energy particle physics. The weak interaction is considered short-ranged due to the large mass of the $W^{\pm}$ and Z bosons.

A summary of the fundamental interactions and their force carrier particles within the SM is given in Table 2.1, where at higher energies, the electromagnetic and weak interactions are combined to one single theory of electroweak unification described in Sec. 2.1.2.

Table 2.1: Summary of the fundamental interactions described by the SM, their associated charge, range, relative strength, and mediator particles [44]. The gravitational force is not shown here, as it is no part of the SM.

Interaction	Charge	Range	Relative strength	Mediator particle	Mediator symbol	Mediator mass
Strong	color	short	1	gluon	g	0
Weak	isospin	short	10^{-7}	$W^{\pm}$ boson	$W^{\pm}$	80.38 GeV
				Z boson	Z	91.19 GeV
Electromagnetic	electric	∞	10^{-2}	photon	γ	0

Die approbierte gedruckte Originalversion dieser Dissertation ist an der TU Wien Bibliothek verfügbar.
The approved original version of this doctoral thesis is available in print at TU Wien Bibliothek.
TU Bibliothek Your knowledge hub WIEN

Fermions

Fermions, the matter particles, are categorized according to the charges they carry. Color-neutral fermions are known as leptons, and color-charged fermions are called quarks, interacting via the strong force. For each fermion, an antiparticle exists, having identical properties but opposite charges. A summary of the fermions and their masses is given in Table 2.2 and are further discussed in the following.

From the six leptons, three are electrically charged and three are neutral. While leptons do not interact strongly, all leptons are subject to the weak interaction. Three generations of leptons exist, where the first generation of charged leptons, the electron (e), is known to be a stable building block of the atomic shell. Heavier charged leptons, the muon (μ) and the tau (τ), decay in weak interactions. Neutrinos (ν) only interact weakly and the neutrino flux limits their detection in colliding-beam experiments.

Six quarks are known to date, interacting via the three fundamental forces in the SM and couple to the corresponding bosons. Their electric charge categorizes them into up-type and down-type quarks, with a fractional elementary electric charge of $+2/3$ and $-1/3$, respectively. Quarks are grouped into three generations, with the first generation consisting of up (u) and down (d) quarks, the building blocks of protons and neutrons, and thus the atomic nuclei. The second and third generations contain quarks with the same quantum numbers as the up (up-type) and down (down-type) quarks, however, they differ in mass and lifetime.

Table 2.2: Summary of the fermions, their charge, and mass for the three generations in the SM [44].

	Generation	Name	Symbol	Electric charge	Isospin	Color charge	Mass
Quarks	1st gen.	up	u	$+2/3\,e$	$+1/2$	✓	2.16 MeV
		down	d	$-1/3\,e$	$-1/2$	✓	4.67 MeV
	2nd gen.	charm	c	$+2/3\,e$	$+1/2$	✓	1.27 GeV
		strange	s	$-1/3\,e$	$-1/2$	✓	0.093 GeV
	3rd gen.	top	t	$+2/3\,e$	$+1/2$	✓	172.76 GeV
		bottom	b	$-1/3\,e$	$-1/2$	✓	4.18 GeV
Leptons	1st gen.	electron	e	$-1\,e$	$-1/2$		0.511 MeV
		e-neutrino	ν_e	0	$+1/2$		<1.1 eV
	2nd gen.	muon	μ	$-1\,e$	$-1/2$		0.106 GeV
		μ-neutrino	ν_μ	0	$+1/2$		<1.1 eV
	3rd gen.	tau	τ	$-1\,e$	$-1/2$		1.777 GeV
		τ-neutrino	ν_τ	0	$+1/2$		<1.1 eV

Die approbierte gedruckte Originalversion dieser Dissertation ist an der TU Wien Bibliothek verfügbar.
The approved original version of this doctoral thesis is available in print at TU Wien Bibliothek.
TU Bibliothek Your knowledge hub WIEN

The top quark

The heaviest known quark is the top quark, an up-type quark with a mass of 172.76 GeV and a particularly short lifetime of $\approx 5 \cdot 10^{-25}$ s [44]. The existence of the top quark was predicted in 1973 [45]. Kobayashi and Maskawa proposed to replace the Glashow–Iliopoulos–Maiani mechanism [46], a 2×2 rotation matrix of the back-then known two generations of quarks, with the 3×3 Cabibbo–Kobayashi–Maskawa (CKM) matrix [45, 46]. By including a complex phase, the CKM matrix allowed to explain the observed charge and parity ($\mathcal{CP}$) violation in kaon decays [47]. However, extending the rotation matrix to a 3×3 CKM matrix is only possible by introducing a third generation of quarks, an isospin doublet formed by an up- and down-type quark, which are now known as the top and bottom quark.

The first success of the theory was the discovery of the third-generation charged lepton, the tau lepton, by the SLAC-LBL experiment in 1975 [48], followed by the discovery of the third-generation down-type quark, the bottom quark, by the Fermilab E288 experiment in 1977 [49]. The discovery of a third generation in the lepton and quark sector already hinted at the existence of an unknown neutrino and the missing up-type quark. Precision measurements of the invisible decay width of the Z boson at the LEP collider [50] confirmed the existence of three generations of neutrinos [51–54]. Due to missing anomalies in the bottom quark decay [55–58], the existence of the top quark was strongly suggested as the last missing fermion in the SM.

Discovered by the CDF [14] and D0 [15] collaborations of the Tevatron collider at Fermilab in 1995, the top quark became one of the most interesting elementary particles to study at particle colliders, with its properties and interactions discussed in Sec. 2.2.

2.1.2 Standard model gauge symmetries

The mathematical formalism of the SM is built on local gauge symmetries specified by the group structure. The complete symmetry group of the SM is denoted as

$$\mathrm{SU}(3) \times [\mathrm{SU}(2) \times \mathrm{U}(1)]_{\mathrm{EW}} \tag{2.1.1}$$

as a product of three symmetry groups, where each describes a specific type of interaction of SM particles. The Poincaré symmetry group is used as a basis, extended by the group formalism of the SM according to the Coleman–Mandula theorem [59].

The basic principle of symmetry groups is used to derive a Lagrangian formalism that describes the physical system and the behavior of fundamental particles in the SM. From the Lagrangian formalism, one can define the gauge-invariant action S as

$$S = \int \mathcal{L}\, d^4x, \tag{2.1.2}$$

where $\mathcal{L}$ is the Lagrangian density, or Lagrangian for short. In order to not violate the conservation laws embedded in the Poincaré symmetry group, the action S, and thus the Lagrangian $\mathcal{L}$, needs to be invariant under the transformation of the symmetry group. Invariance is not necessarily given in the SM, which is why it needs to be restored, as discussed in the following for the three components of the SM.

Die approbierte gedruckte Originalversion dieser Dissertation ist an der TU Wien Bibliothek verfügbar.
The approved original version of this doctoral thesis is available in print at TU Wien Bibliothek.
TU Bibliothek Your knowledge hub WIEN

Quantum electrodynamics

The Lagrangian of quantum electrodynamics (QED) describes the interaction of a massive spin-$\frac{1}{2}$ fermion field ψ with the massless spin-1 photon field and is thus suitable for the mathematical description of electromagnetism. It is based on the famous Dirac equation

$$(i\gamma_\mu\partial^\mu - \mathrm{m})\,\psi = 0, \tag{2.1.3}$$

with the fermion mass m and the Dirac matrices γ_μ. The Lagrangian describing the spin-$\frac{1}{2}$ fermion field is thus given by

$$\mathcal{L}_{\mathrm{Dirac}} = \bar{\psi}\,(i\gamma_\mu\partial^\mu - \mathrm{m})\,\psi = i\bar{\psi}\gamma_\mu\partial^\mu\psi - \mathrm{m}\bar{\psi}\psi, \tag{2.1.4}$$

using the conjugate fermion field $\bar{\psi} = \psi^\dagger\gamma^0$. As can be seen, the Lagrangian is invariant under global U(1) transformations $\psi \to \psi' = e^{i\alpha}\psi$, for a constant α. However, a local transformation, with α depending on the position $\alpha = \alpha(x)$, breaks the U(1) invariance due to the kinetic term

$$\partial_\mu\psi \to \partial_\mu\psi' = \partial_\mu\left(e^{i\alpha(x)}\psi\right) = e^{i\alpha(x)}\left(\partial_\mu\psi + i\left(\partial_\mu\alpha(x)\right)\psi\right). \tag{2.1.5}$$

A spin-1 field A_μ, on the other hand, is described by the Proca Lagrangian

$$\mathcal{L}_{\mathrm{Proca}} = \partial^\mu A^\nu\partial_\mu A_\nu - \partial^\mu A^\nu\partial_\nu A_\mu + \mathrm{m}_A^2 A^\mu A_\mu, \tag{2.1.6}$$

where m_A is the mass of the gauge boson. It is seen that the Lagrangian is invariant under global and local transformations $A_\mu \to A'_\mu = A_\mu - \partial_\mu\alpha(x)$ for massless gauge bosons $\mathrm{m}_A = 0$, such as the photon.

Adding the Lagrangians of the massive spin-$\frac{1}{2}$ fermion field ψ and the massless spin-1 photon field restores the symmetry for local transformations in defining the covariant derivative D_μ as

$$D_\mu = \partial_\mu + iA_\mu, \tag{2.1.7}$$

leading to the invariance of the kinetic term of the Lagrangian

$$D_\mu\psi \to D'_\mu\psi' = \left(\partial_\mu + i\left(A_\mu - \partial_\mu\alpha(x)\right)\right)e^{i\alpha(x)}\psi = e^{i\alpha(x)}D_\mu\psi. \tag{2.1.8}$$

The full QED Lagrangian is given by

$$\mathcal{L}_{\mathrm{QED}} = -\mathrm{m}\bar{\psi}\psi + i\bar{\psi}\gamma_\mu\partial^\mu\psi - \bar{\psi}\gamma_\mu\psi A^\mu + \partial^\mu A^\nu\partial_\mu A_\nu - \partial^\mu A^\nu\partial_\nu A_\mu. \tag{2.1.9}$$

Using the covariant derivative and the definition of the electromagnetic field strength tensor $F_{\mu\nu} = \partial_\mu A_\nu - \partial_\nu A_\mu$, the QED Lagrangian can be written in the compact form

$$\mathcal{L}_{\mathrm{QED}} = \bar{\psi}\,(i\gamma_\mu D^\mu - \mathrm{m})\,\psi - \frac{1}{4}F_{\mu\nu}F^{\mu\nu}. \tag{2.1.10}$$

The Lagrangian now provides a mass and kinetic term for the spin-$\frac{1}{2}$ fermion field, a free spin-1 photon field, and an additional term $\bar{\psi}\gamma_\mu\psi A^\mu$, describing the interaction between the fields ψ and A_μ.

The basic principle of symmetry and the requirement of local gauge invariance leads to a mathematical description of the interaction of formerly free gauge fields. Thus, QED calculations can be used to describe the interaction of a charged fermion, such as the electron, with a photon and have been verified in measuring the magnetic moment of the electron [60] to unprecedented precision. The Noether theorem [61] shows the conservation of the electric charge as a result of the U(1) symmetry.

Die approbierte gedruckte Originalversion dieser Dissertation ist an der TU Wien Bibliothek verfügbar.
The approved original version of this doctoral thesis is available in print at TU Wien Bibliothek.
TU Bibliothek Your knowledge hub WIEN

Electroweak unification

Adding to the success of QED and symmetry groups as the description of electromagnetism in the SM, building a gauge theory for the weak force is the next step. The Wu experiment [62] showed weak gauge bosons only interact with left-handed particles and right-handed antiparticles, maximally violating the conservation of parity ($\mathcal{P}$). Thus, the chiral structure of the SM allows for different interactions on left- and right-handed particles, adding additional difficulty in the formalism of the weak force in symmetry groups. Mediated by three gauge bosons, an attempt to describe the theory uses the SU(2) symmetry group, organizing left-handed fermions in SU(2) doublets and right-handed fermions in singlets.

Starting with two copies of the Dirac Lagrangian $\mathcal{L}_{\text{Dirac}}$ for massless spin-$\frac{1}{2}$ fermion fields

$$\mathcal{L}_{\text{D}_1+\text{D}_2} = i\bar{\psi}\gamma_\mu\partial^\mu\psi, \tag{2.1.11}$$

a fermion doublet is defined by $\psi = \begin{pmatrix}\psi_1\\ \psi_2\end{pmatrix}$ and $\bar{\psi} = \begin{pmatrix}\bar{\psi}_1 & \bar{\psi}_2\end{pmatrix}$. The Lagrangian is invariant under the global transformation $\psi \to \psi' = e^{i\alpha_i\frac{\tau_i}{2}}\psi$, with suitable generators in this two-dimensional representation given by the Pauli matrices τ_i. Similar to the U(1) transformation, local invariance is achieved in defining the covariant derivative as

$$D_\mu = \partial_\mu + i\frac{g}{2}W_\mu^i\tau_i = \partial_\mu + i\frac{g}{2}\begin{pmatrix}W_\mu^3 & W_\mu^1 - iW_\mu^2\\ W_\mu^1 + iW_\mu^2 & -W_\mu^3\end{pmatrix}, \tag{2.1.12}$$

where W_μ^i are three spin-1 boson fields, g is the weak-isospin coupling constant, and the sum over same indices is implicit. Off-diagonal entries can be rewritten in introducing complex gauge fields

$$W_\mu^\pm = \frac{1}{\sqrt{2}}\left(W_\mu^1 \mp iW_\mu^2\right), \tag{2.1.13}$$

representing the charged boson fields. Similar to the U(1) transformation, the covariant derivative adds an interaction term to the Lagrangian, which results in the description of two free spin-$\frac{1}{2}$ fermion fields, three free spin-1 boson fields, and additional interactions represented by the terms $\frac{g}{2}\bar{\psi}\gamma_\mu\psi W^{i\mu}\tau_i$. In the latter, the introduction of the fields $W_\mu^\pm$ becomes useful in representing the electrically charged $\text{W}^\pm$ bosons and their interaction with quarks and leptons when writing them into SU(2) doublets, e.g., for leptons and quarks of the first generation

$$l = \begin{pmatrix}\nu_\text{e}\\ \text{e}\end{pmatrix} \quad \text{and} \quad q = \begin{pmatrix}\text{u}\\ \text{d}\end{pmatrix}, \tag{2.1.14}$$

where doublets are included also for other generations. A conserved quantity, the isospin, is a result of the SU(2) symmetry.

Initially, the electromagnetic and weak interactions were independent theories, QED and quantum flavordynamics, respectively. Subsequently, Glashow, Salam, and Weinberg [1–3] described the two interactions with a single $[\text{SU}(2)\times\text{U}(1)]_\text{EW}$ symmetry group, the

Die approbierte gedruckte Originalversion dieser Dissertation ist an der TU Wien Bibliothek verfügbar.
The approved original version of this doctoral thesis is available in print at TU Wien Bibliothek.
TU Bibliothek Your knowledge hub WIEN

electroweak theory. Similar to the U(1) and SU(2) definitions, the covariant derivative of the unified electroweak SU(2) × U(1) gauge field is given by

$$D_\mu = \partial_\mu + i\frac{g'}{2}B_\mu + i\frac{g}{2}W_\mu^i\tau_i = \partial_\mu + \frac{i}{2}\begin{pmatrix} g'B_\mu + gW_\mu^3 & g\left(W_\mu^1 - iW_\mu^2\right) \\ g\left(W_\mu^1 + iW_\mu^2\right) & g'B_\mu - gW_\mu^3 \end{pmatrix}. \tag{2.1.15}$$

The U(1) gauge field is denoted by B_μ and the SU(2) gauge fields by W_μ^i, with the corresponding coupling constants, the weak hypercharge g' and the weak isospin g, respectively. The field strength tensors $B_{\mu\nu}$ and $W_{\mu\nu}$,

$$B_{\mu\nu} = \partial_\mu B_\nu - \partial_\nu B_\mu \tag{2.1.16}$$

$$W_{\mu\nu}^i = \partial_\mu W_\nu^i - \partial_\nu W_\mu^i + g\epsilon^{ijk}W_{j\mu}W_{k\nu}, \tag{2.1.17}$$

describe the kinetic terms and interactions of the fields, with a structure constant given by the antisymmetric tensor ϵ^{ijk}. The mixing of the U(1) gauge field B_μ and the third component of the SU(2) gauge field W_μ^3 form the photon (A_μ) and Z boson (Z_μ) fields according to

$$A_\mu = \quad B_\mu \cos\theta_W + W_\mu^3 \sin\theta_W \tag{2.1.18}$$

$$Z_\mu = -B_\mu \sin\theta_W + W_\mu^3 \cos\theta_W. \tag{2.1.19}$$

The weak mixing angle θ_W is related to the coupling constants by

$$\cos\theta_W = \frac{g}{\sqrt{g^2 + g'^2}} \quad \text{and} \quad \sin\theta_W = \frac{g'}{\sqrt{g^2 + g'^2}}. \tag{2.1.20}$$

Although the electroweak theory can describe the interactions of fermions with the photon, the $W^\pm$, and Z bosons, the basic principle of deriving the Lagrangian was the bosons to be massless. While this is true for the photon, masses of weak bosons are not predicted by this theory so far. The formalism also forbids adding trivial mass terms for fermions, mixing left- and right-handed chiral states. The mechanism that describes fermion and boson masses, resulting in the only known spin-0 scalar boson, the Higgs boson, is described in EWSB.

Electroweak symmetry breaking and standard model mass terms

Naively adding gauge boson mass terms to the Lagrangian breaks gauge invariance. Spontaneous symmetry breaking, induced by a scalar SU(2) doublet, with an appropriate potential can reconcile gauge symmetry with the phenomenological need for massive gauge bosons. In the BEH mechanism, first discussed by Brout, Englert, and Higgs [6, 7], a complex scalar doublet

$$\phi = \begin{pmatrix} \phi^+ \\ \phi^0 \end{pmatrix} \tag{2.1.21}$$

and a Lagrangian for scalar fields $\mathcal{L}_{\text{Higgs}}$ with an additional potential $V(\phi^\dagger\phi)$,

$$\mathcal{L}_{\text{Higgs}} = (D_\mu\phi)^\dagger (D^\mu\phi) - V\left(\phi^\dagger\phi\right), \tag{2.1.22}$$

Die approbierte gedruckte Originalversion dieser Dissertation ist an der TU Wien Bibliothek verfügbar.
The approved original version of this doctoral thesis is available in print at TU Wien Bibliothek.
TU Bibliothek Your knowledge hub WIEN

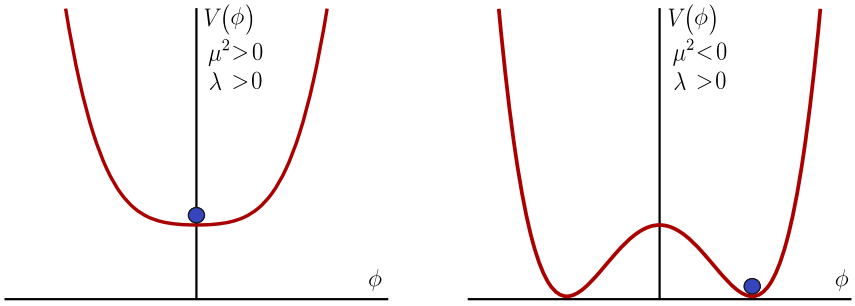

Figure 2.1: The Higgs potential $V(\phi)$ for $\lambda > 0$ with positive (left) and negative (right) values of μ^2. For $\mu^2 < 0$, $\lambda > 0$, the potential forms the famous Mexican-hat shape.

is chosen. The Lagrangian is invariant under local and global $\mathrm{SU}(2) \times \mathrm{U}(1)$ transformations when using the covariant derivative noted in Eq. 2.1.15. The potential of the form

$$V\left(\phi^\dagger\phi\right) = \mu^2\phi^\dagger\phi + \lambda\left(\phi^\dagger\phi\right)^2 \tag{2.1.23}$$

is often referred to as the Higgs potential, which has a trivial minimum at the origin for $\mu^2, \lambda > 0$. As shown in Fig. 2.1, the potential forms a Mexican-hat shape for $\mu^2 < 0$, $\lambda > 0$, with the minimum at

$$|\phi|_{\min} = \sqrt{\frac{-\mu^2}{2\lambda}} = \frac{v}{\sqrt{2}}, \tag{2.1.24}$$

where $v = \sqrt{-\mu^2/\lambda}$ is the Higgs doublet vacuum expectation value (vev). It should be noted that the minimum is not a single point but rather a set of points in a circle in the complex plane. Thus, for $\mu^2 < 0$, $\lambda > 0$, the symmetry is considered broken.

Expanding the Higgs doublet around the minimum breaks the symmetry and leads to

$$\phi(x) = \frac{1}{\sqrt{2}}\begin{pmatrix} 0 \\ v + h(x) \end{pmatrix}, \tag{2.1.25}$$

with the Higgs field $h(x)$. As a result, three Goldstone bosons [63–65] are transformed into the longitudinal component of the massive gauge bosons. The Higgs potential can now be written as

$$V(h) = \lambda v^2 h^2 + \lambda v h^3 + \frac{\lambda}{4}h^4 + \text{const.}, \tag{2.1.26}$$

with the Higgs mass defined by the prefactor of the quadratic term, $\mathrm{m_H} = \sqrt{2\lambda v^2}$, and the cubic and quartic self-couplings of the Higgs boson defined by the second and third term, respectively. The kinetic term of the Lagrangian given in Eq. 2.1.22, using the covariant derivative noted in Eq. 2.1.15, and the definitions of the photon field A_μ (Eq. 2.1.18), the Z boson field Z_μ (Eq. 2.1.19), and the $\mathrm{W}^\pm$ boson fields (Eq. 2.1.13) becomes

$$\begin{aligned}\left(D_\mu\phi\right)^\dagger\left(D^\mu\phi\right) = \frac{1}{2}\partial_\mu h\partial^\mu h + \Bigg[&\left(\frac{gv}{2}\right)^2 W^{\mu+}W^-_\mu \\ &+\frac{1}{2}\left(\frac{v}{2}\right)^2\left(g^2+g'^2\right)Z^\mu Z_\mu \\ &+\frac{1}{2}\left(\frac{v}{2}\right)^2 \cdot 0 \cdot A^\mu A_\mu\Bigg]\left(1+\frac{h}{v}\right)^2.\end{aligned} \tag{2.1.27}$$

Die approbierte gedruckte Originalversion dieser Dissertation ist an der TU Wien Bibliothek verfügbar.
The approved original version of this doctoral thesis is available in print at TU Wien Bibliothek.
TU Bibliothek Your knowledge hub WIEN

From the Lagrangian, one can read off the masses for the gauge bosons

$$\mathrm{m_W} = \frac{gv}{2}, \quad \mathrm{m_Z} = \frac{v}{2}\sqrt{g^2 + g'^2}, \quad \mathrm{m}_A = 0, \tag{2.1.28}$$

resulting in the definition of the weak mixing angle using weak boson masses,

$$\cos\theta_W = \frac{g}{\sqrt{g^2 + g'^2}} = \frac{\mathrm{m_W}}{\mathrm{m_Z}}, \tag{2.1.29}$$

at leading order (LO) precision.

Thus, the electroweak theory formed by the symmetry groups $[\mathrm{SU}(2) \times \mathrm{U}(1)]_{\mathrm{EW}}$ now includes mass terms for massive gauge bosons due to the introduction of a new spin-0 scalar field. Additionally, a massless spin-1 field emerges, which is interpreted as the photon field.

Fermion masses, spoiling the invariance of the SU(2) symmetry when added to the Lagrangian, can be introduced as additional coupling terms to the Higgs field. These coupling terms are described using the SU(2) × U(1) invariant Yukawa term

$$\mathcal{L}_{\mathrm{Yukawa}} = -y_f \left(\bar{\psi}_L \phi \psi_R + \bar{\psi}_R \phi \psi_L\right), \tag{2.1.30}$$

where y_f is the Yukawa coupling and $\psi_{L(R)}$ are left- (right-)handed fermion doublets (singlets). After symmetry breaking, the fermion mass m_f for a given fermion f becomes

$$\mathrm{m}_f = y_f \frac{v}{\sqrt{2}}, \tag{2.1.31}$$

where the mass is proportional to the Higgs field coupling. Various Higgs coupling measurements have been performed at the LHC, in impressive agreement with SM predictions [66].

Assuming massless neutrinos, the mass eigenstates of charged leptons are identical to the weak eigenstates. This is not the case for quarks. A quark weak eigenstate is a mixture of the mass eigenstates, where the mixing matrix is given by the CKM matrix [45, 46]

$$\begin{pmatrix} \mathrm{d}' \\ \mathrm{s}' \\ \mathrm{b}' \end{pmatrix} = \begin{pmatrix} V_{\mathrm{ud}} & V_{\mathrm{us}} & V_{\mathrm{ub}} \\ V_{\mathrm{cd}} & V_{\mathrm{cs}} & V_{\mathrm{cb}} \\ V_{\mathrm{td}} & V_{\mathrm{ts}} & V_{\mathrm{tb}} \end{pmatrix} \begin{pmatrix} \mathrm{d} \\ \mathrm{s} \\ \mathrm{b} \end{pmatrix}, \tag{2.1.32}$$

with the down-type quark mass eigenstates given as d, s, and b, and the weak eigenstates denoted as d′, s′, and b′. Thus, off-diagonal terms in the CKM matrix allow for the mixing of flavor states in the quark sector. Interactions involving the $\mathrm{W}^{\pm}$ bosons, so-called charged-current interactions, can change the flavor of the quarks, while interactions with the photon and the Z boson, neutral-current interactions, are flavor conserving.

Flavor mixing in the neutrino sector, proposed in 1962 [67, 68], was experimentally confirmed by neutrino-oscillation experiments [69, 70]. Similar to the mixing of quark eigenstates in the CKM matrix, the mixing for neutrinos is parametrized by the Pontecorvo–Maki–Nakagawa–Sakata (PMNS) matrix and proofs that at least two of the three neutrinos have mass. Nevertheless, neutrinos are massless in the SM.

Die approbierte gedruckte Originalversion dieser Dissertation ist an der TU Wien Bibliothek verfügbar.
The approved original version of this doctoral thesis is available in print at TU Wien Bibliothek.
TU Bibliothek Your knowledge hub WIEN

Quantum chromodynamics

The SU(3) component of the SM gauge groups is the symmetry group related to the strong force. The underlying theory and mathematical formalism of this interaction is known as quantum chromodynamics (QCD) [71–73]. The strong interaction acts between particles that carry the conserved color charge, which can take three different states, often denoted as red, green, and blue. Similar to Eq. 2.1.4, a Lagrangian of free spin-$\frac{1}{2}$ fermion fields

$$\mathcal{L} = \bar{q}\left(i\gamma_\mu\partial^\mu - \mathrm{m}\right)q = i\bar{q}\gamma_\mu\partial^\mu q - \mathrm{m}\bar{q}q \tag{2.1.33}$$

describes the kinematics of fermion triplets, with $q = \begin{pmatrix} q_\mathrm{r} \\ q_\mathrm{g} \\ q_\mathrm{b} \end{pmatrix}$ and $\bar{q} = \begin{pmatrix} \bar{q}_\mathrm{r} & \bar{q}_\mathrm{g} & \bar{q}_\mathrm{b} \end{pmatrix}$, where entries reflect the three color states. The Lagrangian is locally gauge invariant under the transformation $q \to q' = e^{iT_a\theta^a(x)}q$, with the eight hermitian, traceless generators $T_a = \frac{1}{2}\lambda_a$ and the 3×3 Gell-Mann matrices λ_a [74] when using the covariant derivative

$$D_\mu = \partial_\mu + ig_sG^a_\mu T_a, \tag{2.1.34}$$

with the strong gauge coupling constant g_s and the eight gluon fields G^a_μ corresponding to the electrically neutral, massless spin-1 particles mediating the strong force. Similar to the U(1) symmetry, requiring local gauge invariance results in an interaction term in the QCD Lagrangian. The full QCD Lagrangian becomes

$$\mathcal{L}_\mathrm{QCD} = i\bar{q}\gamma_\mu D^\mu q - \mathrm{m}\bar{q}q - \frac{1}{4}G^a_{\mu\nu}G^{\mu\nu}_a, \tag{2.1.35}$$

with the field strength tensor $G^a_{\mu\nu} = \partial_\mu G^a_\nu - \partial_\nu G^a_\mu - g_s f^a_{bc} G^b_\mu G^c_\nu$ and the SU(3) structure constant f^{abc}. Compared to the electromagnetic field strength tensor, an additional term results from the nonabelian SU(3) gauge group. The generators do not commute with each other, where the Lie algebra for this group is given by

$$[T_a, T_b] = if_{abc}T^c, \tag{2.1.36}$$

resulting in the mathematical description of self-interacting gluons. The interaction term in the Lagrangian given in Eq. 2.1.35 thus leads to quark-antiquark-gluon vertices ($\mathrm{q\bar{q}g}$), and cubic and quartic terms in the gluon field result in three- (ggg) and four-gluon vertices (gggg), respectively.

The noncommutative structure has two consequences for the strong interaction, color confinement and asymptotic freedom [75, 76]. Color confinement predicts that no free quarks or gluons are observed in nature, and only combined colorless states can be formed. Composite states, so-called hadrons, are grouped into mesons and baryons. Mesons consist of a quark and an antiquark ($\mathrm{q\bar{q}}$), with color and anticolor forming a color-neutral state. Three quark states (qqq), known as baryons, are color-neutral due to each quark having a different color state. The more exotic configurations of tetra- ($\mathrm{q\bar{q}q\bar{q}}$) and pentaquarks ($\mathrm{qqqq\bar{q}}$), only recently observed [77, 78], follow the same principle, consisting of combinations with a higher number of (anti)quarks. The principle of color confinement leads to strong interaction being short-ranged, where any free quark will be bound to a colorless state by producing a $\mathrm{q\bar{q}}$ pair out of the vacuum. The latter process is known as hadronization, which plays a crucial rôle in high-energy particle colliders and the simulation of SM processes.

Die approbierte gedruckte Originalversion dieser Dissertation ist an der TU Wien Bibliothek verfügbar.
The approved original version of this doctoral thesis is available in print at TU Wien Bibliothek.
TU Bibliothek Your knowledge hub WIEN

The decreasing strength of the strong interaction with increasing momentum transfer is known as asymptotic freedom. Thus, perturbative calculations are allowed in the high energy regime for the strong interaction, as color-charged particles become asymptotically free for decreasing distance scale.

Standard model Lagrangian

Combining the derived terms for the SM components, the full SM Lagrangian becomes

$$\begin{aligned}\mathcal{L}_{\mathrm{SM}} = &-\frac{1}{4}B_{\mu\nu}B^{\mu\nu} - \frac{1}{4}W^i_{\mu\nu}W_i^{\mu\nu} - \frac{1}{4}G^a_{\mu\nu}G_a^{\mu\nu} \\ &+ i\left(\bar{l}_L\gamma_\mu D^\mu l_L + \bar{e}_R\gamma_\mu D^\mu e_R + \bar{q}_L\gamma_\mu D^\mu q_L + \bar{u}_R\gamma_\mu D^\mu u_R + \bar{d}_R\gamma_\mu D^\mu d_R\right) \\ &+ \left(D_\mu\phi\right)^\dagger\left(D^\mu\phi\right) - \lambda\left(\phi^\dagger\phi - \frac{\nu^2}{2}\right)^2 \\ &- \left(y_d\left(\bar{q}_L\phi\right)d_R + y_u\left(\bar{q}_L\widetilde{\phi}\right)u_R + y_l\left(\bar{l}_L\phi e_R\right) + \mathrm{h.c.}\right), \end{aligned} \tag{2.1.37}$$

with the kinetic and interaction terms for the spin-1 gauge fields and spin-$\frac{1}{2}$ fermions, the Higgs field kinetic term, the Higgs potential, and Yukawa mass terms for quarks and leptons, except neutrinos, where $\widetilde{\phi} = i\tau_2\phi^*$. The covariant derivative of the electroweak or QCD interaction is denoted by D_μ, given in Eq. 2.1.15 and 2.1.34, respectively, and left-(right-)handed doublets (singlets) are denoted with the subscript L (R).

2.1.3 Standard model event simulation

For the comparison with experimental data, SM and possible BSM processes are simulated in Monte Carlo (MC) events. Simulations of events in hadron-collider experiments are vastly dominated by QCD interactions, where hadronic bound states are formed due to color confinement. Soft and collinear singularities, however, do not allow the use of perturbative QCD calculations in the description of the long-distance physics regime. A key ingredient in these simulations is thus the factorization of perturbative QCD calculations [79], allowing to separate processes at different energy scales and the calculation of high-energy cross sections. While the hard-scatter of initial partons, quarks or gluons, is treated perturbatively, the factorization approach introduces a factorization scale μ_F, which separates its regime from soft processes forming final-state hadrons, the parton showering.

The former is parametrized by structure functions $f_a^h(x, \mu_F)$, so-called parton distribution functions (PDFs), which depend on μ_F and the momentum fraction x of a parton a compared to the initial hadron h. PDF sets are determined from fitting theoretical predictions to experimental data, with the PDF distributions from the NNPDF collaboration [80–82] widely used in the simulation of MC events.

Divergences from QCD self-interactions and loop corrections are compensated in applying renormalization techniques [83–85]. These techniques introduce an energy dependence of the strong coupling constant $\alpha_s = g_s^2/4\pi$, with the calculations only valid close to the renormalization scale μ_R.

Die approbierte gedruckte Originalversion dieser Dissertation ist an der TU Wien Bibliothek verfügbar.
The approved original version of this doctoral thesis is available in print at TU Wien Bibliothek.
TU Bibliothek Your knowledge hub WIEN

Using the factorization and renormalization approaches, the cross section of a process at hadron colliders is calculated as

$$\sigma = \sum_{a,\,b} \int_0^1 dx_a\, dx_b \int f_a^{h_1}(x_a, \mu_F)\, f_a^{h_2}(x_b, \mu_F)\, d\hat{\sigma}_{ab\to X}(s, \mu_R, \mu_F), \tag{2.1.38}$$

with the PDFs $f_a^{h_1}$, $f_b^{h_2}$ for the collided partons a, b in the initial hadrons h_1, h_2, and the $ab \to X$ parton-level cross section $\hat{\sigma}_{ab\to X}$, in dependence of the final-state phase space. The parton center-of-mass energy is defined by $s = x_a\, x_b\, S$, where S is the hadron center-of-mass energy. The parameters μ_F and μ_R in the event simulation are typically set to the scale of the energy-momentum transfer of the simulated process, $\mu_F = \mu_R = Q^2$.

Widely used event generators are MadGraph5_aMC@NLO [86] and Powheg v2.0 [87–89], which are interfaced with parton showering algorithms, such as Pythia 8 [90], Herwig++, or Herwig 7 [91], to simulate multiple-parton interactions, parton showering, fragmentation, and hadronization in the initial and final states. The latter makes use of different tunes, which are settings incorporating the underlying-event parameters and defining secondary interactions of other partons in the colliding hadrons [92–94].

2.2 Top quark properties

Discovered at the Tevatron collider at Fermilab in 1995 [14, 15], the top quark is one of the most interesting elementary particles to study. At the LHC, it is expected that more than 136 million top quarks were produced in 2015–2018 data-taking periods using the $t\bar{t}$ production cross section given in Eq. 2.2.3 and the by the LHC delivered integrated luminosity of 163.6 fb^{-1} described in Sec. 3.1.2. This large data set allows for a detailed study of the top quark in pp collisions. Its unique properties, SM couplings, and possible BSM effects in top quark interactions with bosons are discussed in the following.

2.2.1 The mass of the top quark

The Yukawa coupling constant is a free parameter within the SM, and thus, the top quark mass must be obtained experimentally. A direct top quark production was achieved by the Tevatron collider at Fermilab, before it ceased operations in 2011. Its mass has been measured by the CDF and D0 collaborations in proton-antiproton collisions at a center-of-mass energy of 1.8 and 1.96 TeV [95]. Currently, only the LHC at CERN is capable of direct top quark productions. The CMS [96] and ATLAS [97] collaborations have measured the top quark mass at a center-of-mass energy of 7 TeV, combining the measurements with CDF and D0 results to

$$m_t = 173.34 \pm 0.36\ (\text{stat}) \pm 0.67\ (\text{syst})\ \text{GeV}. \tag{2.2.1}$$

The CMS and ATLAS collaborations additionally measured the top quark mass at a center-of-mass energy of 8 and 13 TeV, in good agreement with previous results. A comparison of the measurements is given in Fig. 2.2, where the combined top quark mass [44] is

$$m_t = 172.76 \pm 0.30\ \text{GeV}. \tag{2.2.2}$$

Die approbierte gedruckte Originalversion dieser Dissertation ist an der TU Wien Bibliothek verfügbar.
The approved original version of this doctoral thesis is available in print at TU Wien Bibliothek.
TU Bibliothek Your knowledge hub WIEN

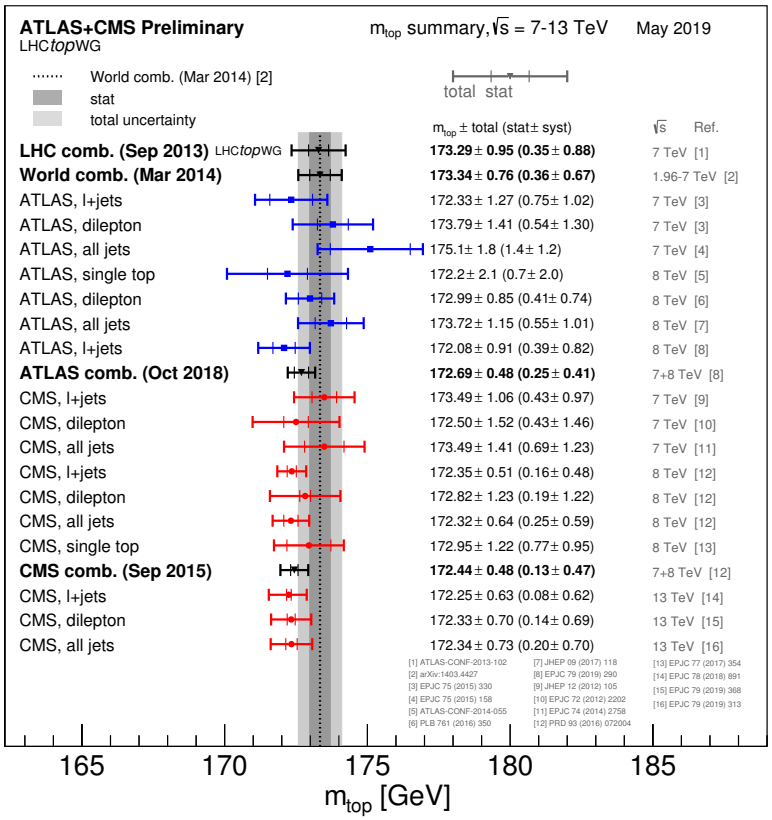

Figure 2.2: Summary of the top quark mass measurements of the ATLAS and CMS collaborations. The measurements are compared to the combined Tevatron measurements. Figure taken from Ref. [98].

As shown in Eq. 2.1.31, the large mass results in a Yukawa coupling y_t close to unity. Due to this exceptionally large coupling, it is expected that the top quark plays a crucial rôle in the electroweak symmetry breaking and possible BSM physics [16–22].

2.2.2 Top quark production at hadron colliders

Top quarks at hadron colliders are dominantly produced in top-antitop pairs ($t\bar{t}$) via the strong interaction. The main production channels are through quark-antiquark annihilation, $q\bar{q} \to t\bar{t}$, and s- and t-channel gluon-fusion processes, $gg \to t\bar{t}$. At the Tevatron collider, colliding protons and antiprotons at a center-of-mass energy of 1.8 and 1.96 TeV, the $t\bar{t}$ pairs were dominantly produced in quark-antiquark annihilations. Due to the significantly higher collision energy, the main production channel at the LHC is the gluon-fusion process. A visualization of the LO diagrams for the dominant top-antitop pair production channels is shown in Fig. 2.3.

For a center-of-mass energy of 13 TeV, the predicted production cross section of a $t\bar{t}$ pair in pp collisions at the LHC is

$$\sigma(pp \to t\bar{t}) = 831.76\ ^{+19.77}_{-29.20}\,(\text{scale})\ \pm 35.06\,(\text{PDF} + \alpha_s)\ \text{pb}, \tag{2.2.3}$$

with a total uncertainty of $\approx 5\,\%$, using a top quark mass of $m_t = 172.5\,\text{GeV}$, the default value in calculations and simulations within the ATLAS and CMS collaborations. The cross

Die approbierte gedruckte Originalversion dieser Dissertation ist an der TU Wien Bibliothek verfügbar.
The approved original version of this doctoral thesis is available in print at TU Wien Bibliothek.
TU Bibliothek Your knowledge hub WIEN

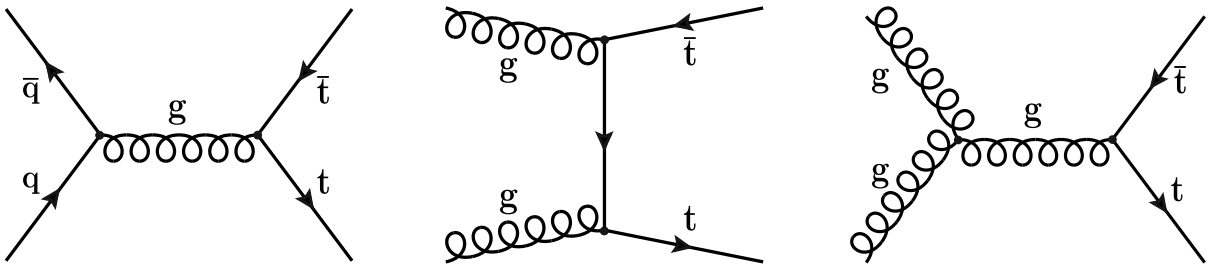

Figure 2.3: Representative diagrams for the production of top-antitop pairs at hadron colliders through quark-antiquark annihilation (left) and gluon fusion in the t- (center) and s-channel (right).

section is calculated with TOP++2.0 [99] at next-to-next-to-leading order (NNLO) in QCD, including the resummation of soft-gluon terms at next-to-next-to-leading logarithmic order (NNLL) precision. The uncertainties arise from variations of μ_F and μ_R scales, α_s, and the PDF sets. The latter is calculated using the PDF4LHC recommendations [100], with the NNPDF2.3 5f FFN [80–82], the MSTW2008 68% CL NNLO [101, 102], and the CT10 NNLO [103, 104] PDF sets. Similar calculations have been performed for various center-of-mass energies, with comparisons to the measurements performed by the CDF, D0, ATLAS, and CMS collaborations shown in Fig. 2.4. The measurements of the cross section as a function of the center-of-mass energy are compared to SM theory predictions, where excellent agreement is found.

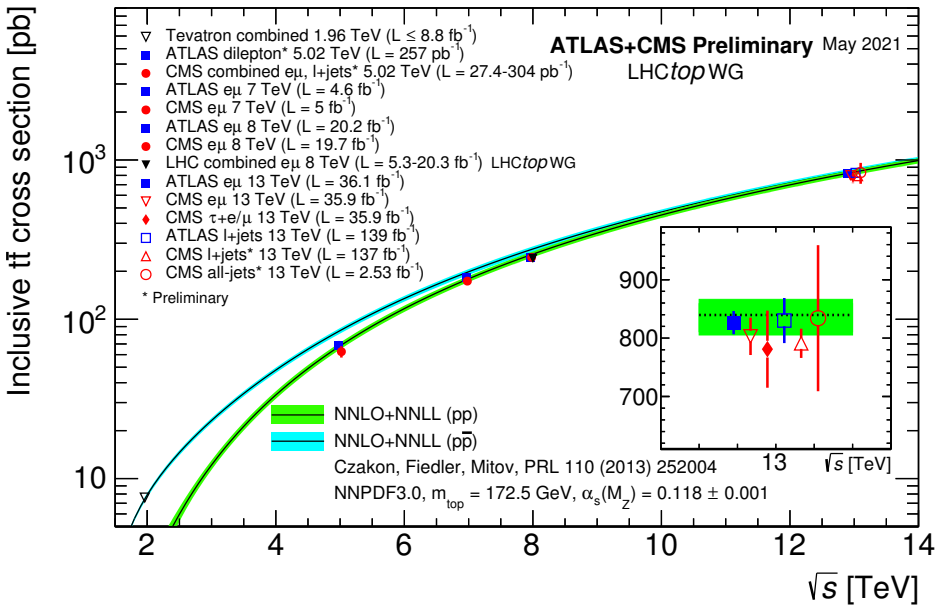

Figure 2.4: Summary of top quark pair production cross section measurements of the ATLAS and CMS collaborations, and the combined Tevatron measurement. The results are compared to theory predictions from next-to-next-to-leading order (NNLO) calculations with next-to-next-to-leading logarithmic order (NNLL) resummation. The colored band represents uncertainties from variations of the μ_F and μ_R scales, α_s, and the PDF sets. Figure taken from Ref. [98].

Die approbierte gedruckte Originalversion dieser Dissertation ist an der TU Wien Bibliothek verfügbar.
The approved original version of this doctoral thesis is available in print at TU Wien Bibliothek.
TU Bibliothek Your knowledge hub WIEN

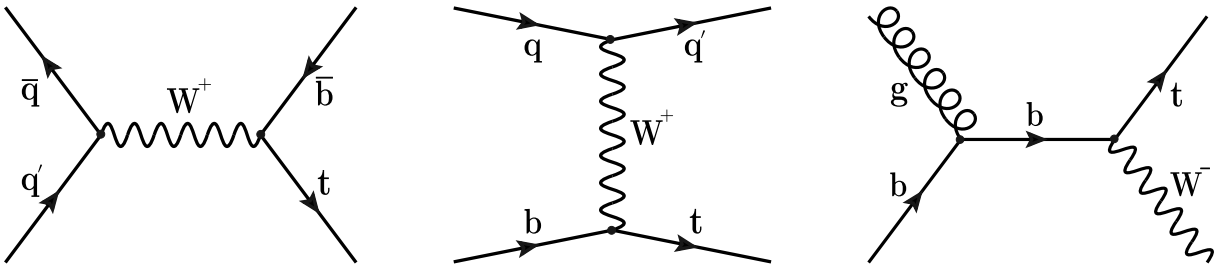

Figure 2.5: Representative diagrams for the production of single top quarks at hadron colliders in the *s*- (left), *t*- (center), and the tW-channel (right).

Single top quarks are produced in weak interactions in three production modes, via the exchange of a W boson in *s*- and *t*-channel diagrams, or in association with a W boson, noted as tW production. Representative diagrams at LO for the three production modes are shown in Fig. 2.5.

The *s*- and *t*-channel production can be kinematically separated, which makes it interesting to study, as potential BSM physics affect the two modes differently [105]. Additionally, single top quark measurements are sensitive to the weak coupling of the top quark, which allows measuring the $|V_{\mathrm{tb}}|$ entry in the CKM matrix and potential anomalous couplings in the Wtb vertex described in Sec. 2.2.4.

At higher-order corrections in QCD, the definition of the tW process overlaps with the $\mathrm{t\bar{t}}$ process. A diagram removal (DR) or diagram subtraction (DS) technique [106] has to be applied, to remove interfering diagrams from the tW simulation. In DR, interfering diagrams are removed at the amplitude level, while for DS, diagrams are removed at the cross section level. Both techniques usually provide similar results, as the interference effects are minor.

The predicted cross sections for the single top quark production are calculated with Hathor v2.1 [107, 108] for the combined top and antitop production to

$$\sigma_{s\text{-channel}} = 10.32 \quad {}^{+0.29}_{-0.24}\,(\text{scale}) \pm 0.27\,(\text{PDF} + \alpha_{\mathrm{s}})\ \text{pb} \tag{2.2.4}$$

$$\sigma_{t\text{-channel}} = 216.99 \quad {}^{+6.62}_{-4.64}\,(\text{scale}) \pm 6.16\,(\text{PDF} + \alpha_{\mathrm{s}})\ \text{pb} \tag{2.2.5}$$

$$\sigma_{\mathrm{tW}} = 71.7 \quad \pm 1.8\,(\text{scale}) \pm 3.5\ \ (\text{PDF} + \alpha_{\mathrm{s}})\ \text{pb} \tag{2.2.6}$$

for a center-of-mass energy of 13 TeV with a top quark mass of 172.5 GeV at next-to-leading order (NLO) in QCD precision. The same conditions for μ_R, μ_F, α_s, and PDF uncertainties as mentioned for the calculation of the $\mathrm{t\bar{t}}$ cross section apply. Measurements performed by the ATLAS and CMS collaborations at various center-of-mass energies are summarized in Fig. 2.6 and compared to theory calculations at the highest order in precision available, where a good agreement is found in all production modes.

2.2.3 Top quark decay

In addition to its high mass, the short lifetime of the top quark makes it unique in the SM. The SM predicts a top quark decay width Γ_{t} of

$$\Gamma_{\mathrm{t}} = \frac{G_F\, \mathrm{m_t^3}}{8\pi\sqrt{2}} \left(1 - \frac{\mathrm{m_W^2}}{\mathrm{m_t^2}}\right)^2 \left(1 + 2\frac{\mathrm{m_W^2}}{\mathrm{m_t^2}}\right) \left[1 - \frac{2\alpha_s}{3\pi}\left(\frac{2\pi^2}{3} - \frac{5}{2}\right)\right] \tag{2.2.7}$$

Die approbierte gedruckte Originalversion dieser Dissertation ist an der TU Wien Bibliothek verfügbar.
The approved original version of this doctoral thesis is available in print at TU Wien Bibliothek.
TU Bibliothek Your knowledge hub WIEN

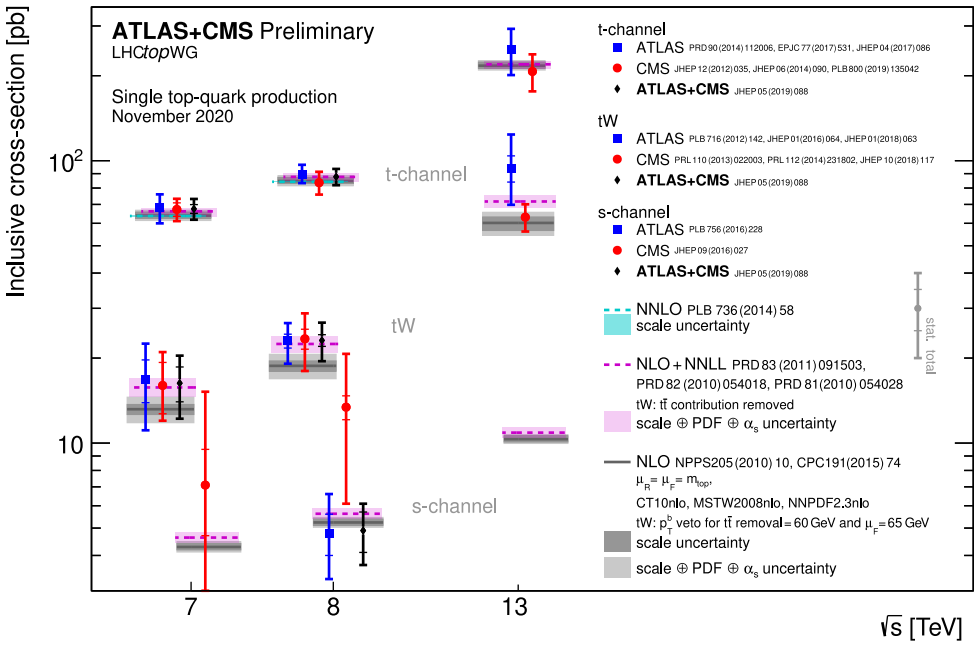

Figure 2.6: Summary of the single top quark production cross section measurements of the ATLAS and CMS collaborations for the three production channels. The results are compared to theory predictions at the highest precision available. The colored band represents uncertainties from variations of the μ_F and μ_R scales, α_s, and the PDF sets. Figure taken from Ref. [98].

at NLO in QCD precision, with the Fermi constant G_F, neglecting higher-order terms proportional to $(m_b/m_t)^2$, α_s^2, and $\alpha_s(m_W/m_t)^2$. The expected top quark decay width of $\Gamma_t = 1.305\,\text{GeV}$, using the W boson and top quark masses given in the Tables 2.1 and 2.2, and $\alpha_s(m_Z) = 0.118$ [109], is in good agreement with measurements [110].

The decay width corresponds to a mean lifetime $\tau_t = \hbar/\Gamma_t \approx 5 \cdot 10^{-25}\,\text{s}$, using the Planck constant $h = 2\pi\hbar$. As the lifetime of the top quark is shorter than the interaction timescale of the strong force $\Lambda_{QCD}^{-1} \approx 10^{-23}\,\text{s}$, no hadrons with top quarks or $t\bar{t}$-quarkonium bound states can form, and the top quark decays before hadronization [111]. In contrast to the lighter quarks, this causes the spin information of the top quark to be passed to the decay products, a unique opportunity for top quark spin measurements.

The top quark decays almost exclusively via the two-body decay $t \to Wb$, reflected by the CKM matrix entry $|V_{tb}| \approx 1$ [44, 112–115]. According to the W boson decay, the top quark decay is categorized into leptonic decays, where the W boson decays into a charged lepton-neutrino pair, and hadronic decays, resulting in a quark-antiquark pair, each hadronizing

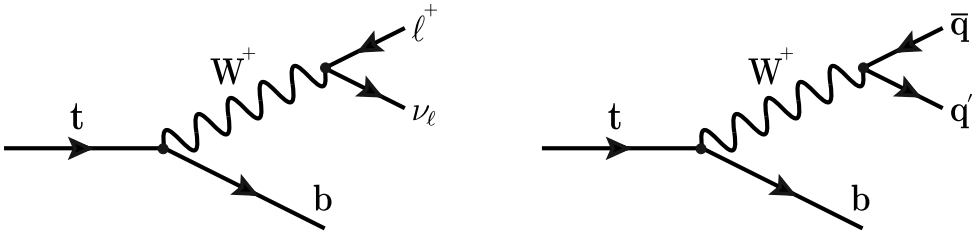

Figure 2.7: Representative diagrams for the decay channels of the top quark in leptonic (left) and hadronic (right) final states.

Die approbierte gedruckte Originalversion dieser Dissertation ist an der TU Wien Bibliothek verfügbar.
The approved original version of this doctoral thesis is available in print at TU Wien Bibliothek.
TU Bibliothek Your knowledge hub WIEN

to a so-called jet. Summing all lepton ($\ell = \mathrm{e}$, μ, τ and $\nu_\ell = \nu_\mathrm{e}$, ν_μ, ν_τ) and quark-antiquark final states, the branching fraction into leptons is $\mathcal{B}(\mathrm{W}^+ \to \ell^+\nu_\ell, \mathrm{W}^- \to \ell^-\bar{\nu}_\ell) \approx 33\,\%$, while for the hadronic channel it is $\mathcal{B}(\mathrm{W} \to \mathrm{q}'\bar{\mathrm{q}}) \approx 67\,\%$ [44]. The top quark decays are visualized in Fig. 2.7.

The decay channels in top quark pair productions can be divided into all-hadronic, semileptonic (ℓ+jets), and dileptonic ($\ell\ell$) channels. A summary of the branching fractions for the possible decay channels of a top-antitop pair is given in Table 2.3. In measurements, subsequent leptonic decays of the tau lepton, with $\mathcal{B}(\tau^- \to \mathrm{e}^-\bar{\nu}_\mathrm{e}\nu_\tau, \tau^- \to \mu^-\bar{\nu}_\mu\nu_\tau) \approx 35\,\%$ [44], enter the lepton signal regions because their short lifetime of $\approx 3 \cdot 10^{-13}\,\mathrm{s}$ [44] leads to displacements smaller than the impact parameter resolution of the CMS tracker for momenta of $\mathcal{O}(\mathrm{m_W}/2)$.

Table 2.3: Summary of the branching fractions $\mathcal{B}$ for the possible decay channels of a top-antitop pair [44].

Decay channel		Branching fraction $\mathcal{B}$
All-hadronic		46 %
Semileptonic	e+jets	15 %
	μ+jets	15 %
	τ+jets	15 %
Dileptonic	ee	1 %
	eμ	2 %
	eτ	2 %
	$\mu\mu$	1 %
	$\mu\tau$	2 %
	$\tau\tau$	1 %

2.2.4 Top quark interactions

Besides the mass and width of the top quark resonance, the couplings to SM bosons are of interest, testing the validity of the SM. As many BSM models [16–22] suggest the top quark to couple to unknown particles at the TeV scale, modifications of its interaction to gauge bosons are indications for new physics. Measurements of processes, where top quark pairs are produced in association with quarks or gluons ($\mathrm{t\bar{t}}$+jets), a W boson ($\mathrm{t\bar{t}W}$), Z boson ($\mathrm{t\bar{t}Z}$), photon ($\mathrm{t\bar{t}}\gamma$), or Higgs boson ($\mathrm{t\bar{t}H}$), collectively denoted as $\mathrm{t\bar{t}}X$, have entered the precision regime and allow for detailed measurements of the top quark interactions.

The top quark Yukawa coupling

The top quark Yukawa coupling is the largest within the SM. With a top quark mass given in Eq. 2.2.2, its Yukawa coupling y_t described in Eq. 2.1.31 is close to unity. The recent success of the LHC in the top quark sector was the observation of one of the heaviest processes known to date: a top quark pair in association with the Higgs boson [116–118]. Measurements of the production rate give access to the tH vertex and thus the Yukawa coupling of the top quark. Measurements are performed at a center-of-mass energy of 13 TeV in the Higgs boson decay channels to $\gamma\gamma$, $\mathrm{b\bar{b}}$, and multilepton final states. The

Die approbierte gedruckte Originalversion dieser Dissertation ist an der TU Wien Bibliothek verfügbar.
The approved original version of this doctoral thesis is available in print at TU Wien Bibliothek.
TU Bibliothek Your knowledge hub WIEN

measured $\mathrm{t\bar{t}H}$ production cross section, normalized to the SM prediction of 507^{+35}_{-50} fb [119] at NLO in QCD, by the CMS [116] (ATLAS [118]) collaboration of $1.26^{+0.31}_{-0.26}$ ($1.32^{+0.28}_{-0.26}$) are in agreement with the SM prediction, restricting possible BSM effects in the top quark sector.

The top quark interaction with the gluon

At the LHC, top quark pair production mainly proceeds via the strong interaction. Representative Feynman diagrams of the $\mathrm{t\bar{t}}$ production modes involving top quark-gluon vertices are shown in Fig. 2.3. In the SM QCD Lagrangian (Eq. 2.1.35), the top quark-gluon interaction $\mathrm{t\bar{t}g}$ is described by the first term of the effective Lagrangian [120]

$$\mathcal{L}_{\mathrm{t\bar{t}g}} = -g_s \bar{\mathrm{t}} \frac{\lambda_a}{2} \gamma^\mu \mathrm{t} G^a_\mu - g_s \bar{\mathrm{t}} \lambda_a \frac{i\sigma^{\mu\nu} q_\nu}{\mathrm{m_t}} \left(d_V^g + i d_A^g \gamma_5\right) \mathrm{t} G^a_\mu, \tag{2.2.8}$$

with the implicit sum over same indices. The second term, with $\sigma^{\mu\nu} = \frac{i}{2}[\gamma^\mu, \gamma^\nu]$, the additional couplings d_V^g and d_A^g, and the gluon four-momentum q_ν modifies the interaction and induces additional structures related to the chromomagnetic and chromoelectric dipole moments. These vanish at tree-level SM calculations, with small contributions in higher-order corrections due to additional interactions of the top quark to gluons, modifying the strong coupling constant. Such corrections are thus part of both, SM predictions and BSM models.

A precise determination of the production rate of $\mathrm{t\bar{t}}$ at hadron collider experiments, together with theory predictions at the highest achievable order, allows for constraining BSM effects in the strong interaction of the top quark. At the current experimental uncertainties of $\approx 5\,\%$ and theory uncertainties of $\approx 3.5\,\%$ [99, 121–126], it is expected that electroweak corrections become important [127]. Thus, the focus of LHC SM measurements and BSM searches shifted to studying processes of top quarks in association with electroweak bosons.

The top quark interaction with the W boson

The Wtb coupling is experimentally probed in top quark decays and the electroweak production of single top quarks, where the former (latter) is shown in Fig. 2.7 (2.5). The Lagrangian

$$\mathcal{L}_{\mathrm{Wtb}} = -\frac{g}{\sqrt{2}} \bar{\mathrm{b}} \gamma^\mu P_L \mathrm{t} W^-_\mu \tag{2.2.9}$$

describes the SM interaction vertex, with the left- (right-)handed projection operator $P_{L,R} = \frac{1}{2}(1 \mp \gamma^5)$. Modifications of the Wtb vertex are introduced in using the effective Lagrangian [120]

$$\begin{aligned} \mathcal{L}_{\mathrm{Wtb}} = &-\frac{g}{\sqrt{2}} \bar{\mathrm{b}} \gamma^\mu \left(V_L P_L + V_R P_R\right) \mathrm{t} W^-_\mu \\ &-\frac{g}{\sqrt{2}} \bar{\mathrm{b}} \frac{i\sigma^{\mu\nu} q_\nu}{\mathrm{m_W}} \left(g_L P_L + g_R P_R\right) \mathrm{t} W^-_\mu + \mathrm{h.c.}, \end{aligned} \tag{2.2.10}$$

with the W boson four-momentum q_ν, additional vector couplings $V_{L,R}$, and tensor couplings $g_{L,R}$. For SM calculations at LO precision, V_L equals the CKM matrix entry $|V_{\mathrm{tb}}| \approx 1$ [44] and V_R, g_L, and g_R vanish.

Die approbierte gedruckte Originalversion dieser Dissertation ist an der TU Wien Bibliothek verfügbar.
The approved original version of this doctoral thesis is available in print at TU Wien Bibliothek.
TU Bibliothek Your knowledge hub WIEN

Helicity fraction measurements of W bosons in top quark decays are sensitive to deviations from additional structures induced by vector and tensor couplings in measuring the angular distributions of top quark decay products. The angle between the charged lepton three-momentum of the W boson decay in the W boson rest frame and the W boson three-momentum in the top quark rest frame defines the helicity angle θ^*. Helicity fractions F_0, F_L, and F_R depend on the cosine of the helicity angle by

$$\frac{1}{\Gamma}\frac{d\Gamma}{d\cos\theta^*} = \frac{3}{8}(1-\cos\theta^*)^2 F_L + \frac{3}{4}\sin^2\theta^* F_0 + \frac{3}{8}(1+\cos\theta^*)^2 F_R, \tag{2.2.11}$$

with $F_0 + F_L + F_R = 1$. Their relation to vector and tensor couplings in Eq. 2.2.10 was demonstrated in Ref. [128]. Exploiting the distribution of $\cos\theta^*$ thus allows for helicity fraction measurements and to constrain anomalous top quark interactions to the W boson.

Measurements have been performed by the CMS experiment with experimental uncertainties in F_0 and F_L below 5 % [129]. The measured W boson helicity fractions of $F_0 = 0.681 \pm 0.012\ (\text{stat}) \pm 0.023\ (\text{syst})$, $F_L = 0.323 \pm 0.008\ (\text{stat}) \pm 0.014\ (\text{syst})$, and $F_R = -0.004 \pm 0.005\ (\text{stat}) \pm 0.014\ (\text{syst})$ are in good agreement with precise theoretical predictions calculated at NNLO in QCD [130–132].

Additionally, measurements of single top quark productions provide information on the Wtb coupling and allow to measure $|V_{\text{tb}}|$ with different sensitivities in the three production channels shown in Fig. 2.5. Especially the t-channel production mode has direct sensitivity to $|V_{\text{tb}}|$ and allows to measure anomalous couplings in the Wtb vertex. Precise measurements have been performed by the CMS and ATLAS collaborations and are shown in Fig. 2.6, in good agreement with SM predictions at NLO in QCD [114, 133]. Precision measurements and higher-order theory calculations thus tightly constrain possible BSM effects in the top quark decay and its electroweak production.

The top quark interaction with the Z boson

The top quark interaction vertex with the Z boson in the SM is given by

$$\mathcal{L}_{\text{ttZ}} = -\frac{g}{2\cos\theta_W}\bar{\text{t}}\gamma^\mu P_L \text{t} Z_\mu. \tag{2.2.12}$$

Modifications of the tZ vertex are introduced in the effective Lagrangian [120]

$$\begin{aligned}\mathcal{L}_{\text{ttZ}} = &-\frac{g}{2\cos\theta_W}\bar{\text{t}}\gamma^\mu\left(X^L_{\text{tt}}P_L + X^R_{\text{tt}}P_R - 2\sin^2\theta_W Q_{\text{t}}\right)\text{t}Z_\mu \\ &-\frac{g}{2\cos\theta_W}\bar{\text{t}}\frac{i\sigma^{\mu\nu}q_\nu}{\text{m}_{\text{Z}}}\left(d^{\text{Z}}_V + id^{\text{Z}}_A\gamma_5\right)\text{t}Z_\mu,\end{aligned} \tag{2.2.13}$$

with $Q_{\text{t}} = \frac{2}{3}$, the Z boson four-momentum q_ν, the additional couplings $X^{L,R}_{\text{tt}}$, and the weak dipole moments $d^{\text{Z}}_{V,A}$. At the tree-level, the couplings take the values $X^L_{\text{tt}} = 1$ and $X^R_{\text{tt}}, d^{\text{Z}}_V, d^{\text{Z}}_A = 0$, where nonzero values can appear in higher-order radiative corrections. Probing the weak neutral coupling of the top quark in studying the tZ vertex is held as a sensitive probe for BSM effects in the top sector. It can be exploited at the LHC in measuring the production cross section of a Z boson in association with a $\text{t}\bar{\text{t}}$ pair ($\text{t}\bar{\text{t}}\text{Z}$) or a single top quark (tZq).

The first observation of the $\text{t}\bar{\text{t}}\text{Z}$ process has been made by the CMS experiment in 2015 [134]. With increased luminosity, measurements of the $\text{t}\bar{\text{t}}\text{Z}$ cross section have now entered the

TU Bibliothek Your knowledge hub WIEN Die approbierte gedruckte Originalversion dieser Dissertation ist an der TU Wien Bibliothek verfügbar. The approved original version of this doctoral thesis is available in print at TU Wien Bibliothek.

precision regime. Detailed studies of the $t\bar{t}Z$ process have been performed, where a precise measurement of the cross section could reduce the experimental uncertainty to 8 % [135]. The measurement of the kinematic spectra of the Z boson was used to set tight constraints on the anomalous (axial-)vector couplings and dipole moments of the top quarks. Even though the $t\bar{t}Z$ cross section measurement is the most precise to date, improvements on uncertainties in the theoretical prediction, currently at $\approx 12\,\%$ [119, 136, 137], are needed to further constrain possible BSM physics effects in weak neutral top quark couplings.

Due to the low production rate predicted in the SM, measurements of the tZq cross section are experimentally challenging. A recent study of the CMS collaboration could observe the very rare process of tZq, where the measured cross section of $111 \pm 13\,(\text{stat})^{+11}_{-9}$ (syst) fb [138] is in agreement with the SM prediction of 94.2 ± 3.1 fb at NLO in QCD [139].

The top quark interaction with the photon

Given the tight experimental constraints on anomalous top quark couplings to weak bosons and the gluon, a current focus of LHC experiments is the direct measurement of possible modified electromagnetic couplings. Top quarks interacting with photons are described in the SM by the first term of the effective Lagrangian [120, 140]

$$\mathcal{L}_{\mathrm{t}\bar{\mathrm{t}}\gamma} = -\mathrm{e}Q_{\mathrm{t}}\bar{\mathrm{t}}\gamma^{\mu}\mathrm{t}A_{\mu} - \mathrm{e}\bar{\mathrm{t}}\frac{i\sigma^{\mu\nu}q_{\nu}}{\mathrm{m_t}}\left(d_V^{\gamma} + id_A^{\gamma}\gamma_5\right)\mathrm{t}A_{\mu}. \tag{2.2.14}$$

While it is intuitive in the SM structure that the top quark has an electric charge of $Q_{\mathrm{t}} = \frac{2}{3}$, the top quark can have alternative values, such as $Q_{\mathrm{t}} = -\frac{4}{3}$ in more exotic models [141, 142]. Such variations of its electric charge affect the interaction of the top quark to the photon and the production rate of the $t\bar{t}\gamma$ process. Although previous measurements [143–146] already excluded this scenario, an anomalous electric (EDM) or magnetic dipole moment (MDM) of the top quark is suggested by many BSM models [147–150].

The second term in the effective Lagrangian given in Eq. 2.2.14, with the photon four-momentum q_ν and the additional couplings d_V^{γ} and d_A^{γ}, adds modifications of the interaction related to the MDM and EDM of the top quark, where the latter is $\mathcal{CP}$-violating. The parameters translate to the anomalous MDM $a_{\mathrm{t}} = (g_{\mathrm{t}} - 2)/2$ with the gyromagnetic factor g_{t} and the EDM d_{t} by [140, 151]

$$d_V^{\gamma} = -\frac{Q_{\mathrm{t}}}{2}a_{\mathrm{t}}, \quad \text{and} \quad d_A^{\gamma} = -\frac{\mathrm{m_t}}{\mathrm{e}}d_{\mathrm{t}}, \tag{2.2.15}$$

respectively. At tree-level in SM calculations the parameters d_V^{γ} and d_A^{γ} vanish. Higher-order corrections add small, but nonzero values to the SM predictions, with $a_{\mathrm{t}}^{\mathrm{SM}} = 0.02$ ($d_V^{\gamma,\mathrm{SM}} = -6.7 \cdot 10^{-3}$) [152] and $|d_{\mathrm{t}}^{\mathrm{SM}}| < 10^{-21}\,\mathrm{ecm}$ ($|d_A^{\gamma,\mathrm{SM}}| < 8.7 \cdot 10^{-6}$) [153]. The EDM is strongly suppressed in the SM and is thus an excellent probe for BSM physics. Loop-induced corrections including new particles add significant contributions to the EDM of the top quark, e.g., vector-like multiplets in the minimal supersymmetric SM predict values up to $|d_{\mathrm{t}}| < 10^{-19}\,\mathrm{ecm}$ ($|d_A^{\gamma}| < 8.7 \cdot 10^{-4}$) [19].

Precision measurements of rare decays, such as $\mathrm{H} \to \gamma\gamma$ [154] and $\mathrm{b} \to \mathrm{s}\gamma$ [155–157], allow setting bounds on the anomalous top quark coupling. The $t\bar{t}\gamma$ process adds an orthogonal method to constrain the anomalous top quark coupling, sensitive to measure anomalies in the $t\gamma$ vertex [140]. Thus, a precise determination of the production rate of top quark

TU Bibliothek Your knowledge hub WIEN
Die approbierte gedruckte Originalversion dieser Dissertation ist an der TU Wien Bibliothek verfügbar.
The approved original version of this doctoral thesis is available in print at TU Wien Bibliothek.

pairs in association with a photon allows setting tight constraints on the EDM and MDM of the top quark. As shown in Eq. 2.2.14, modifications from top quark dipole moments in cross section measurements are proportional to the photon momentum q_ν. A measurement of the kinematic distributions adds additional constraining power to a possible anomalous electromagnetic coupling.

The inclusive cross section of $t\bar{t}\gamma$ has been measured by the CDF collaboration at a center-of-mass energy of 1.96 TeV [158], while ATLAS and CMS collaborations at the LHC have measured the cross section at higher center-of-mass energies, ranging from 7–13 TeV [159–163]. At 8 and 13 TeV, the studies of the ATLAS collaboration [160, 162, 163] measured various kinematic distributions, including $p_T(\gamma)$, differentially. While all of these measurements are in good agreement with SM predictions, the first direct constraints on observables related to the anomalous EDM and MDM of the top quark in the $t\bar{t}\gamma$ process, exploiting the kinematic effects on $p_T(\gamma)$, is the context of this thesis.

2.3 Beyond the standard model

Remarkably simple and powerful, the SM allows for precise theoretical predictions up to the highest energies achievable at current particle colliders. The predicted cross sections of SM processes, spanning nine orders of magnitude, are in impeccable agreement with measurements. A variety of measurements performed by the CMS experiment at the LHC are shown in Fig. 2.8.

Even though the SM is a success, some questions remain unanswered and cannot be described by the theory. This section is dedicated to giving a brief overview of SM shortcomings, with an introduction to the mathematical formalism of the SM-EFT, extending its terms with higher mass dimensions, taking possible BSM effects into account.

2.3.1 Limitations of the standard model

Magnetic moment of the muon

A possible sign for BSM physics comes from the latest measurements of the magnetic moment of the muon. While the measurement of the magnetic moment of the electron is one of the most precise to date and agrees with the SM [60], the experimental results for the muon obtained by the Muon $g-2$ experiment at Fermilab [165] showed a discrepancy of $3.3\,\sigma$ significance. The result is in agreement with previous results at the Brookhaven National Laboratory [166]. Individual measurements have been combined to tensions with theory predictions of $4.2\,\sigma$ [60].

The results of the electric and magnetic dipole moments of the electron and muon were interpreted in a model-independent way using SM-EFT operators. It was found that only very few operators can explain the discrepancy, involving the electroweak dipole operators $\mathcal{O}_{eB}$ and $\mathcal{O}_{eW}$ and the four-fermion operators $\mathcal{O}_{le}$, $\mathcal{O}^{(1)}_{lequ}$, and $\mathcal{O}^{(3)}_{lequ}$ given in Table 2.4 [167].

Die approbierte gedruckte Originalversion dieser Dissertation ist an der TU Wien Bibliothek verfügbar.
The approved original version of this doctoral thesis is available in print at TU Wien Bibliothek.
TU Bibliothek Your knowledge hub WIEN

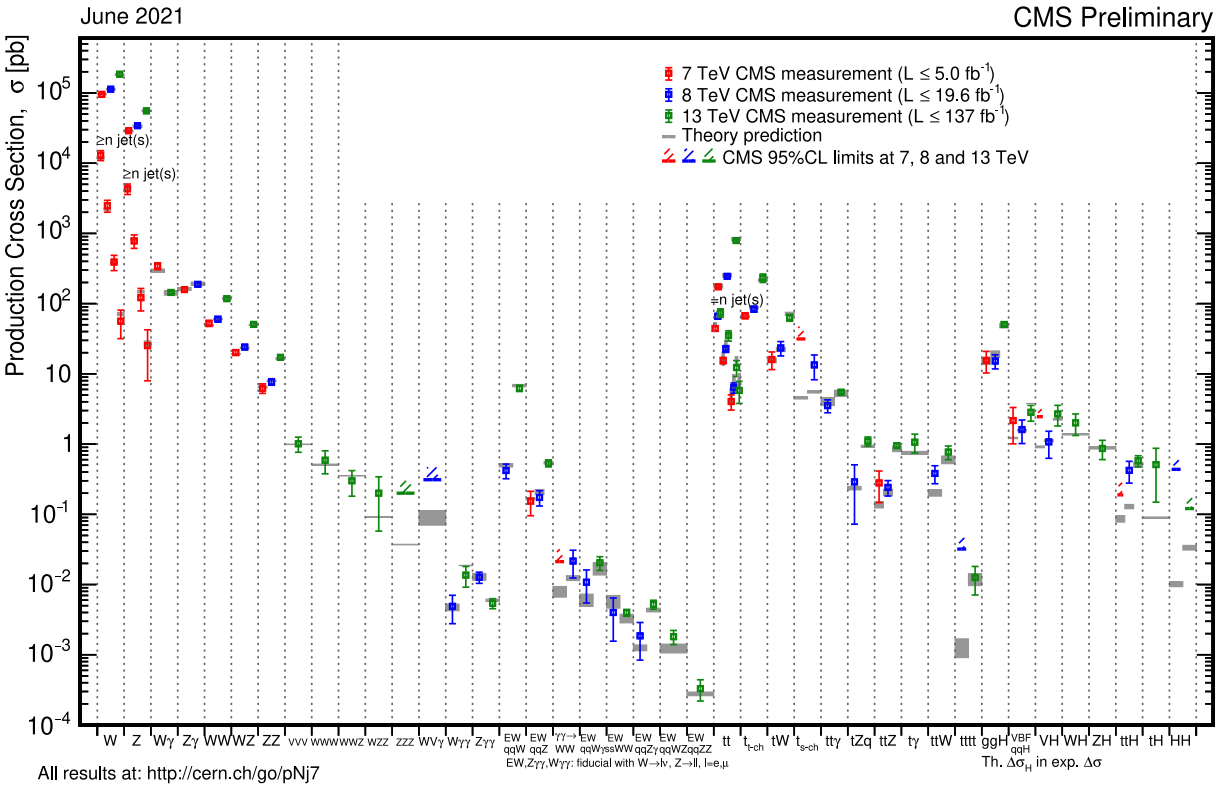

Figure 2.8: Predicted and observed cross sections at different center-of-mass energies for various SM processes with the CMS experiment. The measurements are in agreement with the SM for cross sections spanning over nine orders of magnitude. Figure adapted from Ref. [164].

Flavor anomalies

The SM predicts that the electroweak force acts identical on charged leptons. A set of measurements perfomed by the BaBar [168–170], Belle [171, 172], and LHCb experiments [173–178] suggest a pattern of lepton flavor universality (LFU) violation in observables resulting from the tree-level $b \to c\ell\nu$ and loop-induced $b \to s\ell\ell$ transitions. Charged and neutral current interactions have been measured in the observables

$$R_{D^{(*)}} = \frac{\mathcal{B}(B \to D^{(*)}\tau\bar{\nu}_\tau)}{\mathcal{B}(B \to D^{(*)}\ell\bar{\nu}_\ell)} \quad \text{and} \quad R_{K^{(*)}} = \frac{\mathcal{B}(B \to K^{(*)}\mu^+\mu^-)}{\mathcal{B}(B \to K^{(*)}\mathrm{e}^+\mathrm{e}^-)}, \tag{2.3.1}$$

respectively, with discrepancies at a level of $3.8\,\sigma$ [179] significance to SM predictions. If future results confirm the measurements, LFU violation implies BSM physics with possible unknown interactions between quarks and leptons.

Gauge coupling unification

Higher-order corrections to the gauge couplings can be absorbed in energy-dependent coupling coefficients. Thus, their strength becomes a function of the energy scale of the process. A unification of the three gauge couplings is expected at energies at the order of 10^{16} GeV, the grand unification scale. The SM predicts an evolution of the gauge couplings that comes close to a unification, however it fails to achieve it. Possible new physics at

Die approbierte gedruckte Originalversion dieser Dissertation ist an der TU Wien Bibliothek verfügbar.
The approved original version of this doctoral thesis is available in print at TU Wien Bibliothek.
TU Bibliothek Your knowledge hub WIEN

higher energies can have a significant impact on the evolution of the couplings and thus helps to embed the SM gauge groups into a single, more general theory.

Neutrino masses

The discovery of neutrino oscillations [69, 70] proves that neutrino mass terms, which are no part of the SM, are required. Neutrino oscillations are studied in a broad energy spectrum, with neutrinos originating from particle collisions in collider experiments, solar sources, and astrophysical sources beyond our galaxy, allowing to probe oscillation effects on various scales. With neutrino energies up to the PeV scale, neutrinos are held as a promising candidate for hints on BSM physics [180].

The Planck experiment tightly constrained the upper limit of the sum of neutrino masses to $\sum \mathrm{m}_\nu < 0.12\,\mathrm{eV}$ [9]. Due to the low mass of neutrinos, their mass generation might differ from the SM Yukawa-type mass terms described in Sec. 2.1.2. Thus, other mechanisms are proposed to explain neutrino masses, such as various types of the see-saw mechanism [181–190] or Majorana mass terms [191].

Dark matter and dark energy

In addition to the deviations from SM predictions on the smallest scales, the SM is challenged by evidence for unknown sources of matter and energy in our universe. Studies of the cosmic microwave background [9], the rotation curves of galaxies [10, 11], and microlensing effects [12] hint at the existence of an unknown type of nonluminous matter, so-called dark matter. Recent measurements [9] estimate the dark matter density in our universe of $\Omega_\mathrm{c}h^2 = 0.120 \pm 0.001$ and a density explained by baryonic matter of $\Omega_\mathrm{c}h^2 = 0.0224 \pm 0.0001$. Thus, only $\approx$16 % of the total matter content can be explained by the SM, as it is not able to provide a suitable particle candidate for dark matter.

The remaining majority of energy in our universe is dark energy [8, 9]. Responsible for the accelerating expansion of our universe, the origin of this type of energy is puzzling and left unanswered by the SM.

Only mentioning a selection of SM limitations, many more questions could be raised. Thus, the SM could simply be an effective field theory (EFT), only valid up to an energy Λ, with an extended theory valid beyond.

2.3.2 Standard model effective field theory

Knowing the SM to be incomplete, the search for new physics has been the highest priority for experimentalists and theorists around the world. With the lack of clear experimental signatures in the searches for BSM physics, however, unknown particles might be too heavy to be produced resonantly and thus be out of reach for current collider experiments. Effects from heavy particles, with their mass of the order of Λ, would then decouple at low energies $E \ll \Lambda$ [192], allowing the use of the SM as an EFT. In the absence of a full theoretical model extension of the SM, deviations from SM predictions are parametrized

Die approbierte gedruckte Originalversion dieser Dissertation ist an der TU Wien Bibliothek verfügbar.
The approved original version of this doctoral thesis is available in print at TU Wien Bibliothek.
TU Bibliothek Your knowledge hub WIEN

using the SM-EFT [23–29] as a consistent field theory in a model-independent way. In SM-EFT, indirect effects enter the Lagrangian as higher-dimensional operators $\mathcal{O}_i$, where the SM Lagrangian $\mathcal{L}_{\text{SM}}$ given in Eq. 2.1.37 is extended with higher-order terms, suppressed by powers of the energy Λ. A generic expression of SM-EFT, valid for $E \ll \Lambda$, is

$$\mathcal{L}_{\text{SM-EFT}} = \mathcal{L}_{\text{SM}} + \mathcal{L}^{(5)} + \mathcal{L}^{(6)} + \mathcal{L}^{(7)} + \dots \tag{2.3.2}$$

$$\mathcal{L}^{(d)} = \sum_i \frac{c_i^{(d)}}{\Lambda^{d-4}} \mathcal{O}_i^{(d)}, \tag{2.3.3}$$

with the dimensionality d and the dimensionless Wilson coefficients c_i.

Operators with odd mass-dimension are considered baryon- or lepton-number violating [193–197], with the most prominent unique operator at dimension-five, the Weinberg operator [198], generating Majorana-neutrino mass terms [191]. Interpretations of measurements currently focus on constraining the Wilson coefficients of dimension-six operators, with higher-order operators considered suppressed by higher powers of Λ.

In the most general flavor structure, 2499 real coefficients exist for the dimension-six extension of SM-EFT [24], which is reduced to 59 degrees of freedom (d.o.f.) in assuming minimal flavor violation, baryon-number conservation, and the validity of the equations of motion [30]. The latter set of independent operators is the so-called Warsaw basis and plays a crucial rôle in Higgs and top quark physics.

The independent set of dimension-six operators of the Warsaw basis is shown in Table 2.4, where baryon-number violating operators are often neglected. In this table, the sum over same indices is implicit and the fermion generation indices p, r, s, and t are removed from the operator notation and can be added as e.g. $\mathcal{O}_{uB} \to \mathcal{O}_{uB}^{(pr)}$ when necessary. Wilson coefficients c_i to the corresponding dimension-six operators $\mathcal{O}_i$ follow the same notation, e.g., $c_{uB}^{(pr)}$ for the operator $\mathcal{O}_{uB}^{(pr)}$. The table follows the notation given in Sec. 2.1.2, where additionally left-handed fermion doublets are denoted as q and l, right-handed fermion singlets as e, u, and d, dropping the indices L and R. Dual tensors are defined as $\widetilde{X}_{\mu\nu} = \frac{1}{2}\epsilon_{\mu\nu\rho\sigma}X^{\rho\sigma}$ for $X \in \{G^a, W^i, B\}$, the Higgs doublet is denoted as ϕ, with $\widetilde{\phi} = i\tau_2\phi^*$, $(\phi^\dagger i \overleftrightarrow{D}_\mu^i \phi) = \phi^\dagger\tau^i (iD_\mu\phi) - \left(iD_\mu\phi^\dagger\right)\tau^i\phi$, $(\phi^\dagger i \overleftrightarrow{D}_\mu \phi) = \phi^\dagger (iD_\mu\phi) - \left(iD_\mu\phi^\dagger\right)\phi$, and $C = i\gamma^2\gamma^0$.

Operators relevant in $t\bar{t}$ productions are

$$\mathcal{O}_{uG} = (\bar{q}_p\sigma^{\mu\nu}T^a u_r)\widetilde{\phi}\, G^a_{\mu\nu} \tag{2.3.4}$$
$$\mathcal{O}_G = f^{abc}G^{a\nu}_\mu G^{b\rho}_\nu G^{c\mu}_\rho \tag{2.3.5}$$
$$\mathcal{O}_{\phi G} = \phi^\dagger\phi\, G^a_{\mu\nu}G^{a\mu\nu} \tag{2.3.6}$$
$$\mathcal{O}_{qq}^{(1)} = (\bar{q}_p\gamma_\mu q_r)(\bar{q}_s\gamma^\mu q_t) \tag{2.3.7}$$
$$\mathcal{O}_{qq}^{(3)} = (\bar{q}_p\gamma_\mu\tau^i q_r)(\bar{q}_s\gamma^\mu\tau^i q_t) \tag{2.3.8}$$
$$\mathcal{O}_{uu} = (\bar{u}_p\gamma_\mu u_r)(\bar{u}_s\gamma^\mu u_t) \tag{2.3.9}$$
$$\mathcal{O}_{qu}^{(8)} = (\bar{q}_p\gamma_\mu T^a q_r)(\bar{u}_s\gamma^\mu T^a u_t) \tag{2.3.10}$$
$$\mathcal{O}_{qd}^{(8)} = (\bar{q}_p\gamma_\mu T^a q_r)(\bar{d}_s\gamma^\mu T^a d_t) \tag{2.3.11}$$
$$\mathcal{O}_{ud}^{(8)} = (\bar{u}_p\gamma_\mu T^a u_r)(\bar{d}_s\gamma^\mu T^a d_t), \tag{2.3.12}$$

affecting the top quark-gluon coupling described in Sec. 2.2.4, top quark-fermion interactions, as well as the gluon self-coupling. The operators are thus best probed in $t\bar{t}$ cross section measurements.

Die approbierte gedruckte Originalversion dieser Dissertation ist an der TU Wien Bibliothek verfügbar.
The approved original version of this doctoral thesis is available in print at TU Wien Bibliothek.
TU Bibliothek Your knowledge hub WIEN

Table 2.4: SM-EFT dimension-six operators in the Warsaw basis [30]. The labels p, r, s, and t denote the generation of the fermion fields and operators can be extended by the explicit generation $\mathcal{O}_{uB} \to \mathcal{O}_{uB}^{(pr)}$ when necessary.

X^3		ϕ^6 and $\phi^4 D^2$		$\psi^2\phi^3$	
$\mathcal{O}_G$	$f^{abc}G_\mu^{a\nu}G_\nu^{b\rho}G_\rho^{c\mu}$	$\mathcal{O}_\phi$	$(\phi^\dagger\phi)^3$	$\mathcal{O}_{e\phi}$	$(\phi^\dagger\phi)(\bar{l}_p e_r \phi)$
$\mathcal{O}_{\widetilde{G}}$	$f^{abc}\widetilde{G}_\mu^{a\nu}G_\nu^{b\rho}G_\rho^{c\mu}$	$\mathcal{O}_{\phi\Box}$	$(\phi^\dagger\phi)\Box(\phi^\dagger\phi)$	$\mathcal{O}_{u\phi}$	$(\phi^\dagger\phi)(\bar{q}_p u_r \widetilde{\phi})$
$\mathcal{O}_W$	$\varepsilon^{ijk}W_\mu^{i\nu}W_\nu^{j\rho}W_\rho^{k\mu}$	$\mathcal{O}_{\phi D}$	$\left(\phi^\dagger D^\mu\phi\right)^\star\left(\phi^\dagger D_\mu\phi\right)$	$\mathcal{O}_{d\phi}$	$(\phi^\dagger\phi)(\bar{q}_p d_r \phi)$
$\mathcal{O}_{\widetilde{W}}$	$\varepsilon^{ijk}\widetilde{W}_\mu^{i\nu}W_\nu^{j\rho}W_\rho^{k\mu}$				
$X^2\phi^2$		$\psi^2 X\phi$		$\psi^2\phi^2 D$	
$\mathcal{O}_{\phi G}$	$\phi^\dagger\phi\, G^a_{\mu\nu}G^{a\mu\nu}$	$\mathcal{O}_{eW}$	$(\bar{l}_p\sigma^{\mu\nu}e_r)\tau^i\phi W^i_{\mu\nu}$	$\mathcal{O}_{\phi l}^{(1)}$	$(\phi^\dagger i\overleftrightarrow{D}_\mu\phi)(\bar{l}_p\gamma^\mu l_r)$
$\mathcal{O}_{\phi\widetilde{G}}$	$\phi^\dagger\phi\,\widetilde{G}^a_{\mu\nu}G^{a\mu\nu}$	$\mathcal{O}_{eB}$	$(\bar{l}_p\sigma^{\mu\nu}e_r)\phi B_{\mu\nu}$	$\mathcal{O}_{\phi l}^{(3)}$	$(\phi^\dagger i\overleftrightarrow{D}^i_\mu\phi)(\bar{l}_p\tau^i\gamma^\mu l_r)$
$\mathcal{O}_{\phi W}$	$\phi^\dagger\phi\, W^i_{\mu\nu}W^{i\mu\nu}$	$\mathcal{O}_{uG}$	$(\bar{q}_p\sigma^{\mu\nu}T^a u_r)\widetilde{\phi}\, G^a_{\mu\nu}$	$\mathcal{O}_{\phi e}$	$(\phi^\dagger i\overleftrightarrow{D}_\mu\phi)(\bar{e}_p\gamma^\mu e_r)$
$\mathcal{O}_{\phi\widetilde{W}}$	$\phi^\dagger\phi\,\widetilde{W}^i_{\mu\nu}W^{i\mu\nu}$	$\mathcal{O}_{uW}$	$(\bar{q}_p\sigma^{\mu\nu}u_r)\tau^i\widetilde{\phi}\, W^i_{\mu\nu}$	$\mathcal{O}_{\phi q}^{(1)}$	$(\phi^\dagger i\overleftrightarrow{D}_\mu\phi)(\bar{q}_p\gamma^\mu q_r)$
$\mathcal{O}_{\phi B}$	$\phi^\dagger\phi\, B_{\mu\nu}B^{\mu\nu}$	$\mathcal{O}_{uB}$	$(\bar{q}_p\sigma^{\mu\nu}u_r)\widetilde{\phi}\, B_{\mu\nu}$	$\mathcal{O}_{\phi q}^{(3)}$	$(\phi^\dagger i\overleftrightarrow{D}^i_\mu\phi)(\bar{q}_p\tau^i\gamma^\mu q_r)$
$\mathcal{O}_{\phi\widetilde{B}}$	$\phi^\dagger\phi\,\widetilde{B}_{\mu\nu}B^{\mu\nu}$	$\mathcal{O}_{dG}$	$(\bar{q}_p\sigma^{\mu\nu}T^a d_r)\phi\, G^a_{\mu\nu}$	$\mathcal{O}_{\phi u}$	$(\phi^\dagger i\overleftrightarrow{D}_\mu\phi)(\bar{u}_p\gamma^\mu u_r)$
$\mathcal{O}_{\phi WB}$	$\phi^\dagger\tau^i\phi\, W^i_{\mu\nu}B^{\mu\nu}$	$\mathcal{O}_{dW}$	$(\bar{q}_p\sigma^{\mu\nu}d_r)\tau^i\phi\, W^i_{\mu\nu}$	$\mathcal{O}_{\phi d}$	$(\phi^\dagger i\overleftrightarrow{D}_\mu\phi)(\bar{d}_p\gamma^\mu d_r)$
$\mathcal{O}_{\phi\widetilde{W}B}$	$\phi^\dagger\tau^i\phi\,\widetilde{W}^i_{\mu\nu}B^{\mu\nu}$	$\mathcal{O}_{dB}$	$(\bar{q}_p\sigma^{\mu\nu}d_r)\phi\, B_{\mu\nu}$	$\mathcal{O}_{\phi ud}$	$i(\widetilde{\phi}^\dagger D_\mu\phi)(\bar{u}_p\gamma^\mu d_r)$
$(\bar{L}L)(\bar{L}L)$		$(\bar{R}R)(\bar{R}R)$		$(\bar{L}L)(\bar{R}R)$	
$\mathcal{O}_{ll}$	$(\bar{l}_p\gamma_\mu l_r)(\bar{l}_s\gamma^\mu l_t)$	$\mathcal{O}_{ee}$	$(\bar{e}_p\gamma_\mu e_r)(\bar{e}_s\gamma^\mu e_t)$	$\mathcal{O}_{le}$	$(\bar{l}_p\gamma_\mu l_r)(\bar{e}_s\gamma^\mu e_t)$
$\mathcal{O}_{qq}^{(1)}$	$(\bar{q}_p\gamma_\mu q_r)(\bar{q}_s\gamma^\mu q_t)$	$\mathcal{O}_{uu}$	$(\bar{u}_p\gamma_\mu u_r)(\bar{u}_s\gamma^\mu u_t)$	$\mathcal{O}_{lu}$	$(\bar{l}_p\gamma_\mu l_r)(\bar{u}_s\gamma^\mu u_t)$
$\mathcal{O}_{qq}^{(3)}$	$(\bar{q}_p\gamma_\mu\tau^i q_r)(\bar{q}_s\gamma^\mu\tau^i q_t)$	$\mathcal{O}_{dd}$	$(\bar{d}_p\gamma_\mu d_r)(\bar{d}_s\gamma^\mu d_t)$	$\mathcal{O}_{ld}$	$(\bar{l}_p\gamma_\mu l_r)(\bar{d}_s\gamma^\mu d_t)$
$\mathcal{O}_{lq}^{(1)}$	$(\bar{l}_p\gamma_\mu l_r)(\bar{q}_s\gamma^\mu q_t)$	$\mathcal{O}_{eu}$	$(\bar{e}_p\gamma_\mu e_r)(\bar{u}_s\gamma^\mu u_t)$	$\mathcal{O}_{qe}$	$(\bar{q}_p\gamma_\mu q_r)(\bar{e}_s\gamma^\mu e_t)$
$\mathcal{O}_{lq}^{(3)}$	$(\bar{l}_p\gamma_\mu\tau^i l_r)(\bar{q}_s\gamma^\mu\tau^i q_t)$	$\mathcal{O}_{ed}$	$(\bar{e}_p\gamma_\mu e_r)(\bar{d}_s\gamma^\mu d_t)$	$\mathcal{O}_{qu}^{(1)}$	$(\bar{q}_p\gamma_\mu q_r)(\bar{u}_s\gamma^\mu u_t)$
		$\mathcal{O}_{ud}^{(1)}$	$(\bar{u}_p\gamma_\mu u_r)(\bar{d}_s\gamma^\mu d_t)$	$\mathcal{O}_{qu}^{(8)}$	$(\bar{q}_p\gamma_\mu T^a q_r)(\bar{u}_s\gamma^\mu T^a u_t)$
		$\mathcal{O}_{ud}^{(8)}$	$(\bar{u}_p\gamma_\mu T^a u_r)(\bar{d}_s\gamma^\mu T^a d_t)$	$\mathcal{O}_{qd}^{(1)}$	$(\bar{q}_p\gamma_\mu q_r)(\bar{d}_s\gamma^\mu d_t)$
				$\mathcal{O}_{qd}^{(8)}$	$(\bar{q}_p\gamma_\mu T^a q_r)(\bar{d}_s\gamma^\mu T^a d_t)$
$(\bar{L}R)(\bar{R}L)$ and $(\bar{L}R)(\bar{L}R)$		B-violating (often neglected)			
$\mathcal{O}_{ledq}$	$(\bar{l}_p^j e_r)(\bar{d}_s q_t^j)$	$\mathcal{O}_{duq}$	$\epsilon^{\alpha\beta\gamma}\epsilon_{jk}[(d_p^\alpha)^{\mathrm{T}}Cu_r^\beta]\,[(q_s^{\gamma j})^{\mathrm{T}}Cl_t^k]$		
$\mathcal{O}_{quqd}^{(1)}$	$(\bar{q}_p^j u_r)\epsilon_{jk}(\bar{q}_s^k d_t)$	$\mathcal{O}_{qqu}$	$\epsilon^{\alpha\beta\gamma}\epsilon_{jk}[(q_p^{\alpha j})^{\mathrm{T}}Cq_r^{\beta k}]\,[(u_s^\gamma)^{\mathrm{T}}Ce_t]$		
$\mathcal{O}_{quqd}^{(8)}$	$(\bar{q}_p^j T^a u_r)\epsilon_{jk}(\bar{q}_s^k T^a d_t)$	$\mathcal{O}_{qqq}$	$\epsilon^{\alpha\beta\gamma}\epsilon_{jn}\epsilon_{km}[(q_p^{\alpha j})^{\mathrm{T}}Cq_r^{\beta k}]\,[(q_s^{\gamma m})^{\mathrm{T}}Cl_t^n]$		
$\mathcal{O}_{lequ}^{(1)}$	$(\bar{l}_p^j e_r)\epsilon_{jk}(\bar{q}_s^k u_t)$	$\mathcal{O}_{duu}$	$\epsilon^{\alpha\beta\gamma}[(d_p^\alpha)^{\mathrm{T}}Cu_r^\beta]\,[(u_s^\gamma)^{\mathrm{T}}Ce_t]$		
$\mathcal{O}_{lequ}^{(3)}$	$(\bar{l}_p^j\sigma_{\mu\nu}e_r)\epsilon_{jk}(\bar{q}_s^k\sigma^{\mu\nu}u_t)$				

Die approbierte gedruckte Originalversion dieser Dissertation ist an der TU Wien Bibliothek verfügbar.
The approved original version of this doctoral thesis is available in print at TU Wien Bibliothek.
TU Bibliothek Your knowledge hub WIEN

Modified interactions of the top quark to electroweak gauge bosons are described by the operators

$$\mathcal{O}_{uW} = (\bar{q}_p \sigma^{\mu\nu} u_r)\tau^i \widetilde{\phi}\, W^i_{\mu\nu} \qquad (2.3.13)$$

$$\mathcal{O}_{uB} = (\bar{q}_p \sigma^{\mu\nu} u_r)\widetilde{\phi}\, B_{\mu\nu} \qquad (2.3.14)$$

$$\mathcal{O}^{(3)}_{\phi q} = (\phi^\dagger i \overleftrightarrow{D}^i_\mu \phi)(\bar{q}_p \tau^i \gamma^\mu q_r) \qquad (2.3.15)$$

$$\mathcal{O}^{(1)}_{\phi q} = (\phi^\dagger i \overleftrightarrow{D}_\mu \phi)(\bar{q}_p \gamma^\mu q_r) \qquad (2.3.16)$$

$$\mathcal{O}_{\phi u} = (\phi^\dagger i \overleftrightarrow{D}_\mu \phi)(\bar{u}_p \gamma^\mu u_r), \qquad (2.3.17)$$

affecting single top quark production, top quark decays, and modifications in $t\bar{t}$ productions in association with electroweak gauge bosons. Thus, these operators are best probed in single top quark measurements and top quarks produced in association with the Z boson or the photon.

Electroweak dipole operators after symmetry breaking

The SM-EFT operators in Table 2.4 are defined in terms of the fields of the unbroken SM. Most operators, however, enter the processes after EWSB described in Sec. 2.1.2, modifying the coupling of fermions to the electroweak gauge bosons described in Sec. 2.2.4. Considering rewriting the anomalous interaction of top quarks in terms of SM-EFT operators and Wilson coefficients, a redefinition is needed. The definitions below are restricted to the relevant electroweak dipole operators and Wilson coefficients in $t\bar{t}\gamma$ cross section measurements. A complete derivation can be found in Ref. [199].

Operators related to electroweak dipole moments in the top quark sector can be defined in the view of the broken-phase decomposition

$$\begin{pmatrix} \mathcal{O}^{(33)}_{uB} \\ \mathcal{O}^{(33)}_{uW} \end{pmatrix} = \begin{pmatrix} \cos\theta_W & -\sin\theta_W & 0 \\ \sin\theta_W & \cos\theta_W & 2 \end{pmatrix} \begin{pmatrix} (\bar{t}\sigma^{\mu\nu} P_R\, t)\, A_{\mu\nu}\, (v+h) \\ (\bar{t}\sigma^{\mu\nu} P_R\, t)\, Z_{\mu\nu}\, (v+h) \\ \left(\bar{b}\sigma^{\mu\nu} P_R\, t\right) W^-_{\mu\nu}\, (v+h) \end{pmatrix}. \qquad (2.3.18)$$

The definition in Ref. [199] has chosen to use the combination of the W boson, Z boson, and top quark as d.o.f., which is widely used in the interpretation of experimental results. The corresponding Wilson coefficients in the broken phase are thus given as

$$c^{(\mathrm{I})}_{\mathrm{tW}} = \underset{\mathrm{Re}}{\overset{(\mathrm{Im})}{}} \left(c^{(33)}_{uW}\right) \qquad (2.3.19)$$

$$c^{(\mathrm{I})}_{\mathrm{tZ}} = \underset{\mathrm{Re}}{\overset{(\mathrm{Im})}{}} \left(-\sin\theta_W\, c^{(33)}_{uB} + \cos\theta_W\, c^{(33)}_{uW}\right). \qquad (2.3.20)$$

The Wilson coefficient related to the electromagnetic dipole moment can be described as a linear combination by

$$\begin{aligned} c^{(\mathrm{I})}_{\mathrm{t}\gamma} &= \underset{\mathrm{Re}}{\overset{(\mathrm{Im})}{}} \left(\cos\theta_W\, c^{(33)}_{uB} + \sin\theta_W\, c^{(33)}_{uW}\right) \\ &= -\frac{1}{\tan\theta_W}\, c^{(\mathrm{I})}_{\mathrm{tZ}} + \frac{1}{\sin\theta_W}\, c^{(\mathrm{I})}_{\mathrm{tW}}, \end{aligned} \qquad (2.3.21)$$

parametrizing the anomalous coupling of the top quark to the photon. The reformulation of symmetry arguments in EWSB due to effects of additional SM-EFT operators, e.g.,

Die approbierte gedruckte Originalversion dieser Dissertation ist an der TU Wien Bibliothek verfügbar.
The approved original version of this doctoral thesis is available in print at TU Wien Bibliothek.
TU Bibliothek Your knowledge hub WIEN

the effect of $\mathcal{O}_\phi$ on the Higgs potential given in Eq. 2.1.23, is not considered in the parametrization [28].

Using the broken-phase definition of the Wilson coefficients, a direct connection to the anomalous coupling parameters defined in Sec. 2.2.4 can be drawn. The latter differ from the Wilson coefficients in the broken phase only by a constant, and their deviation from the SM value becomes

$$\delta d_{V(A)}^{\gamma} = \frac{\sqrt{2}}{\mathrm{e}} \frac{v \mathrm{m_t}}{\Lambda^2} \underset{\mathrm{Re}}{^{(\mathrm{Im})}} \left(\cos\theta_W \, c_{uB}^{(33)} + \sin\theta_W \, c_{uW}^{(33)} \right) = \frac{\sqrt{2}}{\mathrm{e}} \frac{v \mathrm{m_t}}{\Lambda^2} \, c_{\mathrm{t}\gamma}^{(\mathrm{I})} \tag{2.3.22}$$

$$\delta d_{V(A)}^{\mathrm{Z}} = \sqrt{2} \frac{v^2}{\Lambda^2} \underset{\mathrm{Re}}{^{(\mathrm{Im})}} \left(-\sin\theta_W \, c_{uB}^{(33)} + \cos\theta_W \, c_{uW}^{(33)} \right) = \sqrt{2} \frac{v^2}{\Lambda^2} \, c_{\mathrm{tZ}}^{(\mathrm{I})} \tag{2.3.23}$$

$$\delta g_R = \sqrt{2} \frac{v^2}{\Lambda^2} \, c_{uW}^{(33)} = \sqrt{2} \frac{v^2}{\Lambda^2} \, c_{\mathrm{tW}}. \tag{2.3.24}$$

The definitions focus on the connection of the Wilson coefficients given in Eqs. 2.3.19–2.3.21 and the corresponding modified Lagrangian given in Sec. 2.2.4. These are of special interest for the SM-EFT interpretation of the $\mathrm{t\bar{t}}\gamma$ cross section measurement given in Chapter 5. Further definitions are given in Ref. [120], as well as a full review of the operators in the top quark sector is shown in Refs. [199, 200].

Cross section effects of effective field theory operators

In requiring baryon- and lepton-number conservation and considering the effect of operators with dimensionality $d \geq 7$ suppressed by higher powers of Λ, the generic Lagrangian given in Eq. 2.3.2 is modified by dimension-six operators to

$$\mathcal{L}_{\text{SM-EFT}} = \mathcal{L}_{\text{SM}} + \sum_i \frac{c_i}{\Lambda^2} \mathcal{O}_i, \tag{2.3.25}$$

with the operators $\mathcal{O}_i$ given in Table 2.4. SM-EFT operators thus modify the matrix element (ME) $\mathcal{M}$ and the predicted cross section σ of a given process by

$$\begin{aligned} \sigma &\propto \left| \mathcal{M}_{\text{SM}} + \sum_i \frac{c_i}{\Lambda^2} \mathcal{M}_{\text{BSM}}^i \right|^2 \\ &= |\mathcal{M}_{\text{SM}}|^2 + \sum_i \frac{c_i}{\Lambda^2} \mathrm{Re}\, \mathcal{M}_{\text{SM}}^* \, \mathcal{M}_{\text{BSM}}^i + \sum_{i,j} \frac{c_i c_j}{\Lambda^4} \mathcal{M}_{\text{BSM}}^{i*} \, \mathcal{M}_{\text{BSM}}^j, \end{aligned} \tag{2.3.26}$$

leading to the cross section dependence

$$\sigma = \sigma_{\text{SM}} + \sum_i \frac{c_i}{\Lambda^2} \sigma_i + \sum_{i,j} \frac{c_i c_j}{\Lambda^4} \sigma_{ij}. \tag{2.3.27}$$

The SM cross section σ_{SM} is extended by interference terms of the SM with dimension-six operators described in the second term, and pure SM-EFT cross section contributions, including their interferences, in the third term. Even though pure SM-EFT contributions are suppressed by Λ^4, they can lead to dominant corrections to the SM cross section in case of small interference terms.

Die approbierte gedruckte Originalversion dieser Dissertation ist an der TU Wien Bibliothek verfügbar.
The approved original version of this doctoral thesis is available in print at TU Wien Bibliothek.
TU Bibliothek Your knowledge hub WIEN

Die approbierte gedruckte Originalversion dieser Dissertation ist an der TU Wien Bibliothek verfügbar.
The approved original version of this doctoral thesis is available in print at TU Wien Bibliothek.

Chapter 3

The LHC and the CMS experiment

The LHC [201–204], operated by the European Organization for Nuclear Research (CERN), is the world's largest particle collider. It is located at the Swiss-French border with four locations to collide proton or heavy-ion beams. Each location corresponds to the position of one of the four main detectors of the LHC, the multi-purpose detectors Compact Muon Solenoid (CMS) [205] and A Toroidal LHC ApparatuS (ATLAS) [206], the A Large Ion Collider Experiment (ALICE) [207] detector focusing on heavy-ion physics, as well as the LHC beauty (LHCb) [208] experiment, mainly studying bottom quarks.

The results of this thesis were obtained from pp collisions collected by the CMS experiment during 2016–2018 data-taking periods. In the following, an introduction to the CERN accelerator complex and the LHC, an overview of the CMS detector, as well as a description of the object reconstruction within the CMS experiment is given.

3.1 The CERN accelerator complex

Founded in 1954, the CERN organization started the operation of its first particle accelerator, the Synchrocyclotron, in 1957. Since then, the effort in accelerating particles and gaining knowledge on the fundamental building blocks of our universe expanded, with larger and more complex accelerators, colliding particle beams at increasing energy. Among others, the accelerator complex now includes facilities for high-energy particle physics, heavy ion physics, neutron physics, neutrino physics, isotope studies, antiproton deceleration and advanced collider technologies.

In 2008, the LHC became operational, with its first particle collisions reported in 2009. From a bottle of hydrogen gas to proton beams accelerated to the record energy of 6.5 TeV, the LHC accelerator complex is the largest machine ever built.

3.1.1 The LHC pre-accelerator chain

Protons are accelerated in multiple steps to achieve the designed collision energy of 14 TeV, and thus, the LHC relies on a pre-accelerator chain. The LHC was designed to use its predecessors as injector chain, where protons are accelerated from an initial hydrogen

Die approbierte gedruckte Originalversion dieser Dissertation ist an der TU Wien Bibliothek verfügbar.
The approved original version of this doctoral thesis is available in print at TU Wien Bibliothek.
TU Bibliothek Your knowledge hub WIEN

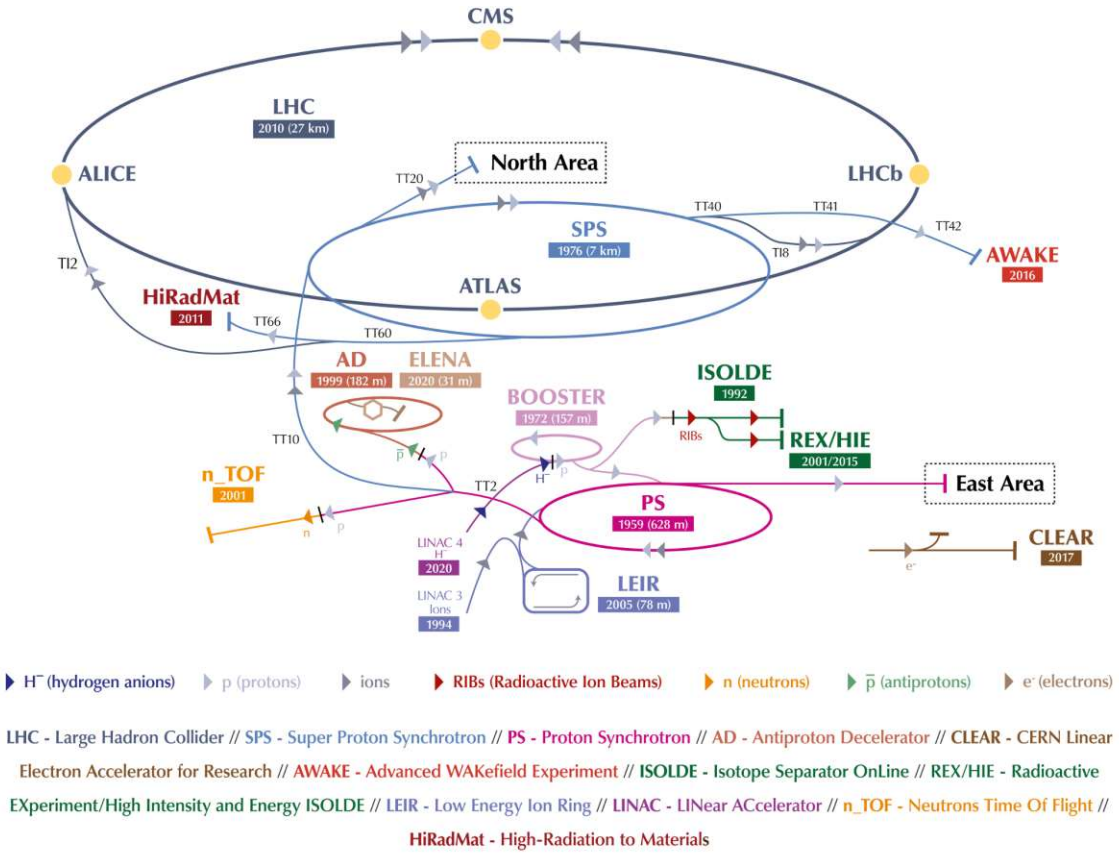

Figure 3.1: The CERN accelerator complex. Key experiments, accelerators and decelerators are shown, with the LHC as the last ring in the acceleration chain for protons and heavy ions. Figure adapted from Ref. [210].

source, via the Linear Accelerator (Linac) 2 [209], the Proton Synchrotron Booster (PSB), the Proton Synchrotron (PS), and the Super Proton Synchrotron (SPS), before high-energy protons are supplied to the LHC. Previous particle colliders were upgraded to meet the technical requirements of the LHC. An overview of the facilities and the accelerator complex is given in Fig. 3.1.

Protons are extracted in ionizing hydrogen using a Duoplasmotron ion source and are subsequently injected in the Linac2, the starting point of the proton beam. Built from its predecessor, the Linac1, several upgrades were performed to meet the increasing requirements of the accelerator complex. After the latest upgrade, the Linac2 accelerates protons to a peak energy of 50 MeV using radiofrequency (RF) cavities operated at $f_{\mathrm{RF}} = 200\,\mathrm{MHz}$, providing currents up to 180 mA [203]. Due to the RF fields, proton beams are formed into longitudinally spaced intervals, so-called buckets, where the number of buckets is defined by the harmonic number $h = f_{\mathrm{RF}}/f_{\mathrm{rev}}$, with the revolution frequency f_{rev}. Each bucket is filled with a proton bunch, however, empty buckets are possible if the spacing between the bunches is needed for operational purposes.

Proton bunches formed by the RF cavities are further injected into four vertically separated synchrotron rings of the PSB, with a radius of 25 m each. In preparation for the LHC, an upgrade of the PSB magnets allowed to increase the output energy of the proton beam from 1.0 to 1.4 GeV. In addition, operations at a harmonic number of $h = 1$, thus only injecting one bunch per synchrotron ring, reduces space-charge effects and losses of the

Die approbierte gedruckte Originalversion dieser Dissertation ist an der TU Wien Bibliothek verfügbar.
The approved original version of this doctoral thesis is available in print at TU Wien Bibliothek.
TU Bibliothek Your knowledge hub WIEN

low-energy proton beam. A two-batch filling scheme, with a total of six proton bunches on a harmonic $h = 7$, thus one empty bucket, is used for the injection into the PS accelerator.

The PS, a synchrotron of 100 m radius including 100 dipole magnets, was the world's highest-energy particle accelerator. Today, it is used as a critical component in the pre-accelerator complex. In a staged procedure, protons are accelerated to 25 GeV and buckets are longitudinally split to achieve the 25 ns spacing between the bunches required for the LHC operations [211].

Up to four PS fillings are injected into the 1100 m radius SPS, the second-largest accelerator at CERN. Formally colliding protons and antiprotons [212], the SPS hosted the UA1 and UA2 experiments, which discovered the $W^{\pm}$ [213, 214] and Z bosons [215, 216]. The SPS, consisting of 744 dipole magnets, now accelerates protons up to 450 GeV and is used in the supply chain for the LHC and many other experiments. A detailed discussion on the LHC pre-accelerator chain can be found in Ref. [203].

For future operations and in preparation for the HL-LHC [217], the pre-accelerator chain is currently upgraded. The Linac2 was replaced in 2020 by a more modern design known as the Linac4 [218], accelerating H^- ions with increased output-energy of 160 MeV and higher beam quality. Two electrons are stripped at the stage of an upgraded PSB, with replaced key components capable of accelerating higher-intensity proton beams up to 2 GeV [219–221]. In addition to a new scheme of the proton-bunch train, these upgrades are expected to meet the requirements of future LHC operations and its planned upgrade to the HL-LHC [222].

3.1.2 The Large Hadron Collider

The LHC is the latest and largest accelerator ring of the CERN accelerator complex. It is built in a 26.7 km circumference underground tunnel at a depth ranging from 45–170 m, that was formally hosting the Large Electron Positron Collider (LEP) [50]. Two counter-rotating beams of charged particles, either protons or heavy ions, are accelerated and stored in evacuated beam pipes, which then are collided at one of the four collision points. The LHC is designed for a pp collision energy of 14 TeV, and was operated at 7 TeV (2010–2011), 8 TeV (2012–2013) and 13 TeV (2015–2018), with short special runs at various other center-of-mass energies and shutdowns for upgrades in between. The current shutdown is dedicated to upgrades of the accelerator, the pre-accelerator chain, as well as the detectors in preparation for the next data-taking period of Run 3, starting in 2022, and the future HL-LHC with increased beam brightness and collision energy of 14 TeV, expected to be operational in late 2027.

The current LHC bunch filling scheme injects up to $n_b = 2808$ proton bunches from twelve batch fillings of the SPS pre-accelerator into the beam pipes. A total of 1232 niobium titanium (NbTi) superconducting dipole magnets, operated at temperatures below 2 K, provide a magnetic field of 8.3 T to bend the beams and keep them on a circular orbit. Spatial and momentum focusing of the beams are performed using quadrupole and sextupole magnets, and multiple superconducting RF cavities, operated at a frequency of $f_{\mathrm{RF}} = 400$ MHz, accelerate the charged particles to the desired collision energy. Special equipment like kicker magnets are used to inject the bunches from the SPS or dump the beams at the end of the operation.

Die approbierte gedruckte Originalversion dieser Dissertation ist an der TU Wien Bibliothek verfügbar.
The approved original version of this doctoral thesis is available in print at TU Wien Bibliothek.
TU Bibliothek Your knowledge hub WIEN

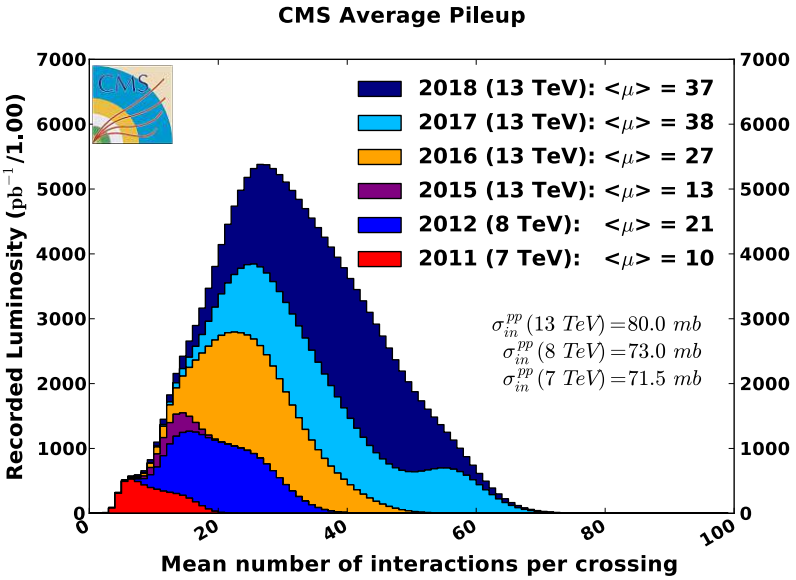

Figure 3.2: Distributions of average numbers of interactions per bunch crossing in pp collisions measured by the CMS experiment at the LHC. The distributions are overlayed for the data-taking periods of 2011 (red), 2012 (blue), 2015 (purple), 2016 (orange), 2017 (light blue), and 2018 (dark blue), with an average number of 10, 21, 13, 27, 38, and 37 simultaneous collisions, respectively. Figure taken from Ref. [223].

Pileup effects

Separated by the 25 ns spacing determined in the PS, the LHC achieves a collision rate of 40 MHz. Due to this high collision rate and the extreme conditions the LHC is operated at, typically several collisions happen simultaneously during the intersection of bunches at the interaction point (IP). This so-called pileup (PU) leads to multiple collisions from the same bunch crossing and thus challenges for the experiments in reconstructing the collision products. The average numbers of interactions per bunch crossing measured by the CMS experiment are shown in Fig. 3.2 for the data-taking periods, reaching up to an average of 38 simultaneous collisions.

Instantaneous luminosity

One of the key parameters in designing a particle collider and defining the possible reach of resulting physics analyses is the instantaneous luminosity

$$\mathcal{L} = \frac{N_b^2 n_b f_{\text{rev}} \gamma}{4\pi \epsilon_n \beta^*} F, \tag{3.1.1}$$

with the proton number per bunch N_b, the number of bunches in the collider n_b, the Lorentz factor γ, the transverse beam emittance ϵ_n, the beta function at the collision point β^*, and a geometric luminosity reduction factor F [204]. The beam emittance is a measure of the spatial and momentum spread of beam particles in the phase space, and F is a reduction of the number of interactions due to the crossing angle of the bunches at the IP. Limitations of the designed luminosity of the LHC thus are, among others, given by beam-beam interactions and the maximum number of protons per bunch, the maximum

Die approbierte gedruckte Originalversion dieser Dissertation ist an der TU Wien Bibliothek verfügbar.
The approved original version of this doctoral thesis is available in print at TU Wien Bibliothek.
TU Bibliothek Your knowledge hub WIEN

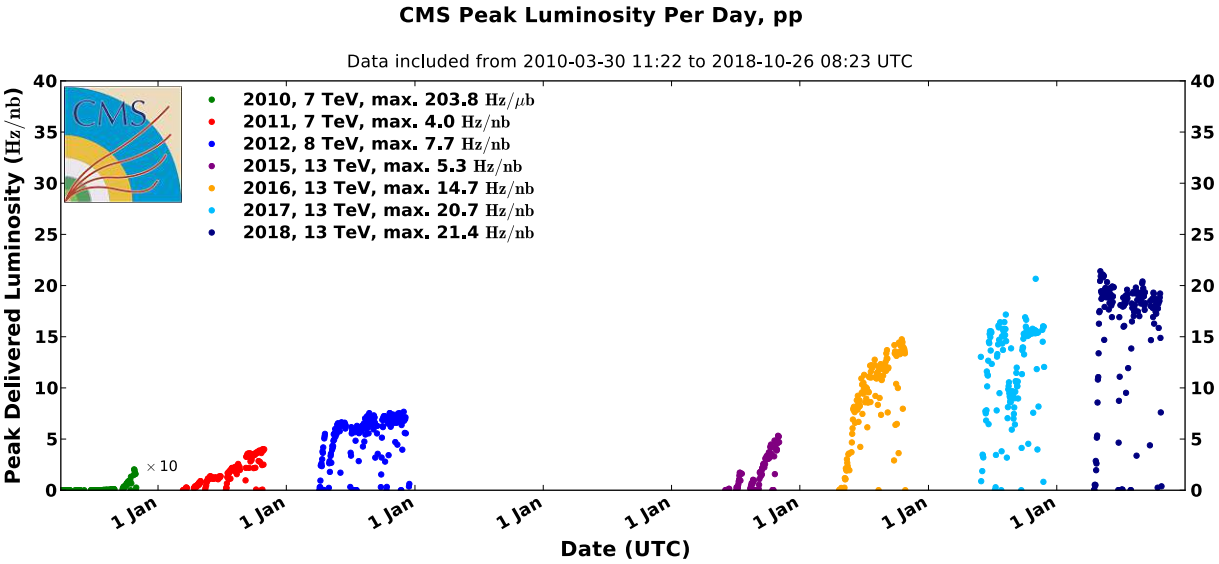

Figure 3.3: Summary of the peak luminosity values delivered to the CMS experiment per day of stable LHC operation for pp collisions. The values are shown for the data-taking periods of 2010 (green), 2011 (red), 2012 (blue), 2015 (purple), 2016 (orange), 2017 (light blue), and 2018 (dark blue). Figure taken from Ref. [223].

number of bunches in the collider ring, the achievable energy of the beam limited by the magnetic field of the dipole magnets, space-charge effects affecting the beam emittance, and the crossing angle of the bunches [204]. While the LHC was designed for a peak luminosity of $\mathcal{L} = 10^{34}\,\mathrm{cm}^{-2}\,\mathrm{s}^{-1} = 10\,\mathrm{nb}^{-1}\,\mathrm{s}^{-1}$ for pp collisions, this goal was surpassed by more than a factor of 2 in 2017 and 2018. Fig. 3.3 shows the peak luminosity values recorded by the CMS experiment in the 2010–2018 data-taking periods.

The instantaneous luminosity $\mathcal{L}$ translates into the expected production rate of a given process of

$$\frac{dN}{dt} = \sigma\,\mathcal{L} \tag{3.1.2}$$

with its production cross section σ. The total number of produced processes during the data-taking periods is thus given by

$$N = \sigma \int \mathcal{L}\,dt = \sigma\,L, \tag{3.1.3}$$

with the integrated luminosity L. The LHC was able to deliver a total integrated luminosity of $L = 193\,\mathrm{fb}^{-1}$ in the years of operation (2010–2018), with a total of $L = 163.6\,\mathrm{fb}^{-1}$ for collisions at a center-of-mass energy of 13 TeV. Thus, it is expected that more than 136 million $\mathrm{t\bar{t}}$ events were produced during Run 2 data taking using the $\mathrm{t\bar{t}}$ production cross section given in Eq. 2.2.3. A summary of the integrated luminosity delivered to the CMS experiment is shown in Fig. 3.4 for the 2010–2018 data-taking periods.

Die approbierte gedruckte Originalversion dieser Dissertation ist an der TU Wien Bibliothek verfügbar.
The approved original version of this doctoral thesis is available in print at TU Wien Bibliothek.
TU Bibliothek Your knowledge hub WIEN

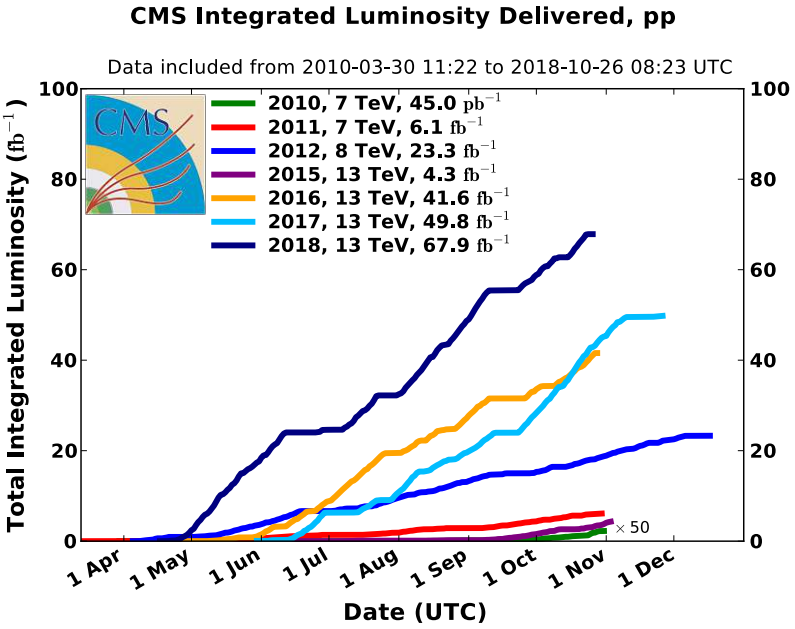

Figure 3.4: The cumulative luminosity delivered to the CMS experiment during stable LHC operations for pp collisions. The values are shown for the data-taking periods of 2010 (green), 2011 (red), 2012 (blue), 2015 (purple), 2016 (orange), 2017 (light blue), and 2018 (dark blue). Figure taken from Ref. [223].

3.2 The CMS experiment

The CMS experiment is a multi-purpose detector, designed for recording and reconstructing pp and heavy-ion collisions. Located at IP 5 about 100 m underground, CMS is a detector of 28.7 m length and 15 m diameter, consisting of cylindrical layers of subdetector modules arranged around the IP. The key design element is the superconducting solenoid magnet [224], which is the reason for "compact" in the name of the experiment. Within the magnet, the silicon pixel and strip trackers [225–227], the electromagnetic calorimeter (ECAL) [228], as well as the hadronic calorimeter (HCAL) [229] are nested around the beam pipe, designed for covering nearly the entire angle around the IP. The muon system [230] is located outside the solenoid. An illustration of the CMS experiment and its subdetectors is shown in Fig. 3.5.

In the following, the coordinate system and the main subsystems of the CMS detector are briefly discussed. A more detailed description can be found in Refs. [205, 231]. The discussion in this section includes the detection of particles in the CMS detector and its subsystems, where the same principles apply for particles and the corresponding antiparticles, with no further distinction made in the text.

3.2.1 CMS coordinate system

The coordinate system of the CMS experiment has its origin at the collision point of the particle beams in the center of the detector, with its x axis pointing towards the center of the LHC and the y axis pointing vertically upwards. The transverse plane is spanned by the x and y axis, and the azimuthal angle ϕ is measured from the x axis within the

Die approbierte gedruckte Originalversion dieser Dissertation ist an der TU Wien Bibliothek verfügbar.
The approved original version of this doctoral thesis is available in print at TU Wien Bibliothek.
TU Bibliothek Your knowledge hub WIEN

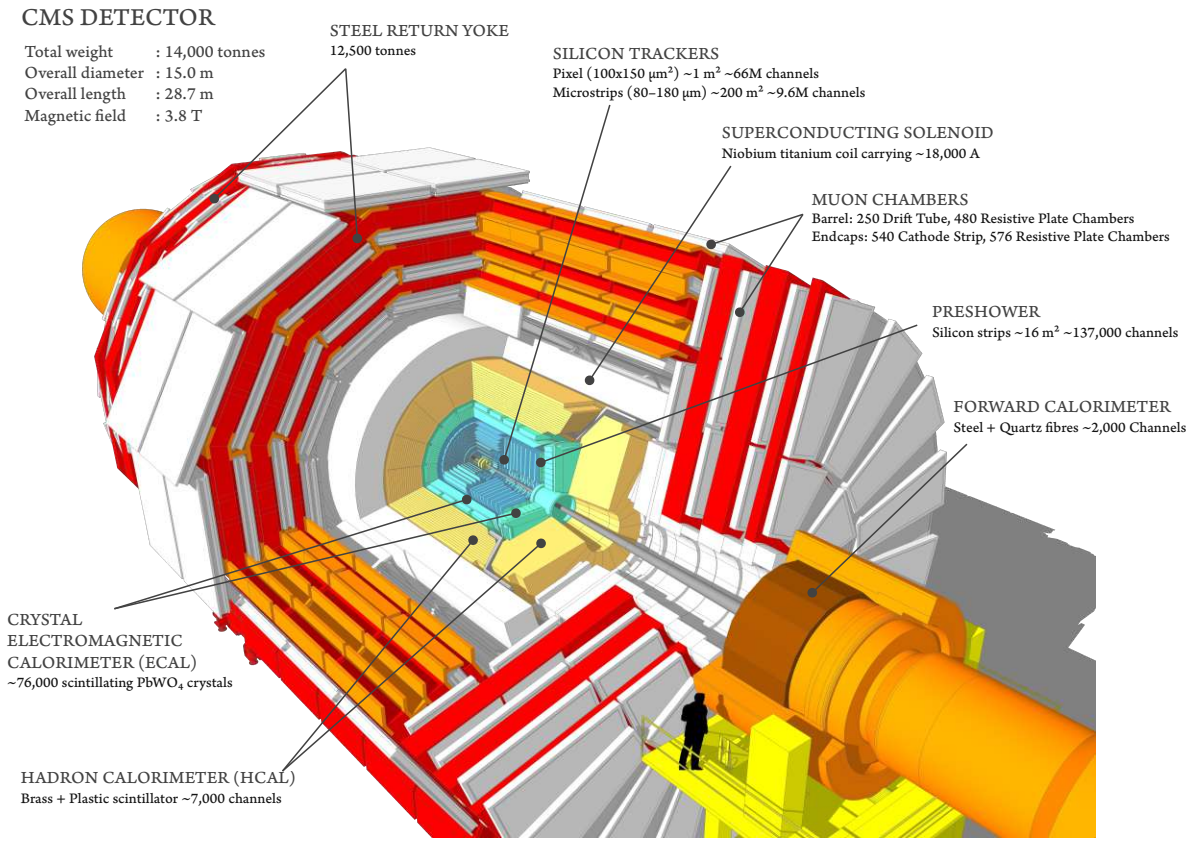

Figure 3.5: Illustration of the CMS detector and its subdetectors. The tracker is the closest subdetector to the IP, surrounded by the electromagnetic and hadronic calorimeters, a superconducting magnet, and the muon chambers. Figure taken from Ref. [232].

transverse plane. Momentum and energy components perpendicular to the beam are thus denoted as transverse momentum p_T and transverse energy E_T. The z axis, perpendicular to the transverse plane, is pointing in the beam direction towards the Jura mountains. The polar angle θ is defined from the z axis. In the description of the detector, as well as in physics analysis, the polar angle is often substituted by the pseudorapidity η, with

$$\eta = -\ln\tan\left(\frac{\theta}{2}\right) = \operatorname{arctanh}\left(\frac{p_z}{p}\right), \tag{3.2.1}$$

where p is the absolute momentum and p_z is its component along the z axis.

3.2.2 Superconducting solenoid magnet

The superconducting solenoid magnet is the core component of the CMS detector. The distinctive feature is its four-layer winding of NbTi wires, operated at a superconducting temperature of 4.6 K. With a diameter of 6.3 m and a length of 12.5 m it is designed to provide a uniform axial magnetic field of 3.8 T. At a nominal current of 19.14 kA the stored energy amounts to a total of 2.6 GJ. These unique technical aspects and the extreme conditions make it challenging to operate the magnet.

Die approbierte gedruckte Originalversion dieser Dissertation ist an der TU Wien Bibliothek verfügbar.
The approved original version of this doctoral thesis is available in print at TU Wien Bibliothek.
TU Bibliothek Your knowledge hub WIEN

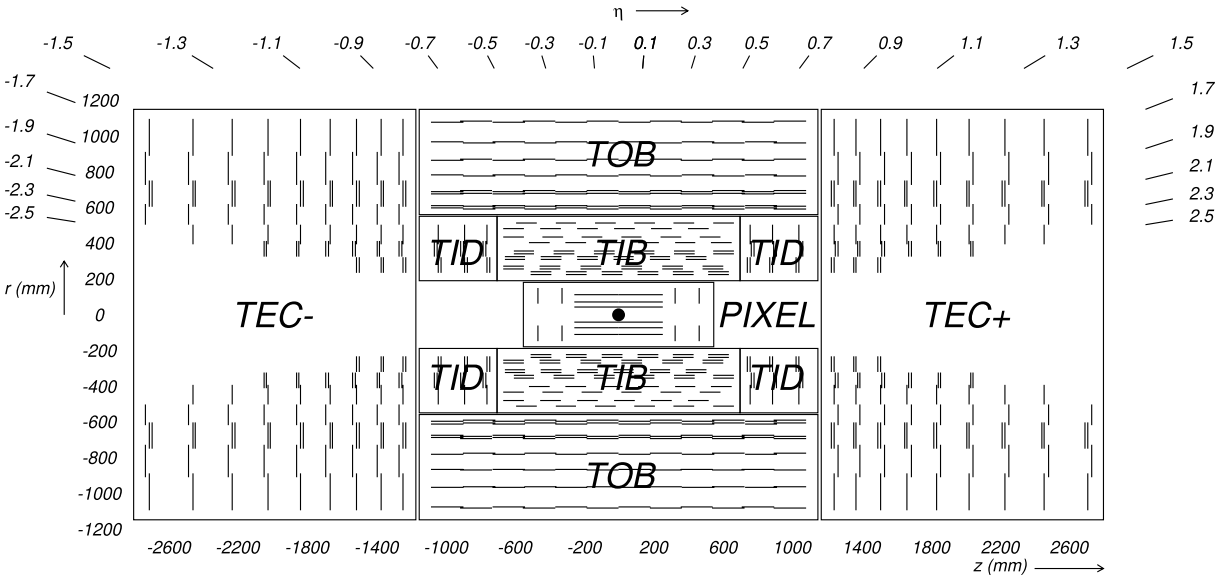

Figure 3.6: Schematic view of the CMS tracking system, with each tracking module indicated by a solid line and back-to-back modules indicated by two lines. Figure taken from Ref. [205].

Five barrel wheels and six endcap disks with a total weight of 10 000 t form the steel yoke, which returns the magnetic flux. The bending power of charged particles allows for strong separation from neutral-particle energy deposits in the calorimeter. In addition, the solenoid magnet serves as an absorber of hadronic particles, and thus, a clean muon signal can be detected in the outer muon system.

3.2.3 Inner tracking system

The precise determination of charged-particle trajectories, emerging from beam collisions at the IP, is performed by the inner tracking system of the CMS detector. It consists of two parts, the pixel detector and strip sensors. The inner tracker is located in a support structure with a diameter of 2.5 m and a total length of 5.8 m, surrounding the collision point. Due to its location close to the IP and the high-luminosity design of the LHC, the inner tracking system has to withstand an intense particle flux, potentially causing severe radiation damage. The requirements on read-out speed, radiation hardness, and granularity thus lead to a design based on silicon detector technology, where a total active silicon area of 198 m^2 form the inner tracking system. A schematic view of the tracking detector and its modules with the initial design of the pixel subdetector is shown in Fig. 3.6.

Pixel detector system

During the 2016 data-taking period, the pixel detector consisted of three layers of pixel modules in the barrel region, arranged at distances $r = 4.4$–10.2 cm to the IP, and two endcaps with two layers each at $|z| = 34.5$ and 46.5 cm. The pixel detector extends to $|\eta| = 2.5$ with a pixel size of $100 \times 150\,\mu m^2$, allowing for measuring at a spatial resolution down to 10 µm for high-p_T tracks. In early 2017, the pixel detector was upgraded [227]

Die approbierte gedruckte Originalversion dieser Dissertation ist an der TU Wien Bibliothek verfügbar.
The approved original version of this doctoral thesis is available in print at TU Wien Bibliothek.
TU Bibliothek Your knowledge hub WIEN

to withstand the increasing spontaneous-luminosity conditions with larger number of PU interactions. A fourth layer closer to the beam pipe was added, with the barrel layers now arranged at distances $r = 3$–$16\,\text{cm}$. With power-converter issues during the 2017 data-taking period [233], the new pixel detector became fully operational in 2018, accounting to an increased tracker performance and improved vertex reconstruction in high-PU conditions.

Silicon strip tracker

The strip tracker consists of ten layers in the barrel and twelve layers in the endcap regions. The regions are denoted as tracker inner barrel (TIB), tracker outer barrel (TOB), tracker inner disk (TID) and tracker endcap (TEC).

The TIB consists of four detection layers, located at $r = 20$–$55\,\text{cm}$, which cover a z range up to $|z| = 70\,\text{cm}$. Additional six layers in the TOB extend the barrel tracker to $r = 116\,\text{cm}$ and $|z| = 118\,\text{cm}$. Three layers in the endcap discs of the TID and additional nine layers in the TEC extend the barrel tracker in the forward (TEC+) and backward (TEC-) regions up to $|z| = 118\,\text{cm}$ and $|z| = 282\,\text{cm}$, respectively [205]. Multiple layers are equipped with a second detector module mounted back-to-back in an angle of 100 mrad to each other, allowing to measure the z (r) directions of charged-particle tracks in barrel (endcap) regions. The CMS strip tracking system extends the pixel detector and provides a full η coverage of up to $|\eta| = 2.5$. The layout ensures that at least nine particle hits, with at least four two-dimensional hits, are detected in the silicon strip tracker up to an η coverage of $|\eta| = 2.4$.

3.2.4 Calorimeters

The energy of electrons, photons, and hadronic particles is measured in calorimeters located within the solenoid magnet but outside the inner tracking system of the CMS detector. The calorimeters are designed to stop the corresponding particles and measure their total energy, with muons and neutrinos passing the detector array. The subdetector is divided into the ECAL, measuring the energy of electrons and photons, and the HCAL, used to measure the energy of hadronic jets.

Electromagnetic calorimeter

The ECAL is a homogeneous calorimeter made of high-density lead tungstate ($PbWO_4$) crystals, which allows for a fast read-out of the signal, fine granularity, and ensures radiation hardness. It is divided into the cylindrical ECAL barrel (EB) and two ECAL endcaps (EE). The former consists of 61200 crystals and is located between the inner radius of $r = 1.24\,\text{m}$ and its outer radius of $r = 1.75\,\text{m}$, extending to $|z| = 3.045\,\text{m}$ in the z direction. Thus, it allows to measure the particle energy up to a pseudorapidity of $|\eta| = 1.479$. Its total volume of scintillating crystals amounts to $8.14\,\text{m}^3$ with a total weight of 67.4 t.

The EE consists of two endcap discs with a radius of $r = 1.71\,\text{m}$, each built from 7324 crystals with a total volume of $2.9\,\text{m}^3$ and a weight of 24 t. The z position of the discs

Die approbierte gedruckte Originalversion dieser Dissertation ist an der TU Wien Bibliothek verfügbar.
The approved original version of this doctoral thesis is available in print at TU Wien Bibliothek.
TU Bibliothek Your knowledge hub WIEN

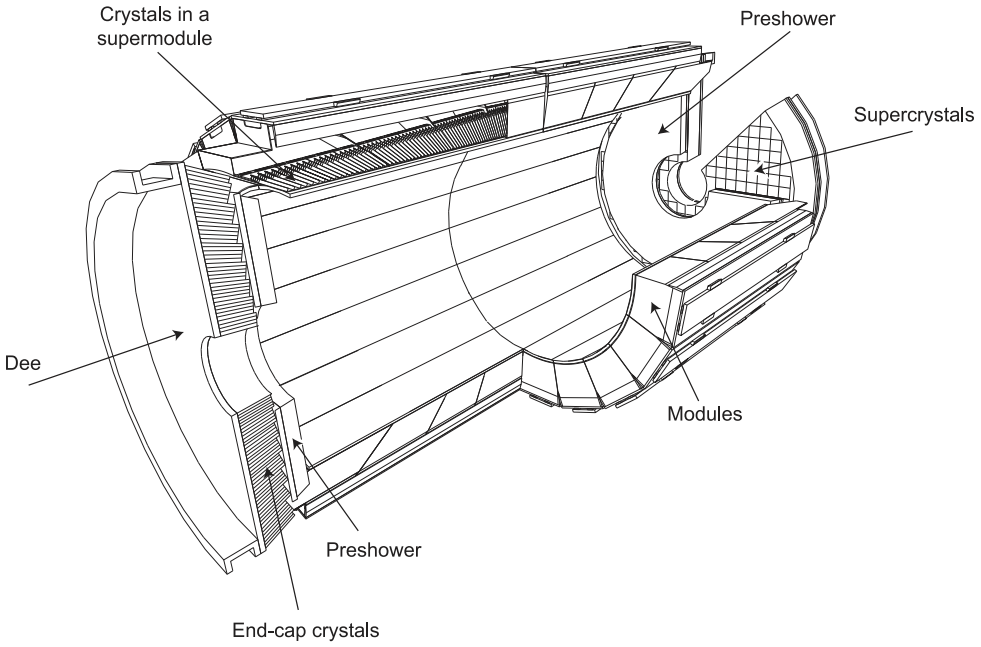

Figure 3.7: Illustration of the electromagnetic calorimeter (ECAL) of the CMS experiment. The module arrangement of the barrel and endcap detectors are shown, with the preshower detectors located in front of the latter. Figure taken from Ref. [205].

ranges from $|z| = 3.17$–$3.9\,\text{m}$, thus covering the pseudorapidity range of $1.479 < |\eta| < 3.0$. The design of the EE allows for precision measurements up to $|\eta| = 2.6$, with energy-flow measurements in the forward direction up to $|\eta| = 3.0$. The gap between the EB and EE at $1.4442 < |\eta| < 1.566$ is typically excluded in measurements of electrons and photons.

The endcap discs are equipped with preshower detectors (ES), located in front of the EE and covering the pseudorapidity range of $1.65 < |\eta| < 2.61$. Two lead absorber planes and two silicon microstrip modules included in an ES module of 185 mm thickness help to distinguish the detector signal of single photons from the signal emerging from the decay of neutral pions to a photon pair, $\pi^0 \to \gamma\gamma$, thus reduce the misidentification rate of a π^0 as a photon.

Particles hitting the scintillator crystals of the ECAL radiate bremsstrahlung photons, which further undergo electron-positron pair production. The cascade of electromagnetic showering results in low-energy electrons and photons, which are absorbed by the crystals and detected from the scintillation light of the ionized atoms of the ECAL. The signal is detected by the read-out electronics consisting of avalanche photodiodes in the barrel and vacuum phototriodes in the endcap regions.

Crystal damages from high particle flux in high-PU collisions lead to a reduction of the light transmission in the ECAL. Damages are tracked in measuring the optical transparency using laser light, and effects are corrected in data. A schematic view of the ECAL is shown in Fig. 3.7, with a detailed description of the calorimeter given in Refs. [205, 228]

Die approbierte gedruckte Originalversion dieser Dissertation ist an der TU Wien Bibliothek verfügbar.
The approved original version of this doctoral thesis is available in print at TU Wien Bibliothek.
TU Bibliothek Your knowledge hub WIEN

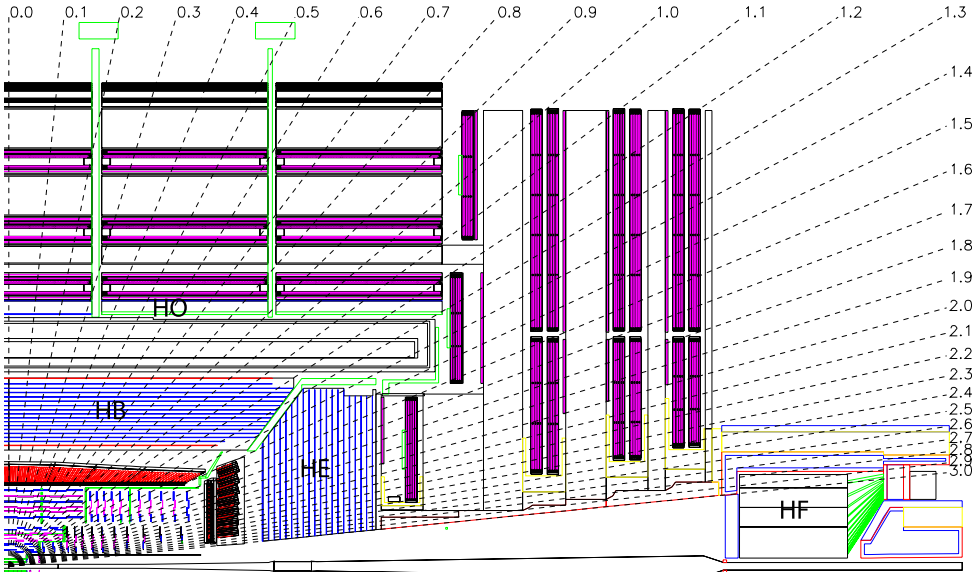

Figure 3.8: Longitudinal view of the hadronic calorimeter (HCAL) of the CMS experiment. The location and composition of the HCAL barrel (HB), HCAL endcap (HE), HCAL outer (HO), and HCAL forward (HF) subdetector modules are shown, with the latter located outside the muon system indicated in purple. Figure taken from Ref. [205].

Hadronic calorimeter

The HCAL is an important calorimeter for measurements of the energy of hadronic jets and missing transverse energy E_T^{miss}. The latter is the result of undetected neutrinos in the decay products of emerging particles from the collisions, or potentially unknown exotic particles as a result of BSM physics. The HCAL consists of flat nonmagnetic brass absorbers, in between plastic scintillators, and double-cladded wavelength-shifting (WLS) fibers attached to the scintillators. The WLS fibers forward the detected signal to hybrid photodiodes, allowing for low material budget within the detector. Hadrons entering the absorber interact with the brass nuclei, with a cascade of hadronic particles resulting from this interaction. The hadronic shower emits light in the plastic scintillator, allowing for measuring its energy.

The HCAL is located as the outermost detector within the solenoid magnet and divided into the HCAL barrel (HB), HCAL outer (HO), HCAL endcap (HE), and HCAL forward (HF) subdetectors, with a schematic few of the subdetectors given in Fig. 3.8.

Located between the ECAL and the magnet at $r = 1.77$–$2.95\,\text{m}$, the HB covers a pseudorapidity range up to $|\eta| = 1.3$. The inner and outer layers of the absorbers are constructed from stainless steel to provide enough structural support for the detector. The HO is located outside the HB, extending its capabilities and is used for detecting late-showering hadrons. Since the ECAL and the HCAL do not provide enough stopping power for hadronic showers in the barrel region, the HO is located in the magnet flux-return yoke, which is used as an additional absorber. It covers a pseudorapidity range up to $|\eta| = 1.26$. The HE extends the coverage of the HB in the forward region of $1.3 < |\eta| < 3.0$.

The most forward subdetector, installed outside the muon system with its front face located at $|z| = 11.2\,\text{m}$, covers the pseudorapidity range of $3.0 < |\eta| < 5.0$. Due to its

Die approbierte gedruckte Originalversion dieser Dissertation ist an der TU Wien Bibliothek verfügbar.
The approved original version of this doctoral thesis is available in print at TU Wien Bibliothek.
TU Bibliothek Your knowledge hub WIEN

location close to the beam pipe, it experiences high particle fluxes. Thus, the operation of this subdetector critically depends on its radiation hardness, where steel plates as absorber material and radiation-resistant quartz fibers as an active medium were chosen for its construction. A detailed description of the calorimeter is given in Ref. [229]

3.2.5 Muon system

The precise measurement of muons was a main focus in the design of the CMS detector. The muon system, located as the outermost subdetector, is used to identify muons, their momentum measurement, and for triggering an event. Due to the high magnetic field provided by the solenoid magnet, the flux-return yoke, and their functionality as hadron absorbers, the muon system allows for a precise momentum measurement over a large kinematic range.

It is divided into the cylindrical barrel and two endcap subdetectors, with a total of $25\,000\,\mathrm{m}^2$ of detector material. The barrel consists of four layers, with 250 drift tube (DT) detector chambers, covering a pseudorapidity region of $|\eta| < 1.2$. Four layers with 540 cathode strip chamber (CSC) modules in the endcaps cover a region of $0.9 < |\eta| < 2.4$, where muons in the region of $0.9 < |\eta| < 1.2$ are detected by both the barrel and endcap muon system. A dedicated trigger system, consisting of 1056 complementary fast-response resistive plate chamber (RPC) modules, was added between the modules in barrel and endcap regions. Six layers in the barrel and three layers in the endcaps provide the ability to trigger with sharp $\mathrm{p_T}$ thresholds in regions of $|\eta| < 1.6$. In total, the muon system covers the full range of up to $|\eta| = 2.4$ without acceptance gaps, however, small efficiency drops were measured between single modules or in the transition region of DT and CSC systems. An schematic view of the muon system is shown in Figs. 3.5 and 3.8 and a detailed discussion is given in Ref. [230].

3.2.6 Data acquisition and the CMS trigger system

As discussed in Sec. 3.1.2, the LHC provides pp bunch crossings at a high frequency of 40 MHz, each with a mean number of up to 38 simultaneous pp collisions. The CMS read-out system produces about 1 MB of data per bunch crossing, resulting in a data stream of $40\,\mathrm{TB\,s^{-1}}$. Most of these collisions are not of interest for the experimental analyses, and thus, storing the data is not feasible. The CMS experiment has deployed a two-tiered trigger system to reduce the data stream to the data acquisition (DAQ) system, recording events for offline processing at a rate below 1 kHz.

The first stage, the level-1 (L1) trigger, relies on an array of field-programmable gate arrays (FPGAs) which process fast trigger information of the energy deposits in the calorimeters and hit patterns in the muon system. Within the L1 trigger architecture, subsystems for the muon system, the global-muon trigger, and the calorimeters, the global-calorimeter trigger, use simple algorithms and detector information with a reduced resolution to construct simplified physics objects. Regional triggers combine and rank these so-called trigger primitives, where the global trigger makes the final trigger decision. Recorded event data are buffered for about 3.2 µs, enough time for the FPGAs to reach a trigger decision. In selecting interesting signatures, the L1 trigger reduces the incoming data

Die approbierte gedruckte Originalversion dieser Dissertation ist an der TU Wien Bibliothek verfügbar.
The approved original version of this doctoral thesis is available in print at TU Wien Bibliothek.
TU Bibliothek Your knowledge hub WIEN

rate to about 100 kHz, which are forwarded by the DAQ system to the second stage, the high-level trigger (HLT).

The HLT uses a computing cluster and specialized reconstruction software, similar to the one described in Sec. 3.3, to reconstruct physics objects with additional track reconstruction using the information of the tracking system. Each computing core processes an event in about 100 ms, with its trigger decision reducing the total rate of stored collision data to below 1 kHz. The data stream of $1\,\mathrm{GB\,s^{-1}}$ is managed and stored by the DAQ system for a sophisticated detector reconstruction at a later stage.

3.3 Object reconstruction in CMS

The CMS software framework processes energy deposits in the calorimeters (clusters) and hit information from the tracking system (tracks) to reconstruct particles and physics objects using the particle-flow (PF) algorithm [231]. Additionally, the PF method is used for cross-calibration of the CMS subdetector systems, identifying detector noise and is implemented in the HLT trigger system. The algorithm was first developed for the ALEPH detector [234] at the LEP collider. CMS is the first hadron-collider experiment to deploy the PF approach. The fine spatial granularity of the CMS subdetector systems, the highly segmented tracker, the fine-grained ECAL, the hermetic HCAL, and the strong magnetic field allow for a good separation of individual particles, a key ingredient for the PF algorithm.

Particles produced in collisions at the IP first enter the inner tracking system, where the interaction of charged particles with the subdetector is recorded. Due to the high magnetic field, the trajectories are bent, which allows for determining the electric charge and momentum of the particle. Neutral particles do not leave a trace in the tracker and are not affected by the magnetic field.

Electrons and photons form an electromagnetic shower in the ECAL and are subsequently absorbed. These showers are recorded as clusters of deposited energy, which allows for determining the energy of the objects. In combination with the information of their trajectories, electrons are distinguished from photons.

Hadronic jets are absorbed in the HCAL, however, they can additionally produce electromagnetic showers in the ECAL. Using the information of clusters in each subdetector allows for measuring their electromagnetic and hadronic energy fraction, and their trajectories distinguish neutral and charged hadrons.

Muons can penetrate the calorimetry and the magnet system, escape the detector and produce hits in the muon system outside the magnet. Hits recorded in the outer subdetector and the inner tracker are used to reconstruct the trajectories and thus measure the electric charge and momentum of the particle.

A schematic view of the CMS detector signatures for various particles, used as an input for the PF algorithm, is shown in Fig. 3.9, with a more detailed description given in the following.

Die approbierte gedruckte Originalversion dieser Dissertation ist an der TU Wien Bibliothek verfügbar.
The approved original version of this doctoral thesis is available in print at TU Wien Bibliothek.
TU Bibliothek Your knowledge hub WIEN

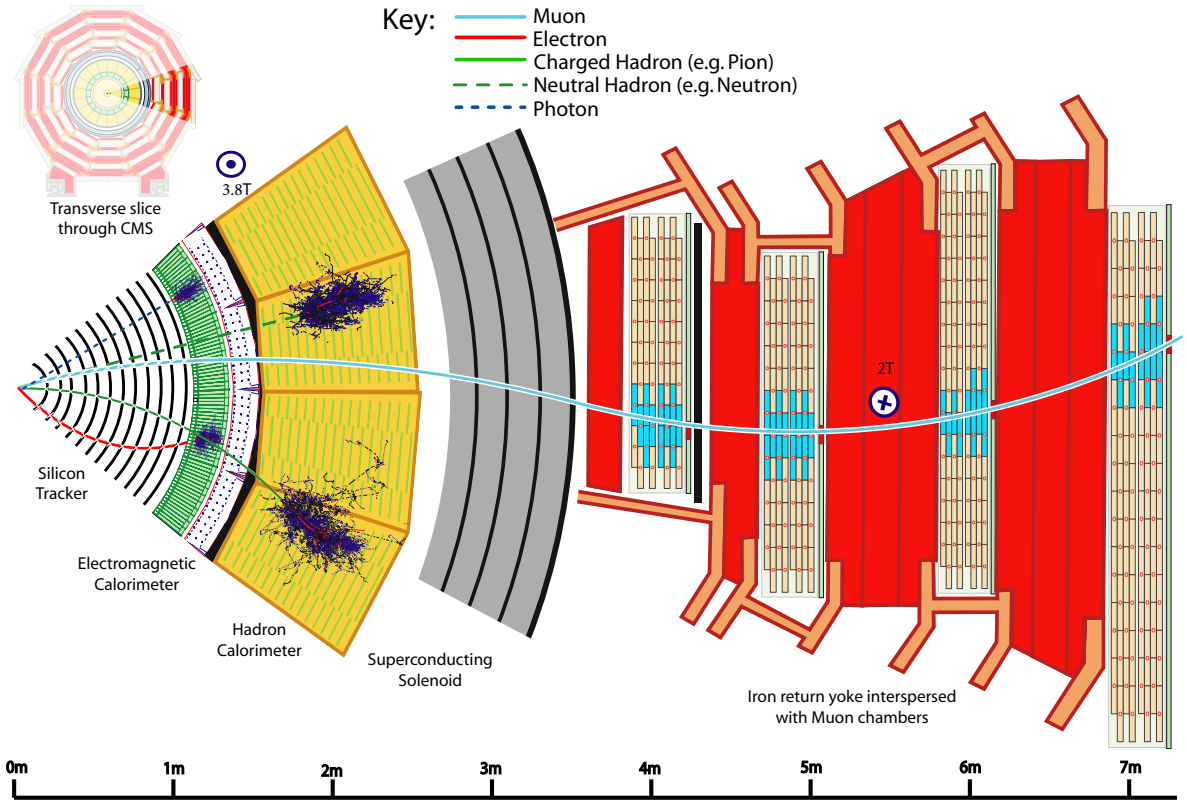

Figure 3.9: Illustration of particle interactions in the subdetector systems of the CMS detector. Information on traces in the tracking system for charged particles, the shower patterns in the electromagnetic and hadronic calorimeters, and detector signals in the muon system are combined in the particle-flow reconstruction algorithm. Figure taken from Ref. [231].

3.3.1 Tracks and clusters

The PF algorithm first identifies local structures in the inner tracker, the calorimeters, and the muon system, without cross-information among the subdetectors. Dedicated algorithms link single detector module hits and are used to reconstruct charged-particle tracks and calorimeter energy deposits. Combining the identified tracks and clusters in the subdetector systems then allows to identify and measure particles hitting the detector. The identification of charged-particle tracks additionally allows for a dedicated vertex reconstruction, distinguishing the hard-scatter event from additional PU interactions.

Track reconstruction

The track reconstruction of charged particles is performed using detector hits in the pixel and strip detector and the outer muon system. A combinatorial track-finding method based on the Kalman filtering (KF) [235] approach is used to find the trajectory of charged particles. An initial seed is generated from a few particle hits that are compatible with the trajectory of a charged particle. Hits from all tracking layers are connected using a pattern-recognition algorithm. A final fit determines the particle properties, such as its

Die approbierte gedruckte Originalversion dieser Dissertation ist an der TU Wien Bibliothek verfügbar.
The approved original version of this doctoral thesis is available in print at TU Wien Bibliothek.
TU Bibliothek Your knowledge hub WIEN

origin, direction, momentum, and electric charge. The performance of the track finder algorithm in terms of misreconstruction rate and reconstruction efficiencies can be found in Ref. [236].

Tracking inefficiencies from missed tracker hits are substantially reduced in lowering the track p_T threshold and accepting fewer hits, with the downside of increasing the rate of misreconstructed tracks [237]. The latter is reduced in applying several tracking iterations, quality criteria on tracking seeds, and criteria on the compatibility of the track origin with the reconstructed IP [238]. The first three iterations require triplets of pixel detector hits, with additional requirements on the distance to the beam axis, resulting in high-quality track reconstruction. Hits associated with the reconstructed track are then masked for the successive iterations to reduce its complexity, where on average 40 (20)% of the hits in the pixel (strip) detector are removed [231]. Tracks with up to two missed hits in the pixel detector are recovered in the fourth and fifth iteration, and displaced tracks without pixel hits are processed in the two iterations thereafter. The eighth iteration aims for tracks in dense cores of high-p_T jets, with possible tracker hits associated with multiple tracks. The last two iterations additionally take the muon system into account and are designed explicitly for muon track reconstruction.

Vertex reconstruction

The reconstructed tracks allow for measuring the IPs of all pp collisions in the event. The vertex with the largest summed p_T^2 of objects is taken as the primary vertex (PV), corresponding to the hard-scatter of an event. An impact parameter for tracks and the associated particle candidate is defined as the distance of the closest point of the track to the PV, where the longitudinal and transverse components are given by d_z and d_{xy}, respectively. The track and vertex reconstructions additionally allow for identifying the particles from additional pp collisions associated with PU vertices.

Cluster reconstruction in the calorimetry

Neutral particles, such as neutral hadrons and photons, are identified using calorimeter signatures. The clustering algorithm measures their energy and direction and separates their energy deposits from those of charged particles. Measurements are separately performed in the ECAL barrel and endcaps, the HCAL barrel and endcaps, as well as the two preshower layers. Initial seeds are identified from large energy deposits in a given cell to reconstruct the clusters. Topological clusters are then formed in aggregating neighboring cells with energy excesses above a given threshold. A Gaussian-mixture model reconstructs clusters of single-particle hits within the topological clusters, with parameters resulting from optimizations based on the energy deposits of neutral pions and kaons, jets, and photons from simulation. The reconstruction is performed using an expectation-maximization algorithm, an iterative algorithm that first keeps the parameters constant to determine the expected energy deposit from single particles and performs a maximum likelihood fit to determine the position and energy of all particles contributing to the topological cluster in a second step.

A linking algorithm connects the track and cluster information to reconstruct PF candidates. Muon candidates are identified and reconstructed as a first step, with detector signatures

Die approbierte gedruckte Originalversion dieser Dissertation ist an der TU Wien Bibliothek verfügbar.
The approved original version of this doctoral thesis is available in print at TU Wien Bibliothek.
TU Bibliothek Your knowledge hub WIEN

of the particles removed from the list of tracks and clusters. The electron reconstruction connects the ECAL and tracking information, where possible bremsstrahlung photons are identified and associated with corresponding particles. In the same step, isolated photons are identified from ECAL clusters. The remaining nonisolated photons, charged and neutral hadrons, and their corresponding jets are then subject to cross-identification, using the signatures of the calorimeters and the tracking system.

3.3.2 Muon reconstruction and identification

The PF algorithm identifies muons by combining measurements in the outer muon system and the inner tracker with high efficiency over the entire detector acceptance. With the additional information from the high-precision momentum measurement in the tracker, the muon reconstruction can be significantly improved [239]. There are, therefore, three essential stages in muon reconstruction.

Standalone muons are reconstructed from clustering and fitting hits in the RPC, CSC, and DT chambers. The track reconstruction is performed using the KF approach, with seeds taken from the DT or CSC detectors.

For tracker muons, inner tracks with $p_T > 0.5\,\text{GeV}$ and a total momentum exceeding 2.5 GeV are extrapolated to the outer muon system. Tracker muons are identified when at least one muon system hit matches the extrapolated inner track.

In global-muon reconstructions, the tracks of standalone muons are matched to inner tracker hits, where the inner tracks have to propagate on a compatible common surface. Global muons are merged with tracker muons to one PF candidate if they share the same inner track. A combined fit determines the global-muon track, with significantly improved momentum resolution for high-p_T muons.

The muon momenta are taken from the p_T of the inner track for $p_T < 200\,\text{GeV}$ and from the smallest χ^2 fit of the track fits above that threshold. Additional requirements on the muon properties enter their identification to distinguish muons from hadrons. The requirements are grouped in muon identification working points to match the specific muon identification criteria of measurements.

Muon identification working points

Global muons have to fulfill an isolation requirement, which is calculated considering calorimeter energy deposits and additional tracks in close angular distance of $\Delta R = \sqrt{\Delta\eta^2 + \Delta\phi^2} < 0.3$ to the muon. The sum of all track p_T and calorimeter energy deposits E_T within the cone is required to be lower than 10 % of the muon p_T, sufficient to reject hadrons misidentified as muons.

The muon fulfills a loose selection criterion (loose ID) [240], if identified as a global or tracker muon. Additional isolation selections are no part of the working point, but recommendations for the momentum sum in a cone of $\Delta R = 0.4$ are to be less than 25 % of the muon p_T. The loose ID is highly efficient for the identification of prompt muons from the PV or the decay of light and heavy quarks.

The tight ID working point [240] requires the muon to be identified as a global and tracker

Die approbierte gedruckte Originalversion dieser Dissertation ist an der TU Wien Bibliothek verfügbar.
The approved original version of this doctoral thesis is available in print at TU Wien Bibliothek.
TU Bibliothek Your knowledge hub WIEN

muon and lowers the isolation recommendations for the candidate to less than 15 %. With a χ^2 of the muon track fit below 10, at least two hits in the muon system, at least one hit in the pixel detector, at least five hits in the silicon strip tracker, and additional requirements on the origin of the track, the tight ID working point is highly efficient in rejecting muons from high-p_T hadrons, in-flight decays, and cosmic sources. Its efficiency ranges from 90 to 95 %, depending on the muon p_T and η [239].

Additionally, the soft muon working point targets low-p_T muon identifications, and the medium ID working point is designed for high efficiency of 99.5 % for prompt muons. These working points are not part of the presented work, and more details can be found in Ref. [240].

3.3.3 Electron and photon reconstruction and identification

The reconstruction of electron tracks is based on the deposited energy in the ECAL clusters, with a transverse energy of $E_T > 4\,\text{GeV}$. The cluster position and energy are used as an initial seed for the tracking algorithm to find the position of inner tracker hits, assuming the cluster originates from an electron. This ECAL-based approach uses clusters in a narrow window in η and an extended window in the ϕ direction to account for electrons radiating bremsstrahlung photons when passing through the tracker material. The grouped energy of the charged lepton and the radiated photons form an ECAL supercluster (SC).

The energy deposit in the ECAL from low-momentum particles or electrons within jets is often biased, the former by widespread radiated photons due to the bending in the magnetic field, the latter by overlapping contributions from surrounding particles. For these, the tracker-based seeding with iterative tracking recovers the efficiency. Electrons are disentangled from charged hadrons in using a Gaussian-sum filter (GSF) [241] to fit the tracks. GSF is the generalization of the KF approach, which uses a Gaussian mixture for modeling the energy loss. This method is better suited for electron track reconstruction than the KF approach, as the radiation of bremsstrahlung photons changes the track curvature, resulting in possible hit losses.

The reconstruction of electrons uses selected seeds from the ECAL- or tracker-based approach and is performed if the ECAL SC matches a track. The reconstruction of photons is performed in the same step, with the PF algorithm only seeded from ECAL SCs with a deposited energy $E_T > 10\,\text{GeV}$, and only if no GSF track is linked to the SC.

The misidentification rate for hadrons is significantly reduced in taking additional information from the HCAL into account. The energy deposit in HCAL cells within $\Delta R = 0.15$ to the ECAL SC has to be less than 10 % of the SC energy for ECAL-based particle candidates. Additionally, the total energy of the particles is corrected for energy losses during the transition of the inner tracker.

Electron identification working points

Further electron identification criteria are based on multivariate analysis (MVA) techniques using boosted decision trees (BDTs), separately trained for barrel and endcap regions. Among others, the BDT input includes variables on the deposited ECAL and HCAL energy, KF and GSF track fitting parameters, tracker hit information, and the origin of

Die approbierte gedruckte Originalversion dieser Dissertation ist an der TU Wien Bibliothek verfügbar.
The approved original version of this doctoral thesis is available in print at TU Wien Bibliothek.
TU Bibliothek Your knowledge hub WIEN

the track [231]. Electron isolation criteria are calculated for particles within an angular distance of $\Delta R = 0.3$ to the electron, with p_T and η dependent thresholds for various working points, separately for barrel and endcap regions [242, 243].

The veto ID working point has an average efficiency of 95 % and is used to veto events with additional leptons. The tight ID working point is optimized for rejecting electrons originating from jets, with an average efficiency of 70 %. The working points include selection criteria on the lateral extension of the ECAL shower in η ($\sigma_{\eta\eta}$), the distance of the SC position to the inner track in η ($\Delta\eta_{in}$) and ϕ ($\Delta\phi_{in}$), the ratio of the deposited energies in the ECAL and HCAL (H/E), the difference of the inverse ECAL energy and track momentum ($E^{-1} - p^{-1}$), the relative isolation criteria (I_{rel}), and the number of missing inner tracker hits ($N_{\text{hit}}^{\text{miss}}$).

Electrons of all working points have to pass a conversion-veto requirement, rejecting electron-positron candidates originating from photons. The selection criteria for the veto ID and tight ID working points are summarized in Table 3.1. Loose and medium ID working points are not part of the presented work, and more details can be found in Refs. [242, 243].

Table 3.1: Summary of the selection criteria for the veto (left) and tight ID (right) electron identification working points for the barrel and endcap regions [243].

	Veto ID		Tight ID	
	Barrel	Endcap	Barrel	Endcap
$\sigma_{\eta\eta}$	< 0.0126	< 0.0457	< 0.0104	< 0.0353
$\Delta\eta_{in}$	< 0.00463	< 0.00814	< 0.00255	< 0.00501
$\Delta\phi_{in}$	< 0.148	< 0.19	< 0.022	< 0.0236
H/E	$< 0.05 + 1.16\ \mathrm{E}_{\mathrm{SC}}^{-1}$ $+0.0324\ \rho\mathrm{E}_{\mathrm{SC}}^{-1}$	$< 0.05 + 2.54\ \mathrm{E}_{\mathrm{SC}}^{-1}$ $+0.183\ \rho\mathrm{E}_{\mathrm{SC}}^{-1}$	$< 0.026 + 1.15\ \mathrm{E}_{\mathrm{SC}}^{-1}$ $+0.0324\ \rho\mathrm{E}_{\mathrm{SC}}^{-1}$	$< 0.0188 + 2.06\ \mathrm{E}_{\mathrm{SC}}^{-1}$ $+0.183\ \rho\mathrm{E}_{\mathrm{SC}}^{-1}$
I_{rel}	$< 0.198 + 0.506\ \mathrm{p}_{\mathrm{T}}^{-1}$	$< 0.203 + 0.963\ \mathrm{p}_{\mathrm{T}}^{-1}$	$< 0.0287 + 0.506\ \mathrm{p}_{\mathrm{T}}^{-1}$	$< 0.0445 + 0.963\ \mathrm{p}_{\mathrm{T}}^{-1}$
$E^{-1} - p^{-1}$	< 0.209	< 0.132	< 0.159	< 0.0197
$N_{\text{hit}}^{\text{miss}}$	≤ 2	≤ 3	≤ 1	≤ 1
Conv. veto	✓	✓	✓	✓

Photon identification working points

Similar to the electron identification, the photon identification in barrel and endcap regions is based on MVA techniques using BDTs [243, 244]. The isolation criteria are calculated with an angular distance parameter of $\Delta R = 0.3$, separately for the isolation against all (I^{tot}), charged (I^{chg}), and neutral (I^{neutr}) particles. Working points are defined for the loose, medium, and tight selection criteria, with averaged efficiencies of 90 %, 80 %, and 70 %, respectively. The working points include selection criteria on the three isolation criteria, H/E, and $\sigma_{\eta\eta}$. The latter is defined as the second moment of a log-weighted distribution of crystal energies in η, calculated in the 5×5 matrix around the most energetic crystal in the photon supercluster [243]. A pixel-seed veto removes photon candidates with associated hits in the pixel detector to reject electron candidates. The selection criteria for the medium ID working point are summarized in Table 3.2. Other working points are not part of the presented work and can be found in Refs. [243, 244].

Die approbierte gedruckte Originalversion dieser Dissertation ist an der TU Wien Bibliothek verfügbar.
The approved original version of this doctoral thesis is available in print at TU Wien Bibliothek.
TU Bibliothek Your knowledge hub WIEN

Table 3.2: Summary of the selection criteria for the medium ID photon identification working point for the barrel (left) and endcap (right) regions [243].

	Medium ID	
	Barrel	Endcap
$\sigma_{\eta\eta}$	< 0.01015	< 0.0271
H/E	< 0.02197	< 0.0326
I^{tot}	$< 2.08 + 0.004017\ \text{p}_\text{T}$	$< 3.032 + 0.0037\ \text{p}_\text{T}$
I^{chg}	< 1.141	< 0.517
I^{neutr}	$< 1.189 + 0.01512\ \text{p}_\text{T}$ $+2.259 \cdot 10^{-5}\ \text{p}_\text{T}^2$	$< 2.716 + 0.0117\ \text{p}_\text{T}$ $+2.3 \cdot 10^{-5}\ \text{p}_\text{T}^2$
Pixel-seed veto	✓	✓

3.3.4 Jet reconstruction and identification

Jets are showers of charged and neutral particles in the detector, originating from the hadronization of quarks and gluons. They mainly consist of charged and neutral hadrons, such as protons, neutrons, kaons, and pions, however nonisolated photons and leptons can occur from the decay of heavy baryons or mesons as part of the jet. Charged hadrons are identified by their tracks in the inner tracking system, where beyond the tracker acceptance of $|\eta| > 2.5$, jets from neutral or charged hadrons cannot be distinguished.

ECAL and HCAL clusters without a link to any track are used to identify nonisolated photons and neutral hadrons, distinguishable by their energy fraction deposited in each subdetector. While neutral hadrons leave on average only a small fraction of 3 % of their energy in the ECAL, photons in hadronic jets carry about 25 % of the jet energy [231]. Additionally, nonisolated photons are separated from isolated ones due to their ECAL signatures, such as the shower shape, and the selection criteria mentioned in Table 3.2. The identified hadrons are clustered to jets using the anti-k_T algorithm [245, 246] and a distance parameter of $\Delta R = 0.4$, where contributions from charged hadrons associated with PU vertices are subtracted [247].

Additional identification criteria are the requirement of at least two jet constituents, where at least one is a charged PF candidate, and a nonzero charged-hadron energy fraction. For the 2016 data-taking period, the charged electromagnetic energy fraction has to be less than 99 %, and for 2016 (2017–2018) data-taking periods, the neutral-hadron and electromagnetic energy fraction is required to be less than 99 % (90 %).

Heavy-flavor jets

The identification of heavy-flavor jets, originating from the hadronization of bottom quarks, gives significant advantages in identifying specific processes in physics analyses. Heavy-flavor jet identification techniques exploit the properties of the bottom quark hadron and allow to distinguish them from light quark and gluon jets.

First attempts were used in the observation of the top quark [14, 15] and since then play a crucial rôle in top quark analyses. The techniques take advantage of the long lifetime of hadrons containing bottom quarks of about 1.5 ps, thus resulting in a secondary vertex

Die approbierte gedruckte Originalversion dieser Dissertation ist an der TU Wien Bibliothek verfügbar.
The approved original version of this doctoral thesis is available in print at TU Wien Bibliothek.
TU Bibliothek Your knowledge hub WIEN

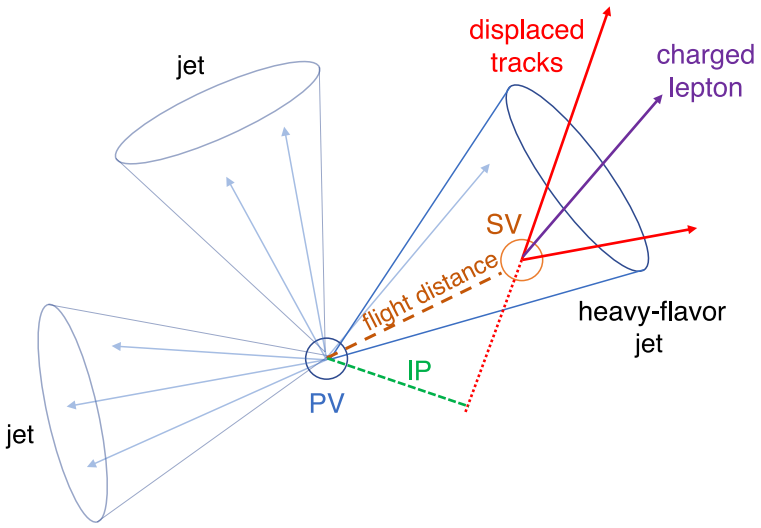

Figure 3.10: Schematic view of a heavy-flavor jet with its displaced secondary vertex (SV) and a resulting charged lepton in the decay product of the bottom quark hadron. Figure adapted from Ref. [248].

(SV) with a displacement to the PV of $c\tau \approx 450\,\mu\text{m}$. On average, heavy-flavor decay products have a larger p_T compared to light-flavor or gluon jets, and in about 10–20 % of the cases, additional leptons are present [248]. These unique features are exploited in the b-jet identification, where an illustration is given in Fig. 3.10.

A deep neural network (DNN) with combined information on SV reconstructions, jet constituents, light-jet probabilities, and jet properties, such as the jet p_T and η to include differences in the jet kinematics, is used to distinguish the jet-flavor categories. With up to six tracks per jet used in the DNN training, the DeepCSV [249] algorithm outperforms other b-jet identification techniques [248].

To be identified as a b jet, selection criteria on the DeepCSV b tagging score are applied. For a medium ID working point, the score must be greater than 0.6321 for the 2016 data-taking period and above 0.4941 (0.4184) in 2017 (2018) data and simulations. The b tagging requirements are optimized for a low misidentification rate, where the rate for the medium ID working point is 1–2 % for light quark and gluon jets and up to 12 % for charm quark jets.

3.3.5 Missing transverse energy

Neutrinos and possible unknown at most weakly-interacting BSM particles escape the CMS experiment undetected. Such particles are measured indirectly using the momentum imbalance of detected objects in the transverse plane. The magnitude of the transverse-momentum imbalance is denoted as missing transverse momentum p_T^{miss}, with its vector $\vec{p}_T^{miss}$ defined as the negative vector-momentum sum of the PF candidates projected onto the transverse plane

$$\vec{p}_T^{miss} = -\sum_{particles} \vec{p}_T. \tag{3.3.1}$$

Die approbierte gedruckte Originalversion dieser Dissertation ist an der TU Wien Bibliothek verfügbar.
The approved original version of this doctoral thesis is available in print at TU Wien Bibliothek.
TU Bibliothek Your knowledge hub WIEN

Additional jet selection criteria avoid double-counting of PF objects, such as photons, electrons, or muons.

No selection criteria are applied on the missing transverse energy in the $t\bar{t}\gamma$ cross section measurement, and thus, p_T^{miss} does not enter the presented analysis directly. However, it is part of the definition of observables, such as the W boson candidate transverse mass $m_T(W)$, with

$$m_T(W) = \sqrt{2\, p_T(\ell)\, p_T^{miss}\, \left[1 - \cos\Delta\phi\left(\ell, \vec{p}_T^{\,miss}\right)\right]}, \tag{3.3.2}$$

calculated from the identified lepton ℓ and $\vec{p}_T^{\,miss}$, where the latter is assumed to reflect the neutrino properties of the leptonically decaying W boson.

Die approbierte gedruckte Originalversion dieser Dissertation ist an der TU Wien Bibliothek verfügbar.
The approved original version of this doctoral thesis is available in print at TU Wien Bibliothek.
TU Bibliothek Your knowledge hub WIEN

Die approbierte gedruckte Originalversion dieser Dissertation ist an der TU Wien Bibliothek verfügbar.
The approved original version of this doctoral thesis is available in print at TU Wien Bibliothek.

Chapter 4

Measurement of the $t\bar{t}\gamma$ cross sections

Definitions and methods used in the measurement of inclusive and differential cross sections of a top quark pair in association with a photon ($t\bar{t}\gamma$) are described in this chapter. The measurement is performed in the single-lepton channel, selecting exactly one electron or muon from the W boson decay. The results are obtained from data collected by the CMS experiment during 2016–2018 data-taking period, which is the first $t\bar{t}\gamma$ cross section measurement using a data set collected by the CMS experiment at a center-of-mass energy of 13 TeV.

Although there is no certainty in knowing the exact composition of the selected events, simulated SM signal and background processes allow for an estimation of their composition and for extracting $t\bar{t}\gamma$ events in dedicated selections. The described methods are designed to accurately identify and select objects according to the kinematic features of the signal process, where selection criteria are applied to construct signal and control regions enriched in signal and background events, respectively. Comprehensive background estimation methods are applied to model events mimicking the $t\bar{t}\gamma$ signal from data, and a statistical analysis is performed to extract the $t\bar{t}\gamma$ cross section in a defined fiducial phase space, taking various sources of systematic uncertainties into account. With uncertainties originating from object identification, the simulation of processes, and the background estimation methods, the result of a profile likelihood fit is used to determine their impact on the measurement. Differential cross section measurements are performed to measure the kinematic observables of $p_T(\gamma)$, $|\eta(\gamma)|$, and $\Delta R(\ell, \gamma)$, with an unfolding method [250] applied to corrected the distributions for detector response and acceptance effects, allowing for comparisons with theoretical predictions from several Monte Carlo (MC) event generators. A detailed description of the methods is given in the following.

4.1 Data set and event simulations

For the accurate understanding of the collected data, it is necessary to precisely simulate SM signal and background processes. Details of the SM event generation are provided in Sec. 2.1.3. The collected data set used in this measurement and signal and background simulations are described in the following.

Die approbierte gedruckte Originalversion dieser Dissertation ist an der TU Wien Bibliothek verfügbar.
The approved original version of this doctoral thesis is available in print at TU Wien Bibliothek.
TU Bibliothek Your knowledge hub WIEN

4.1.1 Data set

The measurements of the $t\bar{t}\gamma$ cross sections use a data set of pp collisions at a center-of-mass energy of $\sqrt{s} = 13\,\text{TeV}$, corresponding to a recorded integrated luminosity of $137\,\text{fb}^{-1}$. The data set was collected by the CMS experiment during Run 2 (2016–2018) data taking, split into subsets for each year with integrated luminosities of $35.9\,\text{fb}^{-1}$ (2016) [251], $41.5\,\text{fb}^{-1}$ (2017) [252], and $59.7\,\text{fb}^{-1}$ (2018) [253]. Recorded events are certified, where collisions during periods with nonoperational subdetectors are discarded. The data set is categorized into primary data sets (PDs), with events grouped based on the L1 trigger decisions. This measurement analyzes PDs, where the L1 trigger decision is made due to the presence of calorimeter and muon system hits, corresponding to the identification of an electron or muon.

4.1.2 Signal and background simulation

Signal and background processes are simulated for each of the three data-taking periods to match the varying conditions of the CMS detector. Particle interactions with the CMS detector material and the detector response are additionally simulated with GEANT4 [254]. PU events are added to the generated processes to mimic the effects of additional pp interactions, with matching PU conditions of the simulated data-taking period. Event generators used for SM process simulations are MadGraph5_aMC@NLO and Powheg v2.0, further interfaced with the default parton showering algorithm Pythia 8 using the CP5 tune [93, 94, 255], and additional simulations use Herwig++ and Herwig 7 for comparison. In simulation, the μ_R and μ_F scales are set to $\mu_R = \mu_F = \frac{1}{2}\sum_i \left(m_i^2 + p_{T,i}^2\right)$, summing over generated final-state particles. Various versions of the NNPDF PDF sets are used. Details on the simulation of the $t\bar{t}\gamma$ signal and relevant background processes are given in the following.

Signal simulation

The $t\bar{t}\gamma$ signal simulation is performed using the MadGraph5_aMC@NLO event generator, with the NNPDF 3.1 [81] PDF set used in all signal simulations. Signal events are generated as a doubly resonant $2 \to 7$ process at LO in QCD precision. The simulation uses the five-flavor scheme, with the collisions of initial-state light quarks, bottom quarks or gluons, producing an intermediate $t\bar{t}$ pair. The decay of the top quarks, described in Sec. 2.2, is simulated at ME level, where simulations are performed for the hadronic, semileptonic, and dileptonic decay channels, including tau leptons. Thus, the photon simulated in the $2 \to 7$ process can originate from an initial-state quark, top quark, W boson, bottom quark, or the light quarks or charged leptons of the W boson decay.

Due to singularities in ME calculations in the infrared limit, low-p_T photons or photons with low angular separation to other objects cannot be included in the ME simulation. Thus, kinematic selections of the objects are applied, where photons are simulated with $p_T(\gamma) > 10\,\text{GeV}$ and $|\eta(\gamma)| < 5$, and charged leptons must satisfy $|\eta(\ell)| < 5$. The processes are simulated with an angular separation of final-state particles to the photon of $\Delta R > 0.1$. Additional signal simulations for high-$p_T(\gamma)$ regions of $100 \leq p_T(\gamma) < 200\,\text{GeV}$ and $p_T(\gamma) \geq 200\,\text{GeV}$ ensure an accurate modeling of the signal process in the tail-regions.

Die approbierte gedruckte Originalversion dieser Dissertation ist an der TU Wien Bibliothek verfügbar.
The approved original version of this doctoral thesis is available in print at TU Wien Bibliothek.
TU Bibliothek Your knowledge hub WIEN

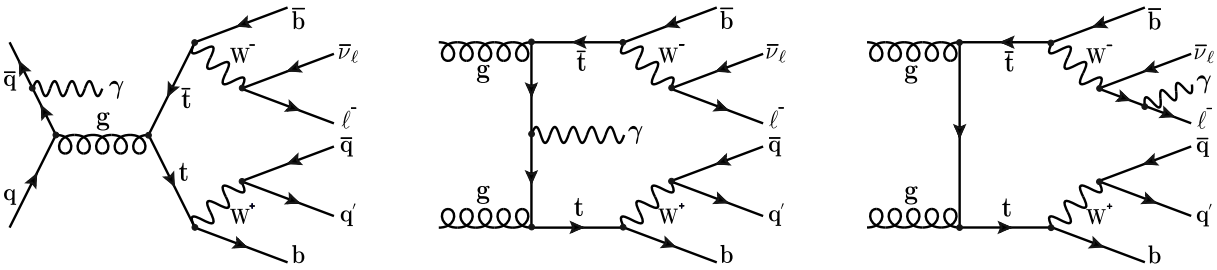

Figure 4.1: Representative diagrams of the $t\bar{t}\gamma$ process for photons originating from the initial-state quark (left), the top quark (center), or the lepton from the W boson decay (right).

Signal simulations are interfaced with PYTHIA 8 using the CP5 tune [93, 94, 255] for multiple-parton interactions, parton showering and the hadronization of final-state particles. Additional events are generated with MADGRAPH5_aMC@NLO interfaced with HERWIG++ using the EE5C tune [93] and with HERWIG 7 using the CH3 tune [92] for comparisons of the results with other showering algorithms.

Representative diagrams of the signal process for photons originating from the initial-state quark (left), the top quark (center), or the lepton from the W boson decay (right) are shown in Fig. 4.1.

$t\bar{t}\gamma$ NLO k-factor calculation

The signal cross section is normalized to NLO in QCD precision, where a k factor is calculated as the ratio of the NLO to LO cross section values scales simulated event yields. As the simulation of the $2 \to 7$ process at NLO in QCD is computationally too expensive, the LO and NLO cross section values for the k-factor calculation are estimated in a $2 \to 3$ process. Events are simulated with photons originating from an initial-state quark or the top quark, inclusively in the top quark decay channels. The simulation is performed using the MADGRAPH5_aMC@NLO event generator in the fiducial phase space region defined in Sec. 4.3.2. The calculated k factor of 1.48 is in good agreement with values presented in Ref. [86].

A shape comparison of distributions from $t\bar{t}\gamma$ simulations at LO and NLO was performed to ensure no shape effects from higher-order simulations. In this comparison, photons from top quark decay products not simulated in the $2 \to 3$ process of the NLO simulation are added from $t\bar{t}$ events, with photons simulated by the PYTHIA 8 showering algorithm. The comparison is shown in Fig. 4.2 for the $p_T(\gamma)$, $|\eta(\gamma)|$, and $\Delta R(\ell, \gamma)$ distributions, where good agreement is found, with remaining deviations from limited event numbers in the simulation.

Background simulations

Background events are simulated with multiple event generators, where $t\bar{t}$ [256, 257], single top quark t- [258] and tW-channel [259], and WW [260, 261] processes are generated with POWHEG v2.0 at NLO in QCD precision, QCD multijet processes are simulated with PYTHIA 8 and other backgrounds are generated at LO and NLO in QCD precision with

Die approbierte gedruckte Originalversion dieser Dissertation ist an der TU Wien Bibliothek verfügbar.
The approved original version of this doctoral thesis is available in print at TU Wien Bibliothek.
TU Bibliothek Your knowledge hub WIEN

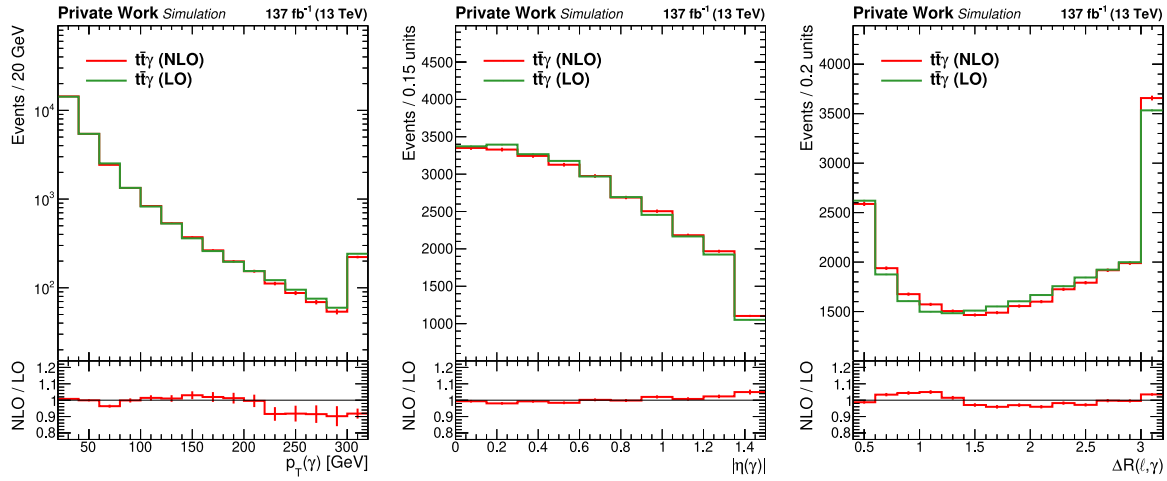

Figure 4.2: Comparison of the $p_T(\gamma)$ (left), $|\eta(\gamma)|$ (center), and $\Delta R(\ell,\gamma)$ (right) distributions of $t\bar{t}\gamma$ simulations at LO (green) and NLO (red) in QCD precision. Distributions from NLO simulations are normalized to the ones at LO for a comparison of their shape.

MadGraph5_aMC@NLO. The latter includes the processes of single top quark s-channel, $t\gamma$, Drell–Yan, W+jets, $W\gamma$, $Z\gamma$, WZ, ZZ, $t\bar{t}Z$, $t\bar{t}W$, and tZq. The NNPDF 3.1 PDF set is used in background simulations, where generators are interfaced with Pythia 8 using the CP5 tune. For the simulation of W+jets, Drell–Yan, $W\gamma$, $Z\gamma$, $t\gamma$, $t\bar{t}W$, $t\bar{t}Z$, tZq, WZ, ZZ, and QCD multijet events in the 2016 data-taking period, the CUETP8M1 tune [93] and the NNPDF 3.0 [81] PDF set are used.

W+jets and Drell–Yan ($W\gamma$) events are simulated at LO in QCD with up to four (three) additional partons and $Z\gamma$, $t\bar{t}W$, WZ, and ZZ events are generated at NLO in QCD with one additional parton in the ME calculation, where double-counting of partons generated with MadGraph5_aMC@NLO and Pythia 8 is prevented using the MLM [262] and FxFx scheme [263], respectively.

The cross sections of the background processes are normalized to the most precise values available. As shown in Sec. 2.2, the $t\bar{t}$ cross section is calculated at NNLO precision, including NNLL soft-gluon resummations [99, 121–126], with its value given in Eq. 2.2.3. Single top quark s- and t-channel (tW-channel) processes are normalized to NLO [107, 108] (NNLO [264]) in QCD precision, with the cross section values given in Eq. 2.2.6. The overlap of $t\bar{t}$ and tW simulations is removed using the diagram removal technique [106]. Drell–Yan and W+jets cross sections are normalized to NNLO [265–269]. A summary of the simulated signal and background processes, the event generator, the simulated precision, and the precision of the cross section normalization are given in Table 4.1.

To simplify the notation of background events, in the following, the process of $t\bar{t}$, single top quark, and $t\gamma$ are grouped and labeled "$t/t\bar{t}$", and the processes of $t\bar{t}Z$, $t\bar{t}W$, tZq, and dibosons are grouped in the "other" category.

Die approbierte gedruckte Originalversion dieser Dissertation ist an der TU Wien Bibliothek verfügbar.
The approved original version of this doctoral thesis is available in print at TU Wien Bibliothek.
TU Bibliothek Your knowledge hub WIEN

Table 4.1: Simulated signal and background processes, the event generator, and the perturbative order of the simulation and the cross section normalization.

Process	Event generator	Perturbative order of simulation	Cross section normalization
$t\bar{t}\gamma$	MadGraph5_aMC@NLO	LO	NLO
$t\bar{t}$	Powheg	NLO	NNLO+NNLL [99, 121–126]
Single t (s-channel)	MadGraph5_aMC@NLO	NLO	NLO [107, 108]
Single t (t-channel)	Powheg	NLO	NLO [107, 108]
tW	Powheg	NLO	NNLO [264]
Drell–Yan, W+jets	MadGraph5_aMC@NLO	LO	NNLO [265–269]
$W\gamma$	MadGraph5_aMC@NLO	LO	NLO
WW	Powheg	NLO	NNLO [270]
$t\gamma$, $Z\gamma$, WZ, ZZ $t\bar{t}Z$, $t\bar{t}W$, tZq	MadGraph5_aMC@NLO	NLO	NLO [136, 271]
QCD multijet	Pythia 8	LO	LO

4.1.3 Phase space overlap removal

The simulation of high-p_T photon emissions at large angular separation at ME level provides a more accurate description of the processes, such as $t\bar{t}\gamma$. However, processes such as $t\bar{t}$ can include hard photons from the parton showering algorithm, with a considerably large phase space already covered by the $t\bar{t}\gamma$ process. To prevent double-counting of events in simulations, this overlapping phase space is removed in requiring (rejecting) events in simulations with (without) a hard photon in ME calculations.

The overlap-removal technique selects events with a generated photon satisfying the $p_T(\gamma)$ and $|\eta(\gamma)|$ thresholds of the generator settings, where only photon candidates in stable simulation states are considered. Additionally, the selected photons must not originate from hadronic sources, such as final-state hadrons, to ensure it originates from the simulated hard process. Thus, the requirement includes only generated photons with quarks, leptons, or SM bosons in the parentage chain. Furthermore, isolation requirements neglect photons within an angular distance ΔR to other generated stable particles with $p_T > 5\,\text{GeV}$, where neutrinos, photons, and leptons from photon conversions are not considered in the latter. The ΔR cone size is adjusted to the generator settings of the simulation with a hard photon in the ME calculation. To remove the phase space overlap, the procedure requires (rejects) events with at least one selected photon fulfilling the criteria in processes with (without) a simulated photon at ME level.

The technique is applied to $t\bar{t}$ simulations to remove the overlapping phase space to the $t\bar{t}\gamma$ process. The selected photon has to fulfill the requirements of $p_T(\gamma) > 10\,\text{GeV}$ and $|\eta(\gamma)| < 5$ to match the generator settings described in Sec. 4.1.2. Photons have to be isolated within $\Delta R = 0.1$, with the same criteria on the simulation state and its origin as mentioned above. Thus, the phase space with photons originating from the hadronization of jets or in decay products of pions or other mesons is covered by the $t\bar{t}$ process.

A similar phase space overlap removal is applied to Drell–Yan and W+jets simulations to remove events consistent with the $Z\gamma$ and $W\gamma$ definitions, respectively. In these cases,

Die approbierte gedruckte Originalversion dieser Dissertation ist an der TU Wien Bibliothek verfügbar.
The approved original version of this doctoral thesis is available in print at TU Wien Bibliothek.
TU Bibliothek Your knowledge hub WIEN

Table 4.2: Summary of the generator-level selection criteria for the phase space overlap removal of simulated processes. The overlap-removal procedure requires (rejects) events with at least one generated photon fulfilling the criteria in processes with (without) a simulated photon at ME level.

	$t\bar{t}\gamma$/ $t\bar{t}$	Wγ/ W+jets	Zγ/ Drell–Yan	tγ/ Single t (t-channel)
$p_T(\gamma^{gen})$ [GeV]	>10	>15	>15	>10
$\lvert\eta(\gamma^{gen})\rvert$	<5.0	<2.6	<2.6	<2.6
ΔR cone size	0.10	0.05	0.05	0.05
Photon origin				Single t production

the generator-level criteria for the photon in the overlap removal are defined to match the simulation settings of the Zγ or Wγ processes. Events are removed from Drell–Yan (Zγ) and W+jets (Wγ) simulations, if (no) photons are found fulfilling the requirements of $p_T(\gamma) > 15\,\text{GeV}$ and $|\eta(\gamma)| < 2.6$, with the isolation cone defined by $\Delta R = 0.05$.

The background simulation additionally includes the tγ process, which is the simulation of single top quark t-channel events with an additional hard photon at ME level. To remove the overlap to the single top quark t-channel simulation, the criteria for the photon are set to $p_T(\gamma) > 10\,\text{GeV}$ and $|\eta(\gamma)| < 2.6$, with an isolation cone size of $\Delta R = 0.05$. The generator settings only include the production of the top quark, where the phase space of tγ does not cover hard-photon productions from top quark decay products. Photons from the top quark decay are thus not considered in the procedure.

The selection criteria for the overlap-removal technique applied to the signal and background simulations are summarized in Table 4.2.

4.2 Trigger, object, and event selections

Objects of the measurement are reconstructed in data and simulation using the PF algorithm described in Sec. 3.3. Events are selected according to trigger decisions described in Sec. 3.2.6 and specific selection criteria, optimized to enrich $t\bar{t}\gamma$ or background events in signal or control regions defined in the analysis, respectively. The measurement is based on counting well-identified electrons, muons, photons, jets, and b-tagged jets in signal and control regions, where for the definition of observables in the QCD multijet background estimation, additionally the observed missing transverse momentum p_T^{miss} is used. The following gives an overview of the trigger, object, and event selections of the measurement, event categorizations, and the corrections applied to simulation to match the conditions observed in data.

Die approbierte gedruckte Originalversion dieser Dissertation ist an der TU Wien Bibliothek verfügbar.
The approved original version of this doctoral thesis is available in print at TU Wien Bibliothek.
TU Bibliothek Your knowledge hub WIEN

4.2.1 Trigger selection

The trigger decision of events in the measurement is based on the observation of a single electron or muon in the CMS detector. Events are required to be selected by the HLT trigger algorithms, where the reconstructed objects have to contain a single lepton fulfilling the identification criteria, with isolation requirements and thresholds on their transverse momentum. The trigger requirements are adjusted in each year of data taking to control the recorded event rates matching the DAQ system capabilities and the conditions of the LHC with increased average PU. The performance of the L1 and HLT trigger capabilities are emulated in the simulation.

Single-electron events are reconstructed using a tight identification working point including tight isolation criteria at the HLT level, with a p_T threshold of 27 (32) GeV in 2016 (2017–2018) data-taking periods. Single-muon events are selected if the HLT trigger algorithms identified an isolated muon in the tracking or muon system, with the p_T threshold of 27 (24) GeV in 2017 (2016, 2018) data-taking periods. A possible overlap of the trigger criteria, where an event is selected by both the single-electron and single-muon trigger is removed in requiring the single-lepton events with a reconstructed electron or muon to be selected by the corresponding trigger.

4.2.2 Object and event selections

Reconstructed objects and events are selected with conditions matching the kinematic features of the signal process, efficiently selecting single-lepton $t\bar{t}\gamma$ events and rejecting events originating from background sources. In the following, the object and event selection criteria are summarized.

Primary vertex selection

The PV described in Sec. 3.3.1 is selected to have the largest summed p_T^2. In the measurement, the selected PV is required to have at least four degrees of freedom (d.o.f.) and to be located in the longitudinal (transverse) plane within $|z| < 24\,\text{cm}$ ($r < 2\,\text{cm}$) to the origin of the CMS coordinate system defined in Sec. 3.2.1.

Lepton selection

The identification of electrons is based on the inner tracker and ECAL information, with the reconstruction and identification working points given in Sec. 3.3.3. Electrons are selected with $p_T(e) > 35\,\text{GeV}$ within $|\eta(e)| < 2.4$, but excluding the gap region between the ECAL barrel and endcap at $1.4442 < |\eta(e)| < 1.566$. Additional selection criteria on ECAL-cluster and tracker observables, summarized in the tight ID working point in Table 3.1, are applied. Isolation criteria are part of the tight ID working point, which, in addition to requirements on the longitudinal (d_z) and transverse (d_{xy}) distance of the electron origin from the PV, is optimized to reject nonprompt electrons originating from jets. Requirements of a maximum number of missed inner tracker hits and the applied conversion veto reject electrons from photon conversions. Events with additional electrons

Die approbierte gedruckte Originalversion dieser Dissertation ist an der TU Wien Bibliothek verfügbar.
The approved original version of this doctoral thesis is available in print at TU Wien Bibliothek.
TU Bibliothek Your knowledge hub WIEN

Table 4.3: Selection criteria for the electron (left) and muon (right) identification in the analysis selection and for the veto on additional leptons. Requirements of electron (muon) identification working points are summarized in Sec. 3.3.3 (3.3.2).

	Electrons		Muons	
	Analysis selection	Veto on additional electrons	Analysis selection	Veto on additional muons
$p_T(\ell)$ [GeV]	>35	>15	>30	>15
$\lvert\eta(\ell)\rvert$	<2.4	<2.4	<2.4	<2.4
$I_{rel}(\ell)$			<0.15	<0.25
$\lvert d_{xy}\rvert$ [cm] in EB (EE)	<0.05 (0.1)	<0.05 (0.1)		
$\lvert d_z\rvert$ [cm] in EB (EE)	<0.1 (0.2)	<0.1 (0.2)		
Identification working point	tight ID	veto ID	tight ID	loose ID

that fulfill the veto ID working point selection criteria given in Table 3.1, with a relaxed threshold on the electron p_T of 15 GeV, are rejected.

The identification of muons is based on cross-information of the outer muon system and the inner tracker, with the muon reconstruction and identification working points described in Sec. 3.3.2. In the analysis, muons are selected with $p_T(\mu) > 30$ GeV if they are found within the pseudorapidity range of the muon system $|\eta(\mu)| < 2.4$. Muons have to fulfill the tight ID working point selection criteria, where additional isolation requirements are applied. For the latter, the relative isolation of the muon within a cone of $\Delta R = 0.4$ has to be less than 15 % [239]. Events with additional muons are rejected, where their identification requirements are relaxed to $p_T(\mu) > 15$ GeV and the loose ID working point. The relative isolation criterion is relaxed to be less than 25 % with the same ΔR cone size. The requirements of electron and muon selections are summarized in Table 4.3.

Photon selection

Photons are identified based on ECAL information, where the identification method and the corresponding working points are described in Sec. 3.3.3. Photons are selected with $p_T(\gamma) > 20$ GeV, if they are found within the ECAL barrel region, $|\eta(\gamma)| < 1.4442$. Selections with photons in ECAL endcap regions are found to have significant background contributions with larger photon misidentification rates. Thus, the analysis selection is restricted to the barrel region. Selected photons are required to fulfill the medium ID working point, with the criteria given in Table 3.2. The identification applies selections on the isolation and shower shape of the photon, where dedicated requirements on the isolation against all, charged, and neutral particles are applied. An angular separation of photons to selected leptons of $\Delta R(\ell, \gamma) > 0.4$ is required to prevent an overlap with lepton candidates and remove bremsstrahlung photons from the selection.

Die approbierte gedruckte Originalversion dieser Dissertation ist an der TU Wien Bibliothek verfügbar.
The approved original version of this doctoral thesis is available in print at TU Wien Bibliothek.
TU Bibliothek Your knowledge hub WIEN

Table 4.4: Selection criteria for the photon identification in the analysis selection (left) and for the veto on additional photons (right). Requirements of photon identification working points are summarized in Sec. 3.3.3.

	Analysis selection	Veto on additional photons
$p_T(\gamma)$ [GeV]	>20	>20
$\lvert\eta(\gamma)\rvert$	<1.4442	<1.4442
$\Delta R(\ell,\gamma)$	>0.4	>0.4
Identification working point	medium ID	medium ID w/o criteria on $\sigma_{\eta\eta}$ and I^{chg}

A veto on additional photons rejects events with photons fulfilling the same selection criteria, but without requirements on the charged isolation I^{chg} and the lateral shower extension $\sigma_{\eta\eta}$, to avoid double-counting of events in the nonprompt photon background estimation method described in Sec. 4.4.2. The requirements of photon selections are summarized in Table 4.4.

Jet and b-tagged jet selection

Charged and neutral particles from the hadronization of bottom quarks, light quarks, and gluons are identified by the PF algorithm and clustered to jets using the anti-k_T algorithm with a distance parameter of $\Delta R = 0.4$. Criteria on the deposited energy in the ECAL and HCAL subdetectors, the neutral- and charged-hadron and electromagnetic energy fractions, as well as the requirement on the number of constituents are described in Sec. 3.3.4 and finally lead to the identification of jets. Additionally, the selection requires $p_T(j) > 30\,\text{GeV}$ and $|\eta(j)| < 2.4$. Leptons and photons can originate from the decay of hadrons and be clustered in a jet. To prevent an overlap in the identification of these objects, an angular separation of jets to selected leptons of $\Delta R(j,\ell) > 0.4$ and to selected photons of $\Delta R(j,\gamma) > 0.1$ is required.

The DeepCSV algorithm, described in Sec. 3.3.4, is used to identify heavy-flavor jets from the hadronization and showering of bottom quarks. The medium ID working point for b jets is optimized for low misidentification rates, where requirements on the DeepCSV b tagging score are given in Sec. 3.3.4. The selection criteria of jets and b-tagged jets are summarized in Table 4.5.

Table 4.5: Selection criteria for the identification of jets and b-tagged jets. Requirements of the b tagging working point are given in Sec. 3.3.4.

$p_T(j)$ [GeV]	>30
$\lvert\eta(j)\rvert$	<2.4
$\Delta R(j,\ell)$	>0.4
$\Delta R(j,\gamma)$	>0.1
b tagging working point	medium ID

Die approbierte gedruckte Originalversion dieser Dissertation ist an der TU Wien Bibliothek verfügbar.
The approved original version of this doctoral thesis is available in print at TU Wien Bibliothek.
TU Bibliothek Your knowledge hub WIEN

4.2.3 Corrections of object and event selection efficiencies

Several corrections are applied to physical observables in data and simulation to ensure an accurate description of signal and background processes and correct specific effects in the detector response and mismodeling in simulation. Most corrections are subject to systematic uncertainties that are propagated to the predicted yields and described in Sec. 4.5.

Pileup correction

Simulated events are generated according to an assumed PU profile and are reweighted to match the one observed in data described in Sec. 3.1.2. The distribution of the true number of interactions in data is estimated using the instantaneous luminosity per bunch crossing for each luminosity section, assuming a total pp cross section of 69.2 mb [272, 273]. The true number of interactions in simulation is taken from each simulated process and reweighted to the estimated distribution in data, separately in each data-taking period. A potential remaining disagreement between data and simulation observed in the distribution of the number of vertices is expected to have a negligible impact in the analysis. Therefore, no additional corrections are applied. A variation on the total inelastic pp cross section is used to estimate systematic uncertainties in the PU modeling.

L1 prefiring correction

Starting at the end of 2016 and extending to the full 2017 data-taking period, the time alignment of the ECAL endcap, serving as an input for L1 trigger decisions, experienced a gradual shift for objects observed in the forward regions at $|\eta| > 2.4$. Since the L1 trigger system is designed to forbid triggering events in consecutive bunch crossings, ECAL trigger objects belonging to the previous bunch crossing generated inefficiencies in the L1 trigger decisions. The effect is known as L1 prefiring [274].

While objects in the forward region do not enter the measurement directly, trigger objects in this region may affect the analysis indirectly, resulting in a systematic uncertainty in the measurement. Prefiring inefficiencies were measured as a function of the jet p_T in high-$|\eta|$ regions at $2.0 < |\eta| < 3.1$ using events that were not affected by the timing shift. The prefiring probabilities for each jet ($\mathcal{P}_{\text{prefire}}$) are shown in Fig. 4.3 as a function of the electromagnetic transverse momentum and the pseudorapidity of the jet. Corrections to simulations are applied, with efficiency factors ϵ calculated using all jets in the event by

$$\epsilon = \prod_{j}^{\text{jets}} 1 - \mathcal{P}_{\text{prefire}}(j). \tag{4.2.1}$$

HEM correction

During the 2018 data-taking period, a power loss in a large section of one of the hadronic endcap calorimeter (HEM) had a significant impact on the identification of photons, leptons, jets, and p_T^{miss} in detector regions of $-3.0 < \eta < -1.3$ and $-1.566 < \phi < -0.87$.

Die approbierte gedruckte Originalversion dieser Dissertation ist an der TU Wien Bibliothek verfügbar.
The approved original version of this doctoral thesis is available in print at TU Wien Bibliothek.
TU Bibliothek Your knowledge hub WIEN

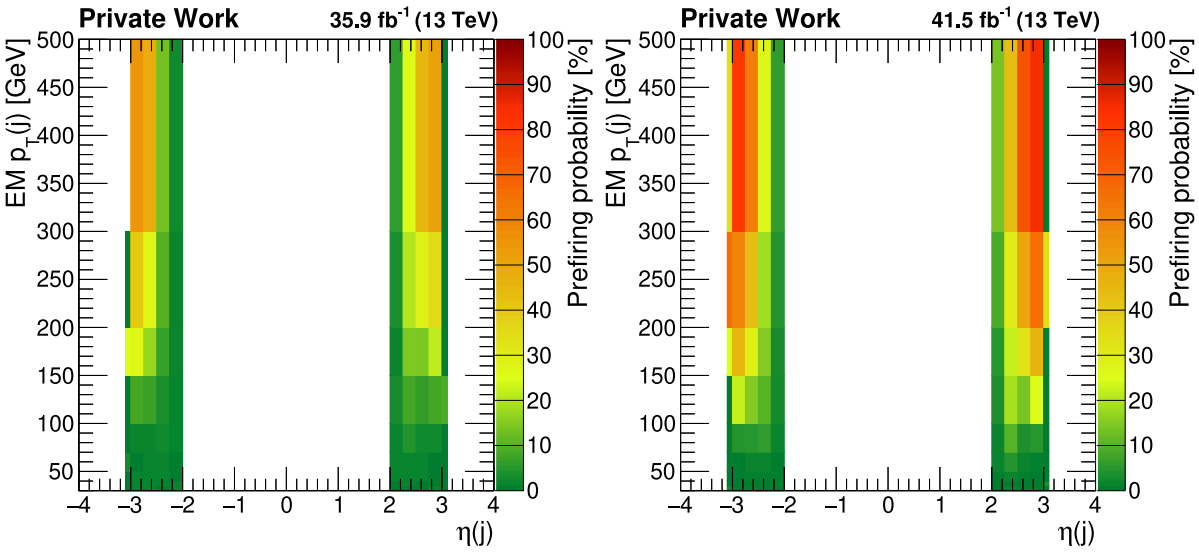

Figure 4.3: Prefiring probabilities provided per jet as a function of its electromagnetic transverse momentum and η for 2016 (left) and 2017 (right) data-taking periods [274]. Figures created from measurements provided by the CMS collaboration.

Since these objects could no longer be separated in these regions, the 2018 data set is split in a pre-HEM and a post-HEM era, with 21.1 and 38.6 fb^{-1} of integrated luminosity, respectively.

In order to account for the HEM effect, events in the post-HEM data set are rejected if electrons or photons with $p_T > 15\,\mathrm{GeV}$ are found in the affected region. This removes spurious objects formed by the ECAL energy deposits with a lack of hadronic activity due to the absence of the corresponding HCAL signal. Simulated events with objects that satisfy the same criteria are weighted by the fraction of the integrated luminosities.

Trigger selection efficiency correction

Trigger selection efficiencies are measured in simulation and data in using the tag-and-probe method. For measuring single-electron [242, 243] (single-muon [240]) trigger efficiencies with $p_T > 25$ (20) GeV, the method exploits the Z boson resonance, with the Z boson decaying to two electrons (muons), $Z \to e^+e^-(\mu^+\mu^-)$. Events are collected by the single-electron (single-muon) triggers, where L1 and HLT trigger objects are matched to reconstructed leptons. The selection includes identifying one lepton, the tag lepton, fulfilling tight identification criteria. Efficiencies are measured in matching the probe lepton to the L1 trigger object and requiring an additional match to the HLT object. The measured efficiencies are close to unity, with a decreasing efficiency in the turn-on curve in low-p_T regions below the lepton analysis selection threshold.

The same method is applied to simulation, where simulated Drell–Yan events are used to measure the trigger efficiencies. Simulated events are corrected by the ratio of observed and simulated efficiencies in bins of lepton p_T and η, to match simulated trigger efficiencies to those observed in data.

Die approbierte gedruckte Originalversion dieser Dissertation ist an der TU Wien Bibliothek verfügbar.
The approved original version of this doctoral thesis is available in print at TU Wien Bibliothek.
TU Bibliothek Your knowledge hub WIEN

The measured scale factors (SFs) and efficiencies for single-electron and single-muon triggers for the three data-taking periods are shown in Ref. [243] and Refs. [275], respectively. Uncertainties in the efficiency measurements are propagated to the event yields and taken as an input in the cross section measurement.

Lepton identification efficiency correction

Similar to trigger efficiency measurements, the electron [242, 243] and muon [239, 240] identification and isolation efficiencies are measured in simulation and data using the tag-and-probe method, exploiting the Z boson resonance. An average efficiency of 70 % is measured for the tight ID electron identification working point described in Sec. 3.3.3. Muon identification efficiencies of the tight ID working point, described in Sec. 3.3.2, range from 90 to 95 % depending on the muon p_T and η.

Simulated events are corrected to match corresponding efficiencies observed in data using SFs in bins of lepton p_T and η. Additionally, corrections on the electron reconstruction efficiencies from tracking inefficiencies are accounted for in applying additional SFs for selected electrons. The measured efficiencies and SFs are given in Ref. [243] for electrons and Ref. [239] for muons. The SFs are close to unity with SF values in the range of 0.9–1.1 in low-p_T or high-$|\eta|$ regions. Efficiency measurement uncertainties lead to a systematic uncertainty in the measurement described in Sec. 4.5.

Photon identification efficiency correction

Photons play an essential part in the $t\bar{t}\gamma$ cross section measurement. Thus, the accurate determination of observed and simulated efficiencies for photon identification is crucial. Photon selection efficiencies are measured in $Z \to e^+e^-$ events using a variant of the tag-and-probe technique. For the photon identification, the tag lepton has to fulfill tight identification criteria, while no requirements on the track of the probe electron are applied. Thus, the method pretends to identify one electron as a photon.

Efficiencies are measured for photons with $p_T(\gamma) > 20\,\text{GeV}$ as a function of p_T and η. Resulting SFs in the barrel region of the CMS detector are close to unity. For photons in the endcap regions at $1.566 < |\eta(\gamma)| < 2.5$, detector inefficiencies lead to deviations of the SFs from unity, with larger uncertainties in the photon identification. Thus, the selection of the $t\bar{t}\gamma$ cross section measurement is restricted to the ECAL barrel region.

Dedicated measurements of high-p_T photon SFs [276] in the 2017–2018 data-taking periods allowed to reduce the uncertainty in photon identifications at $p_T(\gamma) > 200\,\text{GeV}$. The measured SFs in p_T and η for the three data-taking periods with the corresponding uncertainties are shown in Fig. 4.4. Applied corrections for photons in the ECAL barrel region are close to unity with deviations up to 5 % in certain regions of the photon p_T and η. Uncertainties in the photon identification are partly dominant in specific regions of the analyzed phase space. An uncertainty of up to 3.2 % is propagated to the results and their impact on the measurement is described in Sec. 4.5. A detailed review is given in Ref. [243].

Efficiencies of the veto on photons with associated hits in the pixel detector are measured in $Z \to \mu^+\mu^-\gamma$ events. Kinematic selection criteria on the invariant masses of the

Die approbierte gedruckte Originalversion dieser Dissertation ist an der TU Wien Bibliothek verfügbar.
The approved original version of this doctoral thesis is available in print at TU Wien Bibliothek.
TU Bibliothek Your knowledge hub WIEN

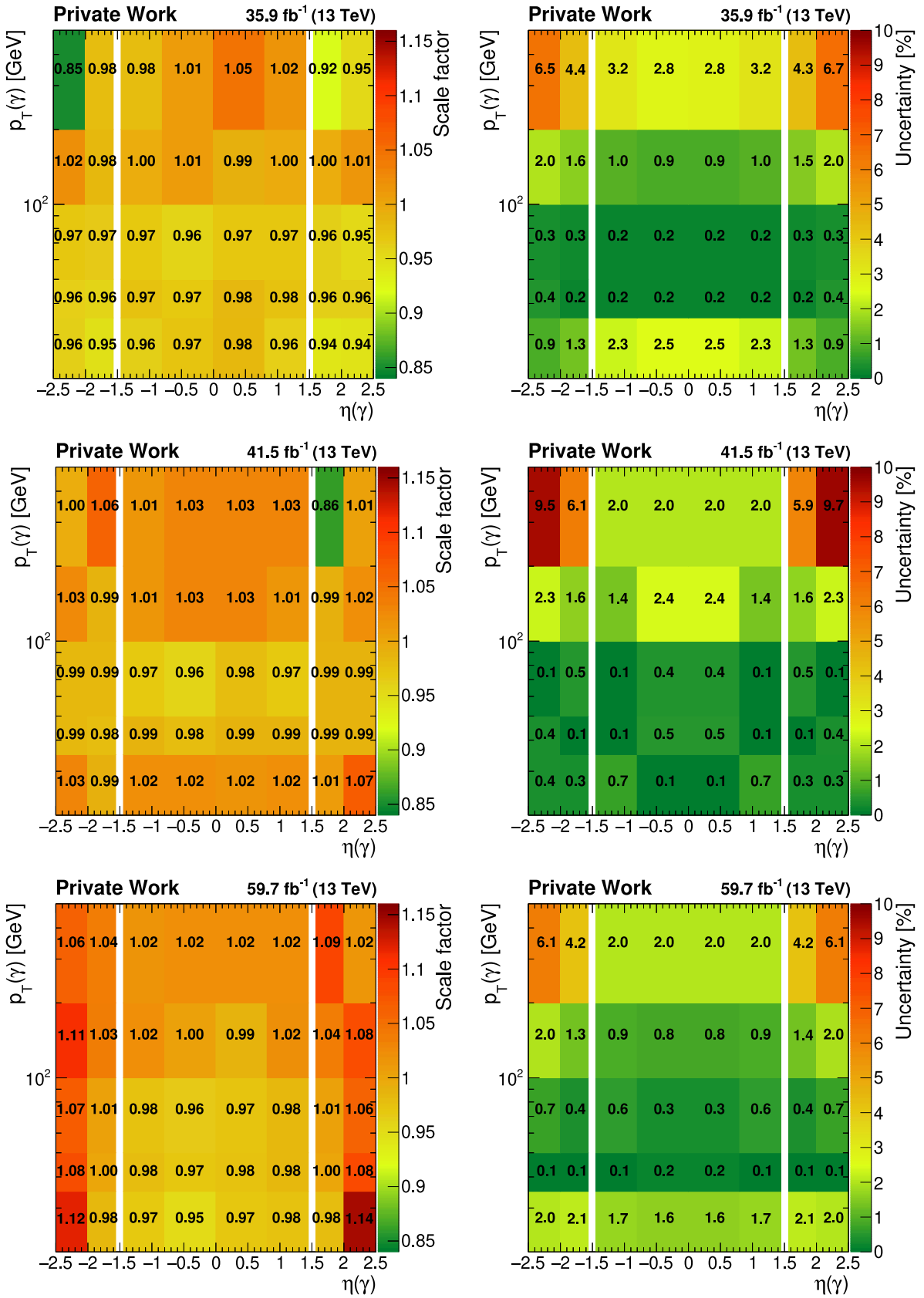

Figure 4.4: Scale factors (left) and uncertainties (right) for the identification of photons as a function of $p_T(\gamma)$ and $\eta(\gamma)$ for the 2016 (upper), 2017 (center), and 2018 (lower) data-taking periods [243]. Figures created from measurements provided by the CMS collaboration.

Die approbierte gedruckte Originalversion dieser Dissertation ist an der TU Wien Bibliothek verfügbar.
The approved original version of this doctoral thesis is available in print at TU Wien Bibliothek.

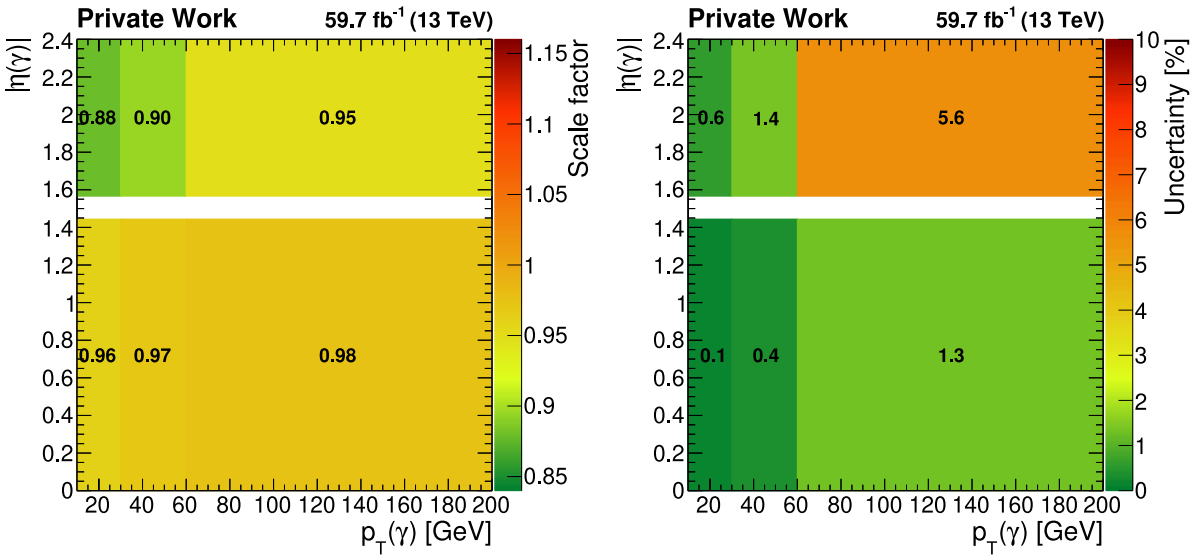

Figure 4.5: Pixel-seed veto SFs (left) and uncertainties (right) of the measurement in the 2018 data-taking period.

dimuon system with and without the photon, $m_{\mu\mu\gamma}$ and $m_{\mu\mu}$, respectively, and the angular separation of the objects ensure the photon to be radiated from one of the muons. The pixel-seed veto efficiencies are measured in data and simulation for each data-taking period, where for the latter, simulated Drell–Yan events are used. The measurements in simulation were revised using simulated $Z\gamma$ events, where similar results were found.

SFs are measured inclusively in $p_T(\gamma)$ in the 2016 and 2017 data-taking periods, with measured SFs of 0.985 ± 0.009 (0.973 ± 0.006) in 2016 and 0.967 ± 0.004 (0.915 ± 0.012) in 2017 for the barrel (endcap) regions. In the 2018 data-taking period, the measurement was performed in three bins of $p_T(\gamma)$, with the SF values (left) and uncertainties (right) shown in Fig. 4.5.

Jet energy correction

Deviations of the reconstructed energy of the clustered jet and the initial parton energy occur due to imperfections in the simulation of the hadronization, underlying event, detector response, and losses of particles to the geometrical acceptance. The energy of a reconstructed jet is calibrated to the average jet energy of jets clustered with generated particles, excluding neutrinos, using the same clustering distance. This calibration is carried out in data and simulation in a staged procedure known as jet energy correction (JEC) to correct the jet four-momentum [277, 278].

First, corrections remove the energy contributions of charged and neutral PU particles. To account for subleading differences in data, balancing measurements with simulated QCD dijet and multijet, Drell–Yan, and γ+jet events are performed and used to calibrate the jets in data. Reconstructed and reference jet energies are used to calculate the jet response as a function of jet p_T and η in simulated dijet events [247]. Detector inhomogeneities are measured in exploiting the momentum conservation and a correction factor is obtained to achieve a uniform response in p_T and η. The absolute jet energy response calibration is

Die approbierte gedruckte Originalversion dieser Dissertation ist an der TU Wien Bibliothek verfügbar.
The approved original version of this doctoral thesis is available in print at TU Wien Bibliothek.
TU Bibliothek Your knowledge hub WIEN

performed using Drell–Yan, γ+jet, and QCD multijet events, allowing for measurements of residual jet energy imbalances. The jet energy corrections are furthermore propagated to the $\vec{p}_T^{\,miss}$ computation, which is referred to as type-I correction.

Uncertainties in the jet energy corrections depend on the jet p_T and η and are further propagated to the predicted yields in the measurement. The variations are found within 2–6 % [278], with resulting systematic uncertainties in the measurement described in Sec. 4.5.

Heavy-flavor tagging efficiency and misidentification rate correction

Efficiencies in the tagging of jets and misidentification rates are measured in data and simulation [248, 279]. Simulated QCD multijet and $t\bar{t}$ events are used to obtain topologies dominated by light quark and gluon jets, charm quark jets, and bottom quark jets from gluon splitting or top quark decays. In simulation, the jet flavor is determined by matching jets to generated hadrons. Distributions of input variables to the DeepCSV algorithm and output discriminator shapes in the topologies are used to assess the agreement of simulation and data [248]. Misidentification rates are measured in QCD multijet events using the negative-tag method [279].

The medium ID working point of the DeepCSV algorithm results in b-jet identification efficiencies of 55–70 % for a jet p_T of 20–400 GeV. The light quark and gluon jet misidentification rate in the same p_T range is 1–2 %, and up to 12 % for charm quark jets. Deviations between observed and simulated values are related to detector modeling, the accuracy of generated interactions, parton showering, and hadronization, with deviations of up to 20 % for the highest discriminator values.

Simulated jets are corrected in applying dedicated SFs to match the b-jet identification efficiencies and misidentification probability of gluon, light quark, or charm quark jets as b jets in data. Various uncertainty sources are considered in the SF measurements, including uncertainties in μ_R and μ_F scales, background modeling, jet energy scale, jet energy resolution, and PU modeling [248, 279]. Resulting systematic uncertainties for correctly and incorrectly identified jets are propagated to the event yields in the measurement and are summarized in Sec. 4.5.

4.2.4 Event categorization

Simulated events are categorized according to the origin of the reconstructed photon by matching the photon to generator-level particles. The matching is performed to particles with stable simulation status if the transverse momentum is found within 50 % of the reconstructed photon value and the angular separation ΔR does not exceed 0.3, where the closest generator-level particle is taken as a match. If the criteria are not fulfilled and the matching algorithm fails to find a suitable candidate, additional checks are performed to categorize the event. Based on the matching algorithm, five categories are established, where events are categorized in genuine photon, misidentified electron, photon with hadronic origin, PU photon, or hadronic fake events. For the measurement of the $t\bar{t}\gamma$ cross sections, the background contributions of the latter three categories are combined to a single category, so-called nonprompt photon events.

Die approbierte gedruckte Originalversion dieser Dissertation ist an der TU Wien Bibliothek verfügbar.
The approved original version of this doctoral thesis is available in print at TU Wien Bibliothek.
TU Bibliothek Your knowledge hub WIEN

- **Genuine photons**
  Reconstructed photons categorized as genuine are matched to generator-level photons originating from a quark, lepton, or SM boson. A photon with hadronic sources in its parentage chain is not considered to be a genuine photon.

- **Misidentified electrons**
  The misidentified electrons category includes events where the reconstructed photon is matched to a generator-level electron.

- **Photons with hadronic origin**
  Reconstructed photons matched to a generator-level photon are categorized as photons with a hadronic origin if the photon originates from hadronic sources, such as baryons and mesons from the hadronization of final-state quarks. In case a neutral pion decays to two photons with similar p_T, the matching algorithm fails if the generated photons are reconstructed as a single particle with a transverse momentum exceeding the sum of both, and none of the generator-photon p_T values are found within 50 % of the reconstructed photon. In this case, the photon is categorized as a photon with hadronic origin if a generated neutral pion without simulation status requirement and at least one generated photon is found within a cone of $\Delta R = 0.3$ to the reconstructed photon.

- **Pileup photons**
  If no generated particles without simulation status requirement are found within an angular separation of $\Delta R = 0.3$, the photon is categorized as PU photon. These events originate from additional interactions added to the simulation to mimic PU effects in the detector. The generator-level information of the PU events is lost in the mixing, and no matching can be performed. PU photons can thus be generator-level photons from hadronic sources or hadronic fakes, where no further distinction can be made. The contribution of this category is found to be small, where the resulting observables of the photon, especially the isolation against charged hadrons I^{chg} and the lateral extension of the ECAL shower $\sigma_{\eta\eta}$, are found to be similar to the ones observed in the combined categories of photons with a hadronic origin and hadronic fakes.

- **Hadronic fakes**
  The hadronic fake category includes photons, which do not fulfill the criteria of any other category. Thus, this category comprises photons matched to any generator-level particle, except electrons or photons.

4.3 Analysis strategy

The method to measure the $t\bar{t}\gamma$ cross sections is designed to accurately identify and select objects of the signal process. Selections on the photon, lepton, jet, and b-jet multiplicities are applied to construct signal and control regions enriched in signal and background processes, respectively. The determination of the $t\bar{t}\gamma$ cross section is performed in a statistical model in likelihood-based tests, where the cross section is extracted in a fiducial phase space region defined close to the reconstruction-level phase space.

Die approbierte gedruckte Originalversion dieser Dissertation ist an der TU Wien Bibliothek verfügbar.
The approved original version of this doctoral thesis is available in print at TU Wien Bibliothek.
TU Bibliothek Your knowledge hub WIEN

In the following, the definitions of the signal and control region selection criteria and the fiducial phase space definition are given. The statistical procedure to extract the $t\bar{t}\gamma$ cross sections in the inclusive and differential measurements is shown, where the latter are used to extract the differential distributions at the particle level.

4.3.1 Signal and control region definitions

In addition to the object and event selection criteria described in Sec. 4.2.1 and 4.2.2, preselection requirements are established to enrich signal and background contributions in certain regions. These signal and control regions are optimized to measure and validate the distributions and normalizations of the signal and the main backgrounds. All events in these regions have to be triggered by the single-lepton triggers described in Sec. 4.2.1, and have to pass the PV selection described in Sec. 4.2.2.

A visualization of the regions in various photon, jet, and b-tagged jet multiplicity bins is shown in Fig. 4.6, with a list of the regions and their selection criteria given in Table 4.6.

Signal regions

The $t\bar{t}\gamma$ signal process is measured in events with an isolated, high-p_T photon and large jet and b-tagged jet multiplicities. The SR3p signal region is defined in selections with exactly one isolated lepton (electron or muon) fulfilling the lepton analysis selection criteria ($N_\ell = 1$), exactly one photon with analysis selection criteria applied ($N_\gamma = 1$), at least three jets ($N_j \geq 3$), where at least one is b-tagged ($N_b \geq 1$). Events with additional photons (leptons) fulfilling the veto requirements are rejected. For the cross section measurements, the region is split in $N_j = 3$ and $N_j \geq 4$ selections, denoted as SR3 and SR4p, respectively.

A selection of distributions in the SR3p signal region is shown in Fig 4.7, where simulated events are categorized according to the event categories described in Sec. 4.2.4. In this figure, the hatched band represents pre-fit systematic uncertainties, and the normalization of background events is performed according to the methods described in Sec. 4.4. The three-jet invariant mass among all identified jets maximizing the vector p_T sum magnitude is denoted as M_3 [280]. The distributions of $p_T(\gamma)$ (upper left), M_3 (upper center), the W boson candidate transverse mass $m_T(W)$ defined in Eq. 3.3.2 (upper right), the invariant mass of lepton and photon $m(\ell,\gamma)$ (lower left), the angular separation of lepton and photon $\Delta R(\ell,\gamma)$ (lower center), and the smallest angular separation of photon and any jet min $\Delta R(j,\gamma)$ (lower right) are shown. An overview of the simulation-based signal and background contributions in the SR3p signal region, split into processes and event categories, is given in Table 4.7.

Control and validation regions

The main background contributions in the signal region are estimated from data, where the methods are described in Sec. 4.4. Baseline selections for control and validation regions with enriched contributions from single background sources are established, where requirements on objects can vary depending on the particular background estimation method.

Die approbierte gedruckte Originalversion dieser Dissertation ist an der TU Wien Bibliothek verfügbar.
The approved original version of this doctoral thesis is available in print at TU Wien Bibliothek.
TU Bibliothek Your knowledge hub WIEN

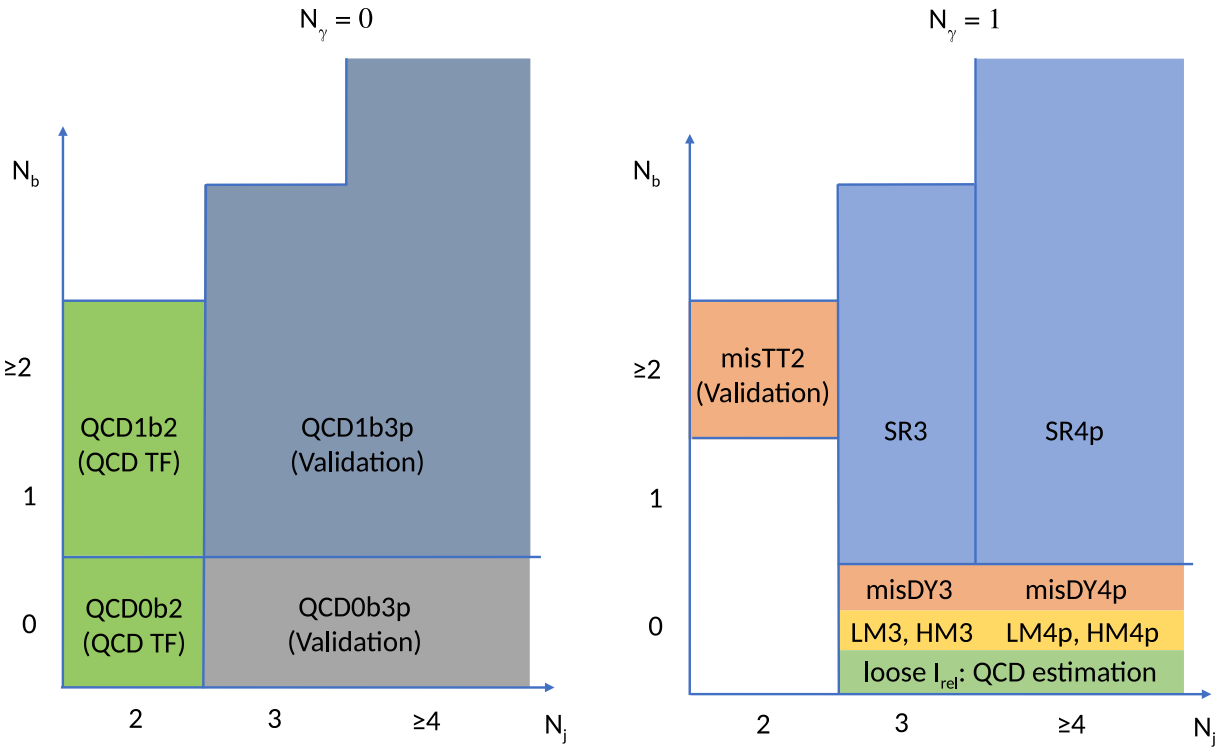

Figure 4.6: Overview of the signal, control, and validation regions in selections of the photon (N_γ), jet (N_j), and b-tagged jet (N_b) multiplicities.

Table 4.6: Overview of the selection criteria for the signal, control, and validation regions.

Region		N_ℓ	N_j	N_b	N_γ	Other requirements
SR3p	SR3	1	3	$\geq$1	1	
	SR4p	1	$\geq$4	$\geq$1	1	
LM3p	LM3	1	3	0	1	$m(\mathrm{e},\gamma) < m_\mathrm{Z} - 10\,\mathrm{GeV}$, $m(\mu,\gamma) < m_\mathrm{Z}$
	LM4p	1	$\geq$4	0	1	$m(\mathrm{e},\gamma) < m_\mathrm{Z} - 10\,\mathrm{GeV}$, $m(\mu,\gamma) < m_\mathrm{Z}$
HM3p	HM3	1	3	0	1	$m(\mathrm{e},\gamma) > m_\mathrm{Z} + 10\,\mathrm{GeV}$, $m(\mu,\gamma) > m_\mathrm{Z}$
	HM4p	1	$\geq$4	0	1	$m(\mathrm{e},\gamma) > m_\mathrm{Z} + 10\,\mathrm{GeV}$, $m(\mu,\gamma) > m_\mathrm{Z}$
misDY3p	misDY3	1	3	0	1	$\lvert m(\mathrm{e},\gamma) - m_\mathrm{Z}\rvert \leq 10\,\mathrm{GeV}$
	misDY4p	1	$\geq$4	0	1	$\lvert m(\mathrm{e},\gamma) - m_\mathrm{Z}\rvert \leq 10\,\mathrm{GeV}$
	misTT2	1	2	2	1	
	QCD0b2	1	2	0	0	
	QCD0b3p	1	$\geq$3	0	0	
	QCD1b2	1	2	$\geq$1	0	
	QCD1b3p	1	$\geq$3	$\geq$1	0	

Die approbierte gedruckte Originalversion dieser Dissertation ist an der TU Wien Bibliothek verfügbar.
The approved original version of this doctoral thesis is available in print at TU Wien Bibliothek.
TU Bibliothek Your knowledge hub WIEN

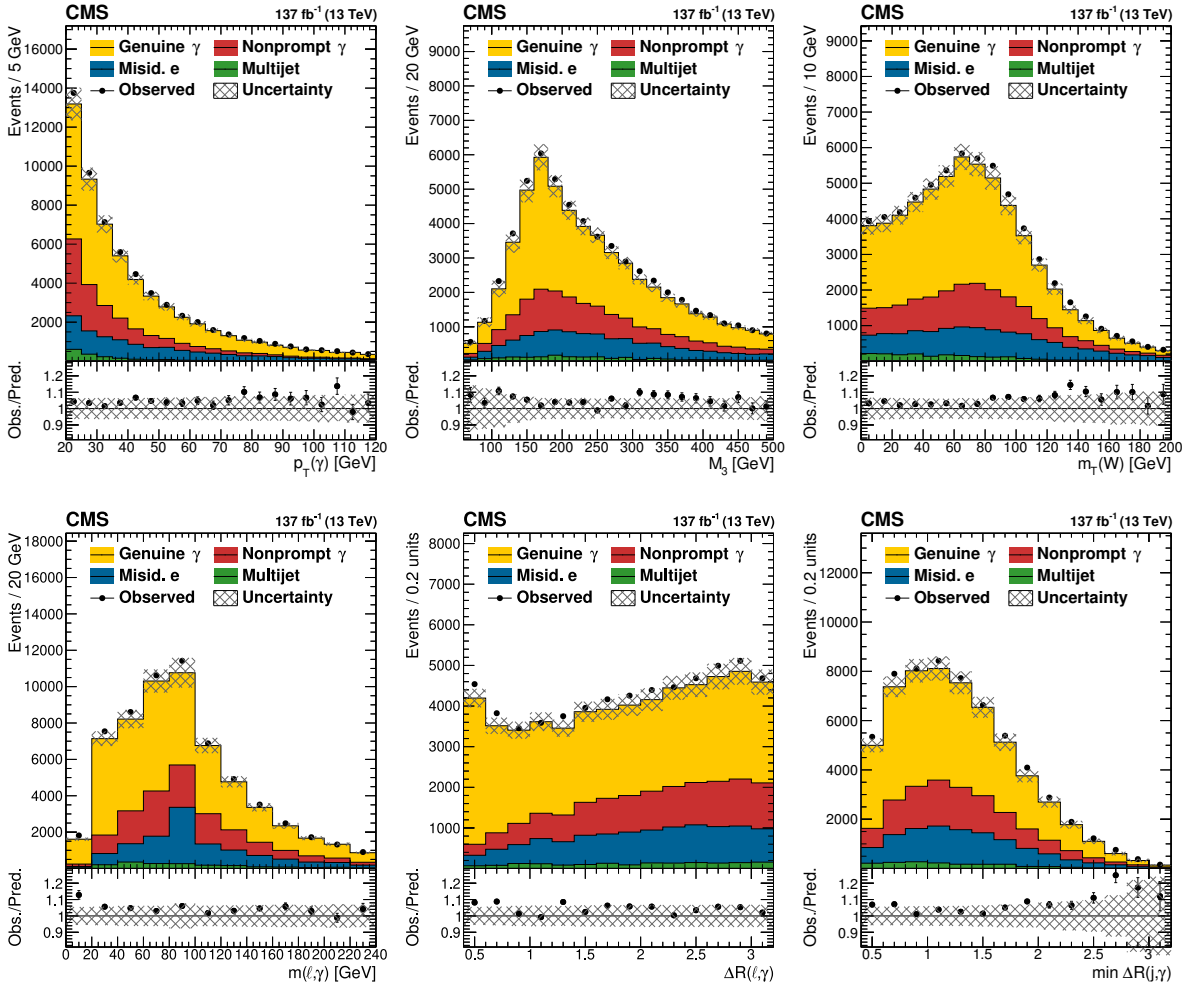

Figure 4.7: Distributions of $p_T(\gamma)$ (upper left), the three-jet invariant mass M_3 (upper center), the W boson candidate transverse mass $m_T(W)$ (upper right), the invariant mass of lepton and photon $m(\ell,\gamma)$ (lower left), the angular separation of lepton and photon $\Delta R(\ell,\gamma)$ (lower center), and the smallest angular separation of photon and any jet min $\Delta R(j,\gamma)$ (lower right) in the SR3p signal region. The normalization of background events is performed according to the methods described in Sec. 4.4. The ratio of observed to predicted event yields is shown in the lower panels and pre-fit systematic uncertainties are shown as hatched bands.

Die approbierte gedruckte Originalversion dieser Dissertation ist an der TU Wien Bibliothek verfügbar.
The approved original version of this doctoral thesis is available in print at TU Wien Bibliothek.

TU WIEN Bibliothek Your knowledge hub
Die approbierte gedruckte Originalversion dieser Dissertation ist an der TU Wien Bibliothek verfügbar.
The approved original version of this doctoral thesis is available in print at TU Wien Bibliothek.

Table 4.7: Overview of the signal and background contributions according to simulations in the SR3p signal region in the combined electron and muon channels, where in addition to the yields in the inclusive SR3p region, three coarse bins in $p_T(\gamma)$ are shown. The table shows the yields in each process (bold), and processes split according to the photon categories for genuine photon (gen γ), misidentified electron (misid e), and nonprompt photon (np γ) events, where the latter is separated in its components for photons with hadronic origin (had γ), hadronic fakes (fake) and PU photons (PU γ). The yields are taken from simulations without corrections to their normalizations applied.

	SR3p							$20 < p_T(\gamma) < 120\,\text{GeV}$						
	Events	Gen γ	Misid e	Np γ	(Had γ	Fake	PU γ)	**Events**	Gen γ	Misid e	Np γ	(Had γ	Fake	PU γ)
$t\bar{t}\gamma$	**26560.2**	26383.3	51.3	125.6	(63	23	14 %)	**24463.2**	24293.1	48.1	122.0	(63	23	14 %)
$t/t\bar{t}$	**18322.0**	4203.4	4228.8	9889.8	(74	10	16 %)	**17668.1**	3935.0	3991.6	9741.5	(74	10	16 %)
$W\gamma$	**3139.6**	3133.4	0.0	6.2	(100	0	0 %)	**2808.2**	2802.0	0.0	6.2	(100	0	0 %)
$Z\gamma$	**1573.9**	1549.5	12.4	12.0	(10	72	18 %)	**1498.8**	1478.2	10.2	10.4	(11	68	21 %)
W+jets	**534.1**	0.0	0.1	534.0	(44	5	51 %)	**521.7**	0.0	0.1	521.6	(42	5	53 %)
Drell–Yan	**1231.0**	126.0	911.2	193.8	(50	18	32 %)	**1147.3**	121.2	835.7	190.4	(49	19	32 %)
QCD multijet	**1147.9**	952.5	3.3	192.1	(25	1	74 %)	**1106.8**	913.8	3.3	189.7	(25	1	74 %)
Other	**630.5**	480.7	70.2	79.6	(71	10	19 %)	**581.3**	442.6	62.8	75.9	(71	10	19 %)
Total	**53139.2**	36828.8	5277.3	11033.1	(71	10	19 %)	**49795.4**	33985.9	4951.8	10857.7	(71	10	19 %)
	$120 \leq p_T(\gamma) < 220\,\text{GeV}$							$p_T(\gamma) \geq 220\,\text{GeV}$						
	Events	Gen γ	Misid e	Np γ	(Had γ	Fake	PU γ)	**Events**	Gen γ	Misid e	Np γ	(Had γ	Fake	PU γ)
$t\bar{t}\gamma$	**1502.4**	1496.6	2.9	2.9	(72	27	1 %)	**594.6**	593.6	0.3	0.7	(74	25	1 %)
$t/t\bar{t}$	**574.0**	221.6	215.0	137.4	(88	11	1 %)	**79.9**	46.8	22.2	10.9	(89	9	2 %)
$W\gamma$	**232.7**	232.7	0.0	0.0	(0	0	0 %)	**98.7**	98.7	0.0	0.0	(0	0	0 %)
$Z\gamma$	**60.0**	57.3	1.1	1.6	(0	100	0 %)	**15.1**	14.0	1.1	0.0	(0	0	0 %)
W+jets	**6.4**	0.0	0.0	6.4	(100	0	0 %)	**6.0**	0.0	0.0	6.0	(100	0	0 %)
Drell–Yan	**76.0**	3.1	69.5	3.4	(100	0	0 %)	**7.7**	1.7	6.0	0.0	(0	0	0 %)
QCD multijet	**29.0**	26.6	0.0	2.4	(25	0	75 %)	**12.1**	12.1	0.0	0.0	(0	0	0 %)
Other	**37.5**	28.3	6.0	3.2	(88	12	0 %)	**11.7**	9.8	1.4	0.5	(82	18	0 %)
Total	**2518.0**	2066.2	294.5	157.3	(86	12	2 %)	**825.8**	776.7	31.0	18.1	(92	7	1 %)

The Wγ and Zγ processes, as well as events with a misidentified electron, are enriched in regions without b-tagged jets ($N_\mathrm{b} = 0$), where selections on $\mathrm{m}(\ell, \gamma)$ are used to separate the processes. The Zγ process is enriched in low-mass (LM) regions, denoted as LM3 (LM4p) for $N_\mathrm{j} = 3$ ($\geq$4) selections, and LM3p for the combined $N_\mathrm{j} \geq 3$ requirement, where the region is defined by $\mathrm{m}(\mu, \gamma) < \mathrm{m_Z}$ in the muon channel and $\mathrm{m}(\mathrm{e}, \gamma) < \mathrm{m_Z} - 10\,\mathrm{GeV}$ in the electron channel. The high-mass (HM) regions are dominated by Wγ events, defined by $\mathrm{m}(\mu, \gamma) > \mathrm{m_Z}$ in the muon channel and $\mathrm{m}(\mathrm{e}, \gamma) > \mathrm{m_Z} + 10\,\mathrm{GeV}$ in the electron channel. The control regions for the three N_j criteria are denoted as HM3, HM4p, and HM3p.

A control region for misidentified electron events is defined in the electron channel in requiring the invariant mass $\mathrm{m}(\mathrm{e}, \gamma)$ to be close to $\mathrm{m_Z}$, with $|\mathrm{m}(\mathrm{e}, \gamma) - \mathrm{m_Z}| \leq 10\,\mathrm{GeV}$. The region is dominated by Drell–Yan events, where the Z boson decays to two electrons, $\mathrm{Z} \to \mathrm{e^+e^-}$, and one of the electrons is misidentified as a photon. The control regions are denoted as misDY3, misDY4p, and misDY3p for the three N_j requirements.

A validation region enriched in $t\bar{t}$ events with a misidentified electron is used to validate the background estimation method, where the region is defined in selecting exactly two (b-tagged) jets ($N_\mathrm{j} = 2$, $N_\mathrm{b} = 2$). The region is dominated by dileptonic $t\bar{t}$ events at the generator level, with at least one electron that is misidentified as a photon, and is denoted as misTT2 in the following.

QCD multijet events are estimated in signal and control regions in a data-based way. The method is described in Sec. 4.4.1 and based on rescaling normalized distributions in lepton isolation sideband regions, where the rescaling is performed using transfer factors (TFs). The TFs are estimated from data in regions without photons ($N_\gamma = 0$) in two-jet selections ($N_\mathrm{j} = 2$), without ($N_\mathrm{b} = 0$) or with at least one b-tagged jet ($N_\mathrm{b} \geq 1$). The regions are denoted as QCD0b2 and QCD1b2, respectively, where selections with at least three jets ($N_\mathrm{j} \geq 3$), denoted as QCD0b3p and QCD1b3p, respectively, are used to validate the method.

Nonprompt photon background contributions are estimated in a data-based way described in Sec. 4.4.2, where sideband regions of the charged isolation I^chg and the lateral shower extension $\sigma_{\eta\eta}$ of the photon defined in Sec. 3.3.3 are used, with no dedicated control region selections established.

4.3.2 Fiducial phase space definition

The fiducial phase space of the measurement is defined at the particle level, with selection criteria applied to objects after parton showering and hadronization but before detector simulation. The region is defined close to the SR3p signal region given in Sec. 4.3.1 and requires exactly one electron or muon, exactly one photon, with at least three particle-level jets from the hadronization of final-state quarks, from which at least one has to be matched to a b hadron.

Leptons have to be found within $|\eta| < 2.4$ and originate from the W boson decay. With no other requirements on the parentage of the lepton applied, the fiducial phase space selection thus includes a small fraction of leptonically decaying tau leptons. A threshold on $\mathrm{p_T}$ is applied in requiring electrons (muons) to have $\mathrm{p_T} > 35$ (30) GeV, matching the selection criteria of the reconstructed phase space defined in Sec. 4.2.2. Leptons are dressed, with the four-momenta of photons from final-state radiation added to the lepton

Die approbierte gedruckte Originalversion dieser Dissertation ist an der TU Wien Bibliothek verfügbar.
The approved original version of this doctoral thesis is available in print at TU Wien Bibliothek.
TU Bibliothek Your knowledge hub WIEN

Table 4.8: Object definitions of the fiducial phase space region defined at the particle level. The isolation criterion of the photon requires no stable particles (except neutrinos) with $p_T > 5\,\text{GeV}$ to be within a cone of $\Delta R = 0.1$.

Photon	e (μ)	Jet	b jet
$p_T > 20\,\text{GeV}$	$p_T > 35$ (30) GeV	$p_T > 30\,\text{GeV}$	$p_T > 30\,\text{GeV}$
$\lvert\eta\rvert < 1.4442$	$\lvert\eta\rvert < 2.4$	$\lvert\eta\rvert < 2.4$	$\lvert\eta\rvert < 2.4$
no hadronic origin	no hadronic origin	$\Delta R(\text{j}, \ell) > 0.4$	$\Delta R(\text{b}, \ell) > 0.4$
$\Delta R(\ell, \gamma) > 0.4$		$\Delta R(\text{j}, \gamma) > 0.1$	$\Delta R(\text{b}, \gamma) > 0.1$
isolated			matched to b hadrons

before their selection, if photons are found within an angular distance of $\Delta R = 0.1$.

Photons are considered if they originate from initial-state quarks, top quarks, bottom quarks, leptons, or SM bosons. The selection additionally requires $p_T(\gamma) > 20\,\text{GeV}$ and the photon to be found within the barrel region of the CMS detector, with $|\eta(\gamma)| < 1.4442$. Photons within a cone of $\Delta R = 0.4$ to the selected leptons are removed. An additional isolation criterion matching the generator settings of the signal simulation is applied, where photons close to other stable particles within a cone of $\Delta R = 0.1$ are not considered. The latter have to satisfy $p_T > 5\,\text{GeV}$, where neutrinos are not taken into account.

Particle-level jets from the hadronization of final-state quarks are clustered with a distance parameter of $\Delta R = 0.4$ using the anti-k_T algorithm [245]. Jets are considered if they satisfy $p_T > 30$ GeV, $|\eta| < 2.4$, and are found outside a cone of $\Delta R = 0.4$ (0.1) to the selected lepton (photon) candidate. Objects are tagged as b jets if matched to b hadrons using a ghost matching method [281].

The selection criteria for the objects defined in the fiducial phase space at the particle level are summarized in Table 4.8.

$t\bar{t}\gamma$ cross section prediction

The fiducial phase space cross section is predicted with MadGraph5_aMC@NLO, interfaced with Pythia 8 using the CP5 tune at NLO in QCD precision. A $t\bar{t}\gamma$ cross section of $\sigma^{\text{NLO}}(t\bar{t}\gamma) = 773 \pm 135\,\text{fb}$ is extracted from simulation, with uncertainties arising from variations of μ_R and μ_F scales, α_s, and the PDF set. The cross section predictions from MadGraph5_aMC@NLO interfaced with Herwig++ using the EE5C tune (Herwig 7 using the CH3 tune) are found to be 8.3 (5.4)% lower compared to simulations using Pythia 8.

A cutflow table for the applied selection criteria in the fiducial phase space region is shown in Table 4.9, separately and combined in the W boson decay channels. The selection criteria are applied sequentially, with the last line showing the final fiducial cross section.

The predicted fiducial phase space cross section can be compared to the $t\bar{t}\gamma$ cross section at reconstruction level in the SR3p signal region of 193 fb, where the event count is given in Table 4.7. From the cross section of events that pass the reconstruction-level selection and are found within the fiducial phase space of 164 fb, the signal efficiency ϵ is calculated as the

Die approbierte gedruckte Originalversion dieser Dissertation ist an der TU Wien Bibliothek verfügbar.
The approved original version of this doctoral thesis is available in print at TU Wien Bibliothek.
TU Bibliothek Your knowledge hub WIEN

Table 4.9: Cutflow table showing the $t\bar{t}\gamma$ cross sections in the fiducial phase space event selections for the signal simulation separately in the W boson decay channels. The selection criteria are applied sequentially, except for lines with indentation, where those requirements are dropped in the lines that follow. Line 5 gives the final fiducial cross section.

	#	Requirement	Cross section [fb]			
			$t\bar{t}\gamma$ (total)	$t\bar{t}\gamma$ (0ℓ)	$t\bar{t}\gamma$ (1ℓ)	$t\bar{t}\gamma$ (2ℓ)
Fiducial phase space	0	Total	15891	6162	7509	2220
	1	Overlap removal	15264	5961	7192	2111
	2	$N_\gamma = 1$	5863	2461	2678	724
	3	$N_\ell = 1$	1225	0	893	332
	3a	$N_\mathrm{e} = 1, N_\mu = 0$	569	0	415	154
	3b	$N_\mathrm{e} = 0, N_\mu = 1$	656	0	478	178
	4	$N_\mathrm{j} \geq 3$	792	0	660	132
	5	$N_\mathrm{b} \geq 1$	773	0	642	131

ratio to the fiducial cross section. The fraction of events migrating into the reconstructed phase space, denoted as f_out, is calculated from the reconstruction-level cross section of events not found in the fiducial phase space of 29 fb. The signal efficiency ϵ and the fraction f_out are calculated to be

$$\epsilon = \frac{\sigma(\mathrm{reco}|\mathrm{fid})}{\sigma(\mathrm{fid})} = 21.2\,\% \quad \text{and} \quad f_\mathrm{out} = \frac{\sigma(\mathrm{reco}|!\mathrm{fid})}{\sigma(\mathrm{reco})} = 15.0\,\%, \tag{4.3.1}$$

with the fiducial phase space region cross section $\sigma(\mathrm{fid})$, the reconstruction-level cross section of the SR3p signal region $\sigma(\mathrm{reco})$, the cross section of events fulfilling both selection criteria $\sigma(\mathrm{reco}|\mathrm{fid})$, and the value for events not part of the fiducial phase space $\sigma(\mathrm{reco}|!\mathrm{fid})$.

4.3.3 Statistical treatment

The measurement of the signal cross section is performed using a profile likelihood test statistic [282–284] constructed from binned Poisson observations from signal and control regions. A likelihood function $\mathcal{L}$ is constructed as a product of Poisson probabilities $P(n|\nu)$ for the observation of n events when ν events are expected $P(n|\nu) = \frac{\nu^n e^{-\nu}}{n!}$.

The parameter of interest is the signal strength modifier r, which is used to measure the ratio of the observed to the predicted $t\bar{t}\gamma$ cross section. The value $r = 0$ corresponds to the background-only hypothesis, and $r = 1$ to the hypothesis where the observation matches the expected $t\bar{t}\gamma$ signal yield. The measurement includes several background components in the signal and control regions. The total number of predicted events in each bin b is thus given by $\nu_b = r\nu_{S,b} + \sum_{m=1}^{N_B} \nu_{B_m,b}$, with the expected signal events $\nu_{S,b}$, the number of background contributions N_B, and the expected background events $\nu_{B_m,b}$ for the background component B_m.

The statistical model involves a set of nuisance parameters $\boldsymbol{\theta}$ of log-normal probability density functions N and relate to the systematic uncertainties $\boldsymbol{\alpha}$ in the measurement.

Die approbierte gedruckte Originalversion dieser Dissertation ist an der TU Wien Bibliothek verfügbar.
The approved original version of this doctoral thesis is available in print at TU Wien Bibliothek.
TU Bibliothek Your knowledge hub WIEN

Unconstrained parameters $\boldsymbol{\beta}$ in the likelihood fit affecting the Wγ and misidentified electron background processes, collectively denoted as B_{free}, reflect the in situ measurements of their normalizations described in Sec. 4.4.3. A detailed discussion on the uncertainties is given in Sec. 4.5.

The likelihood function is written in terms of Poisson distribution products of the signal and control region bins b,

$$\mathcal{L}(n|r,\boldsymbol{\theta},\boldsymbol{\beta}) = \prod_{b=1}^{N_{\text{bins}}} P\left(n_b \middle| r\,\nu_{S,b} \prod_{j=1}^{N_{\text{nuis}}} \alpha_{j,b}^{\theta_j} + \sum_{m=1}^{N_B} \nu_{B_m,b} \prod_{j=1}^{N_{\text{nuis}}} \alpha_{j,m,b}^{\theta_j} \prod_{k=1}^{N_{\text{free}}} \beta_{k,m}\right) \prod_{j=1}^{N_{\text{nuis}}} N\left(\theta_j|0,1\right), \tag{4.3.2}$$

with the total number of bins N_{bins}, N_{nuis} constrained nuisance parameters, N_{free} unconstrained parameters, and the observed events per bin n_b. In the likelihood function, $\beta_{k,m} = \beta_m$ if the unconstrained parameter k is affecting the background component $B_m \in B_{\text{free}}$ and $\beta_{k,m} = 1$ otherwise. The test statistic used in the $t\bar{t}\gamma$ cross section measurement is the profile likelihood ratio

$$q(r) = -2\ln\frac{\mathcal{L}(r,\hat{\boldsymbol{\theta}}_{\boldsymbol{r}},\hat{\boldsymbol{\beta}}_{\boldsymbol{r}})}{\mathcal{L}(\hat{r},\hat{\boldsymbol{\theta}},\hat{\boldsymbol{\beta}})}, \tag{4.3.3}$$

where here and in the following, the notation of the likelihood function is reduced to $\mathcal{L}(n|r,\boldsymbol{\theta},\boldsymbol{\beta}) \to \mathcal{L}(r,\boldsymbol{\theta},\boldsymbol{\beta})$. The set of parameters $(\hat{\boldsymbol{\theta}}_{\boldsymbol{r}},\hat{\boldsymbol{\beta}}_{\boldsymbol{r}})$ maximize $\mathcal{L}$ for a given r and $(\hat{r},\hat{\boldsymbol{\theta}},\hat{\boldsymbol{\beta}})$ maximize the likelihood function. The latter are referred to as post-fit parameters. Extracted signal and background yields in bin b are thus given by

$$\hat{\nu}_{S,b} = \hat{r}\,\nu_{S,b} \prod_{j=1}^{N_{\text{nuis}}} \alpha_{j,b}^{\hat{\theta}_j} \quad \text{and} \quad \hat{\nu}_{B,b} = \nu_{B,b} \prod_{j=1}^{N_{\text{nuis}}} \alpha_{j,b}^{\hat{\theta}_j} \prod_{k=1}^{N_{\text{free}}} \hat{\beta}_{k,b}, \tag{4.3.4}$$

respectively.

Inclusive cross section measurement

To extract the inclusive $t\bar{t}\gamma$ cross section, the fit minimizes the test statistic $q(r)$ to determine the signal strength modifier. Several signal and control regions enter the statistical model, where the fit is performed using the expected signal and background yields determined from simulation and the background estimation procedures described in Sec. 4.4. The fit is performed simultaneously in the SR3 and SR4p signal region defined in Sec. 4.3.1, where the regions are divided in three bins of M_3, with the ranges 0–280 , 280–420 , and >420 GeV. Normalization SFs for the background processes of Wγ, Zγ, and misidentified electron events are measured in situ by including the control regions LM3, LM4p, HM3, HM4p, misDY3, and misDY4p in the construction of the likelihood function. Signal and control regions enter the likelihood fit in bins for each data-taking period, separately for the electron and muon channel.

The $p_T(\gamma)$ dependence of background events including misidentified electrons is extracted in dividing the misDY3 and misDY4p control regions into seven bins, with the $p_T(\gamma)$

TU Bibliothek Your knowledge hub WIEN Die approbierte gedruckte Originalversion dieser Dissertation ist an der TU Wien Bibliothek verfügbar. The approved original version of this doctoral thesis is available in print at TU Wien Bibliothek.

Table 4.10: Thresholds of the binning choices in the differential measurements for $p_T(\gamma)$, $|\eta(\gamma)|$, and $\Delta R(\ell,\gamma)$.

$p_T(\gamma)$ [GeV]	20, 35, 50, 65, 80, 100, 120, 140, 160, 200, 260, ≥320
$\lvert\eta(\gamma)\rvert$	0, 0.15, 0.30, 0.45, 0.60, 0.75, 0.90, 1.05, 1.20, 1.35, 1.4442
$\Delta R(\ell,\gamma)$	0.4, 0.6, 0.8, 1.0, 1.2, 1.4, 1.6, 1.8, 2.0, 2.2, 2.4, 2.6, 2.8, ≥3.0

thresholds of 20, 35, 50, 65, 80, 120, and 160 GeV and additional nuisance parameters in each $p_T(\gamma)$ bin. Similarly, the LM3, LM4p, HM3, and HM4p regions are divided in three coarser bins with thresholds of 20, 65, and 160 GeV.

To measure the $t\bar{t}\gamma$ signal cross section, the inclusive cross section in the fiducial phase space defined in Sec. 4.3.2 is scaled by the extracted signal strength modifier $\hat{r}$. Events that do not enter the fiducial region, with their fraction given in Eq. 4.3.1, are scaled by the same value, with no deviations of the cross section assumed for these events.

Differential cross section measurements

The differential cross section measurement is performed in three distributions, $p_T(\gamma)$, $|\eta(\gamma)|$, and $\Delta R(\ell,\gamma)$, with the thresholds of the binning choices summarized in Table 4.10.

Separate fits are performed for each distribution, simultaneously in the SR3 and SR4p signal region, in bins for each data-taking period and the electron and muon channel. Since the dependence of background normalization SFs on the $|\eta(\gamma)|$ and $\Delta R(\ell,\gamma)$ distributions is found to be negligible, the $p_T(\gamma)$ binning of control regions is kept the same in the inclusive and all three differential cross section measurements.

To measure the $t\bar{t}\gamma$ differential cross sections, a signal strength modifier is extracted for each bin of the three data-taking periods, the lepton channels, and the signal regions. Thus, the likelihood function given in Eq. 4.3.2 is modified by $r \to r_b$ for differential measurements. The observed distributions are then combined to a $N_j \geq 3$ selection in the combined electron and muon channel for each data-taking period and further corrected for detector effects, with the method described in the following.

Unfolding method

Observed distributions from differential cross section measurements need to be corrected for detector response and acceptance effects to allow for comparisons to theoretical predictions. The method is known as unfolding [250], where the measured $p_T(\gamma)$, $|\eta(\gamma)|$, and $\Delta R(\ell,\gamma)$ distributions are corrected to reflect the distributions in the fiducial phase space, defined at the particle level. For the unfolding of the differential distributions, the particle-level phase space is defined in the same selection as for the inclusive measurement given in Sec. 4.3.2, with the particle-level thresholds of the binning choices for the $p_T(\gamma)$, $|\eta(\gamma)|$, and $\Delta R(\ell,\gamma)$ measurements summarized in Table 4.11.

The TUnfold framework [285] is used to extract the measured distributions at the particle level $\mathbf{x}$, where the relation to the reconstruction-level distribution $\mathbf{y}$ is described

Die approbierte gedruckte Originalversion dieser Dissertation ist an der TU Wien Bibliothek verfügbar.
The approved original version of this doctoral thesis is available in print at TU Wien Bibliothek.
TU Bibliothek Your knowledge hub WIEN

Table 4.11: Thresholds of the particle-level binning choices in the differential measurements for $p_T(\gamma)$, $|\eta(\gamma)|$, and $\Delta R(\ell,\gamma)$.

$p_T(\gamma)$ [GeV]	20, 35, 50, 80, 120, 160, 200, 260, ≥320
$\lvert\eta(\gamma)\rvert$	0, 0.3, 0.6, 0.9, 1.2, 1.4442
$\Delta R(\ell,\gamma)$	0.4, 0.8, 1.2, 1.6, 2.0, 2.4, ≥2.8

by the transformation

$$y_i = \sum_{j=1}^{m} A_{ij} x_j \quad \text{for} \quad 1 \leq i \leq n, \tag{4.3.5}$$

with n (m) bins at the reconstruction (particle) level and a response matrix $\mathbf{A}$ calculated as the probabilities for event migrations from the reconstruction- to particle-level bins, where in this case statistical fluctuations are neglected.

For an equal number of bins at the reconstruction and particle level $n = m$, determining the particle-level distribution is simply done by inverting the matrix $\mathbf{A}$. However, this choice can lead to large statistical bin-by-bin fluctuations. While the result is statistically correct, these oscillations do not reflect the expectations of a smooth distribution at the particle level.

A general approach for $n \neq m$ bins is performed in the regularized unfolding algorithm, which finds the stationary point in the Lagrangian [285]

$$\begin{aligned} \mathcal{L}(\mathbf{x},\lambda) = {} & (\mathbf{y}-\mathbf{A}\mathbf{x})^{\mathrm{T}}\,\mathbf{V}_{\mathbf{yy}}^{-1}\,(\mathbf{y}-\mathbf{A}\mathbf{x}) \\ & + \tau^2(\mathbf{x}-f_b\mathbf{x_0})^{\mathrm{T}}\,(\mathbf{L}^{\mathrm{T}}\mathbf{L})\,(\mathbf{x}-f_b\mathbf{x_0}) \\ & + \lambda(Y-\mathbf{e}^{\mathrm{T}}\mathbf{x}), \\ \text{with} \quad Y = {} & \sum_i y_i \\ \text{and} \quad e_j = {} & \sum_i A_{ij}. \end{aligned} \tag{4.3.6}$$

The first term contains the least square minimization, with the covariance matrix $\mathbf{V_{yy}}$. The second term describes the regularization, damping statistical fluctuations at the reconstruction level, which can amplify and thus affect the particle-level distribution. The constant regularization term τ^2, the $n \times n_R$ matrix $\mathbf{L}$, n_R regularization conditions and the bias vector $f_b\mathbf{x_0}$, containing the normalization factor f_b, are used to suppress such fluctuations. Conditions can be chosen to regularize the amplitude, the first derivative, or the curvature, where the default choice in differential cross section measurements is the curvature regularization. The third term is an optional area constraint, with the sum of observations Y and the efficiency vector $\mathbf{e}$. The procedure limits a possible bias on the normalization, correcting the result for the efficiency. This optional term is not part of the unfolding method of this measurement, where no area constraints are applied. A detailed discussion on how to obtain the stationary point in the Lagrangian is found in Ref. [285].

Simulated $t\bar{t}\gamma$ events are used to construct response matrices $\mathbf{A}$ that reflect detector response and acceptance corrections and are the ingredient to unfold the measured differential distributions to the particle level. For the measurements, response matrices are

Die approbierte gedruckte Originalversion dieser Dissertation ist an der TU Wien Bibliothek verfügbar.
The approved original version of this doctoral thesis is available in print at TU Wien Bibliothek.
TU Bibliothek Your knowledge hub WIEN

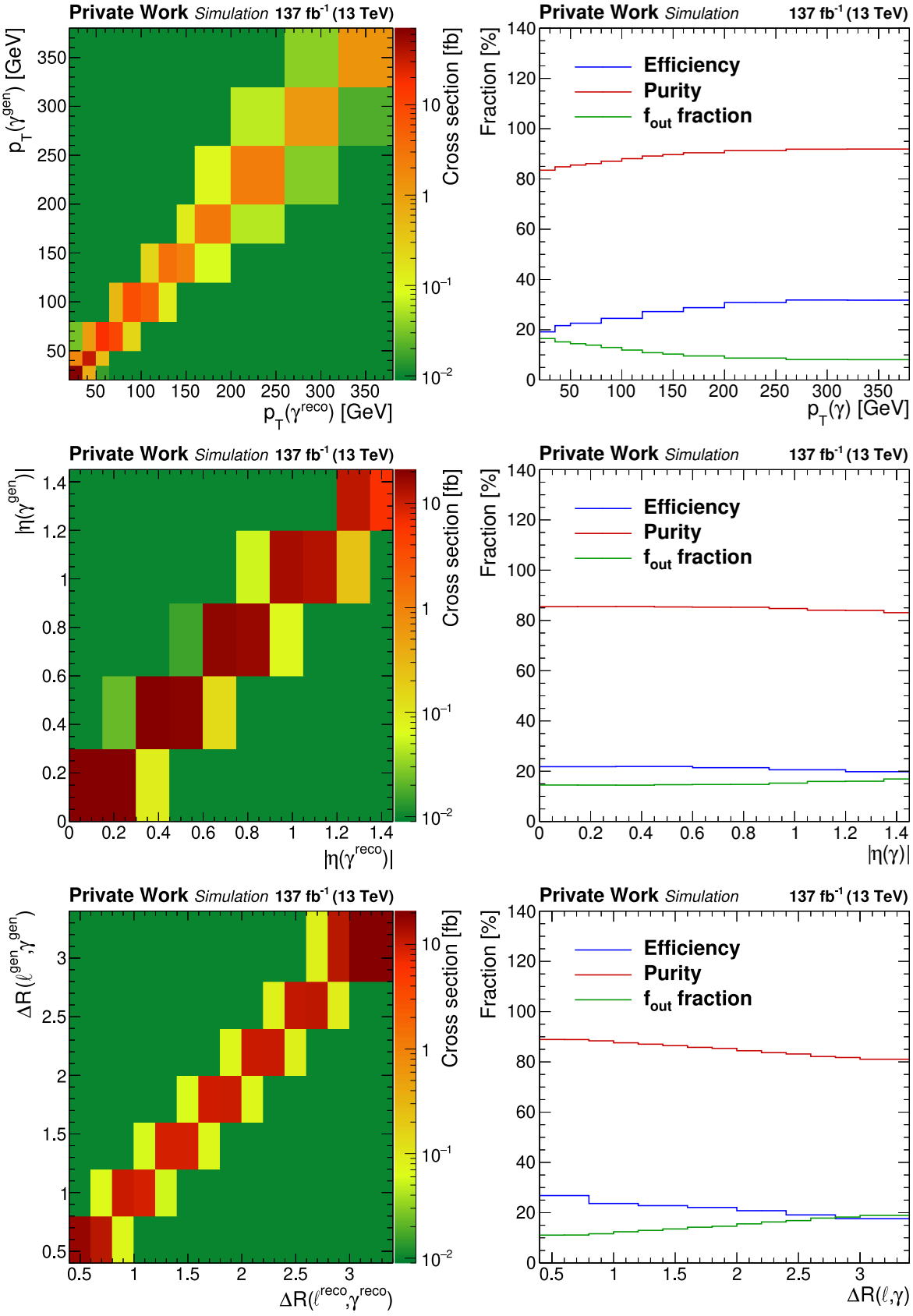

Figure 4.8: Response matrices (left), efficiencies (right, blue), purities (right, red), and f_{out} contributions (right, green) for cross section measurements in $p_T(\gamma)$ (upper), $|\eta(\gamma)|$ (center), and $\Delta R(\ell, \gamma)$ (lower).

Die approbierte gedruckte Originalversion dieser Dissertation ist an der TU Wien Bibliothek verfügbar.
The approved original version of this doctoral thesis is available in print at TU Wien Bibliothek.

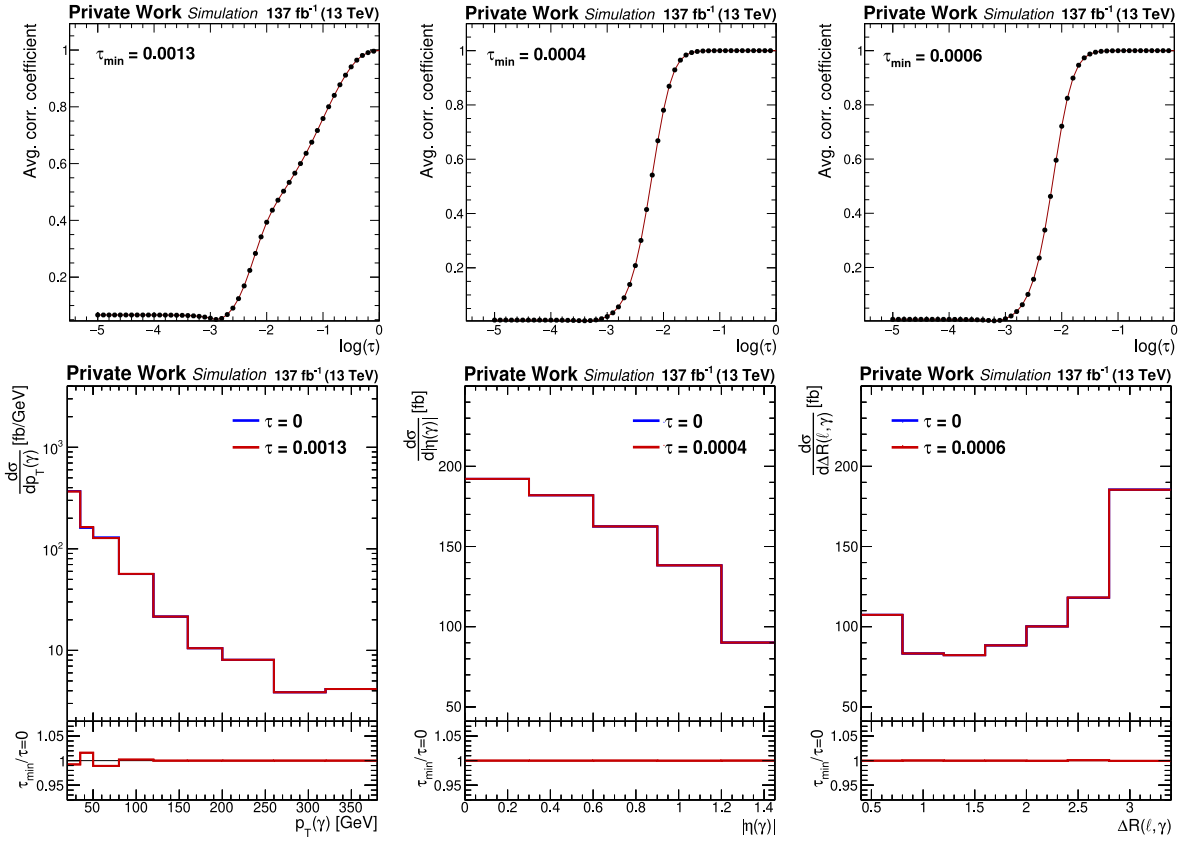

Figure 4.9: The average global correlation coefficient as a function of the regularization strength using curvature regularization (upper) and the expected unfolded distributions for values of the regulator (lower) in $p_T(\gamma)$ (left), $|\eta(\gamma)|$ (center), and $\Delta R(\ell,\gamma)$ (right).

constructed for each data-taking period and unfolded distributions are combined in the unfolding step. The extracted response matrices for the three distributions are shown in Fig. 4.8 (left), where here, the three data-taking periods are combined so a single response matrix for visualization purposes.

Due to the high angular and momentum resolutions of the lepton and photon, the migration of events from particle-level bins to other reconstruction-level bins is suppressed, leading to small off-diagonal contributions in the response matrices. Because of the lower number of bins at the particle level $m < n$, no regularization term is required in the unfolding procedure, setting $\tau = 0$. A scan of the average global correlation coefficient as a function of the regularization strength using curvature regularization is shown in Fig. 4.9 (upper) in $p_T(\gamma)$ (left), $|\eta(\gamma)|$ (center), and $\Delta R(\ell,\gamma)$ (right). The minimum τ_{min} is close to zero and deviations of expected unfolded distributions with a regularization term (lower) are below 2 %.

In this case, Eq. 4.3.6 reduces to the first term, where the unfolding procedure is performed in minimizing the χ^2 expression [286]

$$\chi^2 = (\mathbf{y} - \mathbf{A}\mathbf{x})^{\mathrm{T}}\, \mathbf{V}_{\mathbf{yy}}^{-1}\, (\mathbf{y} - \mathbf{A}\mathbf{x}). \tag{4.3.7}$$

This expression would evaluate to zero for $n = m$, resulting in a simple method equivalent to inverting the response matrix.

Die approbierte gedruckte Originalversion dieser Dissertation ist an der TU Wien Bibliothek verfügbar.
The approved original version of this doctoral thesis is available in print at TU Wien Bibliothek.
TU Bibliothek Your knowledge hub WIEN

The observed distributions $\mathbf{y}$ of the $t\bar{t}\gamma$ process are obtained in subtracting background contributions from the observation after the likelihood fit in the differential measurements, where additionally migration effects are taken into account in subtracting f_{out} contributions per bin. Linearity tests of the unfolding procedure were performed in unfolding suitably reweighted reconstruction-level yields. A negligible difference was found between the unfolded reweighted distributions and distributions with reweighting applied at the particle level.

A comparison of event yields in the fiducial phase space region to yields at the reconstruction level is used to quantify bin-by-bin migrations. The comparison is already shown in Sec. 4.3.2 in the inclusive selection, with the contributions in each bin of the kinematic distributions shown in Fig. 4.8 (right). The signal purity, defined as the reconstructed event fraction originating from the same bin at the particle level, is found to be 83–92 % in $p_T(\gamma)$, 83–86 % in $|\eta(\gamma)|$, and 81–89 % in $\Delta R(\ell, \gamma)$. The signal efficiency ϵ defined in Eq. 4.3.1 is calculated per bin, which ranges from 20–32 % in $p_T(\gamma)$, 20–22 % in $|\eta(\gamma)|$, and 18–27 % in $\Delta R(\ell, \gamma)$. The f_{out} contributions range from 8–17 % in $p_T(\gamma)$, 14–17 % in $|\eta(\gamma)|$, and 11–19 % in $\Delta R(\ell, \gamma)$.

4.4 Background estimation methods

The main background contributions in the signal regions originate from events with a nonprompt photon or a misidentified electron. The underlying process is dominantly found to be $t\bar{t}$ events, where the photon originates from hadronic sources or is misidentified. A summary of event counts and their photon categorization in the SR3p signal region is shown in Table 4.7, with distributions given in Fig. 4.7. Events with nonprompt leptons are subdominant in the signal regions, however, add a nonnegligible contribution in control regions without b-tagged jets. This section summarizes the procedures for the data-based estimations of these dominant background sources.

4.4.1 QCD multijet background

The QCD multijet background, with contributions from a misidentified or nonprompt lepton, is found to be small in signal region selections, however, it is subject to significant uncertainties. Thus, the background is estimated in a data-based procedure built in three steps. First, the QCD multijet background shape (template) is extracted in sideband regions of the lepton isolation criterion in selections without b-tagged jets ($N_b = 0$). In a second step, TFs are estimated in a data-based fitting method, where the QCD0b2 and QCD1b2 control regions with the corresponding isolation sideband regions are used to extract TFs for the QCD multijet estimation in non-b-tagged and b-tagged regions, respectively. In the last step, the extracted template is scaled with the corresponding TFs to correct for normalization differences in the signal or control region to the sideband region, where additional simulation-based corrections are taken into account.

In general, two types of TFs are estimated, one scaling the data-based template to estimate the QCD background in non-b-tagged control regions (TF_{0b}), estimated in the QCD0b2 control region, and one scaling the same template for estimations in b-tagged signal regions (TF_{1b}), estimated in the QCD1b2 region. A detailed discussion is given in the following.

Die approbierte gedruckte Originalversion dieser Dissertation ist an der TU Wien Bibliothek verfügbar.
The approved original version of this doctoral thesis is available in print at TU Wien Bibliothek.
TU Bibliothek Your knowledge hub WIEN

QCD multijet template estimation

The QCD multijet template for signal or control regions are extracted in a high-I_{rel} lepton isolation sideband. This sideband is defined in loosening the I_{rel} requirement on the electron or muon to the condition specified by the additional-lepton veto selection given in Sec. 4.2.2. Events with tightly isolated leptons are rejected in the sideband selection. Additionally, the selection of the region is adapted to select events without b-tagged jets ($N_{\text{b}} = 0$), where this sideband region is found to be dominated by QCD multijet events. Other selection criteria, e.g., jet or photon multiplicities, are kept the same in the sideband and the signal or control region. A data-based template of QCD multijet events is extracted in subtracting electroweak and top quark contributions, such as W+jets, $t\bar{t}$, and Drell–Yan events, from data. A comparison of the extracted template to simulation-based shapes is performed in selections without a photon, where good agreement is found. The comparison of the QCD multijet shapes of $m_{\text{T}}(\text{W})$ distributions in QCD0b2 and QCD1b2 regions for the electron and muon channel are shown in Fig. A.1 in Appendix A.1.1.

QCD multijet transfer factors

The extracted templates are scaled by a TF to evaluate the correct normalization of the QCD multijet background contributions. While the templates are extracted in regions without b-tagged jets, they are used in regions with and without b-tagged jet selections with varying normalization factors. Thus, separate TFs are estimated to scale the template for the use in b-tagged, e.g., SR3p or QCD1b3p, and non-b-tagged regions, e.g., LM3p, HM3p, misDY3p, or QCD0b3p.

The TFs are estimated in a data-based way in extracting the QCD multijet template of $m_{\text{T}}(\text{W})$ in the QCD0b2 sideband region, and fitting the template to data in either the QCD0b2 region for extracting $\text{TF}_{0\text{b}}$, or the QCD1b2 region for extracting $\text{TF}_{1\text{b}}$. In the fit, the normalization of contributions from electroweak background components is left floating, where due to the distinct shape differences of the template and electroweak backgrounds, the fit can determine the normalization factor for the QCD multijet template.

The fit result is shown in Fig. 4.10, with the QCD multijet contribution in the $m_{\text{T}}(\text{W})$ distribution in the QCD0b2 (center) and QCD1b2 (right) control regions fitted to data, and their corresponding sideband region (left) in the electron (upper) and muon (lower) channels. The sideband region shows the dominant QCD multijet contribution, with the electroweak component subtracted from data to extract the template (lower pad).

The isolation criteria on the electron and muon depend on the lepton p_{T} and $|\eta|$, affecting the defined isolation sideband regions. Therefore, the extracted TFs strongly depend on the lepton p_{T} and $|\eta|$. To account for such effects, the QCD multijet estimation is performed in six bins in $p_{\text{T}}(\ell)$ and four bins in $|\eta(\ell)|$, defined by the thresholds given in Table 4.12. With templates and TFs estimated in each of those 24 selections, the total QCD multijet estimation is then given by the sum of scaled templates. For selections in lepton p_{T} and η, the extracted data-based $\text{TF}_{0\text{b}}$ ($\text{TF}_{1\text{b}}$) values vary in the range of 0.9–3.1 (0.1–0.3) for the electron channel and 2.0–3.7 (0.6–1.0) for the muon channel.

Die approbierte gedruckte Originalversion dieser Dissertation ist an der TU Wien Bibliothek verfügbar.
The approved original version of this doctoral thesis is available in print at TU Wien Bibliothek.
TU Bibliothek Your knowledge hub WIEN

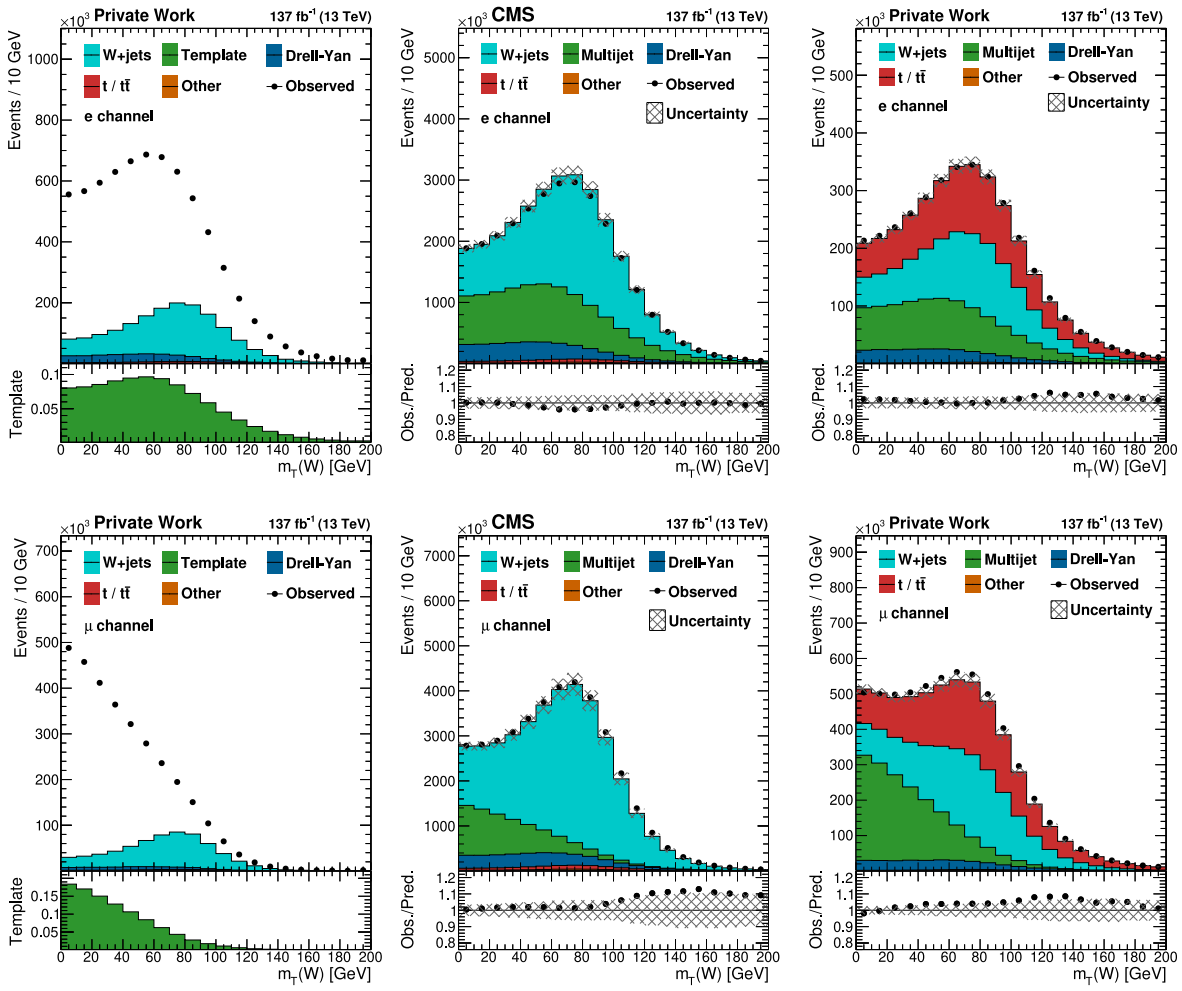

Figure 4.10: The $m_T(W)$ distributions in selections with loosely isolated electrons (upper left) and muons (lower left), with the extracted QCD multijet template shown in the lower pad. The template is obtained in subtracting the electroweak background from data and is used in the fit in selections with tightly isolated leptons and $N_b = 0$ (QCD0b2, center) or $N_b \geq 1$ (QCD1b2, right). The lower pads show the ratios of observed to predicted event yields, and pre-fit systematic uncertainties are visualized as hatched bands.

Table 4.12: Thresholds of the binning choices in the QCD multijet transfer factor estimation.

$p_T(\ell)$ [GeV]	0, 45, 65, 80, 100, ≥120
$\lvert\eta(\ell)\rvert$	0, 1.479, 1.7, ≥2.1

Die approbierte gedruckte Originalversion dieser Dissertation ist an der TU Wien Bibliothek verfügbar.
The approved original version of this doctoral thesis is available in print at TU Wien Bibliothek.
TU Bibliothek Your knowledge hub WIEN

QCD multijet transfer factor corrections

The estimation of TFs is performed in the QCD0b2 or QCD1b2 regions, with selections of $N_j = 2$ and $N_\gamma = 0$. Thus, an implicit assumption is made that the extracted TFs are not depending on the jet or photon multiplicity. Simulated QCD multijet events are used to calculate simulation-based TFs in taking the ratio of event yields in tightly to loosely isolated lepton regions and study their multiplicity dependence. While the jet multiplicity dependence is found to be small for TF_{0b}, the dependence for TF_{1b} is nonnegligible. The comparison is shown in Fig. A.2 in Appendix A.1.2, inclusively in lepton kinematics, for data- and simulation-based TFs in the electron and muon channel.

Simulation-based corrections are applied to account for the jet multiplicity dependence in TF_{1b} values, where the extracted data-based TFs are corrected by the ratio of the simulation-based TFs in the given jet selection to the one calculated in the $N_j = 2$ selection. Simulation-based TFs in selections including photons are subject to large uncertainties, still in agreement with the data-based TFs and thus, no corrections for photon multiplicity dependencies are applied.

Validation of the QCD multijet background estimation

The QCD multijet estimation procedure is validated in regions with $N_j \geq 3$ without photon selections, the QCD0b3p and QCD1b3p regions, without and with selected b-tagged jets, respectively. The $p_T(\ell)$ and $\eta(\ell)$ distributions in the electron and muon channel are shown in Appendix A.1.3 in Fig. A.3 for QCD0b3p and in Fig. A.4 for QCD1b3p, where good agreement is found. Systematic uncertainties resulting from the QCD multijet estimation method are described in Sec. 4.5.

4.4.2 Nonprompt photon background

Events with a photon of hadronic origin, a hadronic fake, and a photon from PU events, combined denoted as nonprompt photon events, are estimated from data in exploiting differences in the shape of the observables $\sigma_{\eta\eta}(\gamma)$ and $I^{chg}(\gamma)$ to those of genuine photon events. Three sideband regions to the signal region are established in inverting one or both of the photon selection criteria on the two variables defined in Table 3.2, with $\sigma_{\eta\eta}(\gamma) \geq 0.011$ and $I^{chg}(\gamma) \geq 1.141\,\text{GeV}$ for the sideband regions. An illustration of the four regions is given in Fig. 4.11, where selections fulfilling the analysis selection criteria are denoted as "low" (Ls for low-$\sigma_{\eta\eta}(\gamma)$ and Lc for low-$I^{chg}(\gamma)$ regions), sideband selections are indicated as "high" (Hs for high-$\sigma_{\eta\eta}(\gamma)$ and Hc for high-$I^{chg}(\gamma)$ regions), and the region where both variables are within the analysis selection criteria (LsLc) is the signal region.

The LsHc sideband is used to estimate the nonprompt photon contribution in the signal region. In this region, the expected yields of genuine photon, misidentified electron, and QCD multijet events are subtracted from data to estimate the contribution of nonprompt photon events. A correction of the normalization, r_{SB}, is estimated from data in high-$\sigma_{\eta\eta}(\gamma)$ selections in the HsLc and HsHc regions, with low-$I^{chg}(\gamma)$ and high-$I^{chg}(\gamma)$ selections, respectively. The correction factor is obtained by taking the ratio of nonprompt photon events of these sideband regions, where again, these are estimated in subtracting prompt

Die approbierte gedruckte Originalversion dieser Dissertation ist an der TU Wien Bibliothek verfügbar.
The approved original version of this doctoral thesis is available in print at TU Wien Bibliothek.
TU Bibliothek Your knowledge hub WIEN

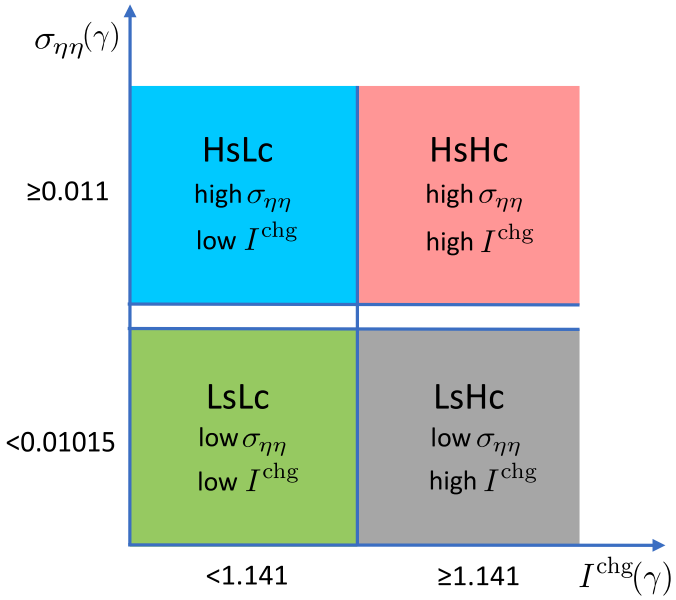

Figure 4.11: Illustration of the regions used in the nonprompt photon background estimation method with their selection criteria on the $I^{\mathrm{chg}}(\gamma)$ and $\sigma_{\eta\eta}(\gamma)$ observables.

photon events from data. The nonprompt photon background estimation is then obtained by multiplying the extracted yield in the LsHc region with r_{SB},

$$\text{nonprompt } \gamma \text{ est.} = \underbrace{\left(\text{data}_{\text{ LsHc}} - \sum \text{MC}^{\text{ prompt}}_{\text{ LsHc}}\right)}_{\text{nonprompt } \gamma \text{ est. in high } I^{\mathrm{chg}}(\gamma)} \times \underbrace{\frac{\text{data}_{\text{ HsLc}} - \sum \text{MC}^{\text{ prompt}}_{\text{ HsLc}}}{\text{data}_{\text{ HsHc}} - \sum \text{MC}^{\text{ prompt}}_{\text{ HsHc}}}}_{r_{\mathrm{SB}} \text{ normalization}} \tag{4.4.1}$$

The distributions of the $I^{\mathrm{chg}}(\gamma)$ (upper) and $\sigma_{\eta\eta}(\gamma)$ (lower) variables in sideband selections to the SR3p signal region for the combined electron and muon channel are shown in Fig. 4.12 for low-$\sigma_{\eta\eta}(\gamma)$ (upper left), high-$\sigma_{\eta\eta}(\gamma)$ (upper right), low-$I^{\mathrm{chg}}(\gamma)$ (lower left), and high-$I^{\mathrm{chg}}(\gamma)$ (lower right) selections. The figures show the nonprompt photon background dominated sideband regions, signal regions dominated by genuine photon events, and an increasing disagreement of observed and simulated events for high-$I^{\mathrm{chg}}(\gamma)$, the reason for the data-based background estimation approach. The dashed lines indicate the border of "low" and "high" selection regions and the hatched band represents pre-fit systematic uncertainties. The technique is performed separately in each bin of the signal region, lepton flavor, and jet multiplicity selection in the inclusive and the three differential measurements.

Correlation corrections

Weak correlations of the $\sigma_{\eta\eta}(\gamma)$ and $I^{\mathrm{chg}}(\gamma)$ variables lead to not fully independent sideband regions. Correlation effects are visualized in Fig. 4.13, showing the $\sigma_{\eta\eta}(\gamma)$ distribution of nonprompt photon events in the combined electron and muon channel gradually evolving with increasing $I^{\mathrm{chg}}(\gamma)$ values. To account for shape differences in the nonprompt photon background estimation method, a simulation-based correction factor κ^{MC} is calculated,

Die approbierte gedruckte Originalversion dieser Dissertation ist an der TU Wien Bibliothek verfügbar.
The approved original version of this doctoral thesis is available in print at TU Wien Bibliothek.
TU Bibliothek Your knowledge hub WIEN

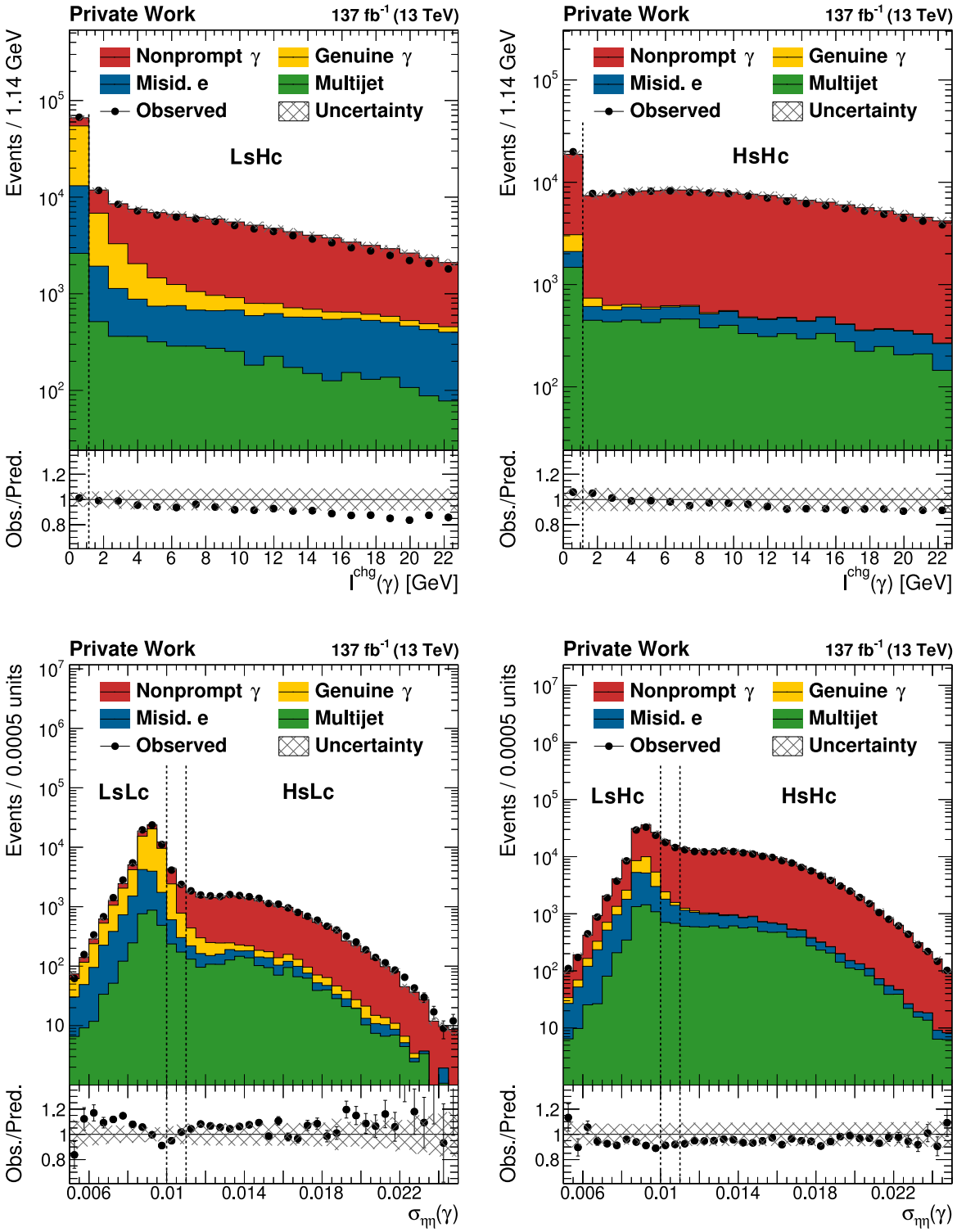

Figure 4.12: Distributions of $I^{\text{chg}}(\gamma)$ (upper) and $\sigma_{\eta\eta}(\gamma)$ (lower) observables for the low-$\sigma_{\eta\eta}(\gamma)$ (upper left), high-$\sigma_{\eta\eta}(\gamma)$ (upper right), low-$I^{\text{chg}}(\gamma)$ (lower left), and high-$I^{\text{chg}}(\gamma)$ (lower right) regions in the combined electron and muon channel. The dashed lines indicate the border of "low" and "high" selection regions. The ratio of observed to predicted event yields is shown in the lower panels and pre-fit systematic uncertainties are shown as hatched bands.

Die approbierte gedruckte Originalversion dieser Dissertation ist an der TU Wien Bibliothek verfügbar.
The approved original version of this doctoral thesis is available in print at TU Wien Bibliothek.
TU Bibliothek Your knowledge hub WIEN

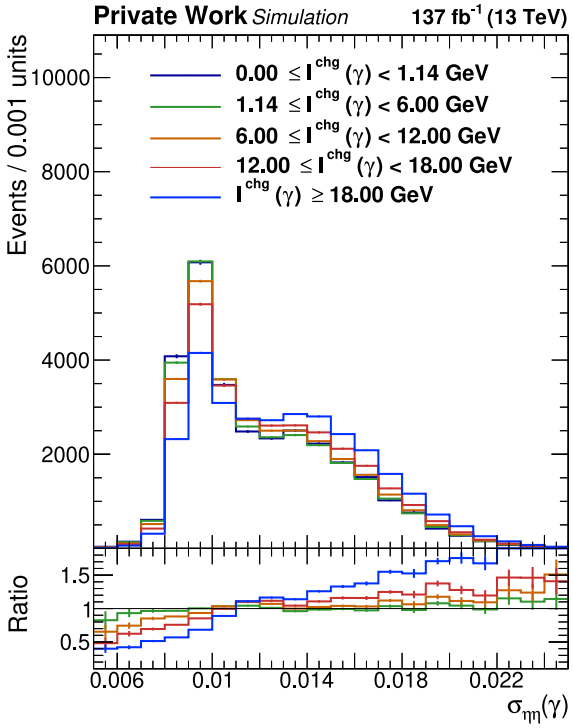

Figure 4.13: Comparison of the $\sigma_{\eta\eta}(\gamma)$ distribution shape in the combined electron and muon channel for the nonprompt photon category in various selections of $I^{\text{chg}}(\gamma)$. The shape difference is corrected for in the nonprompt photon background estimation by a simulation-based factor κ_{MC}.

where κ^{MC} is the double-ratio of r_{SB} to the corresponding value in low-$\sigma_{\eta\eta}(\gamma)$ selections,

$$\kappa_{\text{MC}} = \frac{\sum \text{MC}^{\text{nonprompt}}_{\text{LsLc}}}{\frac{\sum \text{MC}^{\text{nonprompt}}_{\text{LsHc}}}{\frac{\sum \text{MC}^{\text{nonprompt}}_{\text{HsLc}}}{\sum \text{MC}^{\text{nonprompt}}_{\text{HsHc}}}}}. \tag{4.4.2}$$

The correction factor is calculated for each signal region bin and additionally applied to the nonprompt photon estimation given in Eq. 4.4.1, where typical corrections amount to 18 %.

In Table 4.13, the normalization region yields and the prediction of the nonprompt photon background for the SR3p signal region in bins of $p_{\text{T}}(\gamma)$ are listed, combining lepton flavors and data-taking periods. The nonprompt photon contribution according to the simulation and the ratio of the data-driven prediction to the simulated yield are also shown. The uncertainties comprise the statistical uncertainties in the sideband and normalization region measurements, as well as statistical uncertainties in the simulated yields.

Die approbierte gedruckte Originalversion dieser Dissertation ist an der TU Wien Bibliothek verfügbar.
The approved original version of this doctoral thesis is available in print at TU Wien Bibliothek.

Table 4.13: Nonprompt photon contribution in the normalization region (second column) and predictions in the SR3p selection (third column) in bins of $p_T(\gamma)$, combining lepton flavors and data-taking periods. Comparisons to simulation (fourth column) and the ratio of predicted and simulated event yields (fifth column) are shown. Uncertainties comprise the statistical uncertainties in the sideband and normalization region measurements, as well as statistical uncertainties in the simulated yields.

$p_T(\gamma)$ [GeV]	Normalization region	Prediction	Simulation	Ratio
20–35	51155 ± 270	7936 ± 136	6871 ± 87	1.16 ± 0.02
35–50	16576 ± 156	2207 ± 66	2131 ± 30	1.04 ± 0.03
50–65	6925 ± 107	993 ± 43	935 ± 19	1.06 ± 0.05
65–80	3322 ± 76	465 ± 27	474 ± 12	0.98 ± 0.06
80–100	2353 ± 61	325 ± 25	300 ± 15	1.08 ± 0.10
100–120	1194 ± 46	141 ± 15	146 ± 8.1	0.96 ± 0.12
120–140	631 ± 31	90 ± 13	84 ± 5.6	1.07 ± 0.17
140–160	363 ± 27	33 ± 6.7	32 ± 2.5	1.02 ± 0.22
160–200	385 ± 28	40 ± 9.6	32 ± 3.7	1.25 ± 0.33
200–260	222 ± 22	26 ± 9.1	20 ± 3.2	1.35 ± 0.52
260–320	88 ± 16	7.3 ± 4.7	3.1 ± 0.7	2.33 ± 1.61
>320	83 ± 12	3.4 ± 2.5	4.9 ± 3.5	0.69 ± 0.71
Total	83295 ± 352	12267 ± 161	11033 ± 97	1.11 ± 0.02

4.4.3 Misidentified electron and Vγ backgrounds

Events with an electron misidentified as a photon are a dominating background source in the $t\bar{t}\gamma$ signal region. This background is measured in control regions without b-tagged jets in the electron channel and the additional requirement on the consistency of $m(e,\gamma)$ with the Z boson mass, $|m(e,\gamma) - m_Z| \leq 10\,\text{GeV}$. The control regions are defined in Sec. 4.3.1, with regions in the jet multiplicities of exactly three, or at least four jets, denoted as misDY3 and misDY4p, respectively, and the combined region misDY3p. These regions are enriched in Drell–Yan events with a Z boson decaying to two electrons, $Z \to e^+e^-$, where one electron is misidentified as a photon.

Even though Wγ and Zγ processes are subdominant in the signal region, they contribute to the control regions of the misidentified electron process. Thus, it is essential to measure their normalization, to account for effects on the measured misidentified electron normalization SFs. Zγ events with identified genuine photons are enriched in low-$m(\ell,\gamma)$ regions but can contribute significantly in regions close to the Z boson mass. In these events, the Z boson decays to two leptons, where a hard photon is radiated from one lepton, which is subsequently lost, resulting in $m(\ell,\gamma)$ values below or close to m_Z. The normalization of these events is measured in the LM3, LM4p, and LM3p control regions. Wγ events dominate the high-mass regions, where their normalization is measured in the HM3, HM4p, and HM3p control regions.

Die approbierte gedruckte Originalversion dieser Dissertation ist an der TU Wien Bibliothek verfügbar.
The approved original version of this doctoral thesis is available in print at TU Wien Bibliothek.
TU Bibliothek Your knowledge hub WIEN

Table 4.14: The extracted normalization scale factors for the misidentified electron background in the three data-taking periods and the $W\gamma$ and $Z\gamma$ backgrounds.

Scale factor	Value
Misidentified electrons (2016)	2.25 ± 0.29
Misidentified electrons (2017)	2.00 ± 0.27
Misidentified electrons (2018)	1.52 ± 0.17
$Z\gamma$ normalization	1.01 ± 0.10
$W\gamma$ normalization	1.13 ± 0.08

These regions are defined in the electron and muon channel, where the muon channel provides additional separation power of these processes. To account for an accurate description of the QCD multijet background in these regions, this background is estimated in the data-based way described in Sec. 4.4.1.

In the inclusive and differential $t\bar{t}\gamma$ cross section measurements, the control regions of the three and at least four jet selections, LM3, LM4p, HM3, HM4p, misDY3, and misDY4p, are added to the fitting setup described in Sec. 4.3.3, to measure the normalization SFs of misidentified electron, $W\gamma$, and $Z\gamma$ events in situ. For misidentified electron events, normalization SFs are extracted for each data-taking period to account for the replacement of the pixel detector in 2017 and changing operating conditions described in Sec. 3.2.3.

The stability of the procedure is assessed by fitting control regions only, where fits were performed for each data-taking period, separately and combined in the jet multiplicity selections. The extracted SFs in fits with separate jet multiplicity selections are found to agree within the uncertainties. The normalization SFs for the misidentified electron, $Z\gamma$, and $W\gamma$ backgrounds extracted in the nominal fit setup are given in Table 4.14. The $m(\ell, \gamma)$ distributions of these control regions, with the extracted normalization SFs applied are shown in Fig. 4.14 for the electron (left) and muon (right) channel.

Misidentified electron background $p_T(\gamma)$ dependence

Small dependencies in the misidentified electron normalization SFs on $p_T(\gamma)$ are accounted for in creating misidentified electron control regions in bins of the photon transverse momentum. The $p_T(\gamma)$ distributions in the misDY3p control regions are shown in Fig. 4.15 for 2016 (left), 2017 (center), and 2018 (right) data-taking periods, where a good agreement is found in 2016 and 2018, and small deviations in low-$p_T(\gamma)$ regions are found in 2017. Thus, the SFs are measured separately in $p_T(\gamma)$ bins, with regions separated by the thresholds defined in Sec. 4.3.3. Additionally, the ZG3, ZG4p, WG3, and WG4p regions are split in coarse $p_T(\gamma)$ bins to account for residual effects.

Validation of the misidentified electron background estimation

As mentioned before and shown in Table 4.7, events with a misidentified electron are a dominating background source in the signal region. These events originate from dileptonic $t\bar{t}$ events, where one W boson decays to an electron and a neutrino, and the electron is

Die approbierte gedruckte Originalversion dieser Dissertation ist an der TU Wien Bibliothek verfügbar.
The approved original version of this doctoral thesis is available in print at TU Wien Bibliothek.
TU Bibliothek Your knowledge hub WIEN

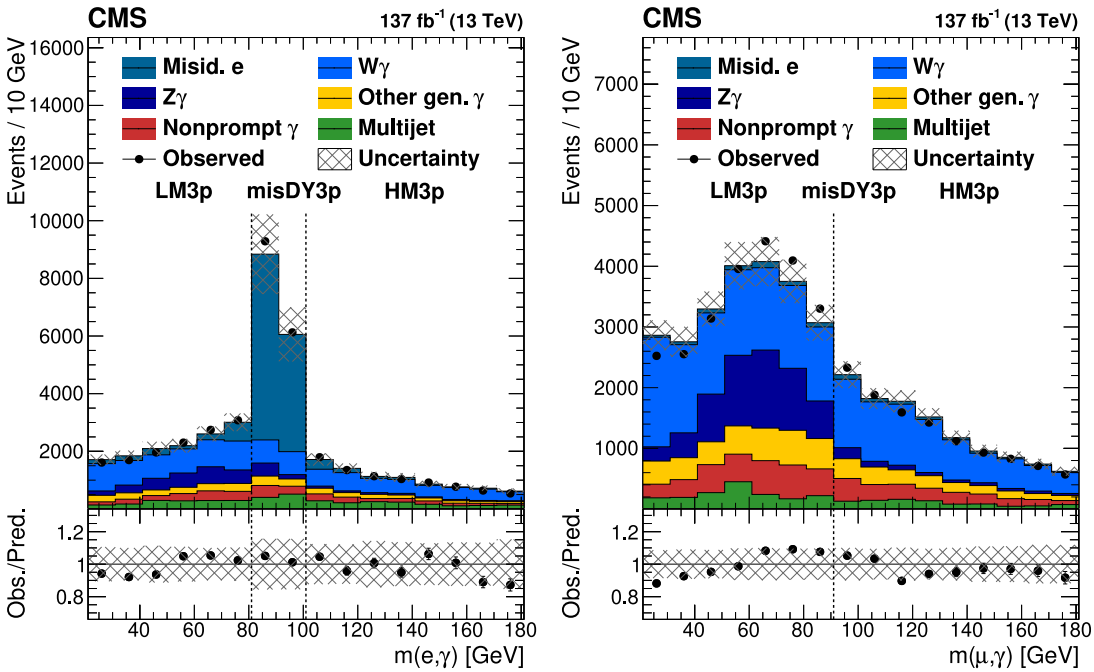

Figure 4.14: Invariant mass of the lepton and photon $m(\ell, \gamma)$ distributions for the electron (left) and muon (right) channel in the $N_j \geq 3$ and $N_b = 0$ selection. The contributions are grouped in event categories, where the genuine photon contributions of the Wγ and Zγ backgrounds are shown separately. The extracted normalization scale factors for the misidentified electron, Wγ, and Zγ backgrounds are applied to simulation. The ratio of observed to predicted event yields is shown in the lower panels and pre-fit systematic uncertainties are shown as hatched bands.

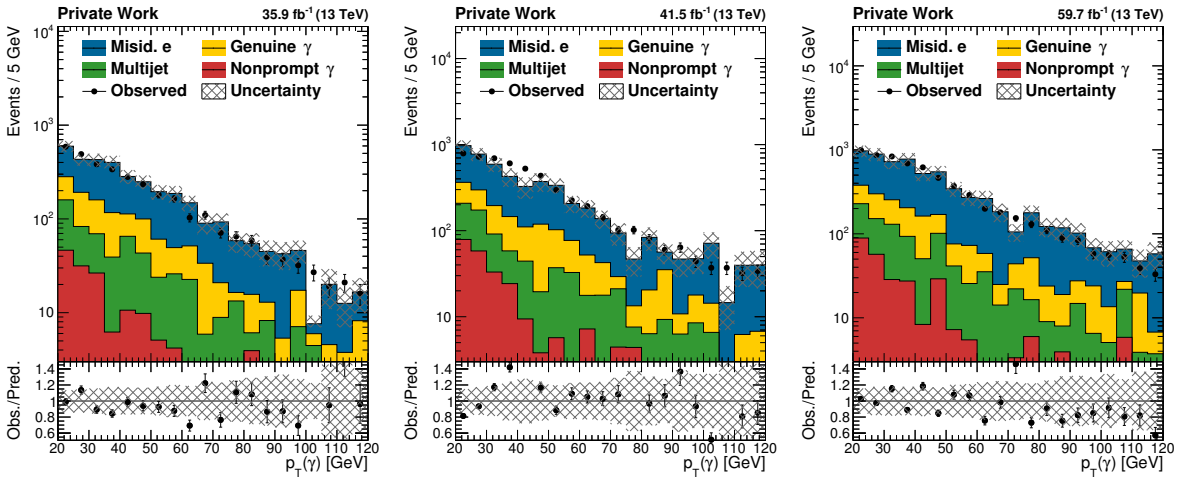

Figure 4.15: Distribution of $p_T(\gamma)$ in the misDY3p control region for the electron channel in 2016 (left), 2017 (center), and 2018 (right) data-taking periods. The extracted normalization scale factors for the misidentified electron, Wγ, and Zγ backgrounds are applied to simulation. The ratio of observed to predicted event yields is shown in the lower panels and pre-fit systematic uncertainties are shown as hatched bands.

Die approbierte gedruckte Originalversion dieser Dissertation ist an der TU Wien Bibliothek verfügbar.
The approved original version of this doctoral thesis is available in print at TU Wien Bibliothek.
TU Bibliothek Your knowledge hub WIEN

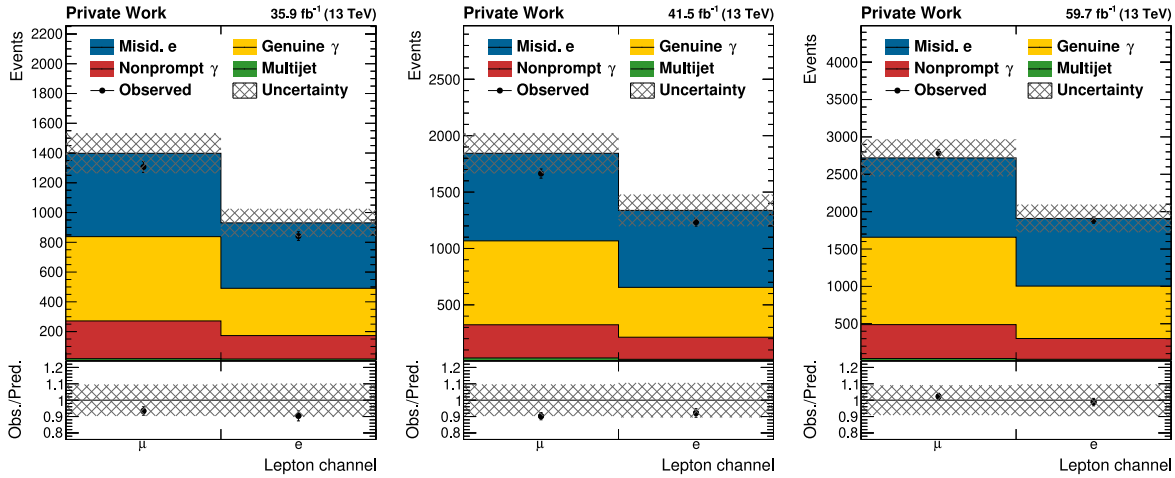

Figure 4.16: Event yields in the misTT2 validation region for the electron and muon channel in 2016 (left), 2017 (center), and 2018 (right) data-taking periods. The extracted normalization scale factors for the misidentified electron, Wγ, and Zγ backgrounds are applied to simulation. The ratio of observed to predicted event yields is shown in the lower panels and pre-fit systematic uncertainties are shown as hatched bands.

misidentified. To check that the in Drell–Yan events measured SFs are applicable in $t\bar{t}$ events, the misTT2 validation region defined in Sec. 4.3.1 is established. With a selection of exactly two jets, where both are identified as b jets, this region is dominated by $t\bar{t}$ events generated in the dileptonic decay channel and thus, contain a large fraction of misidentified electron events. The region is used to validate the extracted normalization SFs, where the event yields for both lepton channels are shown in Fig. 4.16 for 2016 (left), 2017 (center), and 2018 (right) data-taking periods. The extracted normalization SFs for the misidentified electron, Wγ, and Zγ backgrounds are applied to simulation. A good agreement is found in both lepton channels, where deviations of up to 10 % are accounted for in additional uncertainties described in Sec. 4.5.

4.4.4 Other genuine photon backgrounds

Backgrounds from processes with a genuine photon other than the Wγ and Zγ processes only marginally contribute to the signal regions. Processes, such as single top quark productions including a genuine photon, e.g., tγ and tWγ, but also $t\bar{t}$Z, $t\bar{t}$W, tZq, and dibosons, are estimated from simulation, with the cross section normalization calculated at the highest precision available. Additional uncertainties are applied to the event yields in signal and control regions, where details are described in Sec. 4.5.

Die approbierte gedruckte Originalversion dieser Dissertation ist an der TU Wien Bibliothek verfügbar.
The approved original version of this doctoral thesis is available in print at TU Wien Bibliothek.
TU Bibliothek Your knowledge hub WIEN

4.5 Systematic uncertainties

Three groups of systematic uncertainties are considered in the measurement of the $t\bar{t}\gamma$ cross sections. Experimental systematic uncertainties are assigned due to uncertainties in the object and event selection and object calibrations described in Sec. 4.2.3, and the measurement of the integrated luminosity in each data-taking period. Uncertainties in the modeling of $t\bar{t}\gamma$ signal events, e.g., the modeling of the parton shower, hadronization, or the underlying event, described in Sec. 2.1.3, are grouped in theoretical uncertainties. Additionally, uncertainties in the background estimation methods described in Sec. 4.4 are assigned to predicted background event yields.

A detailed description of the assigned uncertainties is given in the following, with a summary given in Table 4.15. The table shows the uncertainty sources in the first column, the correlation treatment of assigned uncertainties among the data-taking periods in the second column, ranges of event yield variations in the third column, and the resulting impact in the inclusive cross section measurement in the fourth column. The resulting systematic, statistical, and total uncertainties in the inclusive cross section measurement given in Sec. 4.6.1 are shown at the bottom of the table. Due to correlations, the quadratic sum of single uncertainty sources is larger than the total systematic uncertainty.

4.5.1 Experimental uncertainties

Integrated luminosity measurement

The individual integrated luminosities are known within uncertainties of 2.5 [251], 2.3 [252], and 2.5 % [253] for 2016, 2017, and 2018 data-taking periods, respectively. These uncertainties are assigned to the measurement in the respective data-taking period, resulting in a total uncertainty in the integrated luminosity of 1.8 %, where the improvement reflects the correlation of systematic effects.

Pileup reweighting

For assessing the uncertainty on the PU-reweighting procedure, the PU profile is estimated from data assuming a total inelastic pp cross section of 69.2 mb [272, 273]. A variation of 4.6 % on the cross section affects the PU-reweighting method and is used to estimate the uncertainty. Assigned uncertainties are fully correlated among the data-taking periods, with resulting variations of simulated event yields of up to 2 % in the inclusive cross section measurement. The uncertainty in the $t\bar{t}\gamma$ cross section from this source is found to be below 0.5 %.

Trigger and lepton identification efficiencies

Uncertainties in derived SFs applied to simulation to match the trigger selection efficiencies in data for single-electron [243] and single-muon [239, 275] triggers are propagated to the expected event yields. A yield variation of up to 0.5 % leads to an uncertainty of lower than 0.5 % in the inclusive cross section measurement.

Die approbierte gedruckte Originalversion dieser Dissertation ist an der TU Wien Bibliothek verfügbar.
The approved original version of this doctoral thesis is available in print at TU Wien Bibliothek.
TU Bibliothek Your knowledge hub WIEN

Table 4.15: Breakdown of the uncertainties in its components. The table shows the source (first column), the correlations between the data-taking periods (second column), typical pre-fit uncertainty ranges (third column), and the corresponding uncertainty in the cross section measurement (fourth column) from the profile likelihood fit.

	Source	Correlation	Uncertainty [%]	
			yield	$\sigma(t\bar{t}\gamma)$
Experimental	Integrated luminosity	partial	2.3–2.5	1.8
	Pileup	100%	0.5–2.0	<0.5
	Trigger efficiency	–	<0.5	<0.5
	Electron reconstruction and identification	100%	0.2–1.7	<0.5
	Muon reconstruction and identification	partial	0.5–0.7	0.7
	Photon reconstruction and identification	100%	0.4–1.4	1.1
	p_T(e) and $p_T(\gamma)$ reconstruction	100%	0.1–1.2	<0.5
	JES	partial	1.0–4.1	1.9
	JER	–	0.4–1.6	0.6
	b tagging	100% (2017/2018)	0.8–1.6	1.1
	L1 prefiring	100% (2016/2017)	0.3–0.9	<0.5
Theoretical	Underlying event	100%	0.1–1.9	<0.5
	Color reconnection	100%	0.4–3.6	<0.5
	ISR/FSR	100%	1.0–5.6	1.9
	PDF	100%	<0.5	<0.5
	ME scales μ_R, μ_F	100%	0.4–4.7	<0.5
Background	QCD multijet normalization	100%	1.3–6.5	0.9
	Nonprompt photon background	100%	1.2–2.7	1.8
	Misidentified e	–	2.5–8.0	1.8
	$Z\gamma$ normalization	100%	0.6–2.5	0.5
	$W\gamma$ normalization	100%	1.0–3.5	2.3
	DY normalization	100%	0.1–1.1	1.0
	$t/t\bar{t}$ normalization	100%	1.0–1.9	0.8
	$tW\gamma$ modeling	100%	1.6–4.4	1.6
	"Other" bkg. normalization	100%	0.3–1.0	<0.5
	Total systematic uncertainty			6.0
	Statistical uncertainty			0.9
	Total			6.0

Die approbierte gedruckte Originalversion dieser Dissertation ist an der TU Wien Bibliothek verfügbar.
The approved original version of this doctoral thesis is available in print at TU Wien Bibliothek.
TU Bibliothek Your knowledge hub WIEN

Similarly, the variation of efficiency SFs for electron (muon) identification and reconstruction lead to a variation of the expected event yields of 0.2–1.7 (0.5–0.7)% and an impact on the inclusive cross section measurement of below 0.5 (0.7)%. An additional uncertainty of 0.5 % is applied to signal region event yields in the muon channel to account for deviations of SFs extracted in Drell–Yan events but applied to other processes such as $t\bar{t}$ and $t\bar{t}\gamma$.

Uncertainties as a result of trigger efficiency measurements and statistical uncertainties in the muon identification efficiency measurements are treated uncorrelated among the data-taking periods, while systematic uncertainties in the latter and uncertainties in electron identification efficiency measurements are treated correlated.

Photon identification efficiencies

Uncertainties in the photon identification are derived by a combination of uncertainties in the identification efficiency SFs and the veto on events with pixel detector seeds. The former are a function of $p_T(\gamma)$ and $\eta(\gamma)$, where for the ECAL barrel regions shown in Fig. 4.4 (right), the energy resolution is in the range of 0.2–2.5 % in low-p_T regions, increasing to 3.2 % for $p_T(\gamma) > 200\,\text{GeV}$ in the 2016 data-taking period. Dedicated measurements of high-p_T photon SFs [276] in the 2017–2018 data-taking periods allow to reduce the uncertainty in photon identifications at $p_T(\gamma) > 200\,\text{GeV}$ to 2 %.

Uncertainties in derived SFs to match the simulated pixel detector seed veto efficiencies to data are measured inclusively in $p_T(\gamma)$ in the 2016 and 2017 data-taking periods and as a function of $p_T(\gamma)$ in 2018, where the latter is shown in Fig. 4.5 (right). The variation leads to a 1.0 (0.4)% uncertainty in the expected event yields in 2016 (2017) and are found within 0.1–1.3 % in 2018.

A total variation of event yields in the inclusive cross section measurement is found to be 0.4–1.4 %, where uncertainties are correlated among the data-taking periods and lead to an impact on the measurement of 1.1 %.

Electron and photon energy scale corrections

Uncertainties in the energy scale of ECAL objects, electrons or photons, are estimated in simultaneously rescaling the electron and photon momenta in simulation as a function of p_T and η. The variations are found to be minor, with effects on the event yields of 0.1–1.2 % and a cross section impact of lower than 0.5 %. The assigned uncertainties are treated correlated among the data-taking periods.

Jet and b-tagged jet corrections

Uncertainties in the jet energy scale (JES) are estimated in rescaling the jet momenta in simulation as a function of the jet p_T and η. The variations are found within 2–6 % [278], resulting in variations of the event yields of 1.0–4.1 % and an impact on the inclusive $t\bar{t}\gamma$ cross section measurement of 1.9 %. JES uncertainties are split in sources, where parts are treated correlated among the data-taking periods. Dominant components originate from

Die approbierte gedruckte Originalversion dieser Dissertation ist an der TU Wien Bibliothek verfügbar.
The approved original version of this doctoral thesis is available in print at TU Wien Bibliothek.
TU Bibliothek Your knowledge hub WIEN

uncertainties in the Drell–Yan and dijet jet-flavor composition (JES–FlavorQCD) and the JES absolute scale (JES–Absolute) [278].

The same technique is used to estimate the uncertainties in the jet energy resolution (JER). JER uncertainties are treated uncorrelated among the data-taking periods, affecting the event yields by 0.4–1.6 %, with an impact on the measurement of 0.6 %.

Jets are corrected to match the b-jet identification efficiencies and misidentification probability of gluon, light quark, or charm quark jets as b jets in data. Systematic uncertainties are estimated from variations of the assigned SFs for correctly and incorrectly identified jets and are propagated to the event yields in the measurement. Uncertainties for corrections of b-jet identification efficiencies and misidentification rates lead to variations of 0.8–1.6 % of the event yields. The uncertainty is treated correlated in 2017–2018 data-taking periods and results in an impact on the cross section measurement of 1.1 %.

L1 prefiring corrections

Corrections of L1 prefiring conditions lead to an additional correlated uncertainty in the measurement applied to 2016–2017 data-taking periods. A systematic variation of 20 % on the corrections for affected objects results in a variation of the event yields of 0.3–0.9 %, with an impact on the measurement of lower than 0.5 %.

4.5.2 Theoretical uncertainties

Renormalization and factorization scales at matrix-element level

Modeling uncertainties arise from the choice of the μ_R and μ_F scales in the modeling of (non)perturbative QCD effects in the ME. Uncertainties are estimated in varying the scale choice in the event generator independently by a factor of 2, where the case of scaling one up and one down is ignored. Two independent nuisance parameters describe the uncertainty in the choice of μ_R and μ_F, which leads to a variation of the signal event yields of 0.4–4.7 %. A test with one nuisance parameter describing the envelope of uncertainties in the choice of μ_R and μ_F leads to a negligible difference. As the same event generator and parton showering algorithm is used in the signal simulation for each data-taking period, the uncertainty is treated correlated, and the impact on the inclusive cross section measurement is found to be lower than 0.5 %.

Parton distribution functions

Acceptance effects from the choice of the PDF sets are assessed in estimating the predicted event yield in each bin with 100 replicas of the used NNPDF PDF sets. The procedure includes the estimation for each replica set, where an envelope of the event yield variations is used as uncertainty. Effects on the signal event yields from PDF choices are found to be lower than 0.5 %, where the correlated uncertainty has a similar impact of lower than 0.5 % on the cross section measurement.

Die approbierte gedruckte Originalversion dieser Dissertation ist an der TU Wien Bibliothek verfügbar.
The approved original version of this doctoral thesis is available in print at TU Wien Bibliothek.
TU Bibliothek Your knowledge hub WIEN

Initial- and final-state radiation

Additional uncertainties arise from the chosen α_s value in the parton showering. The uncertainty is estimated in varying μ_R for QCD emissions in initial- and final-state radiations, denoted as ISR and FSR, respectively, which is effectively varying α_s. Values are varied by a factor of 2, with an effect on the signal event yields of 1.0–5.6 %. Uncertainties are treated correlated among the data-taking periods, resulting in an impact on the cross section measurement of 1.9 %.

Color reconnection

The parton showering of the signal simulation uses Pythia 8 with its default configuration, including a color reconnection model of multiple-parton interactions without early resonance decays. Uncertainties from the Pythia 8 configuration are assessed in estimating the event yields with signal simulations and parton showering, including early resonance decays and Pythia 8 configurations using a gluon-move [287] and a QCD-inspired [288] scheme. These parton showering models are affecting the signal event yields by 0.4–3.6 %. The uncertainty is treated correlated among the data-taking periods, with an impact on the $t\bar{t}\gamma$ cross section of less than 0.5 %.

Underlying event

Variations of the parton showering tune settings allow for estimating an uncertainty on the underlying event [94]. Event yields are extracted with signal simulations using parton showering with varied tune settings, where an effect of 0.1–1.9 % is found. The uncertainty is treated correlated among the data-taking periods, with an impact on the cross section of lower than 0.5 %.

Statistical uncertainties in simulation

The Barlow–Beeston approach [289] is used to account for statistical uncertainties in simulated event yields above a threshold of 20 events. Below, individual Poissonian nuisances are included separately for each signal and background component. Dedicated simulated events in high-$p_T(\gamma)$ regions described in Sec. 4.1.2 allow for reducing the statistical uncertainties in signal simulation, even in differential measurements. Statistical uncertainties from simulation in the nonprompt photon background estimation method are propagated through the data-based estimation procedure and added in the corresponding bin.

4.5.3 Background estimation uncertainties

QCD multijet background estimation

The QCD multijet background is a negligible background in the signal regions, however, it is significant in control regions. Large uncertainties are applied to account for possible

Die approbierte gedruckte Originalversion dieser Dissertation ist an der TU Wien Bibliothek verfügbar.
The approved original version of this doctoral thesis is available in print at TU Wien Bibliothek.
TU Bibliothek Your knowledge hub WIEN

mismodeling in the data-based estimation method. This includes extrapolation uncertainties from the TFs estimated in regions with two jets and without photons to regions with large jet multiplicities and a well-identified photon.

A systematic uncertainty of 50 % is assigned to the QCD multijet background yields, separately for signal and control regions to account for differences in the method for $N_b = 0$ and $N_b \geq 1$ regions. An additional uncertainty of 20 % is assigned to event yields in $N_j \geq 4$ regions, separately for signal and control regions, accounting for potential mismodeling of the jet multiplicity. No other systematic uncertainties are applied to QCD multijet event yields.

The assigned uncertainties are treated correlated among the data-taking periods and lead to a variation of background event yields of 1.3–6.5 %. The impact on the $t\bar{t}\gamma$ cross section of 0.9 % is the result of correlations with uncertainties in the misidentified electron background estimation in control regions.

Nonprompt photon background estimation

Uncertainties in the data-based nonprompt photon background estimation method are estimated from shape comparisons in the sideband regions used in the procedure. A good agreement in all distributions is found, and a systematic uncertainty of 5 % is assigned to the event yields of the nonprompt photon background. In the 2017 data-taking period in selections with $N_j \geq 4$ in the electron channel, an additional uncertainty of 20 % accounts for mismodeling of the $\sigma_{\eta\eta}$ shape in sideband regions, potentially affecting the estimation method.

Uncertainties are treated correlated and lead to a background event yield variation of 1.2–2.7 %, adding an uncertainty of 1.8 % in the cross section measurement.

Misidentified electron and Vγ background normalizations

The normalization of yields with a misidentified electron and event yields of the Wγ and Zγ processes are estimated in control regions. While the normalization of misidentified electron and Wγ events are left floating in the fit, a systematic uncertainty of 30 % is assigned to Zγ event yields. Additional uncertainties of 40 (20)% in $N_j \geq 4$ regions for the Zγ (Wγ and misidentified electron) background account for mismodeling of the jet multiplicity. To measure the $p_T(\gamma)$ dependence of the processes, an additional uncertainty of 40 (20)% is assigned to the misidentified electron (Wγ and Zγ) processes in each $p_T(\gamma)$ bin in the control regions defined in Sec. 4.3.1.

A systematic uncertainty of 10 % is applied to misidentified electron event yields in signal regions to account for extrapolation effects on SFs extracted in Drell–Yan, but applied $t\bar{t}$ events. The latter is the result of the validation of the background estimation method shown in Fig. 4.16.

The uncertainties lead to variations of the background event yields of 2.5–8.0 , 1.0–3.5 , and 0.6–2.5 % for misidentified electron, Wγ, and Zγ processes, respectively. Uncertainties in misidentified electron event yields are treated uncorrelated in the data-taking periods to account for variations in pixel detector operation conditions described in Sec. 3.2.3.

Die approbierte gedruckte Originalversion dieser Dissertation ist an der TU Wien Bibliothek verfügbar.
The approved original version of this doctoral thesis is available in print at TU Wien Bibliothek.
TU Bibliothek Your knowledge hub WIEN

Uncertainties in Wγ and Zγ processes are treated correlated. An impact on the $t\bar{t}\gamma$ cross section measurement of 1.8, 2.3, and 0.5 % is measured for the contributions of misidentified electron, Wγ, and Zγ processes.

Vγ+heavy flavor

The Wγ and Zγ normalization SFs are measured in the control regions without b-tagged jets, however, the signal regions require the presence of at least one b-tagged jet. The applied uncertainties in the b tagging SF cover the component of these processes that enter the signal with N_b requirements via a light jet that is misidentified as a b-tagged jet. An additional systematic uncertainty is attributed to the Wγ and Zγ processes with heavy-flavor jets, where the latter originates from gluon splitting, a collective term for producing heavy-flavor quark pairs.

The uncertainty is assessed in splitting the Wγ and Zγ processes according to the presence of particle-level b jets. The reconstructed b-tagged jet multiplicity distributions for Wγ (left) and Zγ (right) are shown in Fig. 4.17. A fraction of 20 (60)% for Wγ (Zγ) in reconstructed b-tagged regions are generated with a b parton. An additional correlated uncertainty of 20 % is assigned to this contribution in the signal regions, resulting in a variation of 4 (12)% in the Wγ (Zγ) event yields.

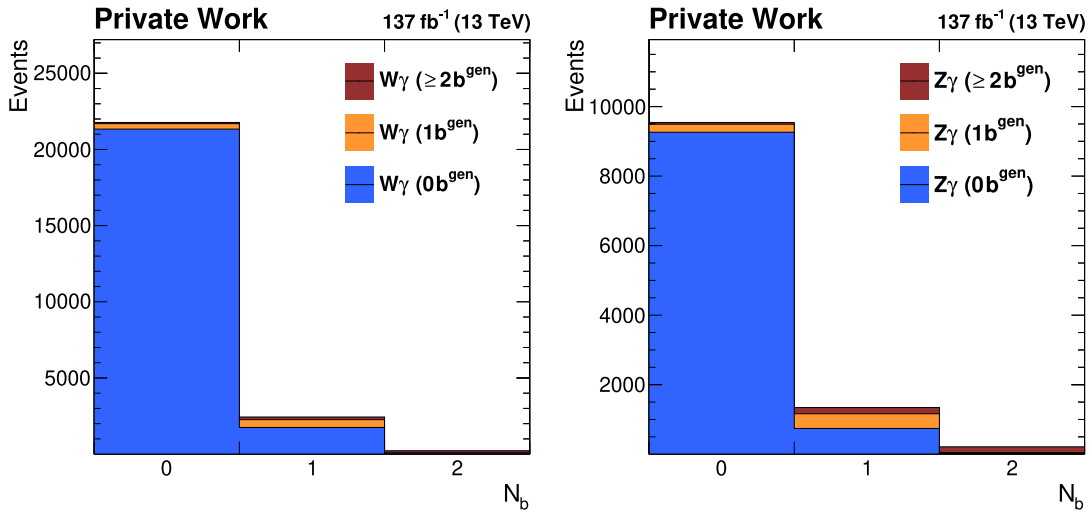

Figure 4.17: Distribution of the reconstructed b-tagged jet multiplicity of the Wγ (left) and Zγ (right) processes split according to the presence of particle-level b jets.

tWγ modeling

The tWγ background is simulated in tW events at NLO in QCD precision using the POWHEG v2.0 event generator and the cross section is calculated at NNLO precision. The background component amounts to less than 3.3 % of the total events in the SR3 and SR4p signal regions. Uncertainties in the tWγ modeling are estimated as the difference of the nominal prediction and a prediction obtained from tWγ simulations at LO in QCD precision using the MADGRAPH5_aMC@NLO event generator. Deviations in the

Die approbierte gedruckte Originalversion dieser Dissertation ist an der TU Wien Bibliothek verfügbar.
The approved original version of this doctoral thesis is available in print at TU Wien Bibliothek.
TU Bibliothek Your knowledge hub WIEN

distributions are less than 44 (30)% in the $p_T(\gamma)$ bins, less than 34 (27)% in the $|\eta(\gamma)|$ bins, and less than 19 (17)% in the $\Delta R(\ell, \gamma)$ bins. The variations affect the event yields in the range of 1.6–4.4 % and lead to an uncertainty in the inclusive cross section measurement of 1.6 %.

Other background normalizations

Additional uncertainties are applied to background components based on predictions from simulation, reflecting the measured cross section uncertainties of the processes. These uncertainties are treated correlated among the data-taking periods. An uncertainty of 8 % is assigned to Drell–Yan event yields, leading to background yield variations of 0.1–1.1 % and an impact in the cross section measurement of 1 % as a result of correlations with uncertainties assigned to the misidentified electron background component. 5 % uncertainty in the $t/t\bar{t}$ normalization reflects the uncertainties described in Sec. 2.2, resulting in background event yield variations of 1.0–1.9 %. This uncertainty adds to the cross section measurement with an impact of 1 %. An uncertainty of 30 % is assigned to genuine photon events in the "other" background category to account for possible cross section effects. This background is found to be negligible in signal regions, where the uncertainty results in a background yield variation of 0.3–1.0 % and an impact on the measurement of lower than 0.5 %.

4.6 Results

The strategy to measure the inclusive and differential $t\bar{t}\gamma$ cross sections is to select events with exactly one electron or muon, one highly energetic photon, and high jet and b-jet multiplicities, with their object selection criteria given in Sec. 4.2.2. Control regions described in Sec. 4.3.1 are established to select events enriched in background processes and extract their normalization from data. Other background processes, such as the QCD multijet and nonprompt photon backgrounds, are estimated in data-based ways and are further discussed in Sec. 4.4. Three groups of experimental, theoretical, and background modeling systematic uncertainties are considered, with the description of the underlying sources given in Sec. 4.5. These uncertainty sources are further used as nuisance parameters in a profile likelihood fit described in Sec. 4.3.3 to extract the inclusive and differential $t\bar{t}\gamma$ cross sections. The measured differential distributions of $p_T(\gamma)$, $|\eta(\gamma)|$, and $\Delta R(\ell, \gamma)$ are unfolded to the particle level, with the unfolding procedure described in Sec. 4.3.3. In the following, the results of the inclusive and differential cross section measurements are discussed.

4.6.1 Inclusive cross section measurement

The inclusive $t\bar{t}\gamma$ cross section is measured in signal and control regions in bins of the lepton flavor, with bins for three and at least four jet selections, where control regions are additionally binned in $p_T(\gamma)$ and signal regions are additionally binned in the three-jet invariant mass M_3 variable. The predicted event yields for signal and background processes, and the observation in the LM3, LM4p, HM3, HM4p, misDY3, and misDY4p control

Die approbierte gedruckte Originalversion dieser Dissertation ist an der TU Wien Bibliothek verfügbar.
The approved original version of this doctoral thesis is available in print at TU Wien Bibliothek.
TU Bibliothek Your knowledge hub WIEN

regions as a result of the profile likelihood fit are shown in Fig. 4.18. The corresponding result of predicted and observed event yields for the SR3 and SR4p signal regions is shown in Fig. 4.19. Table 4.16 shows the predicted number of events in each signal and background component and the observed number of events in the e and μ channels for the SR3 and SR4p signal regions. The data is in good agreement with predictions in all bins of the signal and control regions.

The measured inclusive cross section in the combined lepton flavor and jet multiplicity channel in the fiducial phase space defined in Sec. 4.3.2 is found to be

$$\sigma(t\bar{t}\gamma) = 798 \pm 7\ (\text{stat}) \pm 48\ (\text{syst})\ \text{fb}, \tag{4.6.1}$$

in good agreement with the SM prediction of $\sigma^{\text{NLO}}(t\bar{t}\gamma) = 773 \pm 135\,\text{fb}$ at NLO in QCD precision, extracted from simulation using the MadGraph5_aMC@NLO event generator and Pythia 8 for hadronization and parton showering. Inclusive cross section predictions using Herwig++ (Herwig 7) are found to be 8.3 (5.4)% lower compared to simulations using Pythia 8, with the simulation setup described in Sec. 4.1.2.

The signal strength modifier is measured to be

$$r = 1.032 \pm 0.009\ (\text{stat}) \pm 0.062\ (\text{syst}), \tag{4.6.2}$$

with a measured total uncertainty of 6.0 % in the inclusive $t\bar{t}\gamma$ cross section. Binning the signal regions in the M_3 variable reduces the uncertainty in backgrounds without hadronically decaying top quark, e.g., the $W\gamma$, $Z\gamma$, and misidentified electron background. The binning reduces the total systematic uncertainty in the inclusive $t\bar{t}\gamma$ cross section measurement from 6.7 to 6.0 %.

A similar good agreement with SM predictions is found for cross section measurements in $N_j = 3$ and ≥ 4 selections, separately in the electron and muon channel. A summary of the extracted signal strength modifier values, with their total, statistical, and systematic uncertainties is shown in Fig. 4.20. Uncertainties from theory calculations dominate, with dedicated calculations in the $t\bar{t}\gamma$ single-lepton selection needed to improve the comparison of measurements and predictions.

Table 4.16: Predicted event yields and total post-fit uncertainties for the signal and background components and observed events in the electron and muon channels for the SR3 and SR4p signal regions.

Process	SR3		SR4p	
	e	μ	e	μ
$t\bar{t}\gamma$	4995 ± 168	7821 ± 251	6174 ± 192	9495 ± 280
Misid. e	3710 ± 200	3322 ± 220	1904 ± 134	2015 ± 153
Nonprompt γ	2621 ± 107	4077 ± 161	2315 ± 124	3580 ± 149
Other	1136 ± 102	1866 ± 159	857 ± 110	1360 ± 166
$W\gamma$	1082 ± 77	1486 ± 108	585 ± 48	864 ± 74
QCD multijet	560 ± 104	762 ± 140	302 ± 65	472 ± 102
$Z\gamma$	356 ± 38	640 ± 68	189 ± 25	306 ± 40
Total	14459 ± 178	19976 ± 196	12326 ± 150	18093 ± 173
Observed	14479	19885	12305	18184

Die approbierte gedruckte Originalversion dieser Dissertation ist an der TU Wien Bibliothek verfügbar.
The approved original version of this doctoral thesis is available in print at TU Wien Bibliothek.
TU Bibliothek Your knowledge hub WIEN

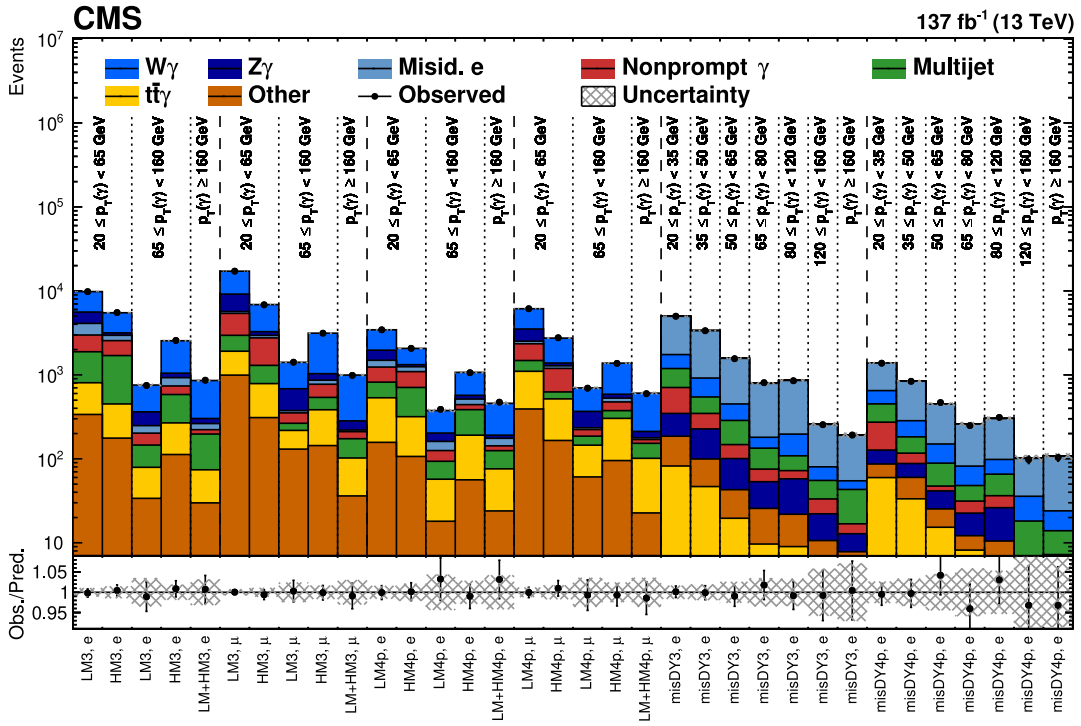

Figure 4.18: Observed and predicted yields in the LM3, HM3, LM4p, HM4p, misDY3, and misDY4p control regions in bins of $p_T(\gamma)$. The lower pad shows the ratio of observed to predicted event yields and systematic uncertainties are visualized as a hatched band.

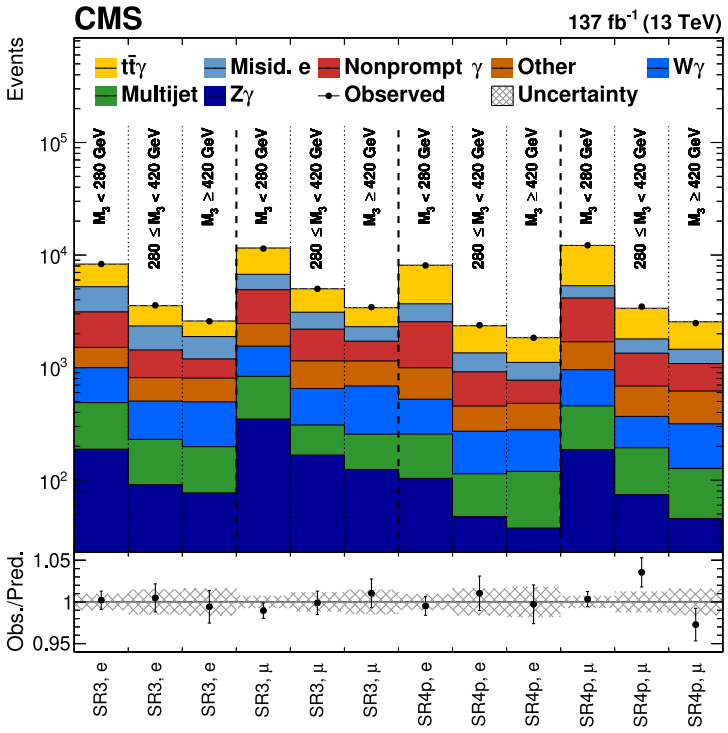

Figure 4.19: Observed and predicted yields in the SR3 and SR4p signal regions in bins of the three-jet invariant mass M_3. The lower pad shows the ratio of observed to predicted event yields and systematic uncertainties are visualized as a hatched band.

Die approbierte gedruckte Originalversion dieser Dissertation ist an der TU Wien Bibliothek verfügbar.
The approved original version of this doctoral thesis is available in print at TU Wien Bibliothek.

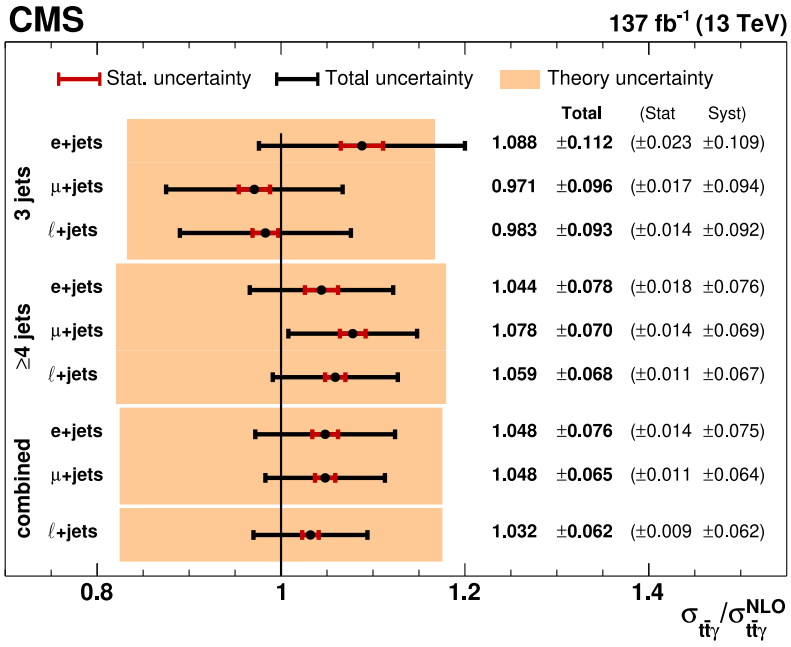

Figure 4.20: Ratios of the measured $t\bar{t}\gamma$ cross sections to predictions for measurements in the $N_j = 3$ (upper), $N_j \geq 4$ (center), and the combination (lower) for the electron, muon, and the combined single-lepton channels. The orange band indicates uncertainties originating from theory predictions.

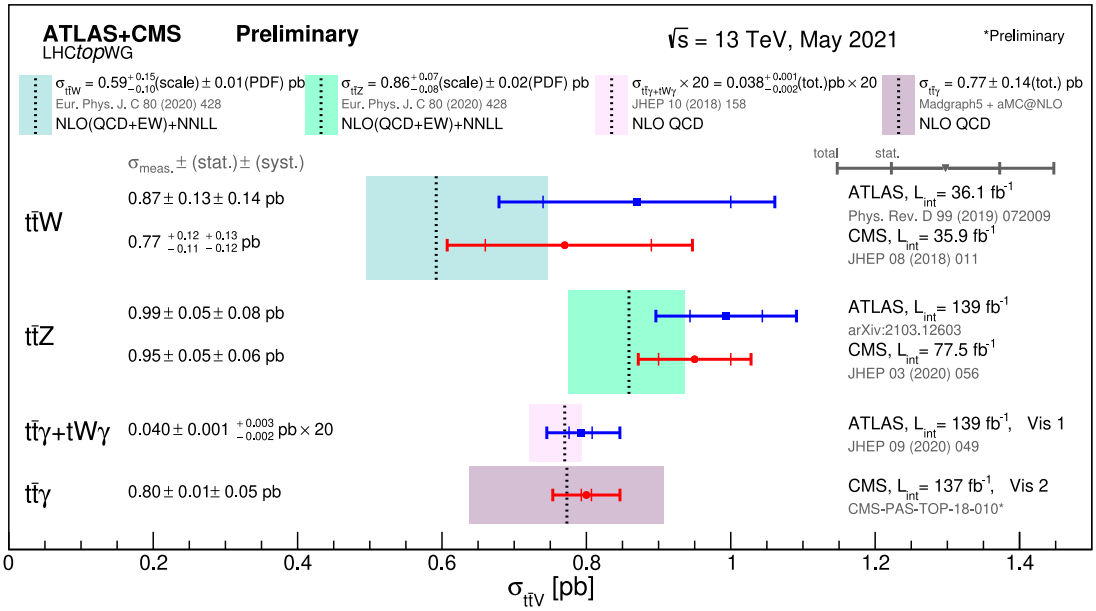

Figure 4.21: Summary of the $t\bar{t}X$ (X = W, Z, or γ) cross section measurements of the CMS and ATLAS collaborations compared to predictions at NLO in QCD precision. "Vis 1" ("Vis 2") highlight the difference in the relevant phase spaces in the $t\bar{t}\gamma$ measurements of ATLAS (CMS). The result of the ATLAS $t\bar{t}\gamma + tW\gamma$ measurement is scaled by a factor of 20 for visualization on the same scale. The figure shows preliminary results, which mildly deviate from the measured cross section presented in this thesis. Figure taken from Ref. [98].

Die approbierte gedruckte Originalversion dieser Dissertation ist an der TU Wien Bibliothek verfügbar.
The approved original version of this doctoral thesis is available in print at TU Wien Bibliothek.
TU Bibliothek Your knowledge hub WIEN

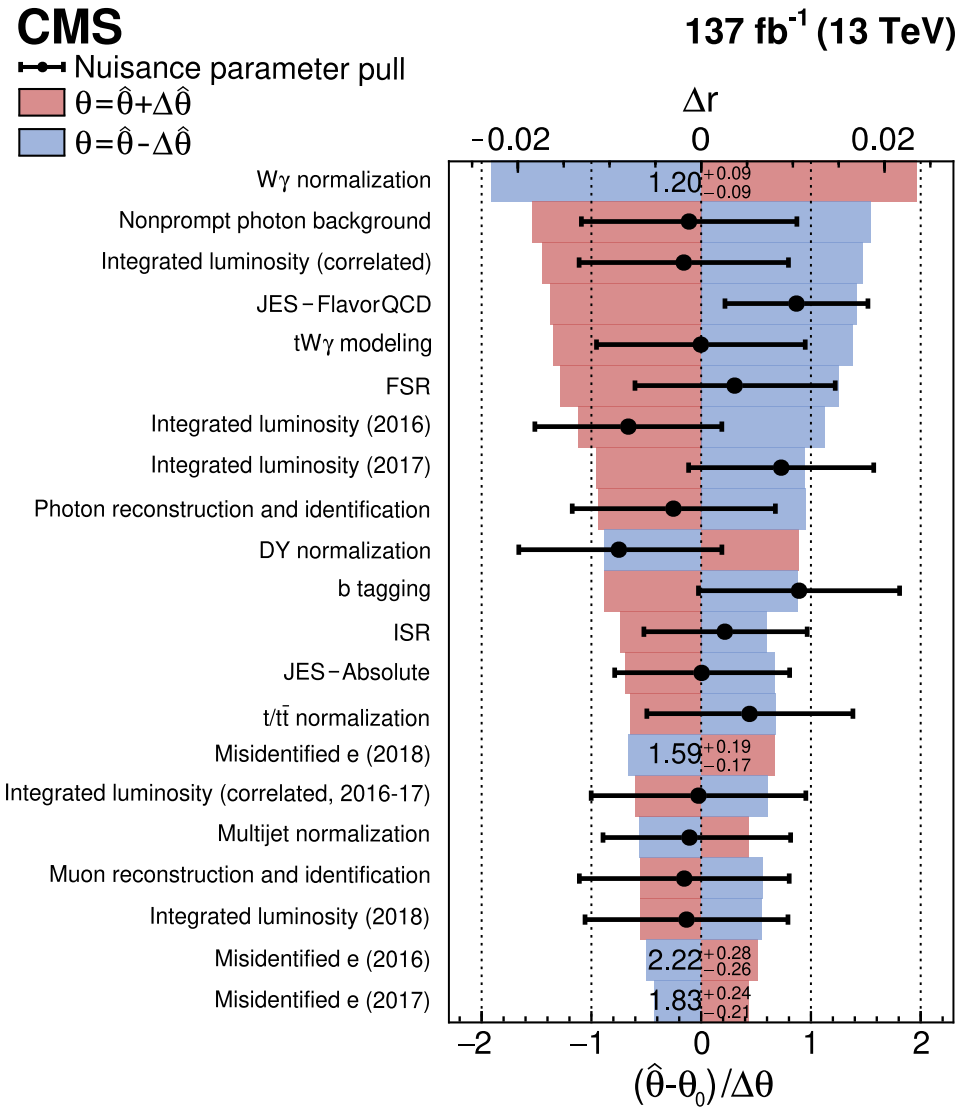

Figure 4.22: Ranking of systematic uncertainties in the profile likelihood fit of the inclusive $t\bar{t}\gamma$ cross section measurement. The red and blue bands indicate the post-fit impact in the measurement. The post-fit values of the nuisance parameters are indicated as black dots and extracted SFs for the normalization of Wγ and misidentified electron events are provided as numerical values. Black lines represent post-fit uncertainties normalized to the pre-fit values (constraints).

Die approbierte gedruckte Originalversion dieser Dissertation ist an der TU Wien Bibliothek verfügbar.
The approved original version of this doctoral thesis is available in print at TU Wien Bibliothek.

The systematic uncertainties split in their sources and their impact on the measurement are summarized in Table 4.15, with dominating experimental uncertainties arising from JES (1.9 %), the measurement of the integrated luminosity (1.8 %), b tagging efficiencies (1.1 %), and the identification of photons (1.1 %). Uncertainties in the background modeling are dominating for the nonprompt photon background estimation (1.8 %), the misidentified electron estimation (1.8 %) and Wγ backgrounds (2.3 %), while theoretical uncertainties dominate for the modeling of ISR and FSR (1.9 %).

The ranking of leading systematic uncertainties according to their impact on the measurement is shown in Fig. 4.22. The post-fit values of nuisance parameters are found to be within the pre-fit uncertainties. Only mild constraints of 35 % for the JES–FlavorQCD nuisance and 25 % for the ISR scale are found. The constraints reflect improvement of the uncertainty in the inclusive $t\bar{t}\gamma$ cross section measurement induced by the binning in M_3.

The results of this measurement are added to the LHCTopWG summary on $t\bar{t}X$ (X = W, Z, or γ) cross section measurements in CMS and ATLAS shown in Fig. 4.21, with a comparison to the dileptonic $t\bar{t}\gamma + tW\gamma$ cross section measurement in the eμ channel performed by the ATLAS collaboration [163], and several measurements of the $t\bar{t}W$ and $t\bar{t}Z$ processes. The figure shows preliminary results, which mildly deviate from the measured cross section presented in this thesis.

4.6.2 Differential cross section measurement

Differential cross section measurements are performed in the distributions of $p_T(\gamma)$, $|\eta(\gamma)|$, and $\Delta R(\ell, \gamma)$, with the binning thresholds given in Table 4.10. A signal strength modifier is measured in each bin of the distributions in each data-taking period, N_j, and lepton flavor selection. The method is discussed in Sec. 4.3.3, with the fit performed for each distribution using the control regions shown in Fig. 4.18. The procedure was tested to reproduce modifications of simulated signal predictions, resulting in agreements within the numerical accuracy.

The measured distributions are combined to a $N_j \geq 3$ selection in the combined electron and muon channel for each data-taking period. After subtracting the background contributions and contributions from reconstructed events that are not part of the fiducial phase space definition, the observed distributions are further unfolded to the particle level.

The observed differential cross sections at the particle level are shown in Fig. 4.23 for $p_T(\gamma)$ (upper left), $|\eta(\gamma)|$ (upper right), and $\Delta R(\ell, \gamma)$ (lower). The particle-level distributions are compared to predictions from simulation using MadGraph5_aMC@NLO interfaced with Pythia 8 (red, solid), Herwig 7 (black, dashed), and Herwig++ (green, dotted) for hadronization and parton showering.

In the procedure, statistical and systematic uncertainty sources extracted from the likelihood fit are unfolded to the particle level and added in quadrature, taking correlations into account. In this method, effects from uncertainties on the response matrices shown in Fig. 4.8 are considered. The resulting statistical and total uncertainty bands are shown as light- and dark-grey bands, respectively. Dominating uncertainty sources in differential measurements are found to be originating from JES and b tagging efficiencies, with photon identification and signal modeling uncertainties dominating in high-$p_T(\gamma)$ regions.

Die approbierte gedruckte Originalversion dieser Dissertation ist an der TU Wien Bibliothek verfügbar.
The approved original version of this doctoral thesis is available in print at TU Wien Bibliothek.
TU Bibliothek Your knowledge hub WIEN

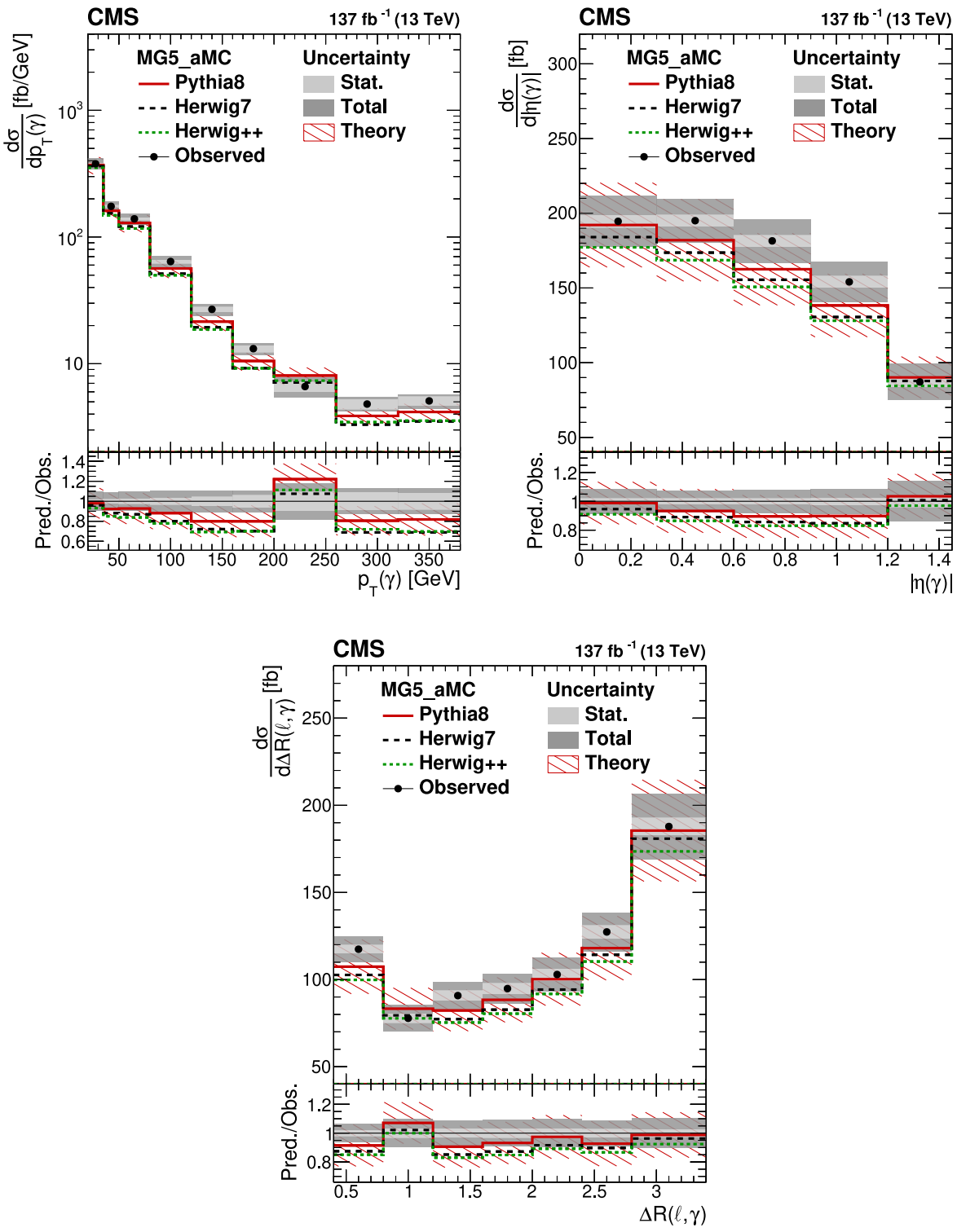

Figure 4.23: Unfolded differential cross sections for $p_T(\gamma)$ (upper left), $|\eta(\gamma)|$ (upper right), and $\Delta R(\ell,\gamma)$ (lower) in the fiducial phase space defined at the particle level. The distributions are compared to predictions from simulations using MadGraph5_aMC@NLO interfaced with Pythia 8 (red, solid), Herwig 7 (black, dashed), and Herwig++ (green, dotted). The total (statistical) uncertainty is shown as a dark- (light-)grey band and theory uncertainties are visualized as hatched red bands.

Die approbierte gedruckte Originalversion dieser Dissertation ist an der TU Wien Bibliothek verfügbar.
The approved original version of this doctoral thesis is available in print at TU Wien Bibliothek.
TU Bibliothek Your knowledge hub WIEN

The uncertainty sources are used to construct the covariance matrices C for the measurements at the particle level, calculated for bin i, j in

$$C_{ij} = \sum_{k,l} u_i^k \, \hat{\rho}_{kl} \, u_j^l, \tag{4.6.3}$$

where u^k and u^l are single uncertainty sources, $\hat{\rho}_{kl}$ is the corresponding correlation parameter of the uncertainties k, l, and $\hat{\rho}_{kk} = 1$. The covariance matrices for statistical and systematic uncertainties are provided in Appendix A.2 in Fig. A.5 for future reinterpretations of the measurements. Correlation matrices are calculated from the covariance matrices in

$$\rho_{ij} = \frac{C_{ij}}{\sqrt{C_{ii} \, C_{jj}}}, \tag{4.6.4}$$

where the correlation matrices of systematic (left) and statistical (right) uncertainties in the fiducial phase space region are given in Fig. 4.24 for $p_T(\gamma)$ (upper), $|\eta(\gamma)|$ (center), and $\Delta R(\ell, \gamma)$ (lower). Bin-by-bin correlations in systematic uncertainties result from background predictions in the distributions and correlated uncertainties in signal modeling, with decreasing correlations in high-$p_T(\gamma)$ regions due to increasing uncorrelated statistical uncertainties in simulations. Lower correlations are found in the first bin in the $\Delta R(\ell, \gamma)$ measurement due to less background contributions. Correlations from statistical uncertainty sources originating from data are found to be below 7 %.

A compatibility test of the measured distributions at the particle level and the predictions from simulations is performed. The evaluated χ^2 test statistics is

$$\chi^2 = \sum_{i,j} \left(\sigma_i^{\text{obs}} - \sigma_i^{\text{pred}} \right) C_{ij}^{-1} \left(\sigma_j^{\text{obs}} - \sigma_j^{\text{pred}} \right), \tag{4.6.5}$$

where σ^{obs} (σ^{pred}) is the observed (predicted) differential cross section and C_{ij} is the total covariance matrix value in the particle-level bin i, j, taking theory uncertainties into account. The evaluated χ^2- and corresponding p-values for the given d.o.f. are summarized in Table 4.17. A good agreement is found for all distributions, with no significant deviations of the observed particle-level distributions from the predictions.

Table 4.17: Compatibility-test values of the measured distributions at the particle level and the predictions from simulations using MadGraph5_aMC@NLO interfaced with Pythia 8, Herwig 7, and Herwig++ for hadronization and parton showering.

		MadGraph5_aMC@NLO w/					
		Pythia 8		Herwig 7		Herwig++	
	d.o.f.	χ^2	p-value	χ^2	p-value	χ^2	p-value
$p_T(\gamma)$	9	12.0	0.21	18.4	0.03	18.5	0.03
$\lvert\eta(\gamma)\rvert$	5	5.2	0.39	6.8	0.24	6.2	0.29
$\Delta R(\ell, \gamma)$	7	6.3	0.51	7.8	0.35	8.0	0.33

Die approbierte gedruckte Originalversion dieser Dissertation ist an der TU Wien Bibliothek verfügbar.
The approved original version of this doctoral thesis is available in print at TU Wien Bibliothek.
TU Bibliothek Your knowledge hub WIEN

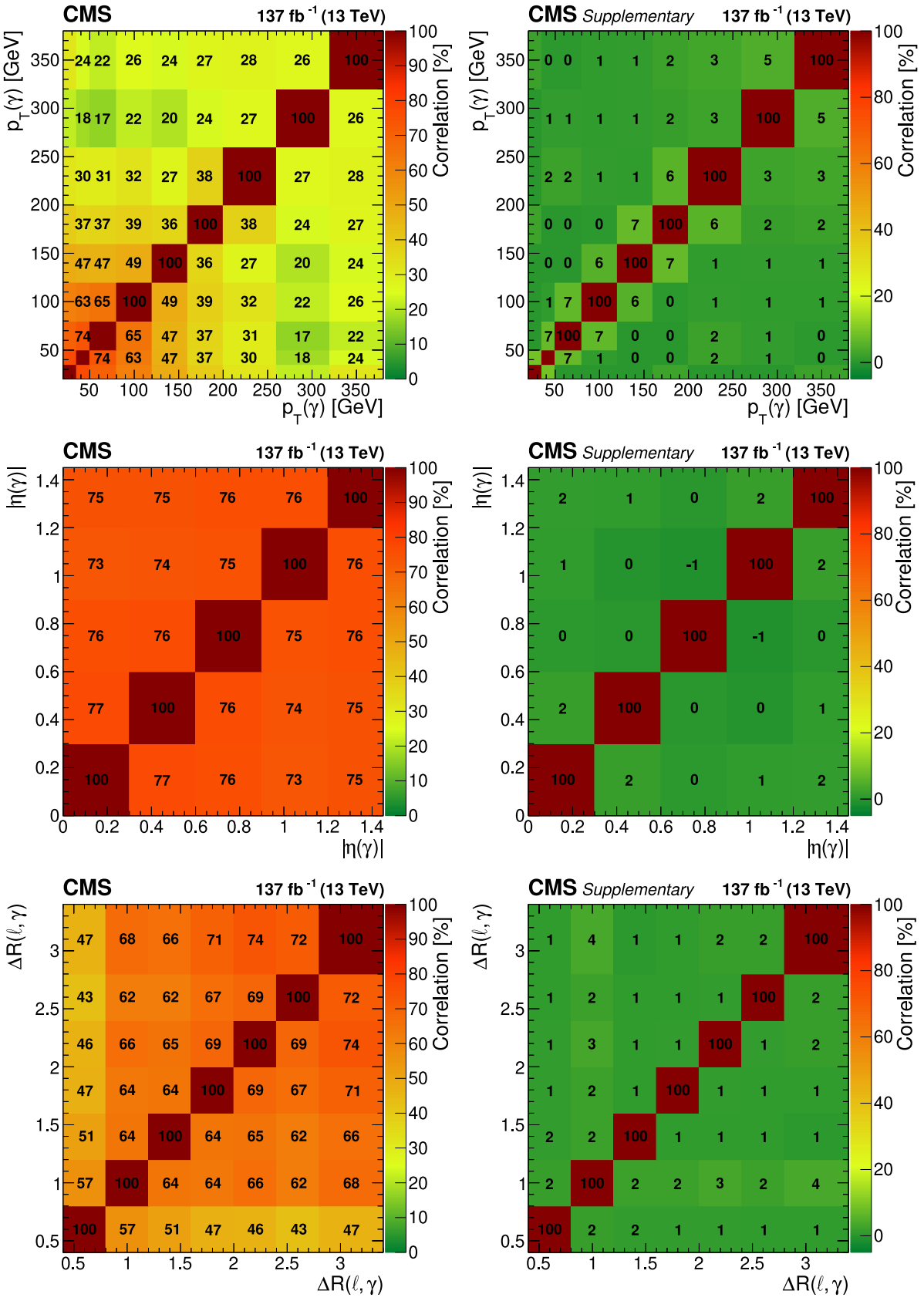

Figure 4.24: The correlation matrices of the systematic (left) and statistical (right) uncertainties for $p_T(\gamma)$ (upper), $|\eta(\gamma)|$ (center), and $\Delta R(\ell,\gamma)$ (lower) in the fiducial phase space defined at the particle level.

Die approbierte gedruckte Originalversion dieser Dissertation ist an der TU Wien Bibliothek verfügbar.
The approved original version of this doctoral thesis is available in print at TU Wien Bibliothek.

Die approbierte gedruckte Originalversion dieser Dissertation ist an der TU Wien Bibliothek verfügbar.
The approved original version of this doctoral thesis is available in print at TU Wien Bibliothek.

Chapter 5

Effective field theory interpretation

The results of the $t\bar{t}\gamma$ cross section measurements are interpreted in the context of SM-EFT to set constraints on possible anomalous top quark couplings. Modified interactions in the $t\bar{t}\gamma$ process can be part of the top quark coupling to the photon, the top quark pair production, and their decay. Anomalous interactions in the production, such as modified top quark-gluon couplings described by parameters related to the chromomagnetic and chromoelectric dipole moment in Eq. 2.2.8, are tightly constrained by $t\bar{t}$+jets measurements [290, 291]. Similarly, the modification of the Wtb vertex shown in Eq. 2.2.9, affecting the top quark decay, is best constrained by measurements of the W boson helicity fractions [129] and in single top quark t-channel productions [128]. Thus, the interpretation of the $t\bar{t}\gamma$ cross section measurements is restricted to direct measurements of the anomalous electroweak dipole moments of the top quark, constraining anomalous top quark-photon couplings. An example of the $t\bar{t}\gamma$ process is shown in Fig 5.1, where a red circle indicates the affected vertex.

A modified top quark-photon vertex is described in the Lagrangian given in Eq. 2.2.14, with the parameters related to the MDM and EDM denoted as d_V^γ and d_A^γ, respectively. Deviations from their SM predictions are quantified in SM-EFT in the Wilson coefficients $c_{t\gamma}$ and $c_{t\gamma}^I$ to the corresponding dimension-six operators in the Warsaw basis used in this interpretation, with the linear dependence to d_V^γ and d_A^γ given in in Eq. 2.3.22.

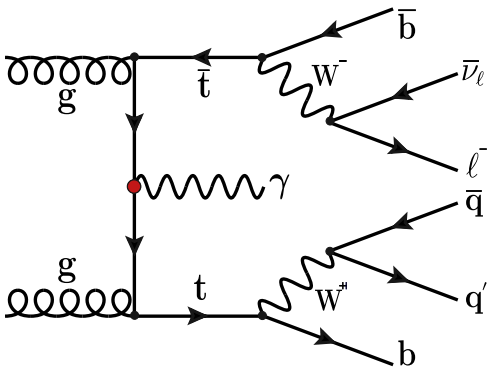

Figure 5.1: Representative diagram of the $t\bar{t}\gamma$ process for a photon originating from the top quark with a modified top quark-photon coupling indicated by a red circle.

Die approbierte gedruckte Originalversion dieser Dissertation ist an der TU Wien Bibliothek verfügbar.
The approved original version of this doctoral thesis is available in print at TU Wien Bibliothek.
TU Bibliothek Your knowledge hub WIEN

These Wilson coefficients are defined after EWSB and are no free parameters within the Warsaw basis. In fact, they are a linear combination of the electroweak dipole operator Wilson coefficients $c_{tZ}^{(I)}$ and $c_{tW}^{(I)}$. The derivation is shown in Eq. 2.3.21, choosing the combination of the W boson, Z boson, and top quark as d.o.f. [199]. In restricting the Wtb vertex to the SM, anomalous electromagnetic dipole moments are proportional to the Z boson dipole moments, with modifications due to the Wilson coefficients c_{tZ} and c_{tZ}^{I} and their corresponding SM-EFT operators.

Measurements of the $t\bar{t}\gamma$ cross sections can constrain possible BSM effects in top quark-photon interaction vertices and the corresponding Wilson coefficients c_{tZ} and c_{tZ}^{I} of the SM-EFT in the Warsaw basis. Due to the photon four-momentum dependence of the vertex modification given in Eq. 2.2.14, the $p_T(\gamma)$ spectrum is a sensitive probe to modifications by these operators. The differential cross section measurements shown in Sec. 4.6.2 are thus suited for restricting possible BSM effects, where for the interpretation of this measurement, other Wilson coefficients are kept at the SM values and the SM-EFT mass scale is set to $\Lambda = 1\,\text{TeV}$.

Constraints on the two Wilson coefficients c_{tZ} and c_{tZ}^{I} are extracted in the two-dimensional parameter space using dedicated simulations of signal and affected background processes. While the setup primarily uses the selection criteria, phase space definitions, and methods described in Chapter 4, a reweighting method of simulated event yields to nonzero values of the Wilson coefficients makes use of additional simulations with modified interaction vertices. The framework of the SM-EFT interpretation of the $t\bar{t}\gamma$ cross section measurements, the reweighting method, signal and background simulations, and the interpretation strategy are described in the following. The extracted individual and profiled confidence level (CL) intervals [282, 292] of the measurement on the two Wilson coefficients c_{tZ} and c_{tZ}^{I} are shown, leading to the tightest direct limits on the top quark anomalous couplings to the photon to date.

5.1 SM-EFT reweighting and event simulations

If scans of the BSM parameter space require generated signal events, even a moderate number of independent Wilson coefficients is prohibitive or severely restricts the achievable granularity. The limitation is eschewed in using a strategy described in Ref. [293] and first applied in SM-EFT interpretations in Ref. [294], with dedicated simulations of affected processes including event weights for parametrizing the BSM effects. With the simulation of SM signal and background processes already described in Sec. 4.1.2, the following gives an introduction to the reweighting framework for BSM parametrizations and the dedicated process simulations used therein.

5.1.1 SM-EFT reweighting framework

BSM effects on SM processes are evaluated in deriving a reweighting factor for affected SM events at the particle level that is applied to nominal event simulations in the measurement.

Die approbierte gedruckte Originalversion dieser Dissertation ist an der TU Wien Bibliothek verfügbar.
The approved original version of this doctoral thesis is available in print at TU Wien Bibliothek.
TU Bibliothek Your knowledge hub WIEN

The parametrization is described by

$$\sigma_{\mathrm{BSM}}^{\mathrm{reco}} = \sigma_{\mathrm{SM}}^{\mathrm{reco}} \times \frac{\sigma_{\mathrm{BSM}}^{\mathrm{gen}}}{\sigma_{\mathrm{SM}}^{\mathrm{gen}}}, \tag{5.1.1}$$

with the SM and BSM cross sections at the reconstruction level $\sigma_{\mathrm{SM}}^{\mathrm{reco}}$ and $\sigma_{\mathrm{BSM}}^{\mathrm{reco}}$, respectively, and $\sigma_{\mathrm{SM}}^{\mathrm{reco}}$ derived from the nominal simulation in the measurement described in Sec. 4.1.2. The reweighting factor is the ratio of the particle-level BSM and SM cross sections $\sigma_{\mathrm{BSM}}^{\mathrm{gen}}$ and $\sigma_{\mathrm{SM}}^{\mathrm{gen}}$.

For parametrizing the reweighting factor, it would be impractical to perform dedicated simulations for multiple points in the BSM parameter space. Thus, events of affected signal and background processes are simulated using MadGraph5_aMC@NLO and the MadWeight [295] plugin, including additional event weights that parametrize BSM effects. SM-EFT operators are affecting the ME and thus the cross section calculation, with the generic parametrization shown in Eq. 2.3.26, resulting in a quadratic dependence in the cross section. In the simulation, the ME is thus reevaluated at several base points in the BSM parameter space to calculate the event weights describing the variation of differential cross sections in the infinitesimal phase space occupied by one event. BSM effect in the event yields can then be parametrized by a second-order polynomial function in the set of Wilson coefficients $\mathbf{c}$ by the weight function w^i of an event i,

$$w^i\left(\frac{\mathbf{c}}{\Lambda^2}\right) = w_0^i + \sum_j w_{1j}^i \frac{c_j}{\Lambda^2} + \sum_{j,k} w_{2jk}^i \frac{c_j c_k}{\Lambda^4}, \tag{5.1.2}$$

with the sum of Wilson coefficients. w_0^i, w_{1j}^i, and w_{2jk}^i are the coefficients in the quadratic parametrization of the weight evaluated from the ME reevaluation at the base points, with the SM contribution, interference terms, and pure SM-EFT effects, respectively. Predicted event yields are then given by the sum of events i in the phase space.

The simulations are performed at a reference point with nonzero values of the Wilson coefficients c_j^{ref} to include all helicity amplitudes. In particular, for Wilson coefficients of dipole operators, such as c_{tZ} and $c_{\mathrm{tZ}}^{\mathrm{I}}$, the interference with the SM is vanishing small, and Wilson coefficients must be chosen nonzero to prevent artificially large weights. The weight function of Eq. 5.1.2 is thus modified by $c_j \to \left(c_j - c_j^{\mathrm{ref}}\right)$ to ensure the SM description for vanishing values of the Wilson coefficients.

With the parametrization of BSM effects, the reweighting factor in Eq. 5.1.1 is then calculated to be

$$\frac{\sigma_{\mathrm{BSM}}^{\mathrm{gen}}\left(\frac{\mathbf{c}}{\Lambda^2}\right)}{\sigma_{\mathrm{SM}}^{\mathrm{gen}}} = \frac{\sum_i w^i\left(\frac{\mathbf{c}}{\Lambda^2}\right)}{\sum_i w^i\left(\{0\}\right)}. \tag{5.1.3}$$

5.1.2 SM-EFT signal and background simulations

For the calculation of the SM-EFT reweighting factor, signal and background processes affected by the studied operators are simulated with MadGraph5_aMC@NLO interfaced with Pythia 8 using the CP5 tune for multiple-parton interactions, parton showering and hadronization. SM-EFT operators are implemented in a standardized universal FeynRules output (UFO) model [296], where the event generator uses the dim6top UFO model [199] at

Die approbierte gedruckte Originalversion dieser Dissertation ist an der TU Wien Bibliothek verfügbar.
The approved original version of this doctoral thesis is available in print at TU Wien Bibliothek.
TU Bibliothek Your knowledge hub WIEN

LO in QCD precision. The simulation is performed with one operator insertion (DIM6=1) at the reference point $c_{tZ}^{ref} = c_{tZ}^{I\,ref} = 1\,(\Lambda/\text{TeV})^2$ and the ME is reevaluated at the base points $(c_{tZ}, c_{tZ}^{I}) = (0,0)$, $(1,0)$, $(0,1)$, $(2,0)$, $(1,1)$, and $(0,2)(\Lambda/\text{TeV})^2$ for all processes.

Semileptonic and dileptonic $t\bar{t}\gamma$ signal events are simulated with the same generator settings as described in Sec. 4.1.2. The hadronic signal contribution is negligible in the fiducial phase space, with the cross section contribution shown in Table 4.9. Thus, the simulation of hadronic $t\bar{t}\gamma$ events is neglected.

Additionally, the affected background processes including a top quark and a photon are simulated with a photon at ME level and modified top quark-photon couplings. The relevant background processes are single top quark productions in association with a photon in the s- and t-channel, denoted as $t\gamma$, and the tW-channel, denoted as $tW\gamma$, with diagrams for these processes without the photon shown in Fig. 2.5. Background processes are simulated with the top quark decay at ME level, inclusively in the top quark decay channels. Similar generator settings as for the signal simulation are used, where photons are simulated with $p_T(\gamma) > 10\,\text{GeV}$ and $|\eta(\gamma)| < 5$, and charged leptons must satisfy $|\eta(\ell)| < 5$. Angular separations of all final-state particles to the photon of $\Delta R > 0.1$ are required.

5.1.3 Validation of the SM-EFT reweighting framework

The SM-EFT reweighting method is validated in comparing distributions of simulated events at dedicated BSM points in the parameter space to those resulting from the reweighting procedure. For this, additional $t\bar{t}\gamma$ simulations are performed for the SM and the specific BSM points of $c_{tZ}^{(I)} = 2$ and $c_{tZ}^{(I)} = -1\,(\Lambda/\text{TeV})^2$ using the same generator settings, however, without the evaluation of additional weights from ME variations at BSM base points. Several particle-level distributions in the fiducial phase space region defined in Sec. 4.3.2 are compared to those of the reweighted signal simulation, where a comparison of the $p_T(\gamma)$ distributions for nonzero values in c_{tZ} (left) and c_{tZ}^{I} (right) are shown in Fig. 5.2. Dedicated simulations at the BSM points are denoted as "simulated" and shown in solid, while the reweighted distributions from a single simulation are denoted as "weighted" and shown in dashed. Excellent agreement is found in the comparison, with remaining deviations in high-$p_T(\gamma)$ regions due to the limited number of simulated events.

Additional tests of the reweighting procedure have been performed to validate the method at the reconstruction level. Distributions of a reduced set of statistically independent simulations for nonzero values of the Wilson coefficients c_{tZ} and c_{tZ}^{I} have been compared to reweighted distributions and excellent agreement was found.

5.2 Sensitivity study

Effects from modifications of the top quark-photon coupling are studied in various distributions, where simulated $t\bar{t}\gamma$ events described in Sec. 5.1.2 and the reweighting framework described in Sec. 5.1.1 are used to weight events at the particle level to several nonzero values of the Wilson coefficients c_{tZ} and c_{tZ}^{I}. The sensitivity study is performed in several distributions, where Fig. 5.3 (upper) shows the distributions of $p_T(\gamma)$ (left), $|\eta(\gamma)|$ (center),

Die approbierte gedruckte Originalversion dieser Dissertation ist an der TU Wien Bibliothek verfügbar.
The approved original version of this doctoral thesis is available in print at TU Wien Bibliothek.
TU Bibliothek Your knowledge hub WIEN

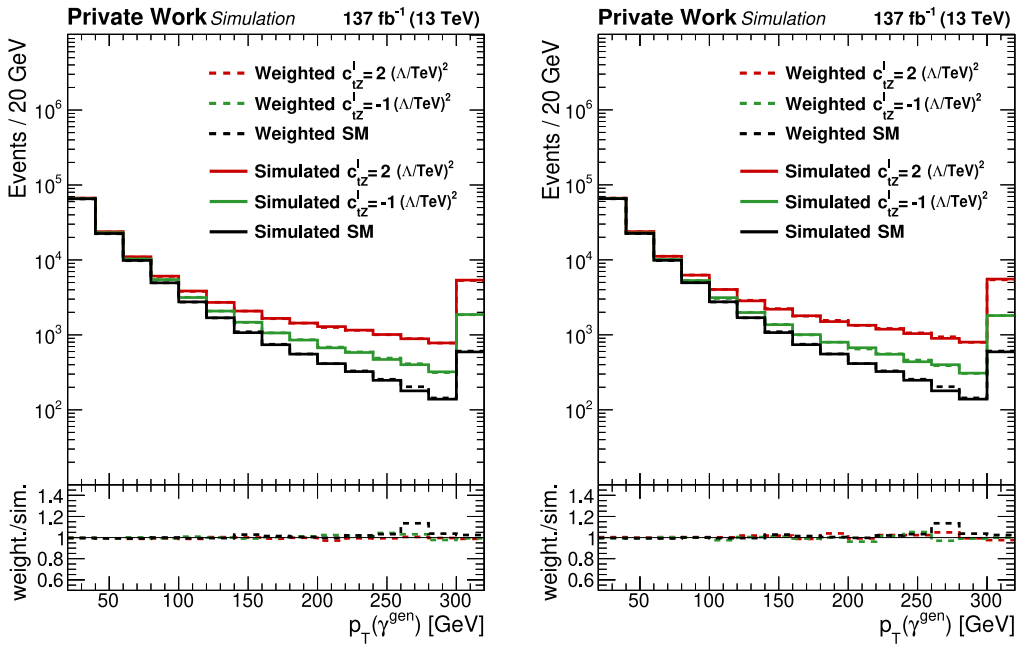

Figure 5.2: Comparison of $p_T(\gamma)$ distributions for the SM (black) and BSM hypotheses in the fiducial phase space selection for c_{tZ} (left) and c_{tZ}^I (right) at values of 2 (red) and $-1\,(\Lambda/\text{TeV})^2$ (green). The distributions using the reweighting method (dashed) are compared to dedicated simulations (solid) for the SM and BSM hypotheses.

and $\Delta R(\ell,\gamma)$ (right) in the fiducial phase space selection described in Sec. 4.3.2 for the BSM hypotheses $c_{tZ} = 1$ (red dashed) and $c_{tZ}^I = 1\,(\Lambda/\text{TeV})^2$ (green dashed). The SM (black solid) is shown for comparison. As expected and given in the photon four-momentum dependence in the Lagrangian of the modified $t\bar{t}\gamma$ interaction in Eq. 2.2.14, the SM-EFT operators have a large effect on the event yield in high-$p_T(\gamma)$ regions (upper left). Additional but small effects are visible in the $|\eta(\gamma)|$ (upper center) and $\Delta R(\ell,\gamma)$ (upper right) distributions.

The same distributions are obtained with effects in $p_T(\gamma)$ reweighted to the SM to test the correlation of BSM effects in $|\eta(\gamma)|$ and $\Delta R(\ell,\gamma)$ with the deviations in high-$p_T(\gamma)$ regions. The distributions are labeled "$p_T(\gamma)$ reweighted" and shown in Fig. 5.3 (lower), where no additional sensitivity is found in $|\eta(\gamma)|$ (lower center) and $\Delta R(\ell,\gamma)$ (lower right). Effects mentioned before are thus purely from modifications in high-$p_T(\gamma)$ regions. The differential $t\bar{t}\gamma$ cross section measurement in $p_T(\gamma)$ is well-suited, but the only distribution that allows for constraining BSM effects in the top quark-photon coupling quantified by the SM-EFT Wilson coefficients c_{tZ} and c_{tZ}^I.

5.3 Interpretation strategy

A two-dimensional grid in the Wilson coefficients c_{tZ} and c_{tZ}^I is constructed to constrain these parameters. In the grid, c_{tZ} and c_{tZ}^I each can take any of the values of 0, ±0.017, ±0.05, ±0.083, ±0.117, ±0.15, ±0.183, ±0.217, ±0.25, ±0.283, ±0.317, ±0.35, ±0.383, ±0.417,

Die approbierte gedruckte Originalversion dieser Dissertation ist an der TU Wien Bibliothek verfügbar.
The approved original version of this doctoral thesis is available in print at TU Wien Bibliothek.
TU Bibliothek Your knowledge hub WIEN

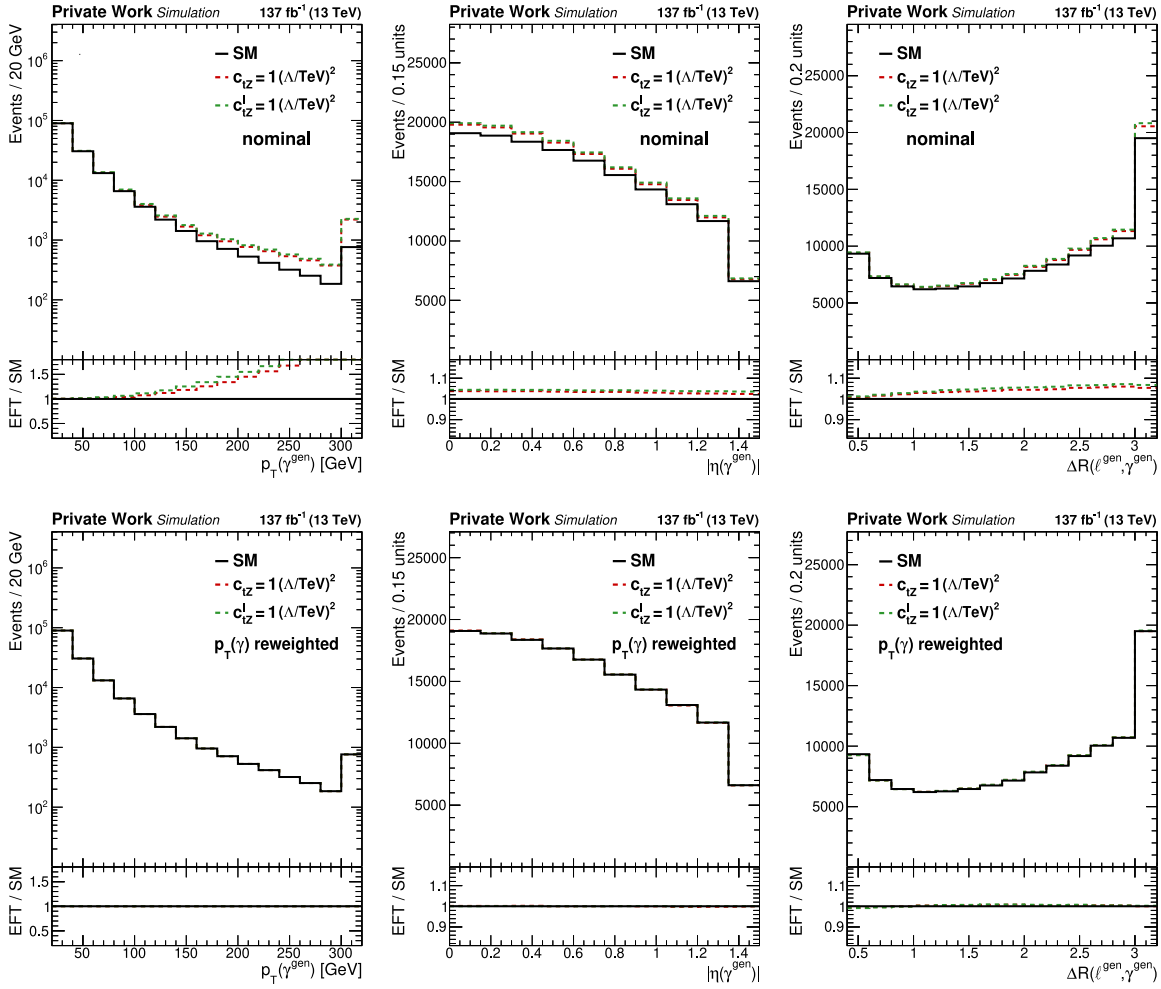

Figure 5.3: Sensitivity studies in the $t\bar{t}\gamma$ process in the $p_T(\gamma)$ (left), $|\eta(\gamma)|$ (center), and $\Delta R(\ell, \gamma)$ (right) distributions in the fiducial phase space selection for the SM (black) and BSM hypotheses for $c_{tZ} = 1$ (red dashed) and $c_{tZ}^{I} = 1\,(\Lambda/\text{TeV})^2$ (green dashed). The upper row shows the BSM effects on the distributions, where the effect in $|\eta(\gamma)|$ and $\Delta R(\ell, \gamma)$ are results of modifications in $p_T(\gamma)$. The lower row shows the same distributions, where the effects on $p_T(\gamma)$ are removed. No additional sensitivity in other distributions is found.

Die approbierte gedruckte Originalversion dieser Dissertation ist an der TU Wien Bibliothek verfügbar.
The approved original version of this doctoral thesis is available in print at TU Wien Bibliothek.

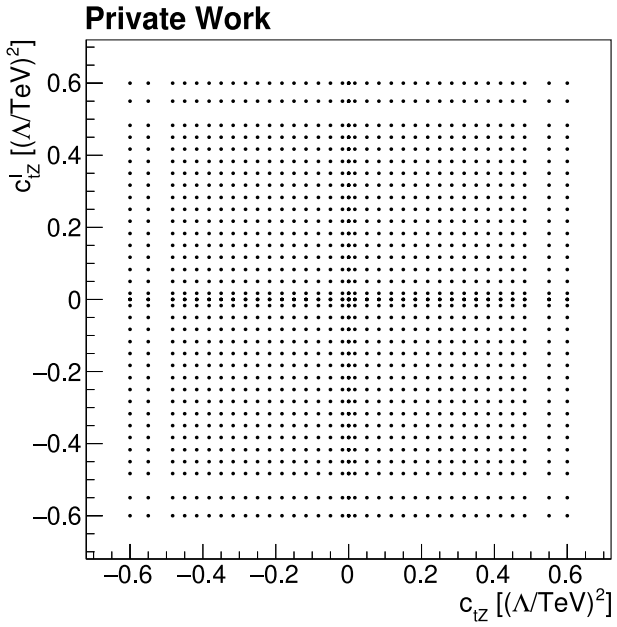

Figure 5.4: Visualization of the two-dimensional grid in the Wilson coefficients c_{tZ} and $c_{\mathrm{tZ}}^{\mathrm{I}}$, where for each of the BSM points, a binned likelihood function is constructed.

± 0.45, ± 0.483, ± 0.55, or $\pm 0.6\,(\Lambda/\mathrm{TeV})^2$, with a visualization in the two dimensions shown in Fig. 5.4.

For each of these BSM points, a binned likelihood function is constructed, using the SR3 and SR4p signal regions in bins of $\mathrm{p_T}(\gamma)$ and control regions for processes with misidentified electrons, Wγ, and Zγ defined in Sec. 4.3.1. The setup corresponds to the differential cross section measurement of the $\mathrm{p_T}(\gamma)$ distribution, with the $\mathrm{p_T}(\gamma)$-binning thresholds defined in Table 4.10. In each signal and control region bin, the by the SM-EFT operators affected signal and background processes $\mathrm{t\bar{t}}\gamma$, tγ, and tWγ are reweighted according to Eq. 5.1.1, with the reweighting factor defined in the fiducial phase space region.

The predicted and observed event yields in the signal and control regions and the constrained and unconstrained nuisance parameters $\boldsymbol{\theta}$ and $\boldsymbol{\beta}$, reflecting the uncertainties, are included in the constructed binned likelihood function $L(\boldsymbol{\theta}, \boldsymbol{\beta})$ as a product of Poisson probabilities, described in Sec. 4.3.3. Uncertainties taken into account are described in Sec. 4.5. While for the $\mathrm{t\bar{t}}\gamma$ cross section measurement, only acceptance effects are included as uncertainties for variations of μ_R and μ_F scales at ME level and variations of the PDF sets given in Sec. 4.5.2, their total variation is taken into account in the BSM interpretation.

The test statistic is the profile likelihood ratio

$$q = -2 \ln \frac{\mathcal{L}(\mathbf{c}, \hat{\hat{\boldsymbol{\theta}}}_{\mathbf{c}}, \hat{\hat{\boldsymbol{\beta}}}_{\mathbf{c}})}{\mathcal{L}(\hat{\boldsymbol{\theta}}, \hat{\boldsymbol{\beta}})}, \tag{5.3.1}$$

with the set of nuisance parameters $(\hat{\hat{\boldsymbol{\theta}}}_{\mathbf{c}}, \hat{\hat{\boldsymbol{\beta}}}_{\mathbf{c}})$ that maximize $\mathcal{L}$ at a given BSM point and the Wilson coefficients denoted as $\mathbf{c} = \left(c_{\mathrm{tZ}}, c_{\mathrm{tZ}}^{\mathrm{I}}\right)$. In the denominator, $(\hat{\boldsymbol{\theta}}, \hat{\boldsymbol{\beta}})$ maximize the likelihood function in the BSM parameter plane. The profile likelihood fit is performed simultaneously in the electron and muon channels and the three data-taking periods for each of the 1225 Wilson coefficient pairs shown in Fig. 5.4 to evaluate the set of nuisance parameters maximizing the likelihood function in any of the points in the BSM parameter plane.

Die approbierte gedruckte Originalversion dieser Dissertation ist an der TU Wien Bibliothek verfügbar.
The approved original version of this doctoral thesis is available in print at TU Wien Bibliothek.
TU Bibliothek Your knowledge hub WIEN

5.4 Results

The result of the profile likelihood fit at the SM point in the $p_T(\gamma)$ distributions of the SR3 (upper) and SR4p (lower) signal regions are shown in Fig. 5.5, separately for the electron (left) and muon (right) channel. A good agreement is found in all distributions, with no deviations from the SM expectations observed. The best-fit point in the Wilson coefficients is $c_{tZ} = -0.28$ and $c^I_{tZ} = -0.02\,(\Lambda/\text{TeV})^2$ indicated in red, and several other nonzero values of the Wilson coefficients are shown in dashed lines for comparison.

One-dimensional scans in the Wilson coefficients c_{tZ} (left) and c^I_{tZ} (right) are shown in Fig. 5.6, where in the upper row, the second Wilson coefficient is profiled, and in the lower row, it is set to the SM value. The one-dimensional 68 (95)% CL intervals are shown as a green (orange) shaded band and the expected results are indicated as a gray line. A second minimum in the profile likelihood scans is observed in the latter as a result of mild tensions with the SM hypothesis and due to similarities in predictions for oppositely signed Wilson coefficients. An example of this similarity is shown in Fig. 5.5 for the Wilson coefficient values $c_{tZ} = \pm 0.45\,(\Lambda/\text{TeV})^2$ in cyan and blue dashed, with similar results for positive and negative values of c_{tZ}.

The one-dimensional 68 and 95 % CL intervals are summarized in Table 5.1 for the second Wilson coefficient profiled or set to the SM value. The SM prediction is within the 95 % CL of the c_{tZ} and c^I_{tZ} best-fit value. Electroweak dipole moments deviating from SM predictions, described in the Lagrangian given in Eq. 2.2.14, predict a harder $p_T(\gamma)$ spectrum not observed in data.

Table 5.1: Summary of the expected and observed 68 and 95 % confidence level (CL) intervals of the Wilson coefficients c_{tZ} and c^I_{tZ} extracted from the one-dimensional fits for scenarios where the second Wilson coefficient is profiled or set to the SM value.

	Wilson coefficient		68 % CL interval $[(\Lambda/\text{TeV})^2]$	95 % CL interval $[(\Lambda/\text{TeV})^2]$
Expected	c_{tZ}	$c^I_{tZ} = 0$	$[-0.19, 0.20]$	$[-0.29, 0.31]$
		profiled	$[-0.19, 0.20]$	$[-0.29, 0.31]$
	c^I_{tZ}	$c_{tZ} = 0$	$[-0.20, 0.20]$	$[-0.30, 0.30]$
		profiled	$[-0.20, 0.20]$	$[-0.30, 0.30]$
Observed	c_{tZ}	$c^I_{tZ} = 0$	$[-0.36, -0.17]$	$[-0.43, 0.38]$
		profiled	$[-0.36, 0.04]$	$[-0.43, 0.38]$
	c^I_{tZ}	$c_{tZ} = 0$	$[-0.36, -0.16], [0.18, 0.35]$	$[-0.43, 0.43]$
		profiled	$[-0.32, 0.31]$	$[-0.42, 0.42]$

Die approbierte gedruckte Originalversion dieser Dissertation ist an der TU Wien Bibliothek verfügbar.
The approved original version of this doctoral thesis is available in print at TU Wien Bibliothek.
TU Bibliothek Your knowledge hub WIEN

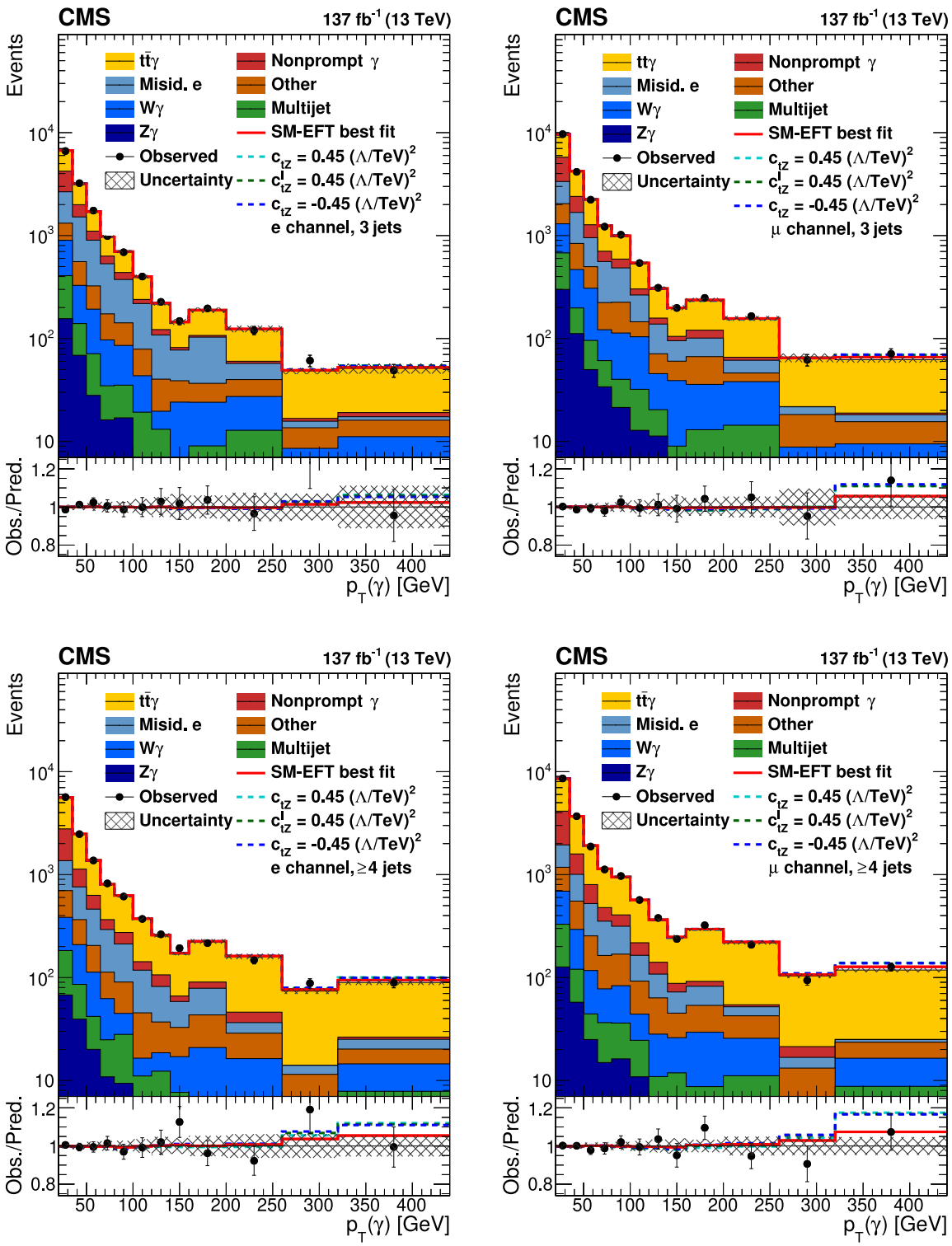

Figure 5.5: Observed and predicted yields for the electron (left) and muon (right) channel in the SR3 (upper) and SR4p (lower) signal regions. The lower pad shows the ratio of observed to predicted event yields and systematic uncertainties are visualized as hatched bands. The red line shows the best-fit result of the SM-EFT interpretation and predictions for other values of the Wilson coefficients are shown for $c_{\mathrm{tZ}} = 0.45$ (cyan), $c_{\mathrm{tZ}}^{\mathrm{I}} = 0.45$ (green), and $c_{\mathrm{tZ}} = -0.45\,(\Lambda/\mathrm{TeV})^2$ (blue).

Die approbierte gedruckte Originalversion dieser Dissertation ist an der TU Wien Bibliothek verfügbar.
The approved original version of this doctoral thesis is available in print at TU Wien Bibliothek.
TU Bibliothek Your knowledge hub WIEN

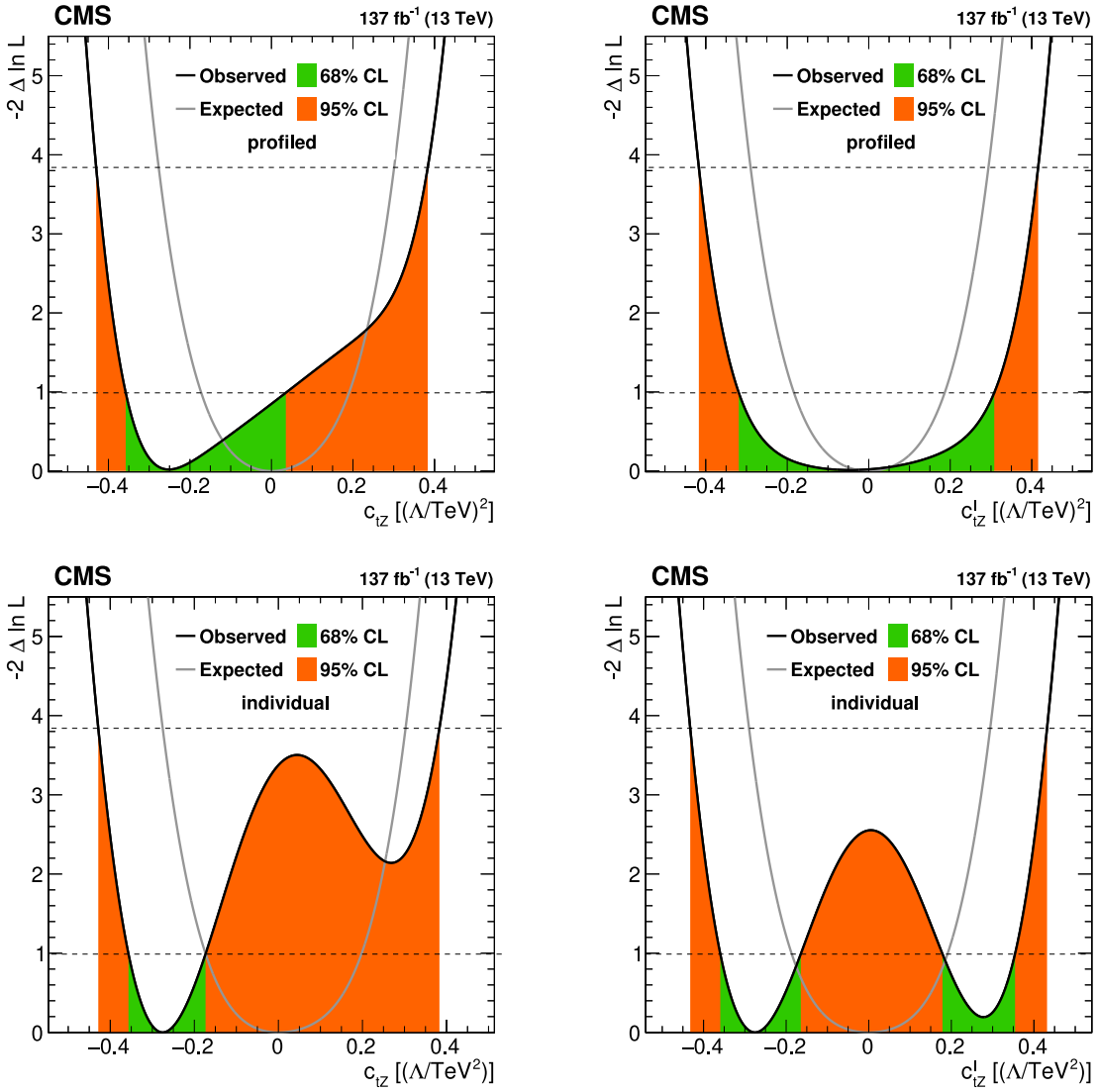

Figure 5.6: Expected (gray) and observed (black) 68 (green) and 95 % (orange) confidence level intervals of the Wilson coefficients c_{tZ} (left) and c_{tZ}^{I} (right) extracted from the one-dimensional scans for scenarios where the second Wilson coefficient is profiled (upper) or set to the SM value (lower).

Die approbierte gedruckte Originalversion dieser Dissertation ist an der TU Wien Bibliothek verfügbar.
The approved original version of this doctoral thesis is available in print at TU Wien Bibliothek.

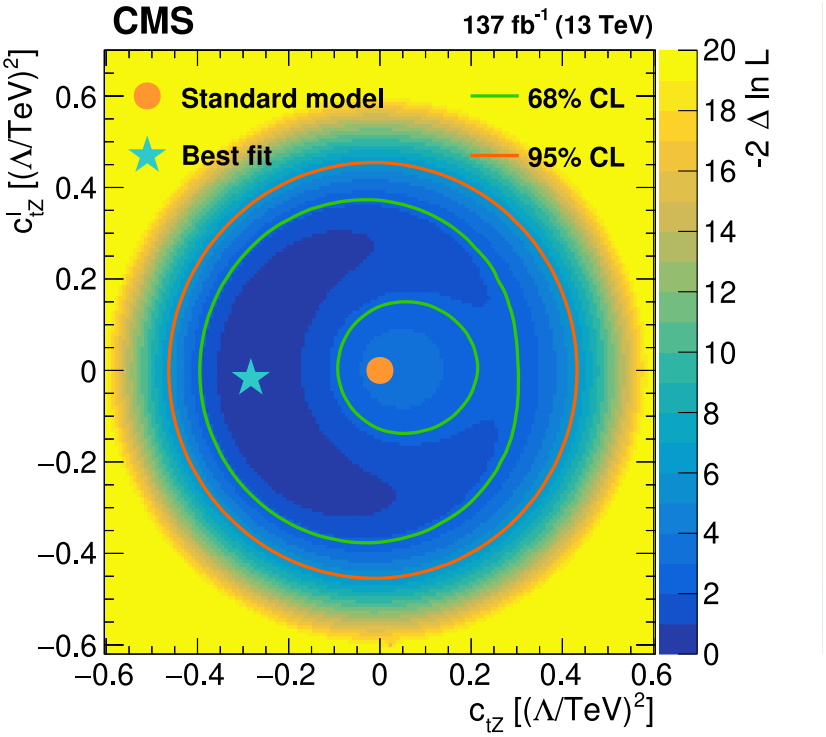

Figure 5.7: Observed 68 (green) and 95 % (orange) CL intervals of the Wilson coefficients c_{tZ} and c^{I}_{tZ} extracted from the two-dimensional scan. The orange dot shows the SM value and the best-fit value is indicated by a blue star.

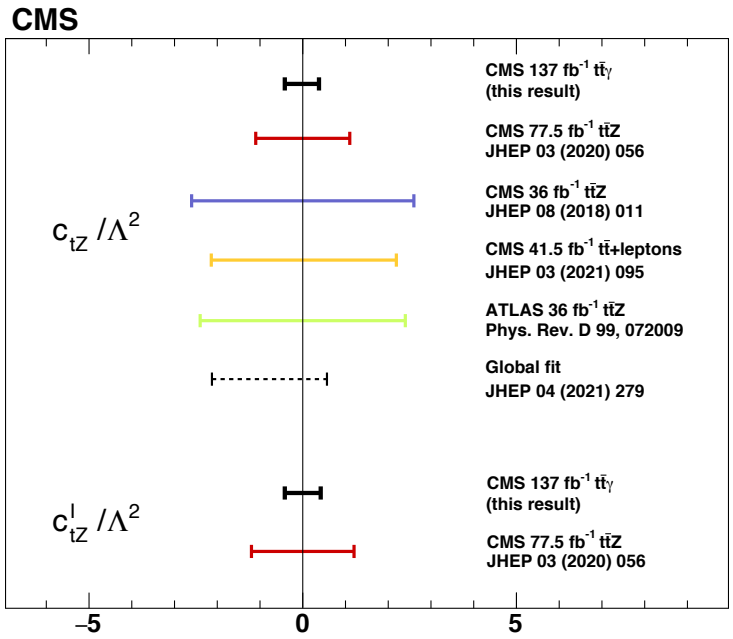

Figure 5.8: Comparison of observed 95 % CL intervals of the Wilson coefficients c_{tZ} and c^{I}_{tZ} from the presented measurement (black), previous results of the CMS collaboration from inclusive [297] (blue) and differential [135] (red) $t\bar{t}Z$ measurements, from $t\bar{t}$ measurements with additional leptons [294] (yellow), results from the ATLAS collaboration [298] (green) and global SM-EFT fits [299] (dashed).

Die approbierte gedruckte Originalversion dieser Dissertation ist an der TU Wien Bibliothek verfügbar.
The approved original version of this doctoral thesis is available in print at TU Wien Bibliothek.
TU Bibliothek Your knowledge hub WIEN

The corresponding two-dimensional profile likelihood scans, spanned by the Wilson coefficients c_{tZ} and c_{tZ}^{I}, are given in Fig. 5.7, with the 68 (95)% CL intervals shown as green (orange) lines. The allowed regions are between the two green or inside the orange contours. A blue star indicates the best-fit value, and the SM is shown as an orange dot at the origin of the plane.

The 95 % CL intervals of this measurement are compared to previous results of the CMS collaboration in inclusive [297] and differential [135] $t\bar{t}Z$ cross section measurements, $t\bar{t}$ measurements with additional leptons [294], and results of the ATLAS collaboration [298]. Additionally, the results are compared to global SM-EFT interpretations [299], where the comparison is shown in Fig 5.8.

Combined SM-EFT interpretation in single-lepton and dilepton final states

A measurement of the $t\bar{t}\gamma$ cross section in the dilepton final states [36] has been performed by the CMS collaboration, probing an orthogonal phase space. A combined SM-EFT interpretation of both measurements is presented in Ref. [36], further improving constraints on the probed Wilson coefficients. The $t\bar{t}\gamma$ cross section measurement in the single-lepton final state has a large number of events in high-$p_T(\gamma)$ regions, with good sensitivity to modifications described by the probed Wilson coefficients. The high purity of the $t\bar{t}\gamma$ dilepton final state provides additional sensitivity. The measurement of the differential $t\bar{t}\gamma$ cross section in the $p_T(\gamma)$ distribution thus results in the tightest direct limits on the top quark anomalous couplings to the photon to date.

Results are combined in constructing a profile likelihood function based on the $t\bar{t}\gamma$ signal regions in bins of $p_T(\gamma)$ in the single-lepton and dilepton final states, including the control regions of the respective analysis. One-dimensional scans of the combined SM-EFT interpretation in the Wilson coefficients c_{tZ} (left) and c_{tZ}^{I} (right) are shown in Fig. 5.9, where the second Wilson coefficient is set to the SM value. The one-dimensional 68 (95)% CL intervals are shown as a green (yellow) shaded band, and expected results are indicated as a black line. The corresponding expected (black) and observed (red) two-dimensional profile likelihood scans are given in Fig. 5.10, with the 68 (95)% CL intervals shown as dashed (solid) lines. The CL intervals are summarized in Table 5.2 for the second Wilson coefficient profiled or set to the SM value.

Die approbierte gedruckte Originalversion dieser Dissertation ist an der TU Wien Bibliothek verfügbar.
The approved original version of this doctoral thesis is available in print at TU Wien Bibliothek.

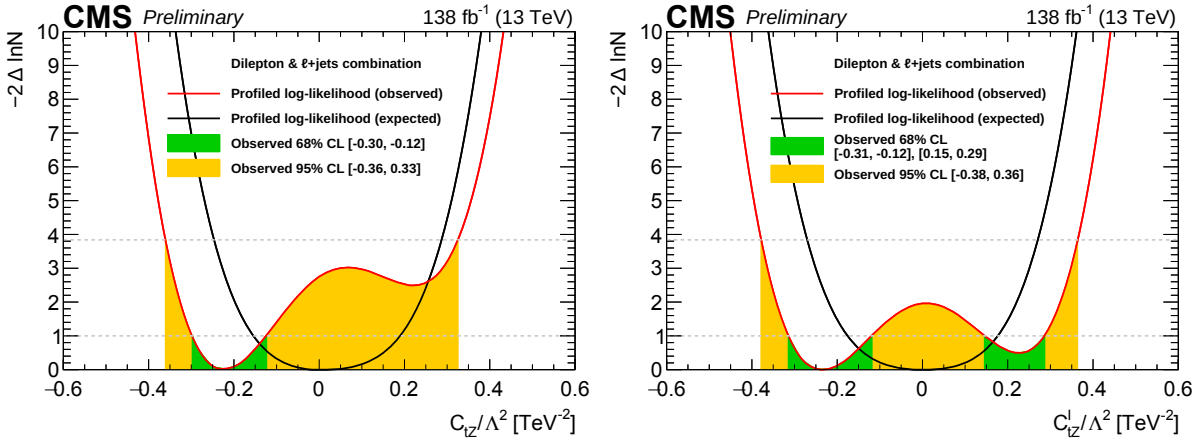

Figure 5.9: Expected (black) and observed (red) 68 (green) and 95 % (yellow) confidence level intervals of the Wilson coefficients c_{tZ} (left) and c^{I}_{tZ} (right) extracted from the one-dimensional scans in the combined interpretation of this result and the $t\bar{t}\gamma$ cross section measurement in the dilepton final state [36]. The CL intervals are obtained for scenarios where the second Wilson coefficient is set to the SM value.

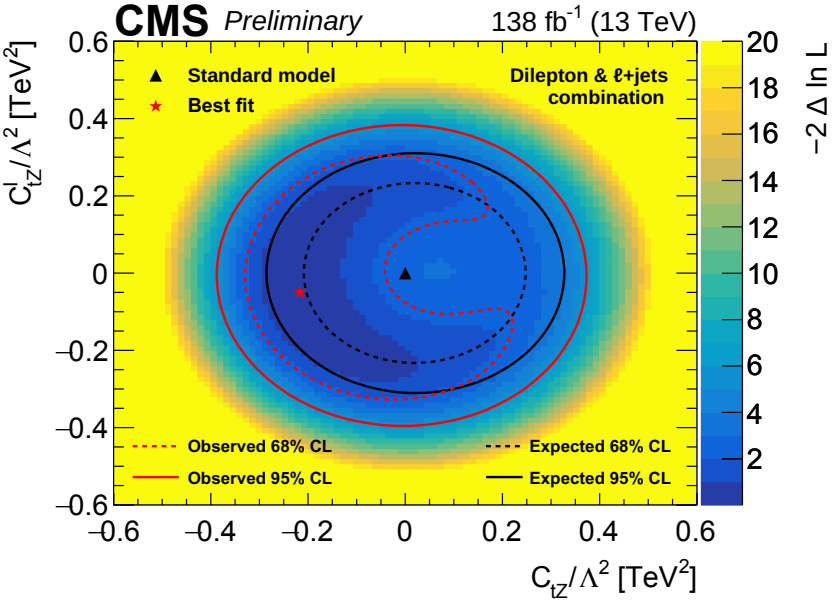

Figure 5.10: Observed (red) and expected (black) 68 (dashed) and 95 % (solid) CL intervals of the Wilson coefficients c_{tZ} and c^{I}_{tZ} extracted from the two-dimensional scan in the combined interpretation of this result and the $t\bar{t}\gamma$ cross section measurement in the dilepton final state [36]. The black triangle shows the SM value and the best-fit value is indicated by a red star.

Die approbierte gedruckte Originalversion dieser Dissertation ist an der TU Wien Bibliothek verfügbar.
The approved original version of this doctoral thesis is available in print at TU Wien Bibliothek.

Table 5.2: Summary of the expected and observed 68 and 95 % confidence level (CL) intervals of the Wilson coefficients c_{tZ} and c_{tZ}^{I} extracted from the one-dimensional fits in the combined interpretation of this result and the $t\bar{t}\gamma$ cross section measurement in the dilepton final state [36]. The CL intervals are obtained for scenarios where the second Wilson coefficient is profiled or set to the SM value.

	Wilson coefficient		68 % CL interval $[(\Lambda/\text{TeV})^2]$	95 % CL interval $[(\Lambda/\text{TeV})^2]$
Expected	c_{tZ}	$c_{tZ}^{I} = 0$	$[-0.16, 0.19]$	$[-0.25, 0.29]$
		profiled	$[-0.22, 0.26]$	$[-0.29, 0.33]$
	c_{tZ}^{I}	$c_{tZ} = 0$	$[-0.18, 0.18]$	$[-0.27, 0.27]$
		profiled	$[-0.24, 0.24]$	$[-0.32, 0.32]$
Observed	c_{tZ}	$c_{tZ}^{I} = 0$	$[-0.30, -0.12]$	$[-0.37, 0.33]$
		profiled	$[-0.34, 0.23]$	$[-0.40, 0.38]$
	c_{tZ}^{I}	$c_{tZ} = 0$	$[-0.32, -0.11], [0.15, 0.29]$	$[-0.38, 0.37]$
		profiled	$[-0.33, 0.31]$	$[-0.40, 0.39]$

Die approbierte gedruckte Originalversion dieser Dissertation ist an der TU Wien Bibliothek verfügbar.
The approved original version of this doctoral thesis is available in print at TU Wien Bibliothek.
TU Bibliothek Your knowledge hub WIEN

Chapter 6

Conclusions

Despite the extraordinary success of the standard model (SM) of particle physics and its predictive power, it is known to be incomplete. While it successfully describes the interaction of known elementary particles, the need for a theory describing energy scales much higher than those reachable by current particle colliders is tightened by evidence for new physics phenomena. The search for physics beyond the SM (BSM) is thus the main focus of the physics program of experiments at the CERN Large Hadron Collider (LHC), such as the CMS experiment.

The discovery of the top quark in 1995 completed the fermion content of the SM. It is the heaviest elementary particle and is expected to play a crucial rôle in the search for BSM physics. With hypothetical new particles coupling to the top quark, measuring possible deviations of top quark interactions from SM predictions is a promising probe for new physics. Modified interactions of the top quark can be part of the production, the decay, or its coupling to electroweak bosons. Anomalous interactions in the production and the decay are already tightly constrained by $\mathrm{t\bar{t}}$+jets and single top quark measurements, and the CMS experiment recently set limits on its modified coupling to the Z boson. The measurement of the top quark interaction with photons is the content of the presented thesis, which allows for measuring its electromagnetic coupling and thus for setting direct limits on its anomalous electromagnetic dipole moments.

As many theoretical models predict deviations of top quark interactions, it is infeasible to compare each BSM scenario against LHC measurements. In this case, the SM effective field theory (SM-EFT) provides a model-independent way to parametrize new physics effects. Using the Warsaw basis, anomalous electromagnetic dipole moments are described by the Wilson coefficients $c_{\mathrm{t}\gamma}$ and $c^{\mathrm{I}}_{\mathrm{t}\gamma}$ and the corresponding dimension-six SM-EFT operators. However, these operators are no free parameters within SM-EFT and they are described by a linear combination of the electroweak operators, with the Wilson coefficients $c^{(\mathrm{I})}_{\mathrm{tZ}}$ and $c^{(\mathrm{I})}_{\mathrm{tW}}$. In restricting the Wtb vertex to the SM, modified interactions of the top quark and the photon are described by the Wilson coefficients c_{tZ} and $c^{\mathrm{I}}_{\mathrm{tZ}}$.

This thesis presents the results of the inclusive and differential cross section measurements of top quark pair productions in association with a photon ($\mathrm{t\bar{t}}\gamma$). The measurements use a data set of $137\,\mathrm{fb}^{-1}$ integrated luminosity, collected by the CMS experiment at a center-of-mass energy of $\sqrt{s} = 13\,\mathrm{TeV}$ during the Run 2 (2016–2018) data taking of the LHC. The $\mathrm{t\bar{t}}\gamma$ cross sections are measured in a fiducial phase space region with a

TU Bibliothek Your knowledge hub WIEN
Die approbierte gedruckte Originalversion dieser Dissertation ist an der TU Wien Bibliothek verfügbar.
The approved original version of this doctoral thesis is available in print at TU Wien Bibliothek.

highly energetic photon, an isolated electron or muon, and at least three jets from the hadronization of quarks, where at least one has to originate from a bottom quark. The photon is measured for a transverse momentum $p_T(\gamma) > 20\,\text{GeV}$ and an absolute value of the pseudorapidity $|\eta(\gamma)| < 1.4442$. Background processes with a prompt photon from the $W\gamma$ and $Z\gamma$ processes, a misidentified electron, a photon originating from the hadronization of quarks, a hadronic fake photon, or a nonprompt lepton are estimated from data. The measured $t\bar{t}\gamma$ cross section in the fiducial phase space of 798 ± 7 (stat) ± 48 (syst) fb is in good agreement with SM predictions from simulations at next-to-leading order in quantum chromodynamics.

The differential cross section measurements are performed in the kinematic observables of $p_T(\gamma)$, $|\eta(\gamma)|$, and the angular separation of the photon and the lepton. The observed distributions are unfolded to the particle level, defined in the same fiducial phase space, and compared to several predictions from simulations using various parton showering algorithms. Statistical and systematic covariance matrices of the differential measurements at the particle level are provided for future reinterpretations of the results.

The results are interpreted in the context of SM-EFT in the Warsaw basis, where especially effects of dimension-six electroweak dipole operators on the $p_T(\gamma)$ spectrum allow for setting tight constraints on the Wilson coefficients c_{tZ} and c_{tZ}^I. Thus, the differential cross section measurement of the $p_T(\gamma)$ spectrum allows to extract the most stringent confidence level (CL) intervals for these two Wilson coefficients to date. The extracted one-dimensional 95 % CL intervals for the second Wilson coefficient profiled (set to zero) are $[-0.43, 0.38]$ ($[-0.43, 0.38]$) and $[0.42, 0.42]$ ($[-0.42, 0.42]$) $(\Lambda/\text{TeV})^2$ for c_{tZ} and c_{tZ}^I, respectively. The SM is within the 95 % CL intervals of the best-fit point in the Wilson coefficients at $c_{tZ} = -0.28$ and $c_{tZ}^I = -0.02\,(\Lambda/\text{TeV})^2$. The constraints are further improved in a combined SM-EFT interpretation of single-lepton and dilepton final states, tightening the 95 % CL intervals for the second Wilson coefficient profiled (set to zero) to $[-0.40, 0.38]$ ($[-0.37, 0.33]$) and $[0.40, 0.39]$ ($[-0.38, 0.37]$) $(\Lambda/\text{TeV})^2$ for c_{tZ} and c_{tZ}^I, respectively.

Die approbierte gedruckte Originalversion dieser Dissertation ist an der TU Wien Bibliothek verfügbar.
The approved original version of this doctoral thesis is available in print at TU Wien Bibliothek.
TU Bibliothek Your knowledge hub WIEN

Chapter A

Appendix

A.1 Validation of QCD multijet backgrounds

A.1.1 Data- and simulation-based template comparison

QCD multijet simulations are subject to large statistical uncertainty and thus lead to mismodeling of the background contributions. A data-based way of estimating the background is established, with details given in Sec. 4.4.1. In this method, data-based QCD multijet templates are extracted in high-I_{rel} lepton isolation sideband regions in subtracting electroweak contributions from data. To ensure a correct modeling of the background, the extracted templates are compared to simulation-based templates. The comparison of the $m_T(W)$ distribution is shown in Fig. A.1, with data- (blue) and simulation-based (red) template shape comparisons in the electron (upper) and muon (lower) channel for the QCD0b2 (left) and QCD1b2 (right) regions. Large statistical uncertainties are found for simulation-based QCD multijet templates, with an overall good agreement to the extracted data-based shapes.

A.1.2 Data- and simulation-based transfer factor comparison

QCD multijet TFs are extracted from data in selections of $N_j = 2$ and $N_\gamma = 0$, with details given in Sec. 4.4.1. For the background estimation, these TFs are then applied in regions with $N_j = 3$ and ≥ 4. To validate the N_j dependence of the TFs, comparisons to TFs extracted from simulated QCD multijet events are performed. The comparison is shown in Fig. A.2 for data- (blue) and simulation-based (red) TFs in the electron (left) and muon (right) channel. Only a negligible N_j dependence is found in regions without b-tagged jet selections (upper). The dependence for b-tagged TFs (lower) is nonnegligible and simulation-based corrections are applied to correct for the N_j dependence.

A.1.3 Distributions in validation regions

The data-based QCD multijet estimation method described in Sec. 4.4.1 is validated in regions with at least three jets and selections without a photon. The regions without and with identified b jets, denoted as QCD0b3p and QCD1b3p, respectively, are described in Sec. 4.3.1. Using the $p_T(\ell)$- and $\eta(\ell)$-binned QCD multijet TF estimation, a good agreement is found in both, the electron and muon channel. Distributions of $p_T(\ell)$ (left) and $\eta(\ell)$ (right) are shown in Fig. A.3 for the QCD0b3p and in Fig. A.4 for the QCD1b3p region, where pre-fit systematic uncertainties are shown as hatched bands.

Die approbierte gedruckte Originalversion dieser Dissertation ist an der TU Wien Bibliothek verfügbar.
The approved original version of this doctoral thesis is available in print at TU Wien Bibliothek.
TU Bibliothek Your knowledge hub WIEN

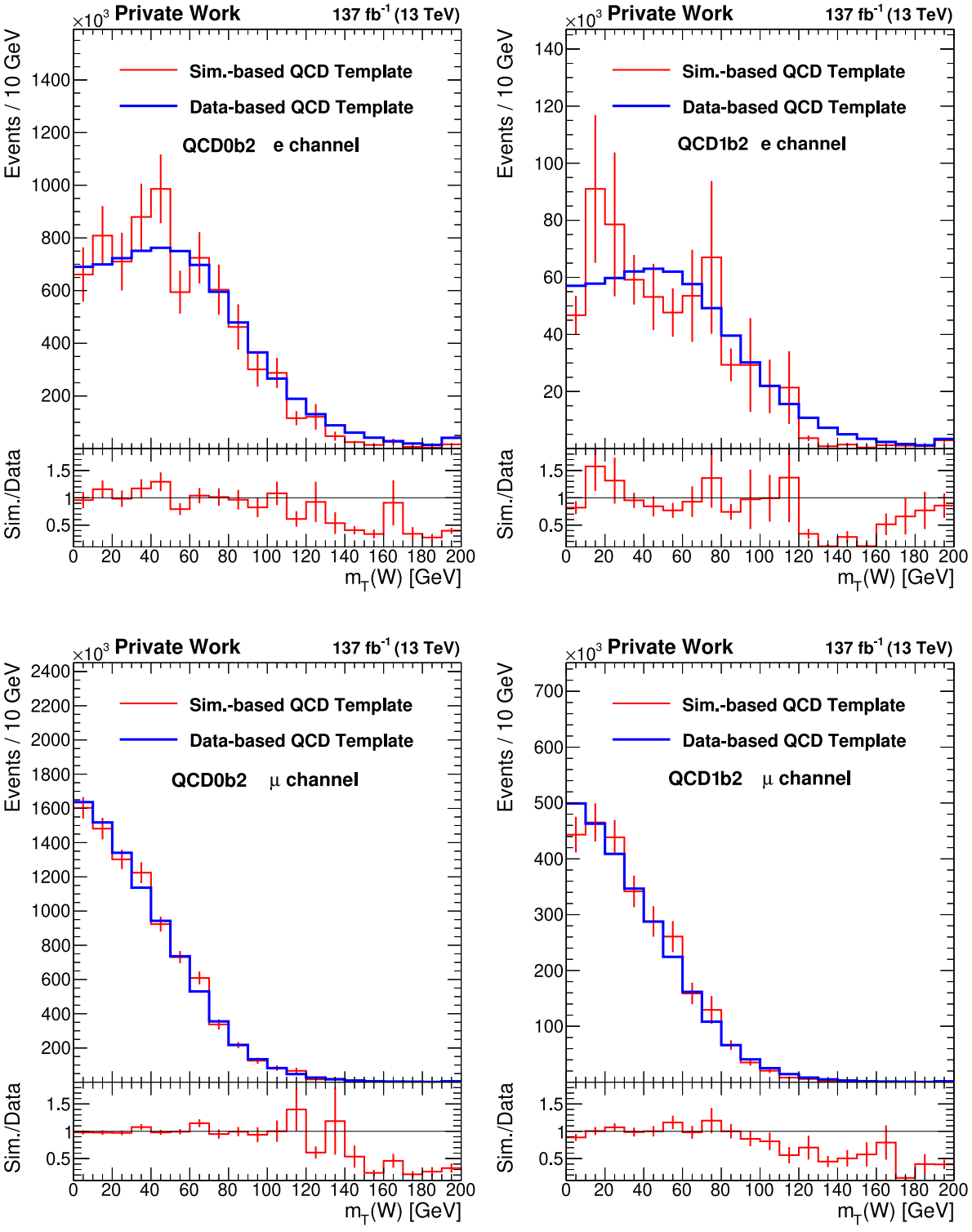

Figure A.1: Shape comparison of data- (blue) and simulation-based (red) QCD multijet templates in the $m_T(W)$ distribution in the electron (upper) and muon (lower) channel in the QCD0b2 (left) and QCD1b2 (right) regions.

Die approbierte gedruckte Originalversion dieser Dissertation ist an der TU Wien Bibliothek verfügbar.
The approved original version of this doctoral thesis is available in print at TU Wien Bibliothek.

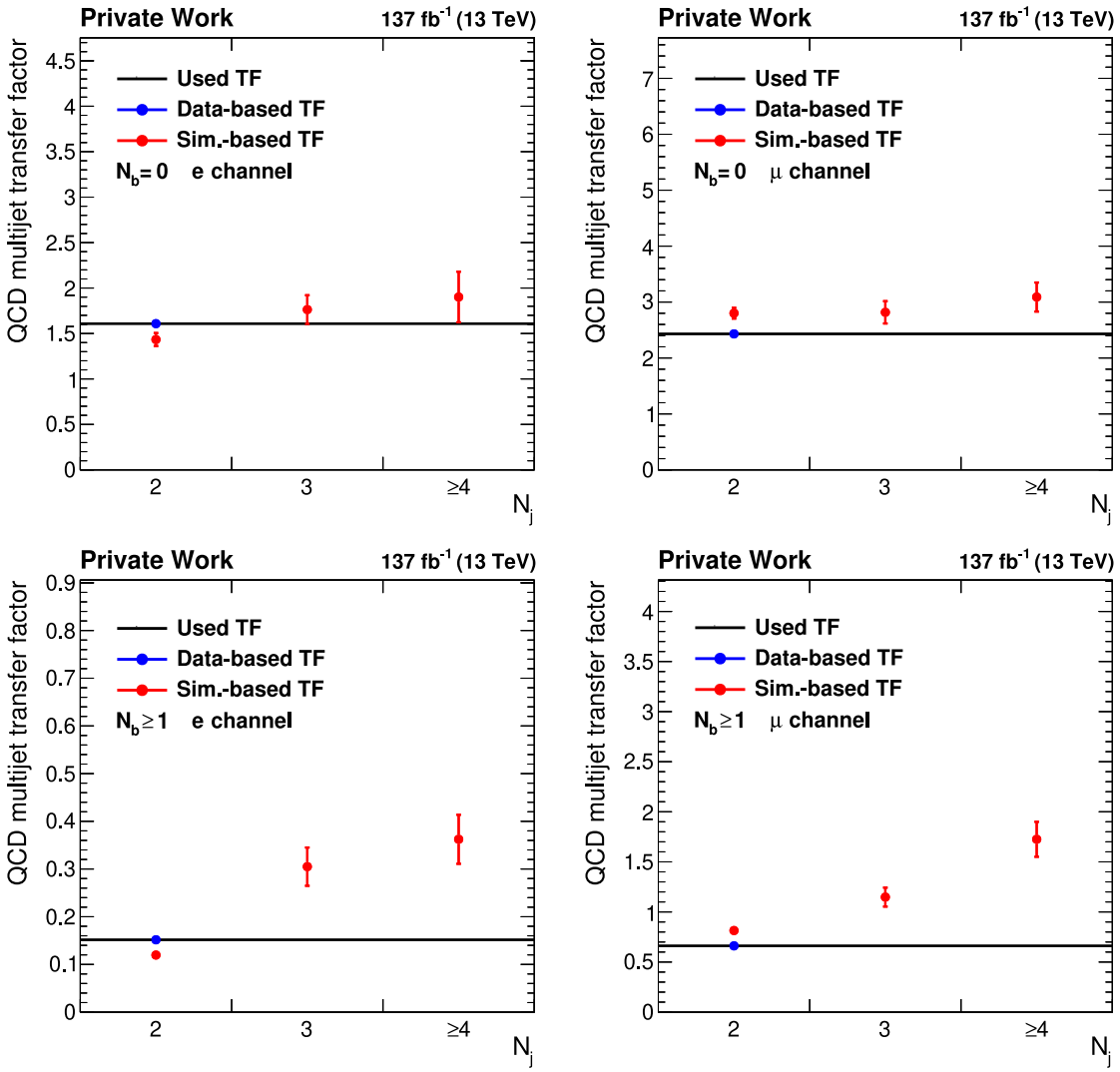

Figure A.2: The extracted QCD multijet transfer factors in $N_\mathrm{b} = 0$ (upper) and $N_\mathrm{b} \geq 1$ (lower) selections in the electron (left) and the muon channel (right) as a function of N_j for measurements in data (blue) and simulation (red). A good agreement is found for $N_\mathrm{b} = 0$ selections and a simulation-based correction is applied to QCD multijet transfer factors in $N_\mathrm{b} \geq 1$ selections to account for their N_j dependence.

Die approbierte gedruckte Originalversion dieser Dissertation ist an der TU Wien Bibliothek verfügbar.
The approved original version of this doctoral thesis is available in print at TU Wien Bibliothek.

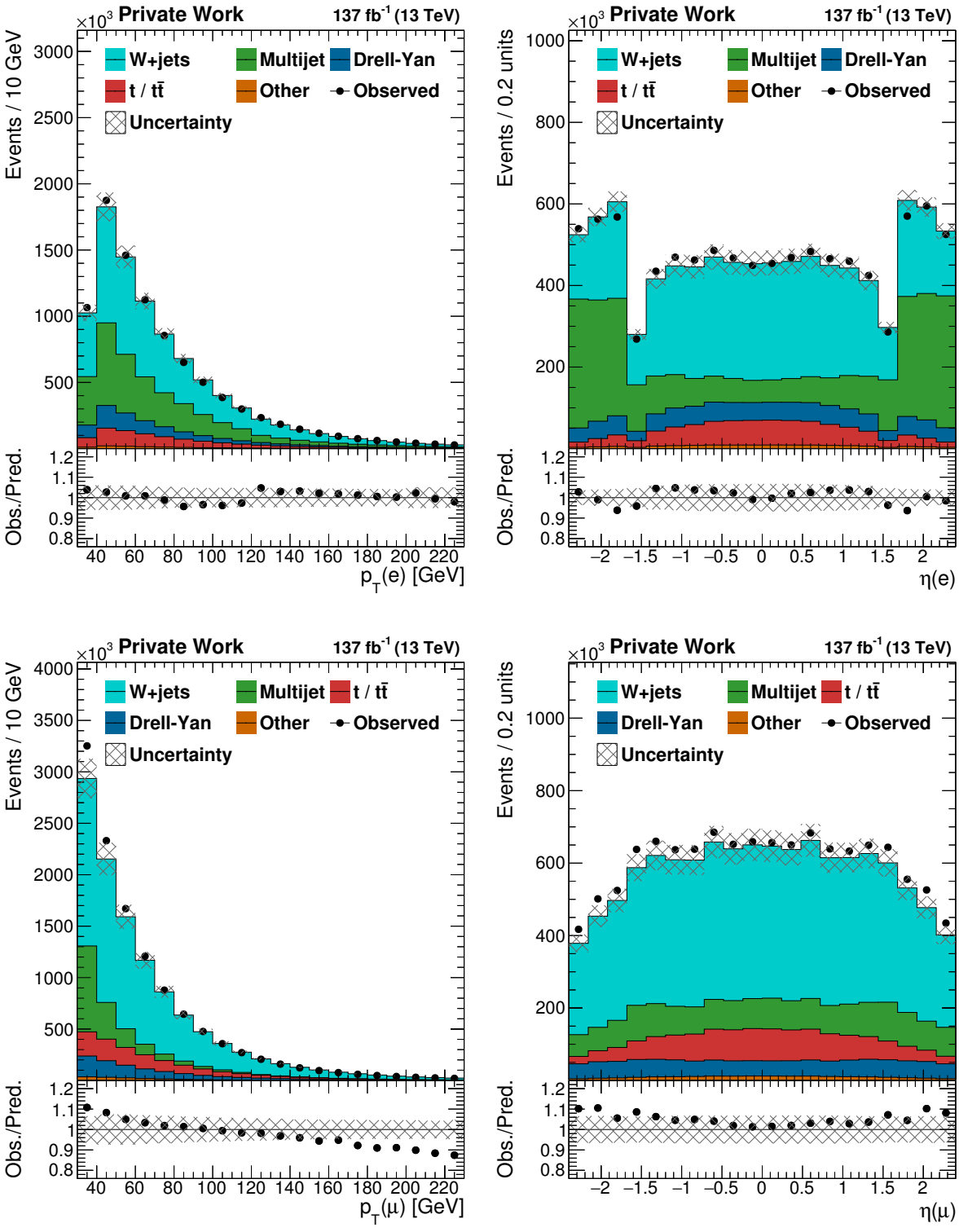

Figure A.3: The $p_T(\ell)$ (left) and $\eta(\ell)$ (right) distributions in the electron (upper) and muon (lower) channel for the QCD0b3p region. The QCD multijet background is estimated in the data-based way described in Sec. 4.4.1. The ratio of observed to predicted event yields is shown in the lower panels and pre-fit systematic uncertainties are shown as hatched bands.

Die approbierte gedruckte Originalversion dieser Dissertation ist an der TU Wien Bibliothek verfügbar.
The approved original version of this doctoral thesis is available in print at TU Wien Bibliothek.

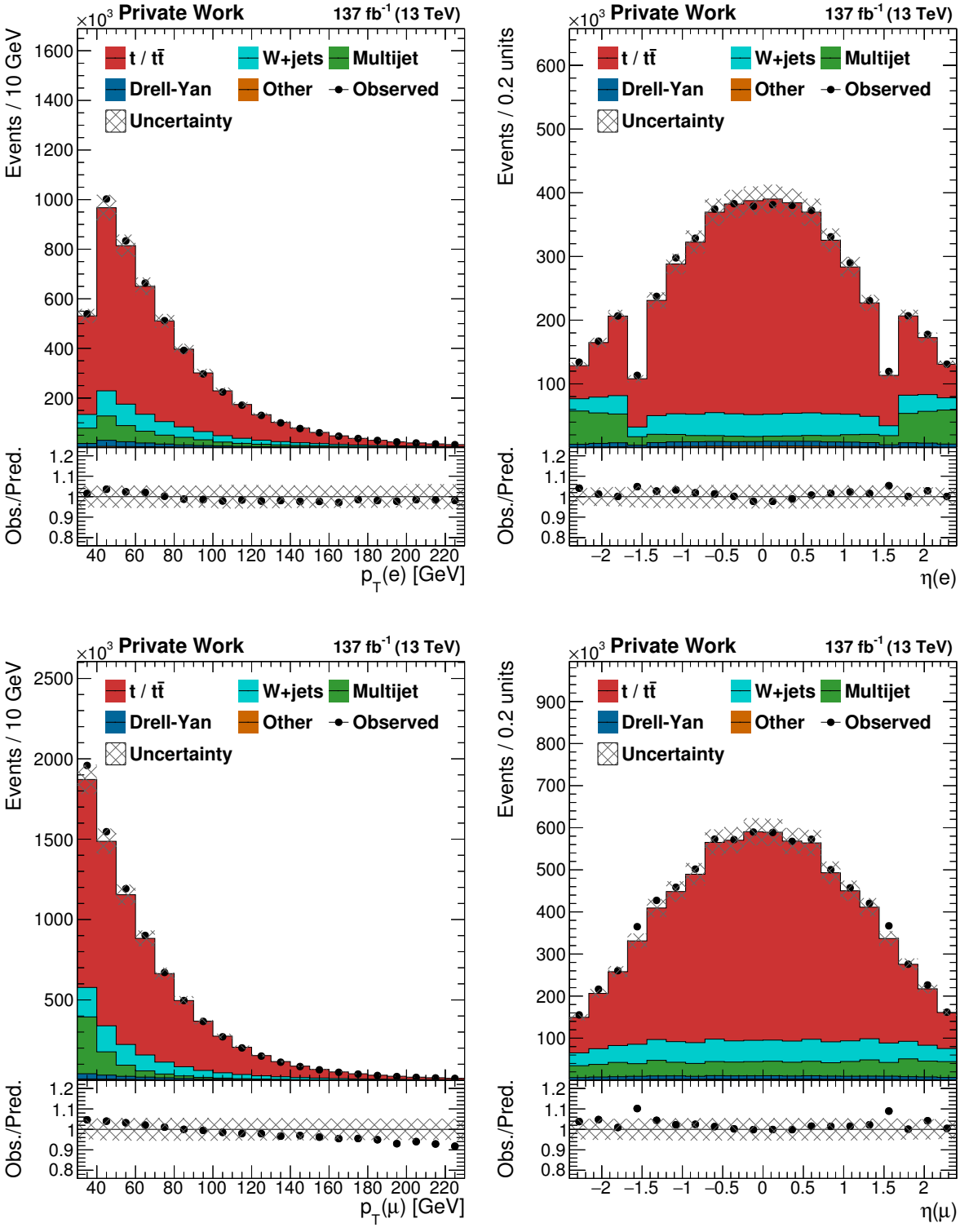

Figure A.4: The $p_T(\ell)$ (left) and $\eta(\ell)$ (right) distributions in the electron (upper) and muon (lower) channel for the QCD1b3p region. The QCD multijet background is estimated in the data-based way described in Sec. 4.4.1. The ratio of observed to predicted event yields is shown in the lower panels and pre-fit systematic uncertainties are shown as hatched bands.

Die approbierte gedruckte Originalversion dieser Dissertation ist an der TU Wien Bibliothek verfügbar.
The approved original version of this doctoral thesis is available in print at TU Wien Bibliothek.

A.2 Fiducial phase space covariance matrices

Differential cross section measurements are performed in the distributions of $p_T(\gamma)$, $|\eta(\gamma)|$, and $\Delta R(\ell, \gamma)$, and unfolded to the particle level. The method is described in Sec. 4.3.3 with the results shown in Sec. 4.6.2. In this procedure, single uncertainty sources extracted from the likelihood fit are unfolded to the fiducial phase space region, allowing to calculate the covariance matrices of the unfolded distributions. The covariance matrices of systematic (left) and statistical (right) uncertainties are given in Fig. A.5 for $p_T(\gamma)$ (upper), $|\eta(\gamma)|$ (center), and $\Delta R(\ell, \gamma)$ (lower), resulting in the correlation matrices given in Fig. 4.24 in Sec. 4.6.2.

Die approbierte gedruckte Originalversion dieser Dissertation ist an der TU Wien Bibliothek verfügbar.
The approved original version of this doctoral thesis is available in print at TU Wien Bibliothek.
TU Bibliothek Your knowledge hub WIEN

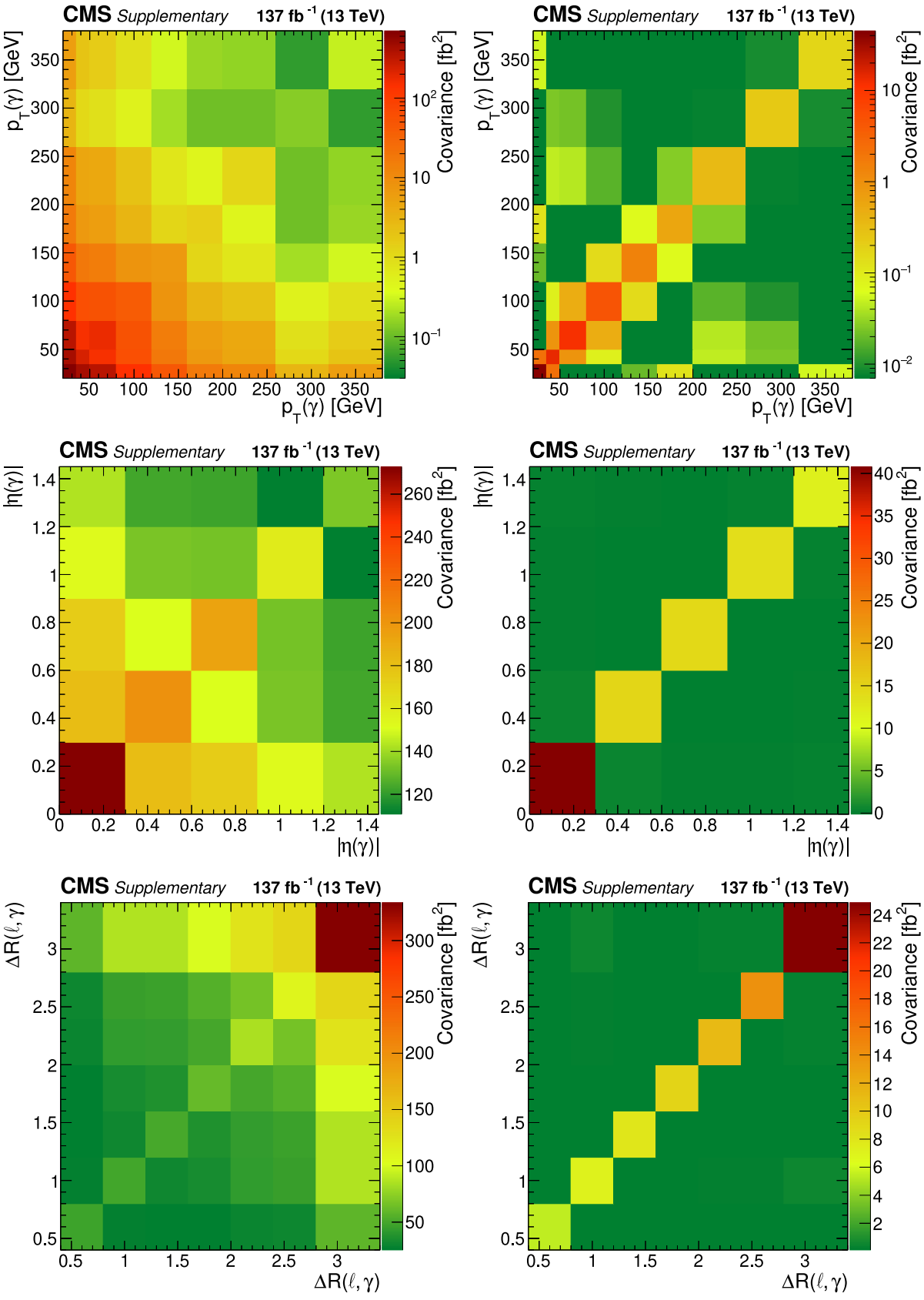

Figure A.5: The covariance matrices of the systematic (left) and statistical (right) uncertainties for $p_T(\gamma)$ (upper), $|\eta(\gamma)|$ (center), and $\Delta R(\ell,\gamma)$ (lower) in the fiducial phase space defined at the particle level.

Die approbierte gedruckte Originalversion dieser Dissertation ist an der TU Wien Bibliothek verfügbar.
The approved original version of this doctoral thesis is available in print at TU Wien Bibliothek.
TU Bibliothek Your knowledge hub WIEN

Die approbierte gedruckte Originalversion dieser Dissertation ist an der TU Wien Bibliothek verfügbar.
The approved original version of this doctoral thesis is available in print at TU Wien Bibliothek.

List of figures

Die approbierte gedruckte Originalversion dieser Dissertation ist an der TU Wien Bibliothek verfügbar.
The approved original version of this doctoral thesis is available in print at TU Wien Bibliothek.
TU Bibliothek Your knowledge hub WIEN

Die approbierte gedruckte Originalversion dieser Dissertation ist an der TU Wien Bibliothek verfügbar.
The approved original version of this doctoral thesis is available in print at TU Wien Bibliothek.
TU Bibliothek Your knowledge hub WIEN

Die approbierte gedruckte Originalversion dieser Dissertation ist an der TU Wien Bibliothek verfügbar.
The approved original version of this doctoral thesis is available in print at TU Wien Bibliothek.
TU Bibliothek Your knowledge hub WIEN

Die approbierte gedruckte Originalversion dieser Dissertation ist an der TU Wien Bibliothek verfügbar.
The approved original version of this doctoral thesis is available in print at TU Wien Bibliothek.

List of tables

Die approbierte gedruckte Originalversion dieser Dissertation ist an der TU Wien Bibliothek verfügbar.
The approved original version of this doctoral thesis is available in print at TU Wien Bibliothek.
TU Bibliothek Your knowledge hub WIEN

Die approbierte gedruckte Originalversion dieser Dissertation ist an der TU Wien Bibliothek verfügbar.
The approved original version of this doctoral thesis is available in print at TU Wien Bibliothek.
TU Bibliothek Your knowledge hub WIEN

List of abbreviations

ALEPH	Apparatus for LEP Physics
ALICE	A Large Ion Collider Experiment
ATLAS	A Toroidal LHC ApparatuS
BDT	boosted decision tree
BSM	beyond the SM
CDF	Collider Detector at Fermilab
CERN	European Organization for Nuclear Research
CKM	Cabibbo–Kobayashi–Maskawa
CL	confidence level
CMS	Compact Muon Solenoid
CSC	cathode strip chamber
d.o.f.	degrees of freedom
DAQ	data acquisition
DNN	deep neural network
DR	diagram removal
DS	diagram subtraction
DT	drift tube
EB	ECAL barrel
ECAL	electromagnetic calorimeter
EDM	electric dipole moment
EE	ECAL endcaps
EFT	effective field theory
ES	preshower detectors
EWSB	electroweak symmetry breaking
Fermilab	Fermi National Accelerator Laboratory
FPGA	field-programmable gate array
FSR	final-state radiation
GSF	Gaussian-sum filter
HB	HCAL barrel
HCAL	hadronic calorimeter

Die approbierte gedruckte Originalversion dieser Dissertation ist an der TU Wien Bibliothek verfügbar.
The approved original version of this doctoral thesis is available in print at TU Wien Bibliothek.

HE	HCAL endcap
HEM	hadronic endcap calorimeter
HF	HCAL forward
HL-LHC	High-Luminosity LHC
HLT	high-level trigger
HM	high-mass
HO	HCAL outer
IP	interaction point
ISR	initial-state radiation
JEC	jet energy correction
JER	jet energy resolution
JES	jet energy scale
KF	Kalman filtering
L1	level-1
LBL	Lawrence Berkeley National Laboratory
LEP	Large Electron Positron Collider
LFU	lepton flavor universality
LHC	Large Hadron Collider
LHCb	LHC beauty
Linac	Linear Accelerator
LM	low-mass
LO	leading order
MC	Monte Carlo
MDM	magnetic dipole moment
ME	matrix element
MVA	multivariate analysis
NbTi	niobium titanium
NLO	next-to-leading order
NNLL	next-to-next-to-leading logarithmic order
NNLO	next-to-next-to-leading order
$PbWO_4$	lead tungstate
PD	primary data set
PDF	parton distribution function
PF	particle-flow
PMNS	Pontecorvo–Maki–Nakagawa–Sakata
pp	proton-proton
PS	Proton Synchrotron
PSB	Proton Synchrotron Booster
PU	pileup
PV	primary vertex

Die approbierte gedruckte Originalversion dieser Dissertation ist an der TU Wien Bibliothek verfügbar.
The approved original version of this doctoral thesis is available in print at TU Wien Bibliothek.
TU Bibliothek Your knowledge hub WIEN

QCD	quantum chromodynamics
QED	quantum electrodynamics
QFT	quantum field theory
RF	radiofrequency
RPC	resistive plate chamber
SC	supercluster
SF	scale factor
SLAC	Stanford Linear Accelerator Center
SM	standard model
SM-EFT	SM effective field theory
SPS	Super Proton Synchrotron
SV	secondary vertex
TEC	tracker endcap
TF	transfer factor
TIB	tracker inner barrel
TID	tracker inner disk
TOB	tracker outer barrel
UA1	Underground Area 1
UA2	Underground Area 2
UFO	universal FeynRules output
vev	vacuum expectation value
WLS	wavelength-shifting

Die approbierte gedruckte Originalversion dieser Dissertation ist an der TU Wien Bibliothek verfügbar.
The approved original version of this doctoral thesis is available in print at TU Wien Bibliothek.
TU Bibliothek Your knowledge hub WIEN

Die approbierte gedruckte Originalversion dieser Dissertation ist an der TU Wien Bibliothek verfügbar.
The approved original version of this doctoral thesis is available in print at TU Wien Bibliothek.

Bibliography

[1] S. L. Glashow. "Partial symmetries of weak interactions". *Nucl. Phys.* 22 (1961), p. 579. DOI: 10.1016/0029-5582(61)90469-2.

[2] S. Weinberg. "A model of leptons". *Phys. Rev. Lett.* 19 (1967), p. 1264. DOI: 10.1103/PhysRevLett.19.1264.

[3] A. Salam. "Weak and electromagnetic interactions". *Conf. Proc. C* 680519 (1968), p. 367. DOI: 10.1142/9789812795915_0034.

[4] CMS Collaboration. "Observation of a new boson at a mass of 125 GeV with the CMS experiment at the LHC". *Phys. Lett. B* 716 (2012), p. 30. DOI: 10.1016/j.physletb.2012.08.021. arXiv: 1207.7235.

[5] ATLAS Collaboration. "Observation of a new particle in the search for the standard model Higgs boson with the ATLAS detector at the LHC". *Phys. Lett. B* 716 (2012), p. 1. DOI: 10.1016/j.physletb.2012.08.020. arXiv: 1207.7214.

[6] P. W. Higgs. "Broken symmetries and the masses of gauge bosons". *Phys. Rev. Lett.* 13 (1964), p. 508. DOI: 10.1103/PhysRevLett.13.508.

[7] F. Englert and R. Brout. "Broken symmetry and the mass of gauge vector mesons". *Phys. Rev. Lett.* 13 (1964), p. 321. DOI: 10.1103/PhysRevLett.13.321.

[8] Supernova Search Team. "Observational evidence from supernovae for an accelerating universe and a cosmological constant". *Astron. J.* 116 (1998), p. 1009. DOI: 10.1086/300499. arXiv: astro-ph/9805201.

[9] Planck Collaboration. "Planck 2018 results. VI. Cosmological parameters". *Astron. Astrophys.* 641 (2020), p. A6. DOI: 10.1051/0004-6361/201833910. arXiv: 1807.06209.

[10] F. Zwicky. "Die Rotverschiebung von extragalaktischen Nebeln". *Helv. Phys. Acta* 6 (1933), p. 110. DOI: 10.1007/s10714-008-0707-4.

[11] V. C. Rubin, N. Thonnard, and W. K. Ford Jr. "Rotational properties of 21 SC galaxies with a large range of luminosities and radii, from NGC 4605 (R = 4 kpc) to UGC 2885 (R = 122 kpc)". *Astrophys. J.* 238 (1980), p. 471. DOI: 10.1086/158003.

[12] D. Maoz and H.-W. Rix. "Early type galaxies, dark halos, and gravitational lensing statistics". *Astrophys. J.* 416 (1993), p. 425. DOI: 10.1086/173248.

[13] D. Clowe, M. Bradac, A. H. Gonzalez, M. Markevitch, S. W. Randall, C. Jones, and D. Zaritsky. "A direct empirical proof of the existence of dark matter". *Astrophys. J. Lett.* 648 (2006), p. L109. DOI: 10.1086/508162. arXiv: astro-ph/0608407.

[14] CDF Collaboration. "Observation of top quark production in $\bar{p}p$ collisions". *Phys. Rev. Lett.* 74 (1995), p. 2626. DOI: 10.1103/PhysRevLett.74.2626. arXiv: hep-ex/9503002.

Die approbierte gedruckte Originalversion dieser Dissertation ist an der TU Wien Bibliothek verfügbar.
The approved original version of this doctoral thesis is available in print at TU Wien Bibliothek.
TU Bibliothek Your knowledge hub WIEN

[15] D0 Collaboration. "Observation of the top quark". *Phys. Rev. Lett.* 74 (1995), p. 2632. DOI: 10.1103/PhysRevLett.74.2632. arXiv: hep-ex/9503003.

[16] W. Hollik, J. I. Illana, S. Rigolin, C. Schappacher, and D. Stockinger. "Top dipole form-factors and loop induced CP violation in supersymmetry". *Nucl. Phys. B* 551 (1999), p. 3. DOI: 10.1016/S0550-3213(99)00396-X. arXiv: hep-ph/9812298. [Erratum: *Nucl. Phys. B* 557 (1999), p. 407].

[17] K. Agashe, G. Perez, and A. Soni. "Collider signals of top quark flavor violation from a warped extra dimension". *Phys. Rev. D* 75 (2007), p. 015002. DOI: 10.1103/PhysRevD.75.015002. arXiv: hep-ph/0606293.

[18] A. L. Kagan, G. Perez, T. Volansky, and J. Zupan. "General minimal flavor violation". *Phys. Rev. D* 80 (2009), p. 076002. DOI: 10.1103/PhysRevD.80.076002. arXiv: 0903.1794.

[19] T. Ibrahim and P. Nath. "The top quark electric dipole moment in an MSSM extension with vector like multiplets". *Phys. Rev. D* 82 (2010), p. 055001. DOI: 10.1103/PhysRevD.82.055001. arXiv: 1007.0432.

[20] T. Ibrahim and P. Nath. "The chromoelectric dipole moment of the top quark in models with vector like multiplets". *Phys. Rev. D* 84 (2011), p. 015003. DOI: 10.1103/PhysRevD.84.015003. arXiv: 1104.3851.

[21] C. Grojean, O. Matsedonskyi, and G. Panico. "Light top partners and precision physics". *JHEP* 10 (2013), p. 160. DOI: 10.1007/JHEP10(2013)160. arXiv: 1306.4655.

[22] F. Richard. "Can LHC observe an anomaly in $t\bar{t}Z$ production?" (2013). arXiv: 1304.3594.

[23] B. Grinstein and M. B. Wise. "Operator analysis for precision electroweak physics". *Phys. Lett. B* 265 (1991), p. 326. DOI: 10.1016/0370-2693(91)90061-T.

[24] R. Alonso, E. E. Jenkins, A. V. Manohar, and M. Trott. "Renormalization group evolution of the standard model dimension six operators III: Gauge coupling dependence and phenomenology". *JHEP* 04 (2014), p. 159. DOI: 10.1007/JHEP04(2014)159. arXiv: 1312.2014.

[25] L. Berthier and M. Trott. "Towards consistent electroweak precision data constraints in the SMEFT". *JHEP* 05 (2015), p. 024. DOI: 10.1007/JHEP05(2015)024. arXiv: 1502.02570.

[26] L. Berthier and M. Trott. "Consistent constraints on the standard model effective field theory". *JHEP* 02 (2016), p. 069. DOI: 10.1007/JHEP02(2016)069. arXiv: 1508.05060.

[27] I. Brivio and M. Trott. "Scheming in the SMEFT... and a reparameterization invariance!" *JHEP* 07 (2017), p. 148. DOI: 10.1007/JHEP07(2017)148. arXiv: 1701.06424. [Addendum: *JHEP* 05 (2018), p. 136].

[28] I. Brivio and M. Trott. "The standard model as an effective field theory". *Phys. Rept.* 793 (2019), p. 1. DOI: 10.1016/j.physrep.2018.11.002. arXiv: 1706.08945.

[29] G. Passarino and M. Trott. "The standard model effective field theory and next to leading order" (2016). arXiv: 1610.08356.

Die approbierte gedruckte Originalversion dieser Dissertation ist an der TU Wien Bibliothek verfügbar.
The approved original version of this doctoral thesis is available in print at TU Wien Bibliothek.
TU Bibliothek Your knowledge hub WIEN

[30] B. Grzadkowski, M. Iskrzynski, M. Misiak, and J. Rosiek. "Dimension-six terms in the standard model Lagrangian". *JHEP* 10 (2010), p. 085. DOI: 10.1007/JHEP10(2010)085. arXiv: 1008.4884.

[31] CMS Collaboration. "Measurement of the inclusive and differential $t\bar{t}\gamma$ cross sections in the single-lepton channel and EFT interpretation at $\sqrt{s} = 13\,\text{TeV}$". *Submitted to JHEP* (2021). arXiv: 2107.01508.

[32] CMS Collaboration. "Measurement of the inclusive and differential $t\bar{t}\gamma$ cross sections in the single-lepton channel and EFT interpretation at $\sqrt{s} = 13\,\text{TeV}$". *HEPData record* (2021). DOI: 10.17182/hepdata.102876.

[33] L. Lechner. "$t\bar{t}+\gamma$ inclusive and differential measurement by CMS". *Submitted to ARISF* (2021). Proceedings of the 55th Rencontres de Moriond 2021 Electroweak Interactions and Unified Theories. URL: https://bit.ly/2XARsaV.

[34] L. Lechner and C. Diez Pardos. "Latest ttgamma results from CMS and comparison with ATLAS". *LHCTOP 2021* (2021). URL: https://bit.ly/3wCvMq9.

[35] L. Lechner. "Measurement of the inclusive and differential $t\bar{t}\gamma$ cross sections and EFT interpretation in the single-lepton channel at CMS". *Joint Annual Meeting of ÖPG and SPS 2021* (2021). URL: https://bit.ly/3z1bVCi.

[36] CMS Collaboration. "Measurement of the inclusive and differential $t\bar{t}\gamma$ cross section and EFT interpretation in the dilepton channel at $\sqrt{s} = 13\,\text{TeV}$". *Prepared for submission to JHEP* (2021). URL: https://bit.ly/39lEmAn.

[37] S. Chatterjee, N. Frohner, L. Lechner, R. Schöfbeck, and D. Schwarz. "Tree boosting for learning EFT parameters". *Submitted to Comput. Phys. Commun.* (2021). arXiv: 2107.10859.

[38] S. Fernbach, L. Lechner, A. Maas, S. Plätzer, and R. Schöfbeck. "Constraining the Higgs valence contribution in the proton". *Phys. Rev. D* 101 (2020), p. 114018. DOI: 10.1103/PhysRevD.101.114018. arXiv: 2002.01688.

[39] N. Andari et al. "Report on the ECFA early-career researchers debate on the 2020 European Strategy Update for Particle Physics" (2020). arXiv: 2002.02837.

[40] P. Azzi et al. "Report from working group 1: Standard model physics at the HL-LHC and HE-LHC". *CERN Yellow Rep. Monogr.* 7 (2019), p. 1. DOI: 10.23731/CYRM-2019-007.1. arXiv: 1902.04070.

[41] J. Schwichtenberg. "Physics from symmetry". *Springer International Publishing* (2015), p. 1. DOI: 10.1007/978-3-319-19201-7.

[42] A. Einstein. "Die Grundlage der allgemeinen Relativitätstheorie". *Annalen der Physik* 354 (1916), p. 769. DOI: 10.1002/andp.19163540702.

[43] Gargamelle Collaboration. "Observation of neutrino-like interactions without muon or electron in the Gargamelle neutrino experiment". *Phys. Lett. B* 46 (1973), p. 138. DOI: 10.1016/0370-2693(73)90499-1.

[44] Particle Data Group. "Review of particle physics". *PTEP* 2020 (2020), p. 083C01. DOI: 10.1093/ptep/ptaa104.

[45] M. Kobayashi and T. Maskawa. "CP violation in the renormalizable theory of weak interaction". *Prog. Theor. Phys.* 49 (1973), p. 652. DOI: 10.1143/PTP.49.652.

Die approbierte gedruckte Originalversion dieser Dissertation ist an der TU Wien Bibliothek verfügbar.
The approved original version of this doctoral thesis is available in print at TU Wien Bibliothek.
TU Bibliothek Your knowledge hub WIEN

[46] N. Cabibbo. "Unitary symmetry and leptonic decays". *Phys. Rev. Lett.* 10 (1963), p. 531. DOI: 10.1103/PhysRevLett.10.531.

[47] J. H. Christenson, J. W. Cronin, V. L. Fitch, and R. Turlay. "Evidence for the 2π decay of the K_2^0 meson". *Phys. Rev. Lett.* 13 (1964), p. 138. DOI: 10.1103/PhysRevLett.13.138.

[48] M. L. Perl et al. "Evidence for anomalous lepton production in e^+-e^- annihilation". *Phys. Rev. Lett.* 35 (1975), p. 1489. DOI: 10.1103/PhysRevLett.35.1489.

[49] S. W. Herb et al. "Observation of a dimuon resonance at 9.5 GeV in 400 GeV proton-nucleus collisions". *Phys. Rev. Lett.* 39 (1977), p. 252. DOI: 10.1103/PhysRevLett.39.252.

[50] "LEP design report: Vol.2. The LEP main ring". *CERN* CERN-LEP-84-01 (1984), p. 1. URL: https://bit.ly/36vqW3j.

[51] ALEPH Collaboration. "Determination of the number of light neutrino species". *Phys. Lett. B* 231 (1989), p. 519. DOI: 10.1016/0370-2693(89)90704-1.

[52] DELPHI Collaboration. "Measurement of the mass and width of the Z^0 particle from multi-hadronic final states produced in e^+e^- annihilations". *Phys. Lett. B* 231 (1989), p. 539. DOI: 10.1016/0370-2693(89)90706-5.

[53] OPAL Collaboration. "Measurement of the Z^0 mass and width with the OPAL detector at LEP". *Phys. Lett. B* 231 (1989), p. 530. DOI: 10.1016/0370-2693(89)90705-3.

[54] L3 Collaboration. "A determination of the properties of the neutral intermediate vector boson Z^0". *Phys. Lett. B* 231 (1989), p. 509. DOI: 10.1016/0370-2693(89)90703-X.

[55] CLEO Collaboration. "Upper limit on flavor changing neutral current decays of the b quark". *Phys. Rev. Lett.* 53 (1984), p. 1309. DOI: 10.1103/PhysRevLett.53.1309.

[56] JADE Collaboration. "Determination of semimuonic branching ratios and fragmentation functions of heavy quarks in e^+e^- annihilation at $\sqrt{s} = 34.6$ GeV". *Z. Phys. C* 33 (1987), p. 339. DOI: 10.1007/BF01552539.

[57] Pluto Collaboration. "Observation of a narrow resonance formed in e^+e^- annihilation at 9.46 GeV". *Phys. Lett. B* 76 (1978), p. 243. DOI: 10.1016/0370-2693(78)90287-3.

[58] C. W. Darden et al. "Evidence for a narrow resonance at 10.01 GeV in electron-positron annihilations". *Phys. Lett. B* 78 (1978), p. 364. DOI: 10.1016/0370-2693(78)90041-2.

[59] S. Coleman and J. Mandula. "All possible symmetries of the S matrix". *Phys. Rev.* 159 (1967), p. 1251. DOI: 10.1103/PhysRev.159.1251.

[60] D. Hanneke, S. Fogwell, and G. Gabrielse. "New measurement of the electron magnetic moment and the fine structure constant". *Phys. Rev. Lett.* 100 (2008), p. 120801. DOI: 10.1103/PhysRevLett.100.120801. arXiv: 0801.1134.

[61] E. Noether. "Invariante Variationsprobleme". *Nachr. d. König. Gesellsch. d. Wiss. zu Göttingen, Math-phys. Klasse* (1918), p. 235. DOI: 10.1080/00411457108231446. arXiv: physics/0503066.

Die approbierte gedruckte Originalversion dieser Dissertation ist an der TU Wien Bibliothek verfügbar.
The approved original version of this doctoral thesis is available in print at TU Wien Bibliothek.
TU Bibliothek Your knowledge hub WIEN

[62] C. S. Wu, E. Ambler, R. W. Hayward, D. D. Hoppes, and R. P. Hudson. "Experimental test of parity conservation in β decay". *Phys. Rev.* 105 (1957), p. 1413. DOI: 10.1103/PhysRev.105.1413.

[63] Y. Nambu. "Quasiparticles and gauge invariance in the theory of superconductivity". *Phys. Rev.* 117 (1960), p. 648. DOI: 10.1103/PhysRev.117.648.

[64] J. Goldstone. "Field theories with superconductor solutions". *Nuovo Cim.* 19 (1961), p. 154. DOI: 10.1007/BF02812722.

[65] J. Goldstone, A. Salam, and S. Weinberg. "Broken symmetries". *Phys. Rev.* 127 (1962), p. 965. DOI: 10.1103/PhysRev.127.965.

[66] ATLAS and CMS Collaborations. "Measurements of the Higgs boson production and decay rates and constraints on its couplings from a combined ATLAS and CMS analysis of the LHC pp collision data at $\sqrt{s} = 7$ and 8 TeV". *JHEP* 08 (2016), p. 045. DOI: 10.1007/JHEP08(2016)045. arXiv: 1606.02266.

[67] B. Pontecorvo. "Inverse β processes and nonconservation of lepton charge". *Zh. Eksp. Teor. Fiz.* 34 (1957), p. 247.

[68] Z. Maki, M. Nakagawa, and S. Sakata. "Remarks on the unified model of elementary particles". *Prog. Theor. Phys.* 28 (1962), p. 870. DOI: 10.1143/PTP.28.870.

[69] SNO Collaboration. "Measurement of the rate of $\nu_e + d \to p + p + e^-$ interactions produced by ^{8}B solar neutrinos at the Sudbury Neutrino Observatory". *Phys. Rev. Lett.* 87 (2001), p. 071301. DOI: 10.1103/PhysRevLett.87.071301. arXiv: nucl-ex/0106015.

[70] Super-Kamiokande Collaboration. "Evidence for oscillation of atmospheric neutrinos". *Phys. Rev. Lett.* 81 (1998), p. 1562. DOI: 10.1103/PhysRevLett.81.1562. arXiv: hep-ex/9807003.

[71] H. Fritzsch, M. Gell-Mann, and H. Leutwyler. "Advantages of the color octet gluon picture". *Phys. Lett. B* 47 (1973), p. 365. DOI: 10.1016/0370-2693(73)90625-4.

[72] D. J. Gross and F. Wilczek. "Asymptotically free gauge theories. II". *Phys. Rev. D* 9 (1974), p. 980. DOI: 10.1103/PhysRevD.9.980.

[73] S. Weinberg. "Non-abelian gauge theories of the strong interactions". *Phys. Rev. Lett.* 31 (1973), p. 494. DOI: 10.1103/PhysRevLett.31.494.

[74] M. Gell-Mann. "Symmetries of baryons and mesons". *Phys. Rev.* 125 (1962), p. 1067. DOI: 10.1103/PhysRev.125.1067.

[75] H. D. Politzer. "Reliable perturbative results for strong interactions?" *Phys. Rev. Lett.* 30 (1973), p. 1346. DOI: 10.1103/PhysRevLett.30.1346.

[76] D. J. Gross and F. Wilczek. "Ultraviolet behavior of non-abelian gauge theories". *Phys. Rev. Lett.* 30 (1973), p. 1343. DOI: 10.1103/PhysRevLett.30.1343.

[77] LHCb Collaboration. "Observation of $J/\psi\phi$ structures consistent with exotic states from amplitude analysis of $B^+ \to J/\psi\phi K^+$ decays". *Phys. Rev. Lett.* 118 (2017), p. 022003. DOI: 10.1103/PhysRevLett.118.022003. arXiv: 1606.07895.

[78] LHCb Collaboration. "Observation of J/ψp resonances consistent with pentaquark states in $\Lambda_b^0 \to J/\psi K^-$p decays". *Phys. Rev. Lett.* 115 (2015), p. 072001. DOI: 10.1103/PhysRevLett.115.072001. arXiv: 1507.03414.

Die approbierte gedruckte Originalversion dieser Dissertation ist an der TU Wien Bibliothek verfügbar.
The approved original version of this doctoral thesis is available in print at TU Wien Bibliothek.
TU Bibliothek Your knowledge hub WIEN

[79] J. C. Collins, D. E. Soper, and G. F. Sterman. "Factorization of hard processes in QCD". *Adv. Ser. Direct. High Energy Phys.* 5 (1989), p. 1. DOI: 10.1142/9789814503266_0001. arXiv: hep-ph/0409313.

[80] R. D. Ball et al. "Parton distributions with LHC data". *Nucl. Phys. B* 867 (2013), p. 244. DOI: 10.1016/j.nuclphysb.2012.10.003. arXiv: 1207.1303.

[81] NNPDF Collaboration. "Parton distributions for the LHC Run II". *JHEP* 04 (2015), p. 040. DOI: 10.1007/JHEP04(2015)040. arXiv: 1410.8849.

[82] NNPDF Collaboration. "Parton distributions from high-precision collider data". *Eur. Phys. J. C* 77 (2017), p. 663. DOI: 10.1140/epjc/s10052-017-5199-5. arXiv: 1706.00428.

[83] G. 't Hooft. "Renormalization of massless Yang-Mills fields". *Nucl. Phys. B* 33 (1971), p. 173. DOI: 10.1016/0550-3213(71)90395-6.

[84] G. 't Hooft. "Renormalizable Lagrangians for massive Yang-Mills fields". *Nucl. Phys. B* 35 (1971), p. 167. DOI: 10.1016/0550-3213(71)90139-8.

[85] G. 't Hooft and M. J. G. Veltman. "Regularization and renormalization of gauge fields". *Nucl. Phys. B* 44 (1972), p. 189. DOI: 10.1016/0550-3213(72)90279-9.

[86] J. Alwall, R. Frederix, S. Frixione, V. Hirschi, F. Maltoni, O. Mattelaer, H. S. Shao, T. Stelzer, P. Torrielli, and M. Zaro. "The automated computation of tree-level and next-to-leading order differential cross sections, and their matching to parton shower simulations". *JHEP* 07 (2014), p. 079. DOI: 10.1007/JHEP07(2014)079. arXiv: 1405.0301.

[87] P. Nason. "A new method for combining NLO QCD with shower Monte Carlo algorithms". *JHEP* 11 (2004), p. 040. DOI: 10.1088/1126-6708/2004/11/040. arXiv: hep-ph/0409146.

[88] S. Frixione, P. Nason, and C. Oleari. "Matching NLO QCD computations with parton shower simulations: The POWHEG method". *JHEP* 11 (2007), p. 070. DOI: 10.1088/1126-6708/2007/11/070. arXiv: 0709.2092.

[89] S. Alioli, P. Nason, C. Oleari, and E. Re. "A general framework for implementing NLO calculations in shower Monte Carlo programs: The POWHEG BOX". *JHEP* 06 (2010), p. 043. DOI: 10.1007/JHEP06(2010)043. arXiv: 1002.2581.

[90] T. Sjöstrand, S. Ask, J. R. Christiansen, R. Corke, N. Desai, P. Ilten, S. Mrenna, S. Prestel, C. O. Rasmussen, and P. Z. Skands. "An introduction to PYTHIA 8.2". *Comput. Phys. Commun.* 191 (2015), p. 159. DOI: 10.1016/j.cpc.2015.01.024. arXiv: 1410.3012.

[91] J. Bellm et al. "Herwig 7.0/Herwig++ 3.0 release note". *Eur. Phys. J. C* 76 (2016), p. 196. DOI: 10.1140/epjc/s10052-016-4018-8. arXiv: 1512.01178.

[92] CMS Collaboration. "Development and validation of HERWIG 7 tunes from CMS underlying-event measurements". *Eur. Phys. J. C* 81 (2021), p. 312. DOI: 10.1140/epjc/s10052-021-08949-5. arXiv: 2011.03422.

[93] CMS Collaboration. "Event generator tunes obtained from underlying event and multiparton scattering measurements". *Eur. Phys. J. C* 76 (2016), p. 155. DOI: 10.1140/epjc/s10052-016-3988-x. arXiv: 1512.00815.

TU Bibliothek Your knowledge hub WIEN
Die approbierte gedruckte Originalversion dieser Dissertation ist an der TU Wien Bibliothek verfügbar.
The approved original version of this doctoral thesis is available in print at TU Wien Bibliothek.

[94] CMS Collaboration. "Extraction and validation of a new set of CMS PYTHIA8 tunes from underlying-event measurements". *Eur. Phys. J. C* 80 (2020), p. 4. DOI: 10.1140/epjc/s10052-019-7499-4. arXiv: 1903.12179.

[95] CDF and D0 Collaborations. "Combination of the top-quark mass measurements from the Tevatron collider". *Phys. Rev. D* 86 (2012), p. 092003. DOI: 10.1103/PhysRevD.86.092003. arXiv: 1207.1069.

[96] CMS Collaboration. "Combination of ATLAS and CMS results on the mass of the top quark using up to 4.9 fb^{-1} of data". *CMS Physics Analysis Summaries* CMS-PAS-TOP-13-005 (2013). URL: https://bit.ly/3r1gQAM.

[97] ATLAS Collaboration. "Combination of ATLAS and CMS results on the mass of the top quark using up to 4.9 fb^{-1} of data". *ATLAS Note* ATLAS-CONF-2012-095 (2012). URL: https://bit.ly/3hYdWbT.

[98] LHC Top Working Group. "LHCTopWG summary plots". *LHCPhysics Web* (2021). URL: https://bit.ly/3e8TtQx.

[99] M. Czakon and A. Mitov. "Top++: A program for the calculation of the top-pair cross-section at hadron colliders". *Comput. Phys. Commun.* 185 (2014), p. 2930. DOI: 10.1016/j.cpc.2014.06.021. arXiv: 1112.5675.

[100] J. Butterworth et al. "PDF4LHC recommendations for LHC Run II". *J. Phys. G* 43 (2016), p. 023001. DOI: 10.1088/0954-3899/43/2/023001. arXiv: 1510.03865.

[101] A. D. Martin, W. J. Stirling, R. S. Thorne, and G. Watt. "Parton distributions for the LHC". *Eur. Phys. J. C* 63 (2009), p. 189. DOI: 10.1140/epjc/s10052-009-1072-5. arXiv: 0901.0002.

[102] A. D. Martin, W. J. Stirling, R. S. Thorne, and G. Watt. "Uncertainties on α_s in global PDF analyses and implications for predicted hadronic cross sections". *Eur. Phys. J. C* 64 (2009), p. 653. DOI: 10.1140/epjc/s10052-009-1164-2. arXiv: 0905.3531.

[103] H.-L. Lai, M. Guzzi, J. Huston, Z. Li, P. M. Nadolsky, J. Pumplin, and C. P. Yuan. "New parton distributions for collider physics". *Phys. Rev. D* 82 (2010), p. 074024. DOI: 10.1103/PhysRevD.82.074024. arXiv: 1007.2241.

[104] J. Gao, M. Guzzi, J. Huston, H.-L. Lai, Z. Li, P. Nadolsky, J. Pumplin, D. Stump, and C. P. Yuan. "CT10 next-to-next-to-leading order global analysis of QCD". *Phys. Rev. D* 89 (2014), p. 033009. DOI: 10.1103/PhysRevD.89.033009. arXiv: 1302.6246.

[105] T. M. P. Tait and C. P. Yuan. "Single top quark production as a window to physics beyond the standard model". *Phys. Rev. D* 63 (2000), p. 014018. DOI: 10.1103/PhysRevD.63.014018. arXiv: hep-ph/0007298.

[106] S. Frixione, E. Laenen, P. Motylinski, B. R. Webber, and C. D. White. "Single-top hadroproduction in association with a W boson". *JHEP* 07 (2008), p. 029. DOI: 10.1088/1126-6708/2008/07/029. arXiv: 0805.3067.

[107] M. Aliev, H. Lacker, U. Langenfeld, S. Moch, P. Uwer, and M. Wiedermann. "HATHOR: HAdronic Top and Heavy quarks crOss section calculatoR". *Comput. Phys. Commun.* 182 (2011), p. 1034. DOI: 10.1016/j.cpc.2010.12.040. arXiv: 1007.1327.

TU Bibliothek Your knowledge hub WIEN
Die approbierte gedruckte Originalversion dieser Dissertation ist an der TU Wien Bibliothek verfügbar.
The approved original version of this doctoral thesis is available in print at TU Wien Bibliothek.

[108] P. Kant, O. M. Kind, T. Kintscher, T. Lohse, T. Martini, S. Mölbitz, P. Rieck, and P. Uwer. "HatHor for single top-quark production: Updated predictions and uncertainty estimates for single top-quark production in hadronic collisions". *Comput. Phys. Commun.* 191 (2015), p. 74. DOI: 10.1016/j.cpc.2015.02.001. arXiv: 1406.4403.

[109] S. Bethke. "Determination of the QCD coupling α_s". *J. Phys. G* 26 (2000), p. R27. DOI: 10.1088/0954-3899/26/7/201. arXiv: hep-ex/0004021.

[110] ATLAS Collaboration. "Measurement of the top-quark decay width in top-quark pair events in the dilepton channel at $\sqrt{s} = 13\,\text{TeV}$ with the ATLAS detector". *ATLAS Note* ATLAS-CONF-2019-038 (2019). URL: https://bit.ly/2UJFtWn.

[111] I. Bigi, Y. Dokshitzer, V. Khoze, J. Kühn, and P. Zerwas. "Production and decay properties of ultra-heavy quarks". *Phys. Lett. B* 181 (1986), p. 157. DOI: 10.1016/0370-2693(86)91275-X.

[112] CDF and D0 Collaborations. "Tevatron Combination of single-top-quark cross sections and determination of the magnitude of the Cabibbo–Kobayashi–Maskawa matrix element V_{tb}". *Phys. Rev. Lett.* 115 (2015), p. 152003. DOI: 10.1103/PhysRevLett.115.152003. arXiv: 1503.05027.

[113] ATLAS and CMS Collaborations. "Combinations of single-top-quark production cross-section measurements and $|f_{LV}V_{\text{tb}}|$ determinations at $\sqrt{s} = 7$ and 8 TeV with the ATLAS and CMS experiments". *JHEP* 05 (2019), p. 088. DOI: 10.1007/JHEP05(2019)088. arXiv: 1902.07158.

[114] CMS Collaboration. "Measurement of the single top quark and antiquark production cross sections in the t channel and their ratio in proton-proton collisions at $\sqrt{s} = 13\,\text{TeV}$". *Phys. Lett. B* 800 (2020), p. 135042. DOI: 10.1016/j.physletb.2019.135042. arXiv: 1812.10514.

[115] CMS Collaboration. "Measurement of the production cross section for single top quarks in association with W bosons in proton-proton collisions at $\sqrt{s} = 13\,\text{TeV}$". *JHEP* 10 (2018), p. 117. DOI: 10.1007/JHEP10(2018)117. arXiv: 1805.07399.

[116] CMS Collaboration. "Observation of $\text{t}\bar{\text{t}}\text{H}$ production". *Phys. Rev. Lett.* 120 (2018), p. 231801. DOI: 10.1103/PhysRevLett.120.231801. arXiv: 1804.02610.

[117] CMS Collaboration. "Search for $\text{t}\bar{\text{t}}\text{H}$ production in the $\text{H} \to \text{b}\bar{\text{b}}$ decay channel with leptonic $\text{t}\bar{\text{t}}$ decays in proton-proton collisions at $\sqrt{s} = 13\,\text{TeV}$". *JHEP* 03 (2019), p. 026. DOI: 10.1007/JHEP03(2019)026. arXiv: 1804.03682.

[118] ATLAS Collaboration. "Observation of Higgs boson production in association with a top quark pair at the LHC with the ATLAS detector". *Phys. Lett. B* 784 (2018), p. 173. DOI: 10.1016/j.physletb.2018.07.035. arXiv: 1806.00425.

[119] LHC Higgs Cross Section Working Group. "Handbook of LHC Higgs cross sections: 4. Deciphering the nature of the Higgs sector". *CERN Yellow Rep. Monogr.* 2 (2017), p. 1. DOI: 10.23731/CYRM-2017-002. arXiv: 1610.07922.

[120] J. A. Aguilar-Saavedra. "A minimal set of top anomalous couplings". *Nucl. Phys. B* 812 (2009), p. 181. DOI: 10.1016/j.nuclphysb.2008.12.012. arXiv: 0811.3842.

[121] M. Beneke, P. Falgari, S. Klein, and C. Schwinn. "Hadronic top-quark pair production with NNLL threshold resummation". *Nucl. Phys. B* 855 (2012), p. 695. DOI: 10.1016/j.nuclphysb.2011.10.021. arXiv: 1109.1536.

Die approbierte gedruckte Originalversion dieser Dissertation ist an der TU Wien Bibliothek verfügbar.
The approved original version of this doctoral thesis is available in print at TU Wien Bibliothek.
TU Bibliothek Your knowledge hub WIEN

[122] M. Cacciari, M. Czakon, M. Mangano, A. Mitov, and P. Nason. "Top-pair production at hadron colliders with next-to-next-to-leading logarithmic soft-gluon resummation". *Phys. Lett. B* 710 (2012), p. 612. DOI: 10.1016/j.physletb.2012.03.013. arXiv: 1111.5869.

[123] P. Bärnreuther, M. Czakon, and A. Mitov. "Percent level precision physics at the Tevatron: First genuine NNLO QCD corrections to $q\bar{q} \to t\bar{t} + X$". *Phys. Rev. Lett.* 109 (2012), p. 132001. DOI: 10.1103/PhysRevLett.109.132001. arXiv: 1204.5201.

[124] M. Czakon and A. Mitov. "NNLO corrections to top-pair production at hadron colliders: The all-fermionic scattering channels". *JHEP* 12 (2012), p. 054. DOI: 10.1007/JHEP12(2012)054. arXiv: 1207.0236.

[125] M. Czakon and A. Mitov. "NNLO corrections to top pair production at hadron colliders: The quark-gluon reaction". *JHEP* 01 (2013), p. 080. DOI: 10.1007/JHEP01(2013)080. arXiv: 1210.6832.

[126] M. Czakon, P. Fiedler, and A. Mitov. "Total top-quark pair-production cross section at hadron colliders through $O(\alpha_s^4)$". *Phys. Rev. Lett.* 110 (2013), p. 252004. DOI: 10.1103/PhysRevLett.110.252004. arXiv: 1303.6254.

[127] J. H. Kühn, A. Scharf, and P. Uwer. "Weak interactions in top-quark pair production at hadron colliders: An update". *Phys. Rev. D* 91 (2015), p. 014020. DOI: 10.1103/PhysRevD.91.014020. arXiv: 1305.5773.

[128] J. A. Aguilar-Saavedra and J. Bernabeu. "W polarisation beyond helicity fractions in top quark decays". *Nucl. Phys. B* 840 (2010), p. 349. DOI: 10.1016/j.nuclphysb.2010.07.012. arXiv: 1005.5382.

[129] CMS Collaboration. "Measurement of the W boson helicity fractions in the decays of top quark pairs to lepton+jets final states produced in pp collisions at $\sqrt{s} = 8\,\text{TeV}$". *Phys. Lett. B* 762 (2016), p. 512. DOI: 10.1016/j.physletb.2016.10.007. arXiv: 1605.09047.

[130] A. Czarnecki, J. G. Korner, and J. H. Piclum. "Helicity fractions of W bosons from top quark decays at NNLO in QCD". *Phys. Rev. D* 81 (2010), p. 111503. DOI: 10.1103/PhysRevD.81.111503. arXiv: 1005.2625.

[131] J. Gao, C. S. Li, and H. X. Zhu. "Top quark decay at next-to-next-to leading order in QCD". *Phys. Rev. Lett.* 110 (2013), p. 042001. DOI: 10.1103/PhysRevLett.110.042001. arXiv: 1210.2808.

[132] M. Brucherseifer, F. Caola, and K. Melnikov. "$O(\alpha_s^2)$ corrections to fully-differential top quark decays". *JHEP* 04 (2013), p. 059. DOI: 10.1007/JHEP04(2013)059. arXiv: 1301.7133.

[133] CMS Collaboration. "Measurement of differential cross sections and charge ratios for t-channel single top quark production in proton-proton collisions at $\sqrt{s} = 13\,\text{TeV}$". *Eur. Phys. J. C* 80 (2020), p. 370. DOI: 10.1140/epjc/s10052-020-7858-1. arXiv: 1907.08330.

[134] CMS Collaboration. "Observation of top quark pairs produced in association with a vector boson in pp collisions at $\sqrt{s} = 8\,\text{TeV}$". *JHEP* 01 (2016), p. 096. DOI: 10.1007/JHEP01(2016)096. arXiv: 1510.01131.

Die approbierte gedruckte Originalversion dieser Dissertation ist an der TU Wien Bibliothek verfügbar.
The approved original version of this doctoral thesis is available in print at TU Wien Bibliothek.
TU Bibliothek Your knowledge hub WIEN

[135] CMS Collaboration. "Measurement of top quark pair production in association with a Z boson in proton-proton collisions at $\sqrt{s} = 13\,\text{TeV}$". *JHEP* 03 (2020), p. 056. DOI: 10.1007/JHEP03(2020)056. arXiv: 1907.11270.

[136] S. Frixione, V. Hirschi, D. Pagani, H. S. Shao, and M. Zaro. "Electroweak and QCD corrections to top-pair hadroproduction in association with heavy bosons". *JHEP* 06 (2015), p. 184. DOI: 10.1007/JHEP06(2015)184. arXiv: 1504.03446.

[137] R. Frederix, S. Frixione, V. Hirschi, D. Pagani, H. S. Shao, and M. Zaro. "The automation of next-to-leading order electroweak calculations". *JHEP* 07 (2018), p. 185. DOI: 10.1007/JHEP07(2018)185. arXiv: 1804.10017.

[138] CMS Collaboration. "Observation of single top quark production in association with a Z boson in proton-proton collisions at $\sqrt{s} = 13\,\text{TeV}$". *Phys. Rev. Lett.* 122 (2019), p. 132003. DOI: 10.1103/PhysRevLett.122.132003. arXiv: 1812.05900.

[139] CMS Collaboration. "Measurement of the associated production of a single top quark and a Z boson in pp collisions at $\sqrt{s} = 13\,\text{TeV}$". *Phys. Lett. B* 779 (2018), p. 358. DOI: 10.1016/j.physletb.2018.02.025. arXiv: 1712.02825.

[140] A. O. Bouzas and F. Larios. "Electromagnetic dipole moments of the top quark". *Phys. Rev. D* 87 (2013), p. 074015. DOI: 10.1103/PhysRevD.87.074015. arXiv: 1212.6575.

[141] D. Chang, W.-F. Chang, and E. Ma. "Alternative interpretation of the Tevatron top events". *Phys. Rev. D* 59 (1999), p. 091503. DOI: 10.1103/PhysRevD.59.091503. arXiv: hep-ph/9810531.

[142] D. Chang, W.-F. Chang, and E. Ma. "Fitting precision electroweak data with exotic heavy quarks". *Phys. Rev. D* 61 (2000), p. 037301. DOI: 10.1103/PhysRevD.61.037301. arXiv: hep-ph/9909537.

[143] CDF Collaboration. "Exclusion of exotic top-like quarks with -4/3 electric charge using jet-charge tagging in single-lepton $t\bar{t}$ events at CDF". *Phys. Rev. D* 88 (2013), p. 032003. DOI: 10.1103/PhysRevD.88.032003. arXiv: 1304.4141.

[144] D0 Collaboration. "Measurement of the electric charge of the top quark in $t\bar{t}$ events". *Phys. Rev. D* 90 (2014), p. 051101. DOI: 10.1103/PhysRevD.90.051101. arXiv: 1407.4837. [Erratum: *Phys. Rev. D* 90 (2014), p. 079904].

[145] ATLAS Collaboration. "Measurement of the top quark charge in pp collisions at $\sqrt{s} = 7\,\text{TeV}$ with the ATLAS detector". *JHEP* 11 (2013), p. 031. DOI: 10.1007/JHEP11(2013)031. arXiv: 1307.4568.

[146] CMS Collaboration. "Constraints on the top-quark charge from top-pair events". *CMS Physics Analysis Summaries* CMS-PAS-TOP-11-031 (2012). URL: https://bit.ly/3i3eDk6.

[147] M. Fael and T. Gehrmann. "Probing top quark electromagnetic dipole moments in single-top-plus-photon production". *Phys. Rev. D* 88 (2013), p. 033003. DOI: 10.1103/PhysRevD.88.033003. arXiv: 1307.1349.

[148] J. A. Aguilar-Saavedra, E. Álvarez, A. Juste, and F. Rubbo. "Shedding light on the $t\bar{t}$ asymmetry: The photon handle". *JHEP* 04 (2014), p. 188. DOI: 10.1007/JHEP04(2014)188. arXiv: 1402.3598.

TU Bibliothek Your knowledge hub WIEN
Die approbierte gedruckte Originalversion dieser Dissertation ist an der TU Wien Bibliothek verfügbar.
The approved original version of this doctoral thesis is available in print at TU Wien Bibliothek.

[149] M. Schulze and Y. Soreq. "Pinning down electroweak dipole operators of the top quark". *Eur. Phys. J. C* 76 (2016), p. 466. DOI: 10.1140/epjc/s10052-016-4263-x. arXiv: 1603.08911.

[150] S. M. Etesami, S. Khatibi, and M. Mohammadi Najafabadi. "Measuring anomalous WWγ and t$\bar{\text{t}}\gamma$ couplings using top+γ production at the LHC". *Eur. Phys. J. C* 76 (2016), p. 533. DOI: 10.1140/epjc/s10052-016-4376-2. arXiv: 1606.02178.

[151] J. A. Aguilar-Saavedra, M. C. N. Fiolhais, and A. Onofre. "Top effective operators at the ILC". *JHEP* 07 (2012), p. 180. DOI: 10.1007/JHEP07(2012)180. arXiv: 1206.1033.

[152] W. Bernreuther, R. Bonciani, T. Gehrmann, R. Heinesch, T. Leineweber, P. Mastrolia, and E. Remiddi. "QCD corrections to static heavy quark form-factors". *Phys. Rev. Lett.* 95 (2005), p. 261802. DOI: 10.1103/PhysRevLett.95.261802. arXiv: hep-ph/0509341.

[153] A. Cordero-Cid, J. M. Hernandez, G. Tavares-Velasco, and J. J. Toscano. "Bounding the top and bottom electric dipole moments from neutron experimental data". *J. Phys. G* 35 (2008), p. 025004. DOI: 10.1088/0954-3899/35/2/025004. arXiv: 0712.0154.

[154] L. Labun and J. Rafelski. "Top anomalous magnetic moment and the two photon decay of Higgs boson". *Phys. Rev. D* 88 (2013), p. 071301. DOI: 10.1103/PhysRevD.88.071301. arXiv: 1209.1046.

[155] J. F. Kamenik, M. Papucci, and A. Weiler. "Constraining the dipole moments of the top quark". *Phys. Rev. D* 85 (2012), p. 071501. DOI: 10.1103/PhysRevD.85.071501. arXiv: 1107.3143. [Erratum: *Phys. Rev. D* 88 (2013), p. 039903].

[156] S. Bißmann, J. Erdmann, C. Grunwald, G. Hiller, and K. Kröninger. "Constraining top-quark couplings combining top-quark and B decay observables". *Eur. Phys. J. C* 80 (2020), p. 136. DOI: 10.1140/epjc/s10052-020-7680-9. arXiv: 1909.13632.

[157] S. Bißmann, C. Grunwald, G. Hiller, and K. Kröninger. "Top and beauty synergies in SMEFT-fits at present and future colliders". *JHEP* 06 (2021), p. 010. DOI: 10.1007/JHEP06(2021)010. arXiv: 2012.10456.

[158] CDF Collaboration. "Evidence for t$\bar{\text{t}}\gamma$ production and measurement of $\sigma_{\text{t}\bar{\text{t}}\gamma}/\sigma_{\text{t}\bar{\text{t}}}$". *Phys. Rev. D* 84 (2011), p. 031104. DOI: 10.1103/PhysRevD.84.031104. arXiv: 1106.3970.

[159] ATLAS Collaboration. "Observation of top-quark pair production in association with a photon and measurement of the t$\bar{\text{t}}\gamma$ production cross section in pp collisions at $\sqrt{s} = 7\,\text{TeV}$ using the ATLAS detector". *Phys. Rev. D* 91 (2015), p. 072007. DOI: 10.1103/PhysRevD.91.072007. arXiv: 1502.00586.

[160] ATLAS Collaboration. "Measurement of the t$\bar{\text{t}}\gamma$ production cross section in proton-proton collisions at $\sqrt{s} = 8\,\text{TeV}$ with the ATLAS detector". *JHEP* 11 (2017), p. 086. DOI: 10.1007/JHEP11(2017)086. arXiv: 1706.03046.

[161] CMS Collaboration. "Measurement of the semileptonic t$\bar{\text{t}}+\gamma$ production cross section in pp collisions at $\sqrt{s} = 8\,\text{TeV}$". *JHEP* 10 (2017), p. 006. DOI: 10.1007/JHEP10(2017)006. arXiv: 1706.08128.

TU Bibliothek Your knowledge hub WIEN
Die approbierte gedruckte Originalversion dieser Dissertation ist an der TU Wien Bibliothek verfügbar.
The approved original version of this doctoral thesis is available in print at TU Wien Bibliothek.

[162] ATLAS Collaboration. "Measurements of inclusive and differential fiducial cross-sections of $t\bar{t}\gamma$ production in leptonic final states at $\sqrt{s} = 13\,\text{TeV}$ in ATLAS". *Eur. Phys. J. C* 79 (2019), p. 382. DOI: 10.1140/epjc/s10052-019-6849-6. arXiv: 1812.01697.

[163] ATLAS Collaboration. "Measurements of inclusive and differential cross-sections of combined $t\bar{t}\gamma$ and $tW\gamma$ production in the eμ channel at 13 TeV with the ATLAS detector". *JHEP* 09 (2020), p. 049. DOI: 10.1007/JHEP09(2020)049. arXiv: 2007.06946.

[164] CMS Collaboration. "Summaries of CMS cross section measurements". *CMSPublic Web* (2021). URL: https://bit.ly/3AWVysm.

[165] Muon g-2 Collaboration. "Measurement of the positive muon anomalous magnetic moment to 0.46 ppm". *Phys. Rev. Lett.* 126 (2021), p. 141801. DOI: 10.1103/PhysRevLett.126.141801. arXiv: 2104.03281.

[166] Muon g-2 Collaboration. "Final report of the muon E821 anomalous magnetic moment measurement at BNL". *Phys. Rev. D* 73 (2006), p. 072003. DOI: 10.1103/PhysRevD.73.072003. arXiv: hep-ex/0602035.

[167] J. Aebischer, W. Dekens, E. E. Jenkins, A. V. Manohar, D. Sengupta, and P. Stoffer. "Effective field theory interpretation of lepton magnetic and electric dipole moments" (2021). arXiv: 2102.08954.

[168] BaBar Collaboration. "Evidence for an excess of $\bar{B} \to D^{(*)}\tau^-\bar{\nu}_\tau$ decays". *Phys. Rev. Lett.* 109 (2012), p. 101802. DOI: 10.1103/PhysRevLett.109.101802. arXiv: 1205.5442.

[169] BaBar Collaboration. "Measurement of an excess of $\bar{B} \to D^{(*)}\tau^-\bar{\nu}_\tau$ decays and implications for charged Higgs bosons". *Phys. Rev. D* 88 (2013), p. 072012. DOI: 10.1103/PhysRevD.88.072012. arXiv: 1303.0571.

[170] BaBar Collaboration. "Measurement of branching fractions and rate asymmetries in the rare decays $B \to K^{(*)}\ell^+\ell^-$". *Phys. Rev. D* 86 (2012), p. 032012. DOI: 10.1103/PhysRevD.86.032012. arXiv: 1204.3933.

[171] Belle Collaboration. "Measurement of the branching ratio of $\bar{B} \to D^{(*)}\tau^-\bar{\nu}_\tau$ relative to $\bar{B} \to D^{(*)}\ell^-\bar{\nu}_\ell$ decays with hadronic tagging at Belle". *Phys. Rev. D* 92 (2015), p. 072014. DOI: 10.1103/PhysRevD.92.072014. arXiv: 1507.03233.

[172] Belle Collaboration. "Measurement of the differential branching fraction and forward-backword asymmetry for $B \to K^{(*)}\ell^+\ell^-$". *Phys. Rev. Lett.* 103 (2009), p. 171801. DOI: 10.1103/PhysRevLett.103.171801. arXiv: 0904.0770.

[173] LHCb Collaboration. "Measurement of the ratio of branching fractions $\mathcal{B}(\bar{B}^0 \to D^{*+}\tau^-\bar{\nu}_\tau)/\mathcal{B}(\bar{B}^0 \to D^{*+}\mu^-\bar{\nu}_\mu)$". *Phys. Rev. Lett.* 115 (2015), p. 111803. DOI: 10.1103/PhysRevLett.115.111803. arXiv: 1506.08614. [Erratum: *Phys. Rev. Lett.* 115 (2015), p. 159901].

[174] LHCb Collaboration. "Measurement of the ratio of the $B^0 \to D^{*-}\tau^+\nu_\tau$ and $B^0 \to D^{*-}\mu^+\nu_\mu$ branching fractions using three-prong τ-lepton decays". *Phys. Rev. Lett.* 120 (2018), p. 171802. DOI: 10.1103/PhysRevLett.120.171802. arXiv: 1708.08856.

[175] LHCb Collaboration. "Test of lepton universality using $B^+ \to K^+\ell^+\ell^-$ decays". *Phys. Rev. Lett.* 113 (2014), p. 151601. DOI: 10.1103/PhysRevLett.113.151601. arXiv: 1406.6482.

Die approbierte gedruckte Originalversion dieser Dissertation ist an der TU Wien Bibliothek verfügbar.
The approved original version of this doctoral thesis is available in print at TU Wien Bibliothek.
TU Bibliothek Your knowledge hub WIEN

[176] LHCb Collaboration. "Search for lepton-universality violation in $B^+ \to K^+\ell^+\ell^-$ decays". *Phys. Rev. Lett.* 122 (2019), p. 191801. DOI: 10.1103/PhysRevLett.122.191801. arXiv: 1903.09252.

[177] LHCb Collaboration. "Test of lepton universality with $B^0 \to K^{*0}\ell^+\ell^-$ decays". *JHEP* 08 (2017), p. 055. DOI: 10.1007/JHEP08(2017)055. arXiv: 1705.05802.

[178] LHCb Collaboration. "Test of lepton universality in beauty-quark decays" (2021). arXiv: 2103.11769.

[179] HFLAV Collaboration. "Averages of b-hadron, c-hadron, and τ-lepton properties as of summer 2016". *Eur. Phys. J. C* 77 (2017), p. 895. DOI: 10.1140/epjc/s10052-017-5058-4. arXiv: 1612.07233.

[180] R. W. Rasmussen, L. Lechner, M. Ackermann, M. Kowalski, and W. Winter. "Astrophysical neutrinos flavored with beyond the standard model physics". *Phys. Rev. D* 96 (2017), p. 083018. DOI: 10.1103/PhysRevD.96.083018. arXiv: 1707.07684.

[181] P. Minkowski. "$\mu \to e\gamma$ at a rate of one out of 10^9 muon decays?" *Phys. Lett. B* 67 (1977), p. 421. DOI: 10.1016/0370-2693(77)90435-X.

[182] M. Gell-Mann, P. Ramond, and R. Slansky. "Complex spinors and unified theories". *Conf. Proc. C* 790927 (1979), p. 315. arXiv: 1306.4669.

[183] R. N. Mohapatra and G. Senjanovic. "Neutrino mass and spontaneous parity nonconservation". *Phys. Rev. Lett.* 44 (1980), p. 912. DOI: 10.1103/PhysRevLett.44.912.

[184] J. Schechter and J. W. F. Valle. "Neutrino masses in SU(2)×U(1) theories". *Phys. Rev. D* 22 (1980), p. 2227. DOI: 10.1103/PhysRevD.22.2227.

[185] R. N. Mohapatra and G. Senjanovic. "Neutrino masses and mixings in gauge models with spontaneous parity violation". *Phys. Rev. D* 23 (1981), p. 165. DOI: 10.1103/PhysRevD.23.165.

[186] G. Lazarides, Q. Shafi, and C. Wetterich. "Proton lifetime and fermion masses in an SO(10) model". *Nucl. Phys. B* 181 (1981), p. 287. DOI: 10.1016/0550-3213(81)90354-0.

[187] C. Wetterich. "Neutrino masses and the scale of B-L violation". *Nucl. Phys. B* 187 (1981), p. 343. DOI: 10.1016/0550-3213(81)90279-0.

[188] J. Schechter and J. W. F. Valle. "Neutrino decay and spontaneous violation of lepton number". *Phys. Rev. D* 25 (1982), p. 774. DOI: 10.1103/PhysRevD.25.774.

[189] B. Brahmachari and R. N. Mohapatra. "Unified explanation of the solar and atmospheric neutrino puzzles in a minimal supersymmetric SO(10) model". *Phys. Rev. D* 58 (1998), p. 015001. DOI: 10.1103/PhysRevD.58.015001. arXiv: hep-ph/9710371.

[190] R. Foot, H. Lew, X. G. He, and G. C. Joshi. "Seesaw neutrino masses induced by a triplet of leptons". *Z. Phys. C* 44 (1989), p. 441. DOI: 10.1007/BF01415558.

[191] E. Majorana. "Teoria simmetrica dell'elettrone e del positrone". *Nuovo Cim.* 14 (1937), p. 171. DOI: 10.1007/BF02961314.

[192] T. Appelquist and J. Carazzone. "Infrared singularities and massive fields". *Phys. Rev. D* 11 (1975), p. 2856. DOI: 10.1103/PhysRevD.11.2856.

Die approbierte gedruckte Originalversion dieser Dissertation ist an der TU Wien Bibliothek verfügbar.
The approved original version of this doctoral thesis is available in print at TU Wien Bibliothek.
TU Bibliothek Your knowledge hub WIEN

[193] A. Kobach. "Baryon number, lepton number, and operator dimension in the standard model". *Phys. Lett. B* 758 (2016), p. 455. DOI: 10.1016/j.physletb.2016.05.050. arXiv: 1604.05726.

[194] C. Degrande, N. Greiner, W. Kilian, O. Mattelaer, H. Mebane, T. Stelzer, S. Willenbrock, and C. Zhang. "Effective field theory: A modern approach to anomalous couplings". *Annals Phys.* 335 (2013), p. 21. DOI: 10.1016/j.aop.2013.04.016. arXiv: 1205.4231.

[195] S. Rao and R. E. Shrock. "Six fermion $(B - L)$ violating operators of arbitrary generational structure". *Nucl. Phys. B* 232 (1984), p. 143. DOI: 10.1016/0550-3213(84)90365-1.

[196] L. Lehman. "Extending the standard model effective field theory with the complete set of dimension-7 operators". *Phys. Rev. D* 90 (2014), p. 125023. DOI: 10.1103/PhysRevD.90.125023. arXiv: 1410.4193.

[197] B. Henning, X. Lu, T. Melia, and H. Murayama. "2, 84, 30, 993, 560, 15456, 11962, 261485, ...: Higher dimension operators in the SM EFT". *JHEP* 08 (2017), p. 016. DOI: 10.1007/JHEP08(2017)016. arXiv: 1512.03433. [Erratum: *JHEP* 09 (2019), p. 019].

[198] S. Weinberg. "Baryon and lepton nonconserving processes". *Phys. Rev. Lett.* 43 (1979), p. 1566. DOI: 10.1103/PhysRevLett.43.1566.

[199] D. Barducci et al. "Interpreting top-quark LHC measurements in the standard-model effective field theory" (2018). arXiv: 1802.07237.

[200] O. Bessidskaia Bylund, F. Maltoni, I. Tsinikos, E. Vryonidou, and C. Zhang. "Probing top quark neutral couplings in the standard model effective field theory at NLO in QCD". *JHEP* 05 (2016), p. 052. DOI: 10.1007/JHEP05(2016)052. arXiv: 1601.08193.

[201] O. S. Bruning, P. Collier, P. Lebrun, S. Myers, R. Ostojic, J. Poole, and P. Proudlock. "LHC design report vol.1: The LHC main ring". *CERN Yellow Rep. Monogr.* (2004), p. 1. DOI: 10.5170/CERN-2004-003-V-1.

[202] O. Buning, P. Collier, P. Lebrun, S. Myers, R. Ostojic, J. Poole, and P. Proudlock. "LHC design report. 2. The LHC infrastructure and general services". *CERN Yellow Rep. Monogr.* (2004), p. 1. DOI: 10.5170/CERN-2004-003-V-2.

[203] M. Benedikt, P. Collier, V. Mertens, J. Poole, and K. Schindl. "LHC design report. 3. The LHC injector chain". *CERN Yellow Rep. Monogr.* (2004), p. 1. DOI: 10.5170/CERN-2004-003-V-3.

[204] L. Evans and P. Bryant. "LHC machine". *JINST* 3 (2008), p. S08001. DOI: 10.1088/1748-0221/3/08/S08001.

[205] CMS Collaboration. "The CMS experiment at the CERN LHC". *JINST* 3 (2008), p. S08004. DOI: 10.1088/1748-0221/3/08/S08004.

[206] ATLAS Collaboration. "The ATLAS experiment at the CERN Large Hadron Collider". *JINST* 3 (2008), p. S08003. DOI: 10.1088/1748-0221/3/08/S08003.

[207] ALICE Collaboration. "The ALICE experiment at the CERN LHC". *JINST* 3 (2008), p. S08002. DOI: 10.1088/1748-0221/3/08/S08002.

[208] LHCb Collaboration. "The LHCb detector at the LHC". *JINST* 3 (2008), p. S08005. DOI: 10.1088/1748-0221/3/08/S08005.

Die approbierte gedruckte Originalversion dieser Dissertation ist an der TU Wien Bibliothek verfügbar.
The approved original version of this doctoral thesis is available in print at TU Wien Bibliothek.
TU Bibliothek Your knowledge hub WIEN

[209] E. Boltezar, H. Haseroth, W. Pirkl, G. Plass, T. R. Sherwood, U. Tallgren, P. Têtu, D. Warner, and M. Weiss. "Performance of the new CERN 50 MeV Linac". *IEEE Trans. Nucl. Sci.* 26 (1979), p. 3674. DOI: 10.1109/TNS.1979.4330576.

[210] E. Mobs. "The CERN accelerator complex - 2019. Complexe des accélérateurs du CERN - 2019". *CERN* (2019). URL: https://bit.ly/3yRyJ7U.

[211] R. Garoby. "Multiple splitting in the PS: Results and alternative filling schemes". *11th Workshop of the LHC* (2001). URL: https://bit.ly/3xAI3g6.

[212] L. Evans, E. Jones, and H. Koziol. "The CERN PPbar collider". *SPS Divisional Reports* (1988), p. 1. URL: https://bit.ly/3wEtarM.

[213] UA1 Collaboration. "Experimental observation of isolated large transverse energy electrons with associated missing energy at $\sqrt{s} = 540\,\text{GeV}$". *Phys. Lett. B* 122 (1983), p. 103. DOI: 10.1016/0370-2693(83)91177-2.

[214] UA2 Collaboration. "Observation of single isolated electrons of high transverse momentum in events with missing transverse energy at the CERN $\bar{p}p$ collider". *Phys. Lett. B* 122 (1983), p. 476. DOI: 10.1016/0370-2693(83)91605-2.

[215] UA1 Collaboration. "Experimental observation of lepton pairs of invariant mass around $95\,\text{GeV/c}^2$ at the CERN SPS collider". *Phys. Lett. B* 126 (1983), p. 398. DOI: 10.1016/0370-2693(83)90188-0.

[216] UA2 Collaboration. "Evidence for $Z^0 \to e^+e^-$ at the CERN $\bar{p}p$ collider". *Phys. Lett. B* 129 (1983), p. 130. DOI: 10.1016/0370-2693(83)90744-X.

[217] I. Béjar Alonso, O. Brüning, P. Fessia, L. Rossi, L. Tavian, and M. Zerlauth. "High-Luminosity Large Hadron Collider (HL-LHC): Technical design report". *CERN Yellow Rep. Monogr.* 10 (2020), p. 1. DOI: 10.23731/CYRM-2020-0010.

[218] M. Vretenar et al. "Linac4 design report". *CERN Yellow Rep. Monogr.* 6 (2006), p. 1. DOI: 10.23731/CYRM-2020-006.

[219] K. Hanke. "Past and present operation of the CERN PS Booster". *Int. J. Mod. Phys. A* 28 (2013), p. 1330019. DOI: 10.1142/S0217751X13300196.

[220] H. Damerau, A. Funken, R. Garoby, S. Gilardoni, B. Goddard, K. Hanke, A. Lombardi, D. Manglunki, M. Meddahi, B. Mikulec, G. Rumolo, E. Shaposhnikova, M. Vretenar, and J. Coupard. "LHC injectors upgrade, technical design report". *CERN* CERN-ACC-2014-0337 (2014), p. 1. URL: https://bit.ly/3wBBNU2.

[221] W. Weterings, B. Balhan, E. Benedetto, J. Borburgh, C. Bracco, C. Carli, B. Goddard, K. Hanke, B. Mikulec, A. Newborough, R. Noulibos, and J. Tan. "Status of the 160 MeV H- injection into the CERN PSB". *Conf. Proc. C* 1205201 (2012), p. 2041. URL: https://bit.ly/2TU3zxX.

[222] B. Schmidt. "The high-luminosity upgrade of the LHC: Physics and technology challenges for the accelerator and the experiments". *J. Phys. Conf. Ser.* 706 (2016), p. 022002. DOI: 10.1088/1742-6596/706/2/022002.

[223] CMS Collaboration. "Public CMS luminosity information". *CMSPublic Web* (2021). URL: https://bit.ly/2UKY5Wk.

[224] CMS Collaboration. "The CMS magnet project: Technical design report". *Technical design report* CMS-TDR-1 (1997), p. 1. URL: https://bit.ly/3hyTwaz.

Die approbierte gedruckte Originalversion dieser Dissertation ist an der TU Wien Bibliothek verfügbar.
The approved original version of this doctoral thesis is available in print at TU Wien Bibliothek.
TU Bibliothek Your knowledge hub WIEN

[225] CMS Collaboration. "The CMS tracker system project: Technical design report". *Technical design report* CMS-TDR-5 (1997), p. 1. URL: https://bit.ly/3xNC3kp.

[226] CMS Collaboration. "The CMS tracker: Addendum to the technical design report". *Technical design report* CMS-TDR-5-add-1 (2000), p. 1. URL: https://bit.ly/3hYvDrT.

[227] CMS Collaboration. "CMS technical design report for the pixel detector upgrade". *Technical design report* CMS-TDR-11 (2012), p. 1. URL: https://bit.ly/3yWWgUZ.

[228] CMS Collaboration. "The CMS electromagnetic calorimeter project: Technical design report". *Technical design report* CMS-TDR-4 (1997), p. 1. URL: https://bit.ly/3kabxxm.

[229] CMS Collaboration. "The CMS hadron calorimeter project: Technical design report". *Technical design report* CMS-TDR-2 (1997), p. 1. URL: https://bit.ly/3xEm9bN.

[230] CMS Collaboration. "The CMS muon project: Technical design report". *Technical design report* CMS-TDR-3 (1997), p. 1. URL: https://bit.ly/3xAZ61D.

[231] CMS Collaboration. "Particle-flow reconstruction and global event description with the CMS detector". *JINST* 12 (2017), p. P10003. DOI: 10.1088/1748-0221/12/10/P10003. arXiv: 1706.04965.

[232] T. Sakuma and T. McCauley. "Detector and event visualization with SketchUp at the CMS experiment". *J. Phys. Conf. Ser.* 513 (2014), p. 022032. DOI: 10.1088/1742-6596/513/2/022032. arXiv: 1311.4942.

[233] F. Faccio, S. Michelis, and G. Ripamonti. "Failure of DCDC modules in the CMS pixel system during the 2017 run". *CERN* EP-ESE-ME (2018). URL: https://bit.ly/3hB1yjb.

[234] ALEPH Collaboration. "Performance of the ALEPH detector at LEP". *Nucl. Instrum. Meth. A* 360 (1995), p. 481. DOI: 10.1016/0168-9002(95)00138-7.

[235] R. Frühwirth. "Application of Kalman filtering to track and vertex fitting". *Nucl. Instrum. Meth. A* 262 (1987), p. 444. DOI: 10.1016/0168-9002(87)90887-4.

[236] CMS Collaboration. "CMS physics: Technical design report volume 1: Detector performance and software". *Technical design report* CMS-TDR-8-1 (2006), p. 1. URL: https://bit.ly/2UHBQAe.

[237] CMS Collaboration. "Track reconstruction performance in CMS". *Nucl. Phys. B Proc. Suppl.* 197 (2009), p. 275. DOI: 10.1016/j.nuclphysbps.2009.10.084. arXiv: 0812.5036.

[238] CMS Collaboration. "Description and performance of track and primary-vertex reconstruction with the CMS tracker". *JINST* 9 (2014), p. P10009. DOI: 10.1088/1748-0221/9/10/P10009. arXiv: 1405.6569.

[239] CMS Collaboration. "Performance of the CMS muon detector and muon reconstruction with proton-proton collisions at $\sqrt{s} = 13\,\text{TeV}$". *JINST* 13 (2018), p. P06015. DOI: 10.1088/1748-0221/13/06/P06015. arXiv: 1804.04528.

[240] CMS Collaboration. "Performance of CMS muon reconstruction in pp collision events at $\sqrt{s} = 7\,\text{TeV}$". *JINST* 7 (2012), p. P10002. DOI: 10.1088/1748-0221/7/10/P10002. arXiv: 1206.4071.

Die approbierte gedruckte Originalversion dieser Dissertation ist an der TU Wien Bibliothek verfügbar.
The approved original version of this doctoral thesis is available in print at TU Wien Bibliothek.
TU Bibliothek Your knowledge hub WIEN

[241] W. Adam, R. Frühwirth, A. Strandlie, and T. Todor. "Reconstruction of electrons with the Gaussian-sum filter in the CMS tracker at the LHC". *CMS Note* CMS-NOTE-2005-001 (2005). URL: https://bit.ly/3r65ont.

[242] CMS Collaboration. "Performance of electron reconstruction and selection with the CMS detector in proton-proton collisions at $\sqrt{s} = 8\,\text{TeV}$". *JINST* 10 (2015), p. P06005. DOI: 10.1088/1748-0221/10/06/P06005. arXiv: 1502.02701.

[243] CMS Collaboration. "Electron and photon reconstruction and identification with the CMS experiment at the CERN LHC". *JINST* 16 (2021), p. P05014. DOI: 10.1088/1748-0221/16/05/P05014. arXiv: 2012.06888.

[244] CMS Collaboration. "Performance of photon reconstruction and identification with the CMS detector in proton-proton collisions at $\sqrt{s} = 8\,\text{TeV}$". *JINST* 10 (2015), p. P08010. DOI: 10.1088/1748-0221/10/08/P08010. arXiv: 1502.02702.

[245] M. Cacciari, G. P. Salam, and G. Soyez. "The anti-k_T jet clustering algorithm". *JHEP* 04 (2008), p. 063. DOI: 10.1088/1126-6708/2008/04/063. arXiv: 0802.1189.

[246] M. Cacciari, G. P. Salam, and G. Soyez. "FastJet user manual". *Eur. Phys. J. C* 72 (2012), p. 1896. DOI: 10.1140/epjc/s10052-012-1896-2. arXiv: 1111.6097.

[247] CMS Collaboration. "Pileup removal algorithms". *CMS Physics Analysis Summaries* CMS-PAS-JME-14-001 (2014). URL: https://bit.ly/3e8HOBl.

[248] CMS Collaboration. "Identification of heavy-flavour jets with the CMS detector in pp collisions at 13 TeV". *JINST* 13 (2018), p. P05011. DOI: 10.1088/1748-0221/13/05/P05011. arXiv: 1712.07158.

[249] D. Guest, J. Collado, P. Baldi, S.-C. Hsu, G. Urban, and D. Whiteson. "Jet flavor classification in high-energy physics with deep neural networks". *Phys. Rev. D* 94 (2016), p. 112002. DOI: 10.1103/PhysRevD.94.112002. arXiv: 1607.08633.

[250] V. Blobel. "Unfolding methods in high-energy physics experiments". *CERN School of Computing* (1984), p. 40. DOI: 10.5170/CERN-1985-009.88.

[251] CMS Collaboration. "CMS luminosity measurements for the 2016 data taking period". *CMS Physics Analysis Summaries* CMS-PAS-LUM-17-001 (2017). URL: https://bit.ly/2T9lD6K.

[252] CMS Collaboration. "CMS luminosity measurement for the 2017 data-taking period at $\sqrt{s} = 13\,\text{TeV}$". *CMS Physics Analysis Summaries* CMS-PAS-LUM-17-004 (2018). URL: https://bit.ly/3e5PLqM.

[253] CMS Collaboration. "CMS luminosity measurement for the 2018 data-taking period at $\sqrt{s} = 13\,\text{TeV}$". *CMS Physics Analysis Summaries* CMS-PAS-LUM-18-002 (2019). URL: https://bit.ly/3r6wYAN.

[254] GEANT4 Collaboration. "GEANT4–A simulation toolkit". *Nucl. Instrum. Meth. A* 506 (2003), p. 250. DOI: 10.1016/S0168-9002(03)01368-8.

[255] P. Skands, S. Carrazza, and J. Rojo. "Tuning PYTHIA 8.1: The Monash 2013 tune". *Eur. Phys. J. C* 74 (2014), p. 3024. DOI: 10.1140/epjc/s10052-014-3024-y. arXiv: 1404.5630.

[256] J. M. Campbell, R. K. Ellis, P. Nason, and E. Re. "Top-pair production and decay at NLO matched with parton showers". *JHEP* 04 (2015), p. 114. DOI: 10.1007/JHEP04(2015)114. arXiv: 1412.1828.

Die approbierte gedruckte Originalversion dieser Dissertation ist an der TU Wien Bibliothek verfügbar.
The approved original version of this doctoral thesis is available in print at TU Wien Bibliothek.
TU Bibliothek Your knowledge hub WIEN

[257] S. Frixione, P. Nason, and G. Ridolfi. "A positive-weight next-to-leading-order Monte Carlo for heavy flavour hadroproduction". *JHEP* 09 (2007), p. 126. DOI: 10.1088/1126-6708/2007/09/126. arXiv: 0707.3088.

[258] S. Alioli, P. Nason, C. Oleari, and E. Re. "NLO single-top production matched with shower in POWHEG: s- and t-channel contributions". *JHEP* 09 (2009), p. 111. DOI: 10.1088/1126-6708/2009/09/111. arXiv: 0907.4076. [Erratum: *JHEP* 02 (2010), p. 011].

[259] E. Re. "Single-top Wt-channel production matched with parton showers using the POWHEG method". *Eur. Phys. J. C* 71 (2011), p. 1547. DOI: 10.1140/epjc/s10052-011-1547-z. arXiv: 1009.2450.

[260] T. Melia, P. Nason, R. Rontsch, and G. Zanderighi. "W^+W^-, WZ and ZZ production in the POWHEG BOX". *JHEP* 11 (2011), p. 078. DOI: 10.1007/JHEP11(2011)078. arXiv: 1107.5051.

[261] P. Nason and G. Zanderighi. "W^+W^-, WZ and ZZ production in the POWHEG-BOX-V2". *Eur. Phys. J. C* 74 (2014), p. 2702. DOI: 10.1140/epjc/s10052-013-2702-5. arXiv: 1311.1365.

[262] J. Alwall et al. "Comparative study of various algorithms for the merging of parton showers and matrix elements in hadronic collisions". *Eur. Phys. J. C* 53 (2008), p. 473. DOI: 10.1140/epjc/s10052-007-0490-5. arXiv: 0706.2569.

[263] R. Frederix and S. Frixione. "Merging meets matching in MC@NLO". *JHEP* 12 (2012), p. 061. DOI: 10.1007/JHEP12(2012)061. arXiv: 1209.6215.

[264] N. Kidonakis. "Theoretical results for electroweak-boson and single-top production". *PoS* DIS2015 (2015), p. 170. DOI: 10.22323/1.247.0170. arXiv: 1506.04072.

[265] K. Melnikov and F. Petriello. "Electroweak gauge boson production at hadron colliders through $O(\alpha_s^2)$". *Phys. Rev. D* 74 (2006), p. 114017. DOI: 10.1103/PhysRevD.74.114017. arXiv: hep-ph/0609070.

[266] S. Catani, L. Cieri, G. Ferrera, D. de Florian, and M. Grazzini. "Vector boson production at hadron colliders: A fully exclusive QCD calculation at NNLO". *Phys. Rev. Lett.* 103 (2009), p. 082001. DOI: 10.1103/PhysRevLett.103.082001. arXiv: 0903.2120.

[267] C. Anastasiou, L. J. Dixon, K. Melnikov, and F. Petriello. "High precision QCD at hadron colliders: Electroweak gauge boson rapidity distributions at NNLO". *Phys. Rev. D* 69 (2004), p. 094008. DOI: 10.1103/PhysRevD.69.094008. arXiv: hep-ph/0312266.

[268] S. Dittmaier, A. Huss, and C. Schwinn. "Mixed QCD-electroweak $O(\alpha_s\alpha)$ corrections to Drell–Yan processes in the resonance region: Pole approximation and non-factorizable corrections". *Nucl. Phys. B* 885 (2014), p. 318. DOI: 10.1016/j.nuclphysb.2014.05.027. arXiv: 1403.3216.

[269] J. M. Lindert et al. "Precise predictions for V+jets dark matter backgrounds". *Eur. Phys. J. C* 77 (2017), p. 829. DOI: 10.1140/epjc/s10052-017-5389-1. arXiv: 1705.04664.

[270] T. Gehrmann, M. Grazzini, S. Kallweit, P. Maierhöfer, A. von Manteuffel, S. Pozzorini, D. Rathlev, and L. Tancredi. "W^+W^- production at hadron colliders in next to next to leading order QCD". *Phys. Rev. Lett.* 113 (2014), p. 212001. DOI: 10.1103/PhysRevLett.113.212001. arXiv: 1408.5243.

Die approbierte gedruckte Originalversion dieser Dissertation ist an der TU Wien Bibliothek verfügbar.
The approved original version of this doctoral thesis is available in print at TU Wien Bibliothek.
TU Bibliothek Your knowledge hub WIEN

[271] M. V. Garzelli, A. Kardos, C. G. Papadopoulos, and Z. Trocsanyi. "$t\bar{t}W^{\pm}$ and $t\bar{t}Z$ hadroproduction at NLO accuracy in QCD with parton shower and hadronization effects". *JHEP* 11 (2012), p. 056. DOI: 10.1007/JHEP11(2012)056. arXiv: 1208.2665.

[272] ATLAS Collaboration. "Measurement of the inelastic proton-proton cross section at $\sqrt{s} = 13\,\text{TeV}$ with the ATLAS detector at the LHC". *Phys. Rev. Lett.* 117 (2016), p. 182002. DOI: 10.1103/PhysRevLett.117.182002. arXiv: 1606.02625.

[273] CMS Collaboration. "Measurement of the inelastic proton-proton cross section at $\sqrt{s} = 13\,\text{TeV}$". *JHEP* 07 (2018), p. 161. DOI: 10.1007/JHEP07(2018)161. arXiv: 1802.02613.

[274] CMS Collaboration. "Performance of the CMS level-1 trigger in proton-proton collisions at $\sqrt{s} = 13\,\text{TeV}$". *JINST* 15 (2020), p. P10017. DOI: 10.1088/1748-0221/15/10/P10017. arXiv: 2006.10165.

[275] CMS Collaboration. "Performance of the CMS muon trigger system in proton-proton collisions at $\sqrt{s} = 13\,\text{TeV}$". *JINST* 16 (2021), p. P07001. DOI: 10.1088/1748-0221/16/07/P07001. arXiv: 2102.04790.

[276] CMS Collaboration. "Search for new particles in events with energetic jets and large missing transverse momentum in proton-proton collisions at $\sqrt{s} = 13\,\text{TeV}$". *CMS Physics Analysis Summaries* CMS-PAS-EXO-20-004 (2021). URL: https://bit.ly/3wArIGM.

[277] CMS Collaboration. "Determination of jet energy calibration and transverse momentum resolution in CMS". *JINST* 6 (2011), p. P11002. DOI: 10.1088/1748-0221/6/11/P11002. arXiv: 1107.4277.

[278] CMS Collaboration. "Jet energy scale and resolution in the CMS experiment in pp collisions at 8 TeV". *JINST* 12 (2017), p. P02014. DOI: 10.1088/1748-0221/12/02/P02014. arXiv: 1607.03663.

[279] CMS Collaboration. "Identification of b-quark jets with the CMS experiment". *JINST* 8 (2013), p. P04013. DOI: 10.1088/1748-0221/8/04/P04013. arXiv: 1211.4462.

[280] CMS Collaboration. "Measurement of the top-antitop production cross section in pp collisions at $\sqrt{s} = 7\,\text{TeV}$ using the kinematic properties of events with leptons and jets". *Eur. Phys. J. C* 71 (2011), p. 1721. DOI: 10.1140/epjc/s10052-011-1721-3. arXiv: 1106.0902.

[281] M. Cacciari and G. P. Salam. "Pileup subtraction using jet areas". *Phys. Lett. B* 659 (2008), p. 119. DOI: 10.1016/j.physletb.2007.09.077. arXiv: 0707.1378.

[282] ATLAS and CMS Collaborations and LHC Higgs Combination Group. "Procedure for the LHC Higgs boson search combination in Summer 2011". *CMS Note* CMS-NOTE-2011-005, ATL-PHYS-PUB-2011-11 (2011). URL: https://bit.ly/3kaJiPm.

[283] G. Cowan, K. Cranmer, E. Gross, and O. Vitells. "Asymptotic formulae for likelihood-based tests of new physics". *Eur. Phys. J. C* 71 (2011), p. 1554. DOI: 10.1140/epjc/s10052-011-1554-0. arXiv: 1007.1727. [Erratum: *Eur. Phys. J. C* 73 (2013), p. 2501].

Die approbierte gedruckte Originalversion dieser Dissertation ist an der TU Wien Bibliothek verfügbar.
The approved original version of this doctoral thesis is available in print at TU Wien Bibliothek.
TU Bibliothek Your knowledge hub WIEN

[284] K. Cranmer. "Practical statistics for the LHC". *2011 European School of High-Energy Physics* (2015), p. 267. DOI: 10.5170/CERN-2014-003.267. arXiv: 1503.07622.

[285] S. Schmitt. "TUnfold: An algorithm for correcting migration effects in high energy physics". *JINST* 7 (2012), p. T10003. DOI: 10.1088/1748-0221/7/10/T10003. arXiv: 1205.6201.

[286] S. Schmitt. "Data unfolding methods in high energy physics". *EPJ Web Conf.* 137 (2017), p. 11008. DOI: 10.1051/epjconf/201713711008. arXiv: 1611.01927.

[287] S. Argyropoulos and T. Sjöstrand. "Effects of color reconnection on $t\bar{t}$ final states at the LHC". *JHEP* 11 (2014), p. 043. DOI: 10.1007/JHEP11(2014)043. arXiv: 1407.6653.

[288] J. R. Christiansen and P. Z. Skands. "String formation beyond leading colour". *JHEP* 08 (2015), p. 003. DOI: 10.1007/JHEP08(2015)003. arXiv: 1505.01681.

[289] R. J. Barlow and C. Beeston. "Fitting using finite Monte Carlo samples". *Comput. Phys. Commun.* 77 (1993), p. 219. DOI: 10.1016/0010-4655(93)90005-W.

[290] CMS Collaboration. "Measurements of $t\bar{t}$ differential cross sections in proton-proton collisions at $\sqrt{s} = 13\,\text{TeV}$ using events containing two leptons". *JHEP* 02 (2019), p. 149. DOI: 10.1007/JHEP02(2019)149. arXiv: 1811.06625.

[291] CMS Collaboration. "Measurement of the top quark polarization and $t\bar{t}$ spin correlations using dilepton final states in proton-proton collisions at $\sqrt{s} = 13\,\text{TeV}$". *Phys. Rev. D* 100 (2019), p. 072002. DOI: 10.1103/PhysRevD.100.072002. arXiv: 1907.03729.

[292] A. L. Read. "Presentation of search results: The CL_s technique". *J. Phys. G* 28 (2002), p. 2693. DOI: 10.1088/0954-3899/28/10/313.

[293] J. Brehmer, K. Cranmer, F. Kling, and T. Plehn. "Better Higgs boson measurements through information geometry". *Phys. Rev. D* 95 (2017), p. 073002. DOI: 10.1103/PhysRevD.95.073002. arXiv: 1612.05261.

[294] CMS Collaboration. "Search for new physics in top quark production with additional leptons in proton-proton collisions at $\sqrt{s} = 13\,\text{TeV}$ using effective field theory". *JHEP* 03 (2021), p. 095. DOI: 10.1007/JHEP03(2021)095. arXiv: 2012.04120.

[295] P. Artoisenet and O. Mattelaer. "MadWeight: Automatic event reweighting with matrix elements". *PoS* CHARGED2008 (2008), p. 025. DOI: 10.22323/1.073.0025.

[296] C. Degrande, C. Duhr, B. Fuks, D. Grellscheid, O. Mattelaer, and T. Reiter. "UFO - The universal FeynRules output". *Comput. Phys. Commun.* 183 (2012), p. 1201. DOI: 10.1016/j.cpc.2012.01.022. arXiv: 1108.2040.

[297] CMS Collaboration. "Measurement of the cross section for top quark pair production in association with a W or Z boson in proton-proton collisions at $\sqrt{s} = 13\,\text{TeV}$". *JHEP* 08 (2018), p. 011. DOI: 10.1007/JHEP08(2018)011. arXiv: 1711.02547.

[298] ATLAS Collaboration. "Measurement of the $t\bar{t}Z$ and $t\bar{t}W$ cross sections in proton-proton collisions at $\sqrt{s} = 13\,\text{TeV}$ with the ATLAS detector". *Phys. Rev. D* 99 (2019), p. 072009. DOI: 10.1103/PhysRevD.99.072009. arXiv: 1901.03584.

[299] J. Ellis, M. Madigan, K. Mimasu, V. Sanz, and T. You. "Top, Higgs, diboson and electroweak fit to the standard model effective field theory". *JHEP* 04 (2021), p. 279. DOI: 10.1007/JHEP04(2021)279. arXiv: 2012.02779.

Die approbierte gedruckte Originalversion dieser Dissertation ist an der TU Wien Bibliothek verfügbar.
The approved original version of this doctoral thesis is available in print at TU Wien Bibliothek.
TU Bibliothek Your knowledge hub WIEN

Acknowledgements

I wrote this thesis with a smile in one eye and a tear in the other. Finalizing the last chapter marked the end of a journey through my academic education. Years of conviction and surprises, successes and setbacks, joy and misery, hard work and of course beer. While I call it "the end", by no means it is the end. Every end is a beginning and a new chapter starts, with many challenges, mysteries, and enjoyable moments I am looking forward to. Still, it is time to pause and thank the ones who shared the bumpy road with me.

I am very grateful to all current and former colleagues at HEPHY and colleagues at CERN throughout all institutes involved. Especially I want to thank Robert Schöfbeck for the support during the last years and for making this thesis possible in providing the guidance and funding for this research project. I also want to thank Jochen Schieck for the support and additional funding in the beginning of the project. I am grateful to Suchita Kulkarni and Wolfgang Waltenberger for introducing me to particle physics in my master thesis and beyond and for the exciting discussions we had. Thanks to all colleagues at UGent, with special thanks to Gianny Mestach, for their hospitality during my stay in Ghent and the collaboration during this project. I also want to thank all current and former PhD, master, bachelor, and project work students I worked with at HEPHY during the last years. I am grateful to Daniel Spitzbart, Navid Rad, Markus Spanring, Thomas Madlener, Mateusz Zarucki, all Lukases, and everyone I had the joy working and sharing the office with. Thank you for the help and collaboration over the years.

I want to thank all my friends, with special thanks to Dominic Blöch, Caroline Gossler, Nicole Zechner, Lukas Weichhart, Priya Hussain, Janik Andrejkovic, Felix Ulrich-Pur, and Maja Sajatovic. It started as colleagues at HEPHY or university, who became true friends outside of HEP and work. Speaking about true friends, I especially want to thank Sebastian Templ. There were times where I spent more time with you than with anyone else. I am very grateful that I met you on the first day of university, for sharing so many courses, but especially for the enjoyable moments outside of work. Thank you all for joining the road with me and for the support during the years. I will always be there to take the Hobbits to Isengard with you again.

I am also grateful to my parents, my sister Sandra, and my brother Benjamin. Thank you for your support during tough times, for your guidance in making the right decisions, your encouragements, and for being there whenever I needed you the most.

At last, I would like to express my sincere appreciation and thanks to Claudia. Thank you for believing in me and never losing trust. I cannot thank you enough for your support, the discussions we had and will have, and all the joy you brought to my life. Without you, this would not have been possible. I am looking forward to all the wonderful years ahead with you.

Thank you!

Die approbierte gedruckte Originalversion dieser Dissertation ist an der TU Wien Bibliothek verfügbar.
The approved original version of this doctoral thesis is available in print at TU Wien Bibliothek.
TU Bibliothek Your knowledge hub WIEN